EBM Experimental Biology and Medicine

Volume 250 | Issue 9

Experimental Biology and Medicine

Editor-in-Chief

Nicola Conran
University of Campinas, Brazil

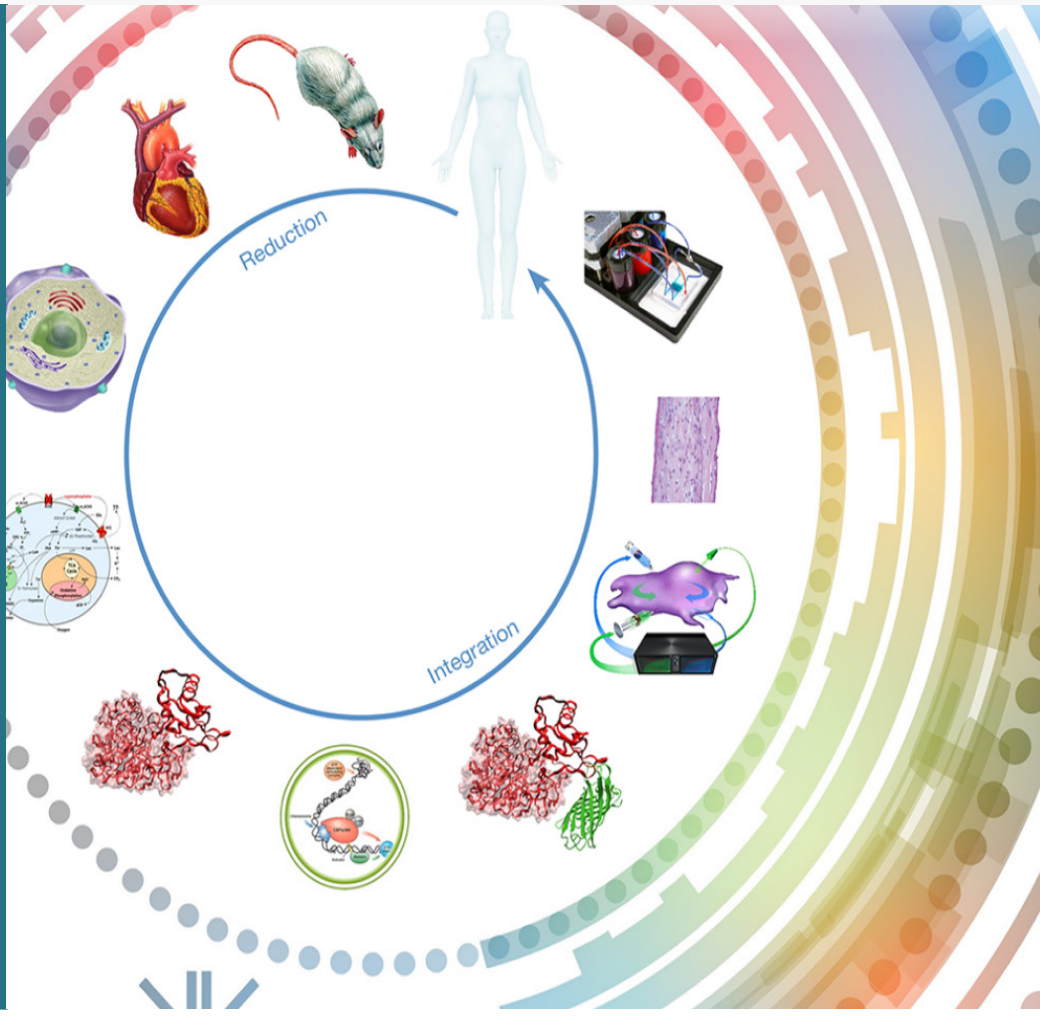

ISBN 978-2-8325-7295-5
DOI 10.3389/978-2-8325-7295-5

frontiers | Publishing Partnerships

Society for Experimental Biology and Medicine
3220 N Street NW, #179
Washington DC 20007, USA
Executive Director – ed@sebm.org

www.sebm.org

EBM Experimental Biology and Medicine

Editorial Board

ISSN 1535-3699
ISBN 978-2-8325-7295-5
DOI 10.3389/978-2-8325-7295-5

Generative AI statement
Any alternative text (Alt text) provided alongside figures in the articles in this ebook has been generated by Frontiers with the support of artificial intelligence and reasonable efforts have been made to ensure accuracy, including review by the authors wherever possible. If you identify any issues, please contact us.

EBM Experimental Biology and Medicine

2025 | Volume 250 | Issue 9 | ISSN 1535-3699

Table of contents

AI in Biology and Medicine

Original Research

07 Bioinformatics-based screening and validation of ferroptosis-related genes in sepsis and type 2 diabetes mellitus

Heng Xiao, Zhonghua Ding, Cheng Liu, Xu He and Yanyan Tao

AI in Biology and Medicine

Original Research

24 High-fidelity, personalized cardiac modeling via AI-driven 3D reconstruction and embedded silicone rubber printing

Xuefang Wang, Yixin Li, Zhiqi Liang, Ruxu Du and Ting Song

Environmental Health/Biomarkers/Precision Medicine

Original Research

39 The causal relationship between obstructive sleep apnea and otitis media: a bidirectional Mendelian randomization study

Ruixin Guo, Yifan Zhang, Yijie Chen, Wenqi Sha, Wanyi Kou, Chensi Xu, Yuran Lei, Ningrui Zhang, Liu Yang, Yun Guo, Huihui Zhang and Zhenghui Wang

Genomics, Proteomics and Bioinformatics

Original Research

49 Glaucoma and cardiovascular disease: a bidirectional two-sample Mendelian randomization analysis

Dongdong Jin, Jie Sun, Wei Zhang, Mingxuan Zhang and Chengfang Li

Genomics, Proteomics and Bioinformatics

Original Research

62 TIMAP downregulation in Burkitt's lymphoma reveals key molecules and signaling pathways in B-cell lymphomagenesis

Marya Obeidat, Saleh Tadros, Batool Ismail and Ayah Al-Khaldi

Infectious Diseases

Brief Communication

79 ApoE COG 133 mimetic peptide improves survival, infection burden, and *Clostridioides difficile* toxin-A-induced intestinal damage in mice

Orleâncio G. R. de Azevedo, Jae H. Shin, Rosemayre S. Freire, Gabriella C. V. Ciurleo, Gerly A. C. Brito, Michael P. Vitek, Richard L. Guerrant, Reinaldo B. Oriá and Cirle A. Warren

Translational Research

Original Research

88 Therapeutic effects of mesenchymal stromal cell secretome in liver fibrosis with acute lung injury

Ane Caroline Ribeiro Novaes Martins, Karina Ribeiro Silva, Anna Carolina de Souza Pereira, Gustavo Claudino Paris, Ana Lúcia Rosa Nascimento, Verônica Aiceles, Erika Afonso Costa Cortez, Alessandra Alves Thole and Simone Nunes de Carvalho

EBM Experimental Biology and Medicine

TYPE Original Research
PUBLISHED 21 October 2025
DOI 10.3389/ebm.2025.10612

OPEN ACCESS

*CORRESPONDENCE
Yanyan Tao,
taoyanyan1981@163.com
Xu He,
HeXu9109@163.com

RECEIVED 01 April 2025
ACCEPTED 09 October 2025
PUBLISHED 21 October 2025

CITATION
Xiao H, Ding Z, Liu C, He X and Tao Y (2025) Bioinformatics-based screening and validation of ferroptosis-related genes in sepsis and type 2 diabetes mellitus.
Exp. Biol. Med. 250:10612.
doi: 10.3389/ebm.2025.10612

Bioinformatics-based screening and validation of ferroptosis-related genes in sepsis and type 2 diabetes mellitus

Heng Xiao[1], Zhonghua Ding[1], Cheng Liu[2], Xu He[3]* and Yanyan Tao[1]*

[1]Department of Emergency Medicine, First Affiliated Hospital of Bengbu Medical University, Bengbu, Anhui, China, [2]Department of Critical Care Medicine, First Affiliated Hospital of Bengbu Medical University, Bengbu, Anhui, China, [3]Department of Pharmacy, Peking University People's Hospital, Beijing, China

Abstract

Emerging clinical evidence underscores a bidirectional epidemiological linkage between sepsis and type 2 diabetes mellitus (T2DM). This study mechanistically investigates the underlying pathogenesis of this comorbidity, specifically focusing on the role of ferroptosis-related genes in its pathogenesis. A total of 1204 shared genes between sepsis and T2DM were screened using datasets from sepsis (GSE65682) and T2DM (GSE76894). GO and KEGG enrichment analyses, combined with WGCNA, were performed to identify key pathways and hub genes. Three signaling pathways—MAPK, adherens junction, and peroxisome—were significantly associated with the sepsis-T2DM interaction. Subsequent Pearson correlation analysis implicated ferroptosis as a critically involved process. Five core ferroptosis-related genes, including CDC25B, DPP7, FBXO31, PTCD3, and CNPY2, were were identified and experimentally validated using qRT-PCR. Furthermore, based on cMAP, we screened eight candidate drugs targeting these genes. Echinacea and Ibudilast were predicted to possess the greatest preclinical potential among them. This study provides a deeper insight into the shared pathogenesis of sepsis and T2DM, highlighting the pivotal role of ferroptosis in the development and progression of this comorbidity. Our findings offer preliminary insights into the sepsis-T2DM comorbidity, highlighting ferroptosis as a potential key pathological mechanism and identifying candidate targets for future therapeutic exploration.

KEYWORDS

ferroptosis, sepsis, type 2 diabetes mellitus, drug prediction, pathway

Impact statement

Advances in modern sequencing technologies, bioinformatics analysis have enabled researchers to explore the interrelationships between diseases and the direct links in their pathogenesis using human samples, rather than relying solely on animal or cellular models. This approach allows for the generation of more robust and convincing conclusions. In this study, we employed bioinformatics analysis combined with qRT-PCR validation to identify key genes and signaling pathways involved in sepsis and T2DM. Our findings provide new insights into the molecular mechanisms underlying ferroptosis in sepsis with T2DM and suggest potential therapeutic interventions for further exploration. This integrative approach holds promise for improving our understanding of this complex disease intersection and informing the development of targeted therapies.

Introduction

Sepsis is a life-threatening condition characterized by a dysregulated host response to infection, leading to organ dysfunction. It remains a major global health challenge, with mortality rates exceeding 10% worldwide [1]. In 2017, sepsis incidence reached 50 million new cases, resulting in 11 million deaths and an alarming mortality rate of 22% [2]. Septic shock accounts for 8–10% of intensive care unit (ICU) fatalities, with persistently high associated mortality [3]. A recent systematic review reported a mortality rate of 27% among sepsis patients, underscoring the urgent need for improved therapeutic strategies [4]. The World Health Organization has identified sepsis and septic shock as critical public health priorities, emphasizing the necessity of enhanced prevention, diagnosis, and treatment strategies [5]. Early identification and intervention of "high-risk" sepsis patients are recognized as critical for improving clinical outcomes, underscoring the demand for novel approaches to reliably stratify patient risk and guide personalized treatment.

The global prevalence of diabetes, particularly T2DM, has been steadily increasing. According to the International Diabetes Federation (IDF), the number of people living with diabetes reached 536 million in 2021 and is projected to rise to 783 million by 2045, with approximately 80% of diabetic patients residing in middle- and low-income countries. The growth rate of diabetes is notably higher in these regions compared to high-income countries [6]. T2DM and its complications remain a leading cause of hospitalization, disability, and mortality [7, 8]. Hyperglycemia significantly increases the risk of infection, with diabetic patients exhibiting a 2-6-fold higher likelihood of developing sepsis-related complications compared to non-diabetic individuals [9–14]. Furthermore, diabetic patients demonstrate increased sepsis-associated morbidity and mortality, potentially due to impaired immune responses and delayed resolution of inflammation. Additionally, diabetic patients show higher rates of colonization by drug-resistant pathogens, including methicillin-resistant *Staphylococcus aureus* (MRSA), compared to non-diabetic patients [15]. These observations underscore the critical role of diabetes as a significant comorbidity in sepsis pathophysiology.

Ferroptosis, an iron-dependent form of regulated cell death driven by lipid peroxide accumulation, has emerged as a key mechanism in disease progression. Excessive reactive oxygen species (ROS) generation creates a pro-inflammatory microenvironment, driving pathological changes through lipid peroxidation and subsequent damage to biomolecules and cellular membranes [16]. This process triggers multiple forms of regulated cell death including ferroptosis [17, 18].In the report by Meng et al, it was demonstrated that the upregulation of HMOX1 is the cause of increased ferroptosis during the development of diabetic atherosclerosis [19]. Growing evidence indicates that ferroptosis occurs mainly under conditions such as metabolic disorders and oxidative stress and that ferroptosis in immune or other cell types can modulate the immune response, thereby contributing to the pathogenesis of both sepsis and T2DM [20].The present study was initially inspired by two considerations: firstly, while the established literature acknowledges the role of ferroptosis in sepsis and the epidemiological association between T2DM and severe infection [21], we noted a distinct lack of direct evidence focusing on ferroptosis-related genes in the specific comorbid context of human sepsis and T2DM. Secondly, our clinical observations were consistent with this documented comorbidity [22]. It was this identified gap that prompted our study to explore potential underlying mechanisms. Our findings provide preliminary evidence suggesting ferroptosis as a plausible pathway, and based on our current knowledge, we believe this may be an early contribution to this particular area of inquiry.

Advances in modern sequencing technology and bioinformatics have enabled researchers to explore the interrelationships among diseases and the direct links in their pathogenesis using human samples, rather than relying solely on animal or cellular models [23]. This approach allows for the generation of more robust and convincing conclusions. In this study, we employed bioinformatics analysis combined with qRT-PCR validation to identify key genes and signaling pathways involved in sepsis and T2DM. Based on these findings, we hypothesized that ferroptosis-related genes (FRGs) may serve as shared genetic mediators contributing to the worse outcomes of sepsis in patients with T2DM. Using integrated bioinformatics analysis of public sepsis and T2DM GEO datasets, we aimed to identify and validate candidate FRGs, explore their immune microenvironment associations, and assess their diagnostic value in sepsis complicating T2DM.

Materials and methods

Data download

The Series Matrix File data file of GSE76894 was downloaded from NCBI GEO public data[1], annotated as GPL570, and the expression profile data of 103 patients were included, of which control group 84 cases and 19 cases in the disease group. Download the Series Matrix File data file of GSE65682 from NCBI GEO public database, the annotated file is GPL13667, a total of 802 patients were included in the expression profile data, of which 42 cases were in the control group and 760 cases were in the disease group (Supplementary Table S1). All datasets were preprocessed to ensure data quality and consistency, including background correction, normalization, and batch effect removal.

Differential expression and functional enrichment analysis

Differential expression analysis was conducted using the R package "Limma". This method identified genes showing significant differential expression between disease samples and control groups. A significance threshold of $p < 0.05$ was applied. The log2 fold change cutoff was set at $|log2FC| > 0$ following iterative adjustments to retain a robust gene set for downstream analyses. DEGs were visualized using volcano plots and heatmaps. Functional annotations for the identified genes were explored with the R package "ClusterProfiler." Gene Ontology and Kyoto Encyclopedia of Genes and Genomes analyses assessed associated biological themes and pathways. Terms and pathways with both p-values and corrected q-values below 0.05 were deemed statistically significant.

WGCNA analysis

A weighted gene co-expression network was constructed using the WGCNA-R package. This approach identifies gene modules with highly correlated expression patterns. The analysis transformed a weighted adjacency matrix into a topological overlap matrix (TOM) to assess network connectivity. Hierarchical clustering was then applied to the TOM matrix, generating a clustering tree structure. Distinct branches of this tree correspond to different gene modules, with each module represented by a unique color. Genes were assigned to modules based on their expression pattern similarities, effectively grouping the entire gene set into multiple co-expression modules.

Immune cell infiltration analysis

The single-sample gene set enrichment analysis (ssGSEA) was employed to evaluate immune cell composition within the microenvironment. This method quantifies 29 distinct human immune cell phenotypes, encompassing T cells, B cells, and natural killer cells. The analysis utilized a validated custom gene set (immune.gmt), widely applied in tumor immunology. This gene set integrates core immune cell signatures from Bindea et al [24]. With critical functional features, including immune checkpoints and cytolytic activity, from Danaher et al [25]. The ssGSEA algorithm estimated relative abundances of 29 immune cell types from the gene expression profiles. Spearman correlation analysis was subsequently performed to assess relationships between gene expression and immune cell infiltration levels. For data preprocessing, probe expression values corresponding to duplicate gene symbols were averaged to ensure gene symbol uniqueness. Genes showing zero average expression across all samples were excluded from the analysis, retaining only those with detectable expression signals.

Transcriptional regulation analysis of key genes

Transcription factor prediction was conducted using the R package "RcisTarget." All analyses in this package are grounded in motif-based assessments. The normalized enrichment score (NES) for each motif is calculated relative to the complete motif database. Additional annotation files were generated by leveraging motif similarity and corresponding gene sequences. The analytical process first involved calculating the area under the curve for each motif and gene set pair. This calculation derived from recovery curves generated through gene-set-to-motif sequencing. Subsequently, the NES for individual motifs was determined by comparing their area under the curve (AUC) values against the distribution of all motifs within the gene set.

miRNA network construction

MicroRNAs (miRNAs) are short non-coding RNAs that mediate post-transcriptional regulation via mRNA degradation or translational repression. This study investigated potential miRNA regulation of candidate genes. Experimentally validated miRNAs targeting the key genes were identified through the miRcode database. A comprehensive miRNA-mRNA interaction network was subsequently constructed and visualized using Cytoscape software.

Cmap drug prediction

The Connectivity Map (CMap) resource, developed by the Broad Institute [26], provides a gene expression profiling

1 https://www.ncbi.nlm.nih.gov/geo/info/datasets.html

database that captures cellular responses to chemical perturbations. This platform enables the discovery of functional relationships between small molecules, genes, and disease states. The database comprises microarray data documenting expression changes induced by 1309 small molecule compounds across five human cell lines [27]. Treatment conditions vary substantially, incorporating different concentrations and exposure durations. This study utilized disease-specific differentially expressed genes to predict potential therapeutic compounds from the CMap database.

Collection of patients and healthy controls

The study enrolled fifteen participants comprising five sepsis patients with T2DM comorbidity, five sepsis patients without diabetes, and five healthy controls. All patient recruitment was conducted through the Department of Emergency Internal Medicine at the First Affiliated Hospital of Bengbu Medical University (Supplementary Table S2). T2DM diagnosis followed the American Diabetes Association 2021 criteria [28], requiring meeting at least one of these laboratory parameters: random plasma glucose ≥11.1 mmol/L, 2-h OGTT plasma glucose ≥11.1 mmol/L, fasting plasma glucose ≥7.0 mmol/L, or glycated hemoglobin A1C ≥ 6.5%. The study protocol received approval from the Human Ethics Committee of the First Affiliated Hospital of Bengbu Medical University. All procedures conformed to the ethical principles outlined in the Helsinki Declaration.

Total RNA extraction and qRT-PCR

Morning fasting peripheral blood samples (5 mL) were collected in ethylene diamine tetraacetic acid (EDTA) containing tubes from all participants. Plasma separation was achieved through centrifugation. Peripheral blood mononuclear cells (PBMCs) were subsequently isolated via Ficoll gradient centrifugation. Total RNA extraction utilized RNAiso Plus reagent (Takara, Japan). Reverse transcription was performed with the 5 × PrimeScript RT Master Mix (Takara, Japan). PCR amplification employed the TB Green PCR Core Kit (Takara, Japan) on a CFX96TM real-time system (Bio-Rad, United States). The housekeeping gene Beta-actin served as an internal reference for normalization. Relative mRNA expression levels were determined using the 2^{-} (−ΔΔCT) method. All primer sequences appear in Supplementary Table S3. Statistical analysis of qRT-PCR data involved ANOVA implementation in GraphPad Prism (v6.0). A threshold of $p < 0.05$ defined statistical significance.

Statistical analysis

All statistical analyses were performed using R language (version 4.2.2). All statistical tests were two-sided and $p < 0.05$ was statistically significant.

Results

Identification of differential expression genes and functional enrichment analysis

The overall workflow of this study is summarized in the Figure 1. Gene expression profiles were obtained from two publicly available datasets: GSE76894 (NCBI GEO) comprising 103 individuals (84 healthy controls and 19 T2DM patients), and GSE65682 (NCBI GEO) containing data from 802 sepsis patients (42 healthy controls and 760 disease cases). Differential gene expression analysis was performed using the Limma R package, with a significance threshold set at $P < 0.05$, $|\log2\ FC| > 0$. This analysis identified 4,945 DEGs in the T2DM dataset (2460 were upregulated, and 2485 were downregulated) and 9061 DEGs in the sepsis dataset (4983 upregulated and 4078 downregulated) (Figure 2A). Intersection analysis identified 1,204 shared DEGs (707 upregulated and 497 downregulated), highlighting genes commonly dysregulated in both conditions (Figure 2B).

Functional annotation of these intersecting genes was conducted via GO and KEGG enrichment analyses. GO terms revealed significant enrichment in processes such as regulation of supramolecular fiber organization, protein localization to organelles, and protein modification. KEGG pathway analysis highlighted involvement in key signaling pathways including the MAPK cascade, adherens junction formation, and peroxisomal β-oxidation. These findings underscore shared molecular mechanisms underlying T2DM and sepsis pathobiology (Figure 2C).

Identification of key genes and diagnostic efficacy via WGCNA

To systematically identify key genes associated with disease progression and assess their diagnostic potential, we conducted a comprehensive analysis using WGCNA on two independent datasets (GSE76894 and GSE65682). This approach enabled us to uncover shared molecular mechanisms underlying T2DM and sepsis. In the GSE76894 dataset, we determined an optimal soft-threshold power (β) of 17 to ensure the formation of a scale-free network topology, a hallmark of biological networks. Hierarchical clustering of the topological overlap matrix (TOM) revealed five distinct gene modules (Figure 3A). Notably, the blue module exhibited the highest

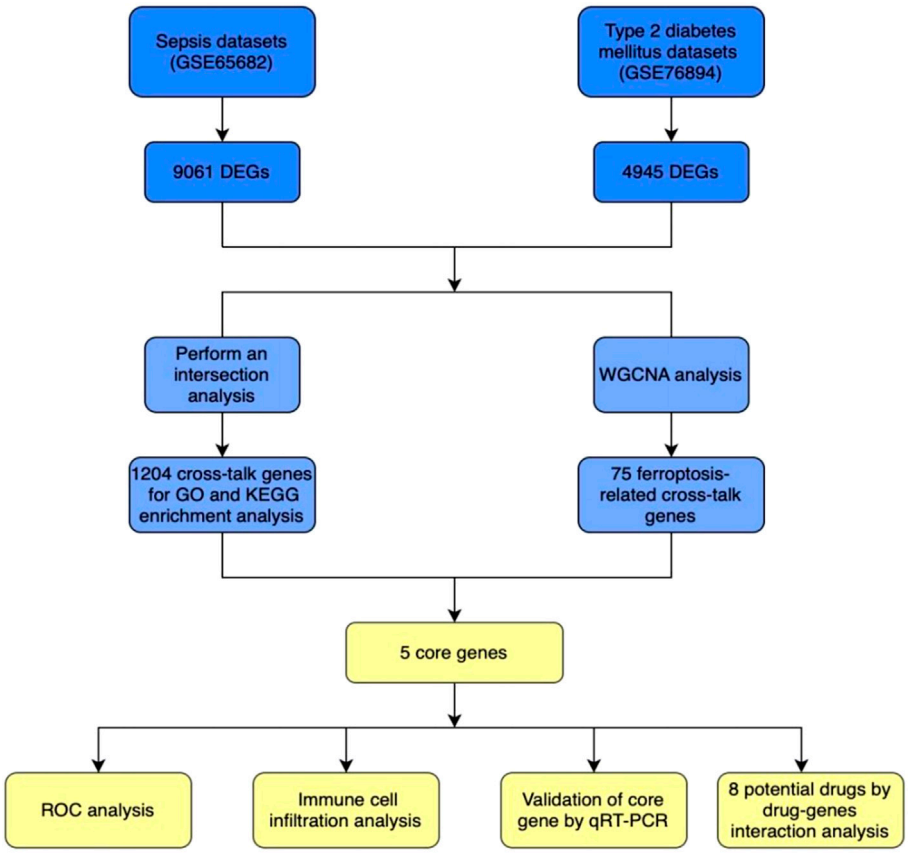

FIGURE 1
The detailed procedures of this study.

correlation with T2DM (correlation coefficient = 0.86, p = 6e-31), suggesting its relevance to disease pathogenesis. In the GSE65682 dataset, a β value of 19 was selected to preserve network scale-free properties. This analysis yielded twelve gene modules (Figure 3B), with the magenta module showing the strongest negative correlation with sepsis (correlation coefficient = −0.61, p = 5e-83). We have supplemented the version of the R package used in this study in the Supplementary Table S4.

To identify overlapping genes between the two datasets, we performed an intersection analysis of the most disease-associated modules, resulting in 75 shared genes (Figure 3C). Further refinement by intersecting these genes with previously identified DEGs yielded five candidate genes: CDC25B, DPP7, FBXO31, PTCD3, and CNPY2 (Figure 3C), These genes emerged as promising biomarkers for both T2DM and sepsis, warranting further investigation into their functional roles.

To evaluate their diagnostic utility, we performed receiver operating characteristic (ROC) curve analysis. In the GSE65682 sepsis dataset, these genes showed high discriminative ability, with AUC values reaching 0.970 (CDC25B), 0.965 (FBXO31), and 0.967 (PTCD3) (Figures 3D,E). The specific AUC and NES thresholds have been provided in the Supplementary Table S5. These results suggest a strong discriminative ability of these genes for sepsis within this specific dataset. However, these results were obtained from a single dataset and require validation in independent cohorts before any clinical application can be considered.

Deciphering the immune microenvironment and key gene correlations in T2DM

The immune microenvironment, a dynamic interplay of immune cells, extracellular matrix components, growth factors, inflammatory mediators, and distinct physicochemical properties, is pivotal for shaping disease progression, diagnostic outcomes, and therapeutic responses. To investigate the role of key genes in T2DM progression, we conducted a comprehensive analysis of their associations with immune infiltration using the GSE76894 dataset. Quantitative assessment of immune cell

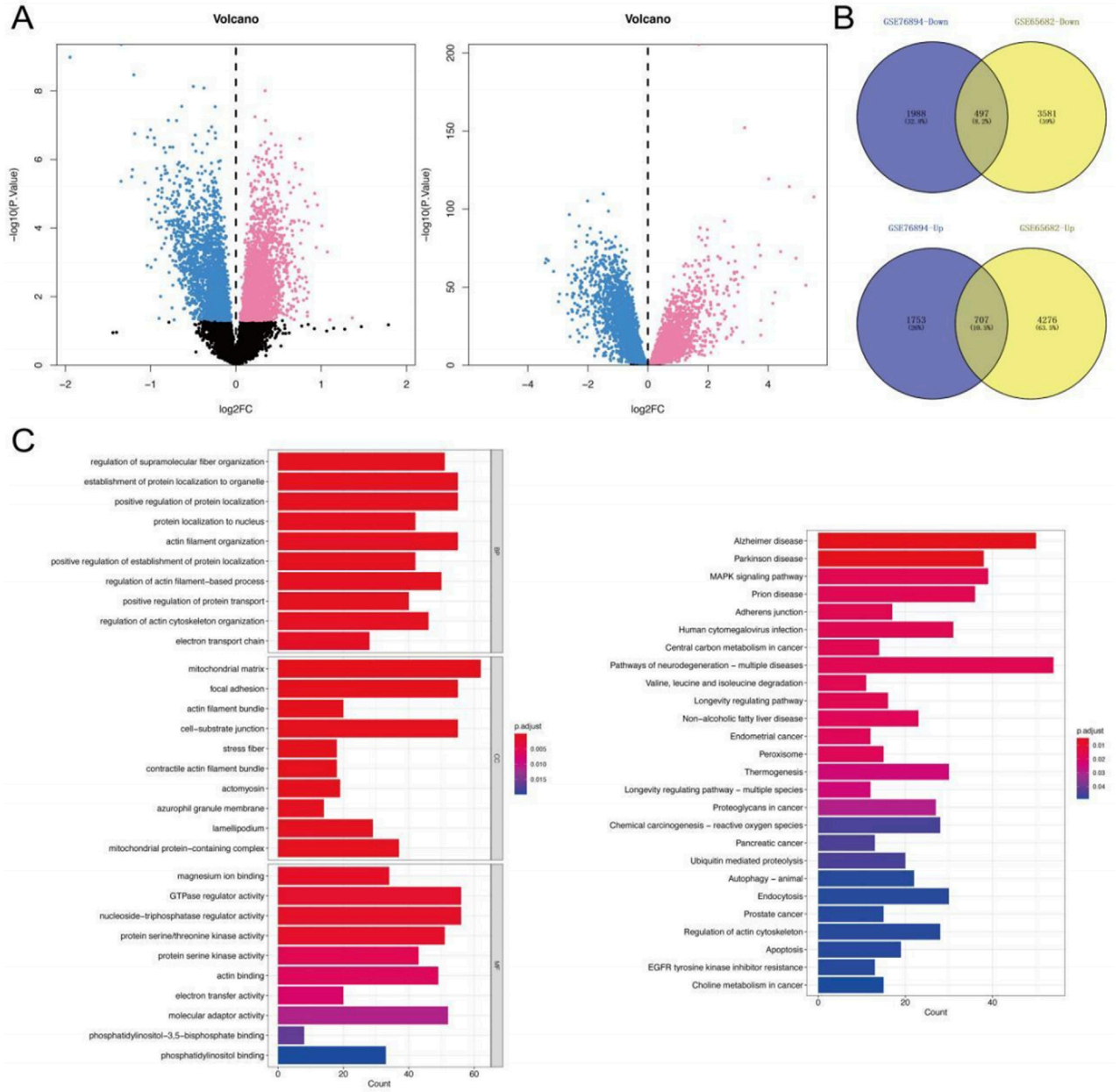

FIGURE 2
DEGs and Function enrichment analysis. **(A)** GSE76894 and GSE65682 datasets showed the Down and Up-regulated genes in Volcano map. (Up-regulated genes are marked in red and down-regulated genes in blue). **(B)** Venn diagrams of intersecting genes from two databases. **(C)** GO and KEGG enrichment analysis of DEGs. $P < 0.05$ is considered significant.

composition across patients revealed significant differences in immune cell distribution between T2DM patients and healthy controls (Figures 4A,B). Specifically, T2DM patients exhibited elevated levels of B cells, chemokine receptor activity (CCR), cytolytic activity, plasmacytoid dendritic cells (pDCs), and Type II interferon response compared to controls (Figure 4C), indicating an active yet potentially dysregulated immune landscape.

We further examined correlations between the key genes and immune features. CDC25B was positively correlated with tumor-infiltrating lymphocytes (TILs), Th1 cells, and macrophages, while negatively correlated with T-cell co-stimulation, B cells, and CCR (Figure 4D). DPP7 was positively correlated with Th1 cells, neutrophils, and TILs, and negatively correlated with CCR, APC co-inhibition, and checkpoint proteins

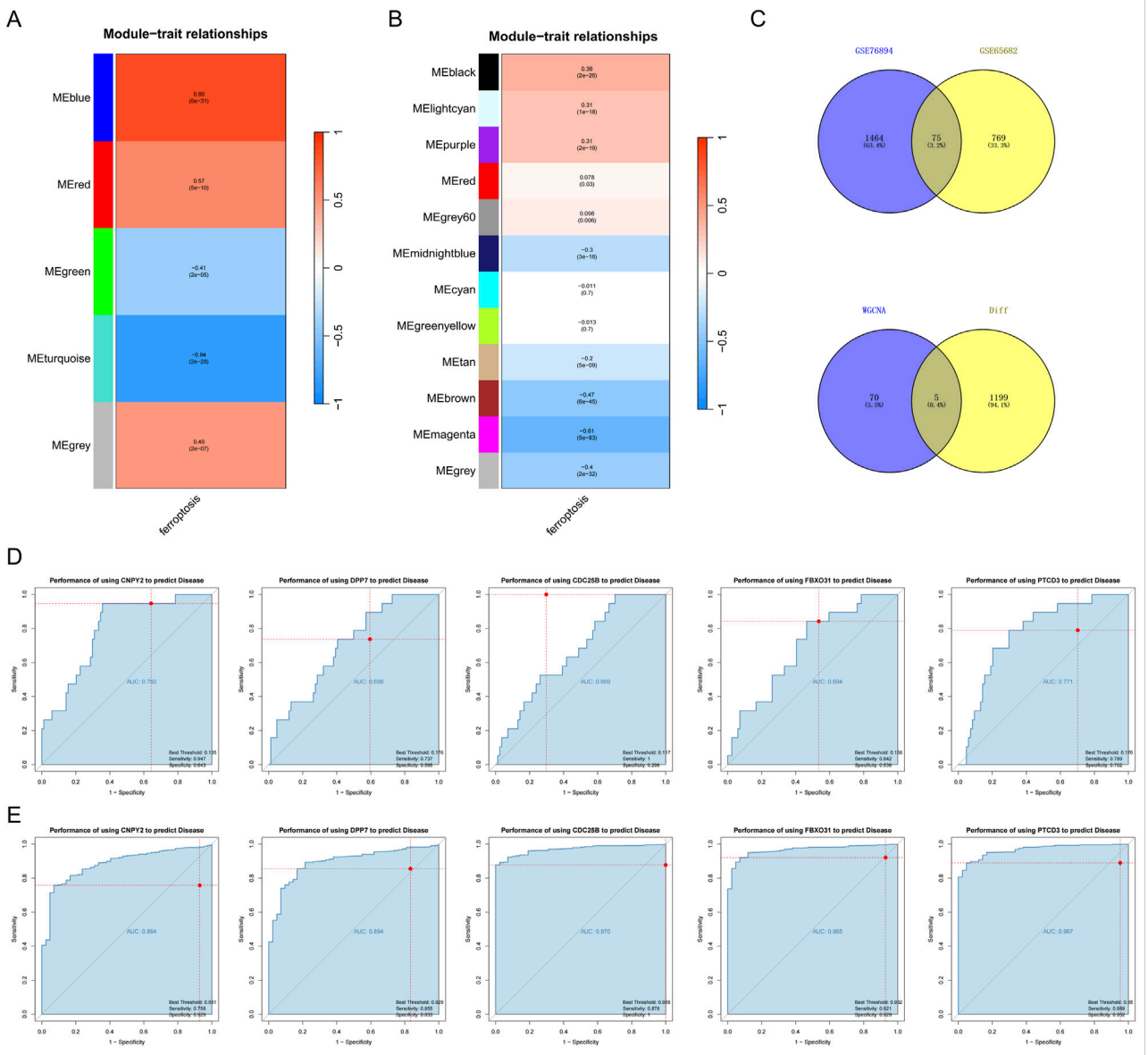

FIGURE 3
Key genes and the Diagnostic Efficacy. **(A)** Genes highly associated with T2DM in the GSE76894 database; **(B)** genes negatively associated with sepsis in the GSE65682 database; **(C)** Intersection of genes in the most relevant modules of the two database sets. **(D,E)** ROC curve analysis.

(Figure 4D). Similarly, FBXO31 demonstrated significant positive correlations with Th1_cells, Mast_cells, TIL, and significantly negatively correlated with B_cells, CCR, Type_II_IFN_Reponse (Figure 4D). PTCD3 was significantly positively correlated with Neutrophils, Th1_cells, TIL, and significantly negatively correlated with CCR, APC_co_inhibition, Check -point (Figure 4D). CNPY2 was significantly positively correlated with Th1_cells, Mast_cells, TIL, and significantly negatively correlated with B_cells, CCR, Type_II_IFN_Reponse (Figure 4D). Together, these results suggest that the key genes play multifaceted roles in shaping immune responses in T2DM, potentially contributing to immune dysregulation and disease pathogenesis.

Immune microenvironment and key gene interactions in sepsis

To investigate the role of key genes in modulating immune responses during sepsis, we analyed the GSE65682 dataset. Quantification of immune cell composition and examination of immune cell interactions revealed distinct immunological

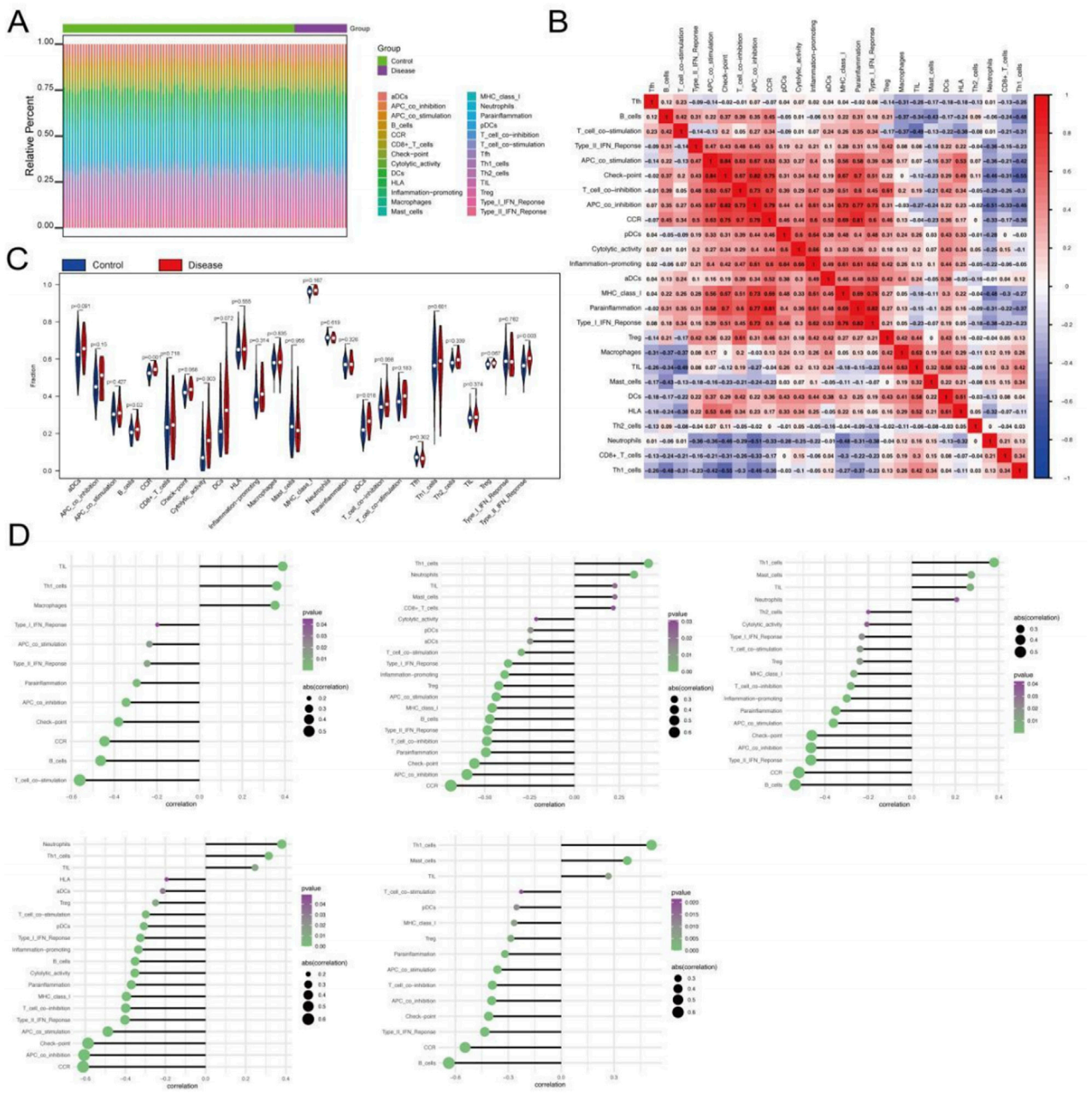

FIGURE 4
Relationship between genes and immune infiltration. **(A–C)** Immune cell infiltration differences between T2DM patients and controls. **(D)** Correlation between key genes and immune cell types.

signatures in sepsis (Figure 5A). Compared to healthy controls, sepsis patients exhibited significantly elevated levels of Tregs (regulatory T cells), Type II interferon response, and immature dendritic cells (iDCs) (Figure 5B), suggesting a unique immune landscape in sepsis, characterized by augmented regulatory and inflammatory pathways, potentially reflecting the complex interplay between immune activation and systemic inflammation.

We further explored the relationships between the key genes and immune cell infiltration. CDC25B expression showed positive correlations with TILs, T-cell co-stimulation, and $CD8^+$ T cells, while negatively correlated with Tregs, neutrophils, and macrophages (Figure 5C). Similarly, DPP7 was positively correlated with TILs, HLA (human leukocyte antigen), and T-cell co-stimulation, while

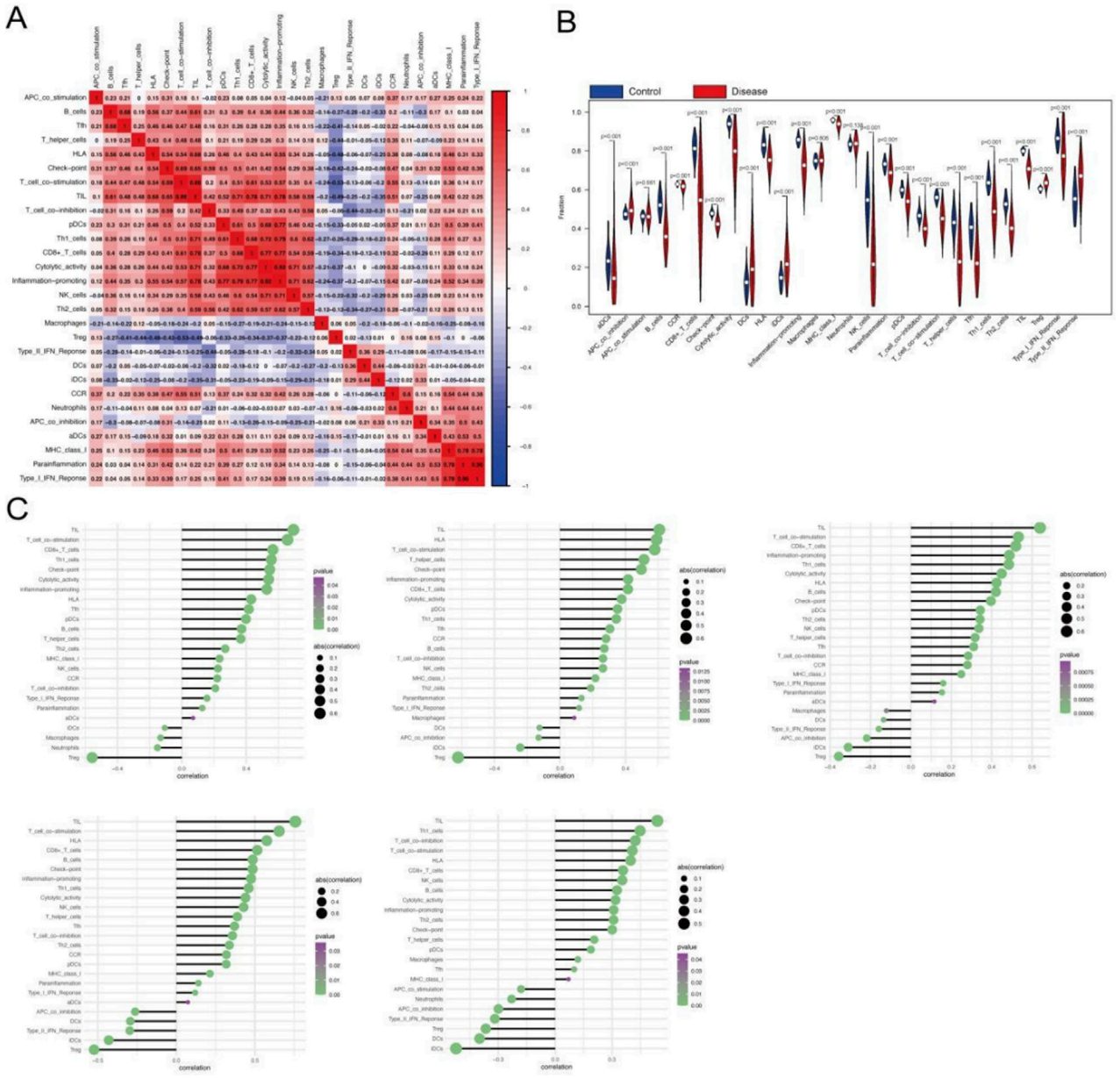

FIGURE 5
Relationship between genes and immune infiltration in the GSE65682 dataset. **(A,B)** Differential expression of immune cell infiltration between disease and healthy controls. **(C)** Correlation between key genes and immune cell types.

negatively correlated with Tregs, iDCs, and APC co-inhibition (Figure 5C). Related patterns were observed for FBXO31, PTCD3, and CNPY2, which also demonstrated significant correlations with multiple immune cell subsets (Figure 5C), underscoring their collective involvement in sepsis immunopathology. These findings suggest that the identified key genes may help shape the immune microenvironment in sepsis, potentially influencing disease progression and immune regulation.

Immunoregulatory roles of key genes in both T2DM and sepsis

To investigate the immunoregulatory roles of the identified key genes in T2DM and sepsis, we conducted an integrative analysis using the TISIDB database to examine their correlations with immunomodulatory factors—including immunosuppressants, immunostimulators, chemokines, and receptors. Results demonstrated that these genes exhibit intricate associations with

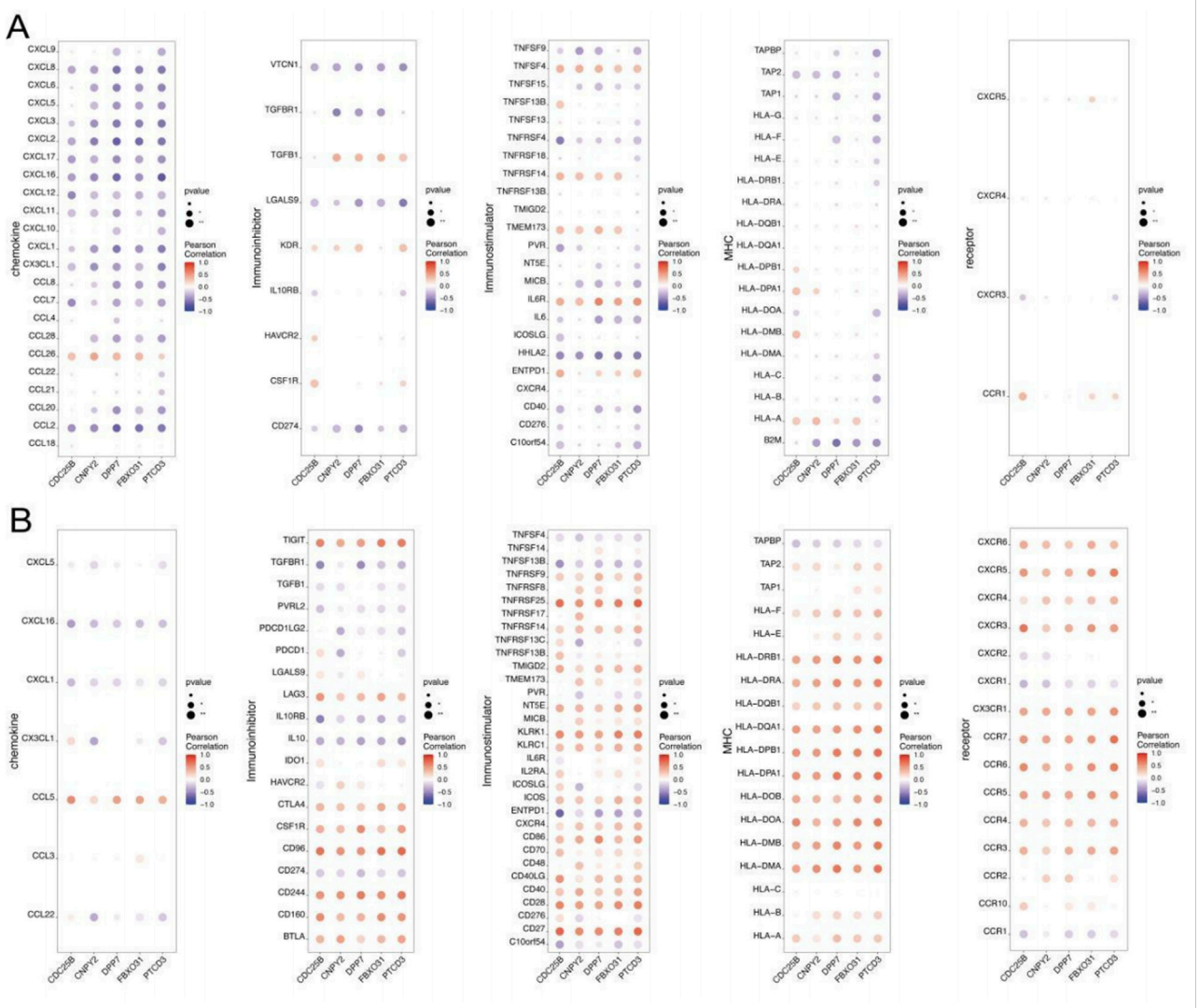

FIGURE 6
(A,B) Correlation between key genes and various immunomodulators in the TISIDB database.

immune cell infiltration levels and are likely involved in shaping the immune landscape of both diseases (Figures 6A,B). While the observed correlations between key genes and immune cell populations provide intriguing insights into potential immune mechanisms, we acknowledge that these findings are derived from computational deconvolution algorithms which have inherent limitations. The correlations may reflect both biological relationships and methodological constraints. However, the consistency of patterns across multiple genes and the alignment with known biology of these diseases (e.g., the elevated levels of Tregs and Type II interferon response in sepsis) suggest that at least some of these associations are biologically meaningful. Future studies with single-cell RNA sequencing or flow cytometry validation are needed to confirm these findings and distinguish true biological signals from potential computational artifacts. The elevated levels of regulatory T cells and type II interferon responses in sepsis patients reported in relevant literature can provide certain reference basis [29]. Further validation using single-cell RNA sequencing or flow cytometry will be essential to confirm these relationships and distinguish true immune regulatory mechanisms from analytical noise.

Regulatory mechanisms underlying key gene expression

We next investigated the potential regulatory mechanisms of the five key genes through transcription factor (TF) and miRNA analyses. TF enrichment analysis revealed cisbp_M5975 as the top motif (NES = 8.73), suggesting a primary role in transcriptional regulation (Figure 7A). Concurrently, miRcode-based screening

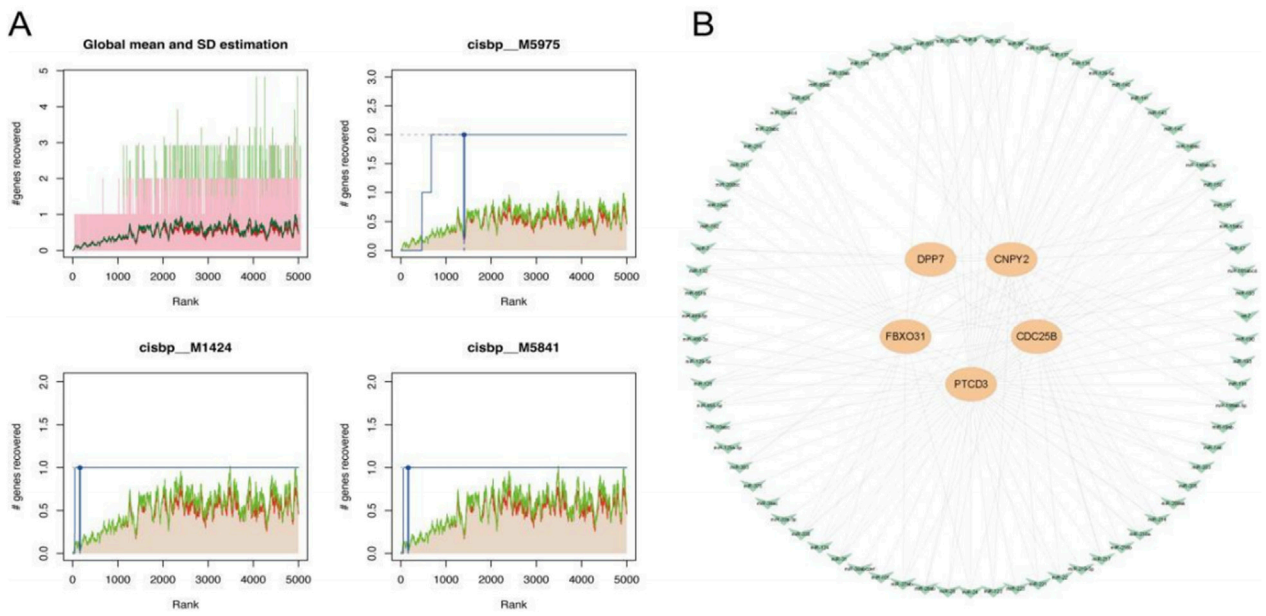

FIGURE 7
(A) TF enrichment analysis based on cumulative recovery curve and motif annotation; **(B)** miRNA-mRNA interaction.

identified 76 miRNAs forming 156 regulatory pairs with the key genes, visualized as a complex network in Figure 7B. These findings uncover transcriptional and post-transcriptional regulatory layers, highlighting potential intervention points for T2DM and sepsis.

Analysis of disease-associated genes and drug prediction in type 2 diabetes and sepsis

We further explored the expression patterns of disease-associated genes by retrieving T2DM-related genes from the GeneCards database[2]. Analysis of top-ranked T2DM genes revealed significant expression differences between control and disease groups for genes including ABCC8, GCK, HNF1A, HNF1B, INS, INSR, and WFS1 (Figure 8A). Notably, PTCD3 showed a strong positive correlation with ABCC8 (Pearson r = 0.714), while DPP7 was negatively correlated with INSR (Pearson r = −0.634) (Figure 8A). These findings suggest potential co-regulatory mechanisms involving these genes in T2DM pathogenesis.

Similarly, sepsis-related genes obtained from GeneCards were analyzed across patient groups. Genes such as CSF3, ELANE, F5, and GALT exhibited significant differential expression between sepsis patients and controls (Figure 8B). Correlation analysis showed that CNPY2 was positively correlated with MIF (Pearson r = 0.69), while CDC25B was negatively correlated with TLR2 (Pearson r = −0.616) (Figure 8B). These correlations suggest that the key genes may be involved in shared molecular pathways influencing both T2DM and sepsis pathogenesis.

To identify potential therapeutic interventions, we used the CMap database to predict drugs targeting the DEGs in T2DM and sepsis. CMap drug prediction was performed using differentially expressed genes derived from the expression profiles of the two diseases. Genes were selected based on log2FC, with the top 150 up-regulated genes and the top 150 down-regulated genes being used for the analysis. For T2DM, whose perturbational gene expression profiles were negatively correlated with the disease signature, including ISOX, THM-I-94, Vorinostat, and WT-171 (Figure 8C)—corresponding to the top four compounds with the lowest connectivity scores (denoted as "Score") in the Supplement2. Similarly, for sepsis, analysis highlighted AZD-8055, GW-843682X, HLI-373, and Phenazone as potential therapeutics, corresponding to the top compounds in the Supplement3 and showing strong negative correlations with the sepsis expression profile (Figure 8D), suggesting their potential to attenuate the septic condition.

Validation of core gene expression by qRT-PCR

To experimentally validate our findings, we quantified the expression levels of the shared genes across different sample groups using qRT-PCR (Figure 9). The results demonstrated a

2 https://www.genecards.org/

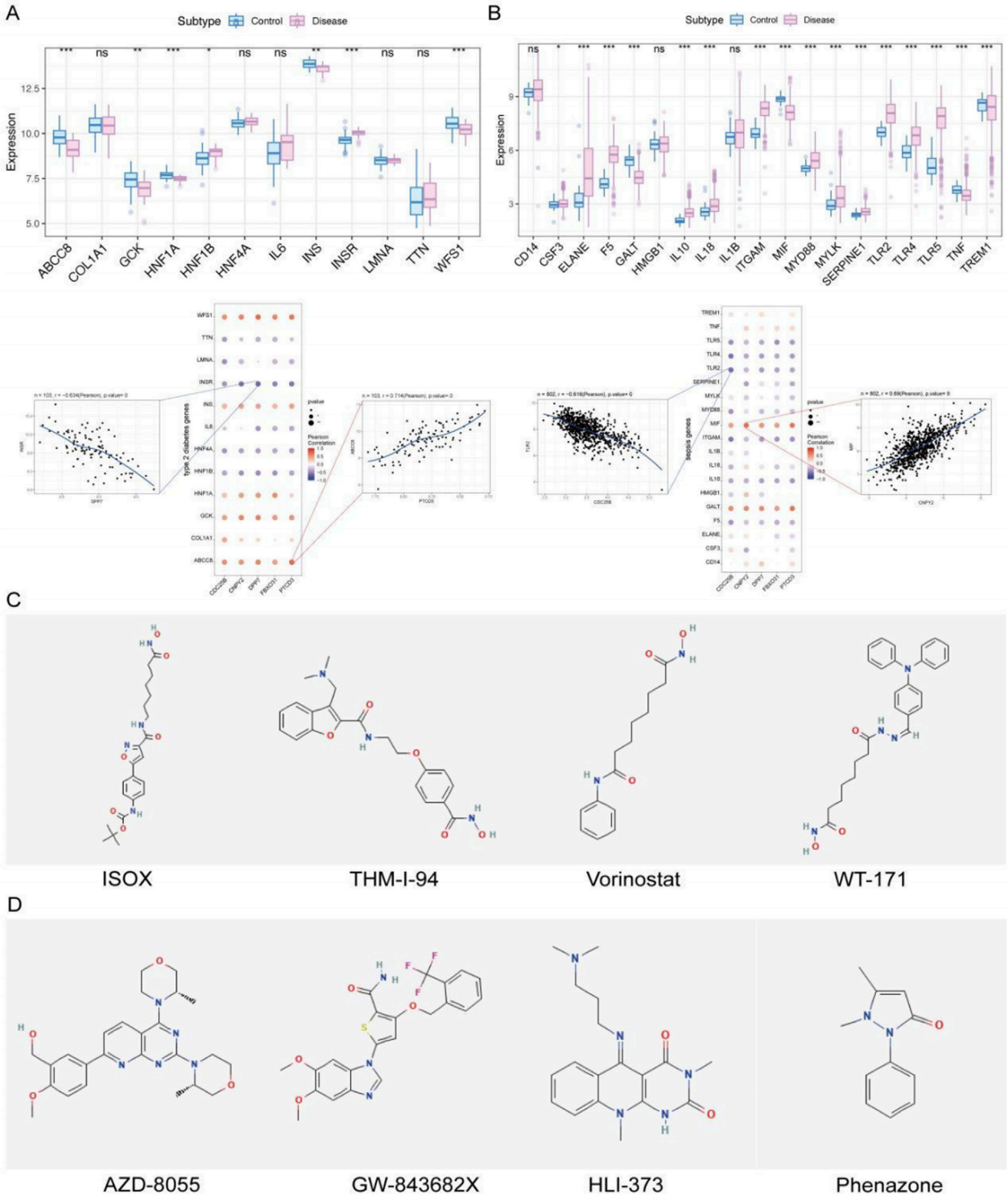

FIGURE 8
(A,B) Expression patterns of disease-related genes in T2DM and sepsis, along with correlations between key genes and disease-related genes. **(C,D)** Drug repurposing predictions using the CMap database for T2DM and sepsis, showing candidate drugs with negative correlations to disease-specific expression profiles.

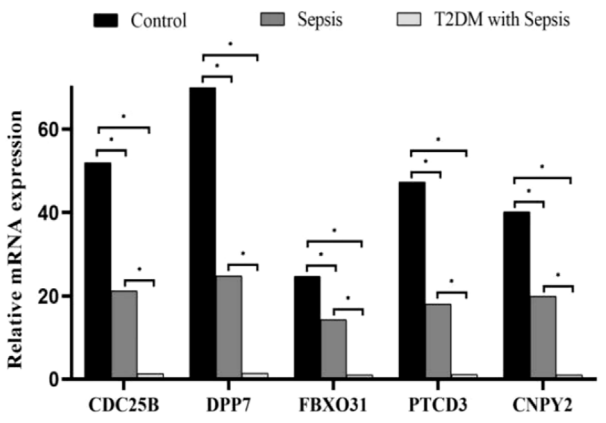

FIGURE 9
qRT-PCR validation of core gene expression levels across different groups. Relative expression levels of CDC25B, DPP7, FBXO31, PTCD3 and CNPY25 were compared between control, sepsis, and sepsis with T2DM groups. Data were analyzed using one-way ANOVA, with $P < 0.05$ indicating statistical significance (*$P < 0.05$).

significant reduction in the mRNA levels of these genes in the sepsis group compared to the control group ($P < 0.05$). Notably, the expression was further decreased in patients with sepsis complicated by T2DM ($P < 0.05$).

Discussion

The burden of sepsis and its association with T2DM

Sepsis accounts for nearly 20% of global annual deaths, with more than 20 deaths occurring per minute due to sepsis-related complications [30]. It remains one of the most severe acute complications in critically ill patients, particularly those with infections [31]. Beyond its acute effects, sepsis is associated with poor long-term outcomes, including high hospitalization costs, prolonged recovery periods, and significant health burdens, which severely impacts patients' quality of life. This highlights the critical need for early prevention and treatment of sepsis.

Patients with diabetes mellitus face a sixfold higher risk of sepsis compared to non-diabetic individuals [32]. Notably, over 20% of sepsis patients also have diabetes mellitus [33]. High blood glucose levels and an increase in the coefficient of variation of blood glucose are significantly associated with mortality from sepsis in the ICU, and the impact on death increases with the severity of sepsis [34].T2DM, which constitutes more than 90% of diabetes cases, is primarily characterized by insulin resistance and β-cell dysfunction, with the latter playing a central role in disease progression. β-cell dysfunction occurs more frequently in critically ill patients because they need to overcome the prevalent insulin-resistant state. Moreover, in patients with severe illness, more than four organ failures or death, β-cell dysfunction often occurs from the very beginning [35].Understanding the molecular and immune mechanisms linking sepsis and T2DM is critical for developing targeted therapies and improving outcomes for patients with these conditions.

Immune dysregulation in sepsis and T2DM

The high morbidity and mortality rates associated with sepsis, particularly among diabetic patients, highlight the importance of understanding the underlying immune dysregulation. Our findings indicate that T2DM may elevates the risk of sepsis, consistent with previous studies indicating that diabetic patients are 2–6 times more likely to develop sepsis than non-diabetic individuals. In T2DM, chronic hyperglycemia contributes to immune dysfunction, increasing susceptibility to infections such as sepsis. Our analysis of immune infiltration in T2DM revealed elevated levels of B cells, chemokine receptor activity (CCR), and Type II interferon response, suggesting an enhanced yet dysregulated immune response.

Sepsis itself is characterized by a complex immune response, often involving both hyperinflammation and immunosuppression. In our analysis of the GSE65682 dataset, we observed increased levels of Tregs, Type II interferon response, and iDCs, reflecting the dual nature of immune dysregulation in sepsis. These findings align with previous studies demonstrating that sepsis could lead to both immune hyperactivity (resulting in tissue damage) and immune suppression (increasing susceptibility to secondary infections).

Key genes involved in sepsis and T2DM pathogenesis

Differential gene expression and co-expression network analyses identified five key genes—CDC25B, DPP7, FBXO31, PTCD3, and CNPY2—that play critical roles in immune response and cellular regulation in sepsis and T2DM.

CDC25B, a key member of the cell division cycle 25 family, is a phosphoprotein essential for cell cycle regulation, particularly the G2/M transition. It was significantly correlated with immune cell populations such as tumor-infiltrating lymphocytes, Th1 cells, and macrophages in sepsis patients, suggesting a role beyond proliferation to immune regulation. Polypyrimidine tract-binding protein 1 (PTBP1), an RNA-binding protein expressed throughout B-cell development, regulates CDC25B mRNA abundance and splicing, further implicating CDC25B in B-cell development and immune function [36]. Our findings suggest that CDC25B may serve as a central mediator of immune cell differentiation and function in sepsis.

DPP7 is a serine protease, also known as quiescent cellular proline dipeptidase (QPP, DPP2, DPPII), which is a proline-cleaved aminopeptidase, a dipeptidyl peptidase capable of removing the

N-terminal dipeptide, and edits proteins that are soluble proteins [37]. Knockdown of DPP7 increased apoptosis, and complete knockout is embryonically lethal in mice. DPP7 has been implicated in immune responses and lymphocyte apoptosis [38, 39]. In our study, DPP7 expression positively correlated with immune activation markers (e.g., T-cell co-stimulation, HLA expression) and negatively with immunosuppressive factors (e.g., Tregs, APC co-inhibition), suggesting a dual role in immune regulation during sepsis and T2DM.

FBXO31, an E3 ubiquitin ligase, is well-known for its role in the DNA damage response where it mediates Cyclin D1 degradation to halt the cell cycle. Notably, a groundbreaking recent study [40] has redefined its function, revealing that FBXO31 also serves as a crucial surveillance mechanism for oxidative protein damage by targeting C-terminal amidated proteins for degradation. Given the central role of oxidative stress in sepsis pathogenesis, we hypothesize that FBXO31 may contribute to immune regulation during sepsis by maintaining proteostasis in immune cells. Specifically, we propose that FBXO31 helps clear oxidatively damaged proteins, thereby preserving cellular function and mitigating immune dysfunction. This proposed mechanism, however, remains a testable hypothesis requiring further experimental validation.

PTCD3, a mitochondrial ribosomal protein, was associated with both immunosuppressive and immunostimulatory factors in sepsis, linking mitochondrial dysfunction to immune dysregulation [41]. Given that mitochondrial dysfunction is a hallmark of ferroptosis, the association between PTCD3 and immune cell regulation may provide a novel mechanism by which ferroptosis contributes to immune suppression and organ dysfunction in sepsis patients.

Ferroptosis as a central mechanism in sepsis and T2DM

Ferroptosis, a form of iron-dependent regulated cell death driven by lipid peroxidation, has emerged as a critical mechanism in the progression of sepsis and T2DM. Iron metabolism is closely linked to β-cell function, participating in insulin secretion, proliferation, differentiation, and glucose metabolism. Dysregulated iron metabolism and ROS accumulation contribute to β-cell loss via ferroptosis. In the context of sepsis, ferroptosis is associated with pathogen-induced inflammatory responses, further connecting iron dysregulation to immune-mediated cell death [42, 43]. Evidence from animal models supports its role: AMPK activation reduced ferroptosis in the hippocampus of mice with diabetes, improving cognitive ability [44]. And nobiletin, a plant-based polymethoxy flavone, can regulate the composition of the intestinal microbiota in septic mice [45]. By modulating the intestinal microbiota, it can alleviate ferroptosis in liver injury caused by sepsis. Our findings further support that ferroptosis may play a key role in the progress of both conditions, particularly in the context of chronic inflammation and oxidative stress. Key genes identified were enriched in ferroptosis-related pathways such as peroxisome signaling, which regulates oxidative stress.

The interplay among iron metabolism, ROS accumulation, and immune dysfunction underscores the importance of ferroptosis in sepsis, especially in diabetic patients. Chronic hyperglycemia predisposes individuals to oxidative stress, exacerbating inflammation and promoting ferroptosis, likely contributing to the increased mortality observed in diabetic sepsis patients.

Implications for therapeutic interventions

Using the CMap database, we identified several potential therapeutic targeting dysregulated pathways in sepsis and T2DM. Compounds such as ISOX and Vorinostat—which has been reported to exhibit efficacy in anti-tumor and anti-epileptic contexts. Notably, Vorinostat, as a histone deacetylase inhibitor, is crucial for the regulation of ferroptosis [46]. THM-I-94 were identified as potential modulators of T2DM-associated gene dysregulation, while drugs like AZD-8055 and HLI-373 showed strong negative correlations with the sepsis gene expression profile, suggesting their potential to attenuate or reverse disease progression in sepsis patients.

In addition, studies have shown that Echinacea extract can be used to improve the immune system and treat respiratory symptoms caused by bacterial infections [47].Ibudilast can act as an inhibitor and bind to phosphodiesterase 4 (PDE4), a new target for inflammatory diseases, to achieve the effect of inhibiting inflammatory responses [48]. The identification of these compounds offers promising avenues for therapeutic intervention.

This study offers important insights into the molecular mechanisms linking sepsis and T2DM, but several limitations should be acknowledged. First, our findings are derived exclusively from publicly available datasets, which may introduce batch effects, platform-specific biases, or demographic limitations that affect generalizability. Second, the immune infiltration estimates were generated through computational deconvolution methods (e.g., CIBERSORT), which infer rather than directly measure immune cell abundances and should be interpreted with caution. Functional experiments are required to confirm these observations. Additionally, while computational methods provided valuable estimates of potential therapeutic drugs, more precise experimental approaches and clinical testing are needed. Finally, the emerging role of ferroptosis in these conditions also requires further exploration. The complex interplay between sepsis, T2DM, and other comorbidities complicates the interpretation of results, highlighting the need for deeper mechanistic studies and validation in diverse patient populations.

To address these limitations mechanistically, we propose a multi-phase experimental framework for future investigation. *In vitro*, we will measure established ferroptosis markers in blood or tissue samples from septic patients with and without T2DM,

correlating these with hub gene expression and clinical parameters to validate the pathophysiological relevance of our findings. Then primary human immune cells will be cultured under high-glucose conditions and subjected to genetic perturbation (e.g., siRNA-mediated knockdown or overexpression) of key hub genes, combined with pharmacological modulation of ferroptosis (including ferroptosis inhibitors (e.g., ferrostatin-1, liproxstatin-1)). These experiments will directly assess effects on ferroptotic markers—such as lipid peroxidation, GPX4 activity, and ACSL4 expression—along with functional immune readouts. *In vivo*, the cecal ligation and puncture model will be employed in diabetic (e.g., db/db) mice, integrating tissue-specific knockout approaches with treatment using candidate compounds to evaluate outcomes including survival, organ injury, and immune status. Finally, the intricate interplay among sepsis, T2DM, and associated comorbidities underscores the critical need for such in-depth mechanistic exploration.

Conclusion

In conclusion, our study indicates the potential importance of key genes including CDC25B, DPP7, FBXO31, and PTCD3 in the shared pathogenesis of sepsis and T2DM. These genes may play a key role in immune regulation, cell cycle control, and ferroptosis, suggesting their promise as candidate therapeutic targets. Through our analysis of the potential molecular connections between these conditions, we provide a conceptual foundation for advancing precision medicine strategies aimed at improving outcomes in patients with sepsis, particularly those with comorbid diabetes. Future research should prioritize experimental validation of the identified candidate targets and further elucidate the functional role of ferroptosis in the progression of sepsis and T2DM.

Author contributions

HX, ZD, CL, and YT conducted the experimental work. The manuscript was primarily written by HX and ZD. HX and XH conceived and designed the research framework. All authors contributed to the article and approved the submitted version.

Data availability

The data utilized in this study were sourced from the NCBI GEO database, accessible at https://www.ncbi.nlm.nih.gov/geo/info/datasets.html.

Ethics statement

The studies involving humans were approved by First Affiliated Hospital of Bengbu Medical University. The studies were conducted in accordance with the local legislation and institutional requirements. The participants provided their written informed consent to participate in this study.

Funding

The author(s) declare that financial support was received for the research and/or publication of this article. This study was supported by Key Natural Science Research Project of Anhui Educational Committee, Grant/Award Number: No. 2023AH051996; Key Natural Project of Bengbu Medical College, Grant/Award Number: Nos 2021byzd157 and 2022byzd039; Traditional Chinese Medicine Research Project of Anhui Association of Traditional Chinese Medicine (No. 2024ZYYXH156).

Acknowledgments

We are grateful for all the financial support for this work.

Conflict of interest

The author(s) declared no potential conflicts of interest with respect to the research, authorship, and/or publication of this article.

Generative AI statement

The author(s) declare that no Generative AI was used in the creation of this manuscript.

Any alternative text (alt text) provided alongside figures in this article has been generated by Frontiers with the support of artificial intelligence and reasonable efforts have been made to ensure accuracy, including review by the authors wherever possible. If you identify any issues, please contact us.

Supplementary material

The Supplementary Material for this article can be found online at: https://www.ebm-journal.org/articles/10.3389/ebm.2025.10612/full#supplementary-material

References

1. Singer M, Deutschman CS, Seymour CW, Shankar-Hari M, Annane D, Bauer M, et al. The third international consensus definitions for sepsis and septic shock (Sepsis-3). *JAMA* (2016) **315**(8):801–10. doi:10.1001/jama.2016.0287

2. Rudd KE, Johnson SC, Agesa KM, Shackelford KA, Tsoi D, Kievlan DR, et al. Global, regional, and national sepsis incidence and mortality, 1990-2017: analysis for the global burden of disease Study. *The Lancet* (2020) **395**(10219):200–11. doi:10.1016/S0140-6736(19)32989-7

3. Vincent JL, Jones G, David S, Olariu E, Cadwell KK. Frequency and mortality of septic shock in Europe and North America: a systematic review and meta-analysis. *Crit Care* (2019) **23**(1):196. doi:10.1186/s13054-019-2478-6

4. Fleischmann-Struzek C, Mellhammar L, Rose N, Cassini A, Rudd KE, Schlattmann P, et al. Incidence and mortality of hospital- and ICU-treated sepsis: results from an updated and expanded systematic review and meta-analysis. *Intensive Care Med* (2020) **46**(8):1552–62. doi:10.1007/s00134-020-06151-x

5. Reinhart K, Daniels R, Kissoon N, Machado FR, Schachter RD, Finfer S. Recognizing sepsis as a global health priority - a WHO resolution. *N Engl J Med* (2017) **377**(5):414–7. doi:10.1056/NEJMp1707170

6. Sun H, Saeedi P, Karuranga S, Pinkepank M, Ogurtsova K, Duncan BB, et al. IDF diabetes atlas: global, regional and country-level diabetes prevalence estimates for 2021 and projections for 2045. *Diabetes Res Clin Pract* (2022) **183**:109119. doi:10.1016/j.diabres.2021.109119

7. Ong KL, Stafford LK, McLaughlin SA, Boyko EJ, Vollset SE, Smith AE, et al. Global, regional, and national burden of diabetes from 1990 to 2021, with projections of prevalence to 2050: a systematic analysis for the global burden of disease study 2021. *The Lancet* (2023) **402**(10397):203–34. doi:10.1016/S0140-6736(23)01301-6

8. Monge L, Gnavi R, Carnà P, Broglio F, Boffano GM, Giorda CB. Incidence of hospitalization and mortality in patients with diabetic foot regardless of amputation: a population study. *Acta Diabetol* (2020) **57**(2):221–8. doi:10.1007/s00592-019-01412-8

9. Schuetz P, Castro P, Shapiro NI. Diabetes and sepsis: preclinical findings and clinical relevance. *Diabetes Care* (2011) **34**(3):771–8. doi:10.2337/dc10-1185

10. Shah BR, Hux JE. Quantifying the risk of infectious diseases for people with diabetes. *Diabetes Care* (2003) **26**(2):510–3. doi:10.2337/diacare.26.2.510

11. Frydrych LM, Fattahi F, He K, Ward PA, Delano MJ. Diabetes and sepsis: risk, recurrence, and ruination. *Front Endocrinol (Lausanne)* (2017) **8**:271. doi:10.3389/fendo.2017.00271

12. Frydrych LM, Bian G, O'Lone DE, Ward PA, Delano MJ. Obesity and type 2 diabetes mellitus drive immune dysfunction, infection development, and sepsis mortality. *J Leukoc Biol* (2018) **104**(3):525–34. doi:10.1002/JLB.5VMR0118-021RR

13. Bertoni AG, Saydah S, Brancati FL. Diabetes and the risk of infection-related mortality in the U.S. *Diabetes Care* (2001) **24**(6):1044–9. doi:10.2337/diacare.24.6.1044

14. Li Q, Gong X. Clinical significance of the detection of procalcitonin and C-reactive protein in the intensive care unit. *Exp Ther Med* (2018) **15**(5):4265–70. doi:10.3892/etm.2018.5960

15. Stacey HJ, Clements CS, Welburn SC, Jones JD. The prevalence of methicillin-resistant *Staphylococcus aureus* among diabetic patients: a meta-analysis. *Acta Diabetol* (2019) **56**(8):907–21. doi:10.1007/s00592-019-01301-0

16. Zhang J, Wang X, Vikash V, Ye Q, Wu D, Liu Y, et al. ROS and ROS-mediated cellular signaling. *Oxidative Med Cell Longevity* (2016) **2016**:4350965. doi:10.1155/2016/4350965

17. Khan I, Yousif A, Chesnokov M, Hong L, Chefetz I. A decade of cell death studies: breathing new life into necroptosis. *Pharmacol and Ther* (2021) **220**:107717. doi:10.1016/j.pharmthera.2020.107717

18. Christgen S, Tweedell RE, Kanneganti TD. Programming inflammatory cell death for therapy. *Pharmacol and Ther* (2022) **232**:108010. doi:10.1016/j.pharmthera.2021.108010

19. Meng Z, Liang H, Zhao J, Gao J, Liu C, Ma X, et al. HMOX1 upregulation promotes ferroptosis in diabetic atherosclerosis. *Life Sci* (2021) **284**:119935. doi:10.1016/j.lfs.2021.119935

20. Zhao P, Li X, Yang Q, Lu Y, Wang G, Yang H, et al. Malvidin alleviates mitochondrial dysfunction and ROS accumulation through activating AMPK-α/UCP2 axis, thereby resisting inflammation and apoptosis in SAE mice. *Front Pharmacol* (2023) **13**:1038802. doi:10.3389/fphar.2022.1038802

21. Xl L, Gy Z, R G, N C. Ferroptosis in sepsis: the mechanism, the role and the therapeutic potential. *Front Immunol* (2022) **13**:956361. doi:10.3389/fimmu.2022.956361

22. Carey IM, Critchley JA, DeWilde S, Harris T, Hosking FJ, Cook DG. Risk of infection in type 1 and type 2 diabetes compared with the general population: a matched cohort study. *Diabetes Care* (2018) **41**(3):513–21. doi:10.2337/dc17-2131

23. Chen C, Hou J, Tanner JJ, Cheng J. Bioinformatics methods for mass spectrometry-based proteomics data analysis. *Int J Mol Sci* (2020) **21**(8):2873. doi:10.3390/ijms21082873

24. Bindea G, Mlecnik B, Tosolini M, Kirilovsky A, Waldner M, Obenauf AC, et al. Spatiotemporal dynamics of intratumoral immune cells reveal the immune landscape in human cancer. *Immunity* (2013) **39**(4):782–95. doi:10.1016/j.immuni.2013.10.003

25. Danaher P, Warren S, Dennis L, D'Amico L, White A, Disis ML, et al. Gene expression markers of tumor infiltrating leukocytes. *J ImmunoTherapy Cancer* (2017) **5**:18. doi:10.1186/s40425-017-0215-8

26. Lamb J, Crawford ED, Peck D, Modell JW, Blat IC, Wrobel MJ, et al. The connectivity map: using gene-expression signatures to connect small molecules, genes, and disease. *Science* (2006) **313**(5795):1929–35. doi:10.1126/science.1132939

27. Wu C, Feng H, Tian M, Chu B, Liu X, Zeng S, et al. Identification and validation of diagnostic genes IFI44 and IRF9 in insomnia-associated autoimmune uveitis. *Front Immunol* (2025) **16**:1519371. doi:10.3389/fimmu.2025.1519371

28. American Diabetes Association. 2. Classification and diagnosis of diabetes: standards of medical care in Diabetes-2021. *Diabetes Care* (2021) **44**(Suppl. 1):S15–S33. doi:10.2337/dc21-S002

29. He W, Yao C, Wang K, Duan Z, Wang S, Xie L. Single-cell landscape of immunological responses in elderly patients with sepsis. *Immun Ageing* (2024) **21**(1):40. doi:10.1186/s12979-024-00446-z

30. Kempker JA, Martin GS. A global accounting of sepsis. *The Lancet* (2020) **395**(10219):168–70. doi:10.1016/S0140-6736(19)33065-X

31. Lakshmikanth CL, Jacob SP, Chaithra VH, de Castro-Faria-Neto HC, Marathe GK. Sepsis: in search of cure. *Inflamm Res* (2016) **65**(8):587–602. doi:10.1007/s00011-016-0937-y

32. Xin Q, Xie T, Chen R, Wang H, Zhang X, Wang S, et al. Predictive nomogram model for major adverse kidney events within 30 days in sepsis patients with type 2 diabetes mellitus. *Front Endocrinol (Lausanne)* (2022) **13**:1024500. doi:10.3389/fendo.2022.1024500

33. van Vught LA, Scicluna BP, Hoogendijk AJ, Wiewel MA, Klein Klouwenberg PM, Cremer OL, et al. Association of diabetes and diabetes treatment with the host response in critically ill sepsis patients. *Crit Care* (2016) **20**(1):252. doi:10.1186/s13054-016-1429-8

34. Lu Z, Tao G, Sun X, Zhang Y, Jiang M, Liu Y, et al. Association of blood glucose level and glycemic variability with mortality in sepsis patients during ICU hospitalization. *Front Public Health* (2022) **10**:857368. doi:10.3389/fpubh.2022.857368

35. Das S, Misra B, Roul L, Minz NT, Pattnaik M, Baig MA. Insulin resistance and beta cell function as prognostic indicator in multi-organ dysfunction syndrome. *Metab Syndr Relat Disord* (2009) **7**(1):47–51. doi:10.1089/met.2008.0025

36. Monzón-Casanova E, Matheson LS, Tabbada K, Zarnack K, Smith CW, Turner M. Polypyrimidine tract-binding proteins are essential for B cell development. *Elife* (2020) **9**:e53557. doi:10.7554/elife.53557

37. Zhen EY, Jin Z, Ackermann BL, Thomas MK, Gutierrez JA. Circulating FGF21 proteolytic processing mediated by fibroblast activation protein. *Biochem J* (2016) **473**(5):605–14. doi:10.1042/BJ20151085

38. Altshuler DM, Gibbs RA, Peltonen L, Dermitzakis E, Schaffner SF, Yu F, et al. Integrating common and rare genetic variation in diverse human populations. *Nature* (2010) **467**(7311):52–8. doi:10.1038/nature09298

39. Marku A, Galli A, Marciani P, Dule N, Perego C, Castagna M. Iron metabolism in pancreatic beta-cell function and dysfunction. *Cells* (2021) **10**(11):2841. doi:10.3390/cells10112841

40. Muhar MF, Farnung J, Cernakova M, Hofmann R, Henneberg LT, Pfleiderer MM, et al. C-terminal amides mark proteins for degradation via SCF-FBXO31. *Nature* (2025) **638**(8050):519–27. doi:10.1038/s41586-024-08475-w

41. Lightowlers RN, Chrzanowska-Lightowlers ZM. Human pentatricopeptide proteins: only a few and what do they do? *RNA Biol* (2013) **10**(9):1433–8. doi:10.4161/rna.24770

42. Yang Y, Wang Y, Guo L, Gao W, Tang TL, Yan M. Interaction between macrophages and ferroptosis. *Cell Death Dis* (2022) **13**(4):355. doi:10.1038/s41419-022-04775-z

43. Pan W, Xiang L, Liang X, Du W, Zhao J, Zhang S, et al. Vitronectin destroyed intestinal epithelial cell differentiation through activation of PDE4-Mediated ferroptosis in inflammatory bowel disease. *Mediators Inflamm* (2023) **2023**: 1–16. doi:10.1155/2023/6623329

44. Xie Z, Wang X, Luo X, Yan J, Zhang J, Sun R, et al. Activated AMPK mitigates diabetes-related cognitive dysfunction by inhibiting hippocampal ferroptosis. *Biochem Pharmacol* (2023) **207**:115374. doi:10.1016/j.bcp.2022.115374

45. Huang W, Chen H, He Q, Xie W, Peng Z, Ma Q, et al. Nobiletin protects against ferroptosis to alleviate sepsis-associated acute liver injury by modulating the gut microbiota. *Food Funct* (2023) **14**(16):7692–704. doi:10.1039/d3fo01684f

46. Yang Z, Su W, Zhang Q, Niu L, Feng B, Zhang Y, et al. Lactylation of HDAC1 confers resistance to ferroptosis in colorectal cancer. *Adv Sci* (2025) **12**(12): e2408845. doi:10.1002/advs.202408845

47. Sharifi-Rad M, Mnayer D, Morais-Braga MFB, Carneiro JNP, Bezerra CF, Coutinho HDM, et al. Echinacea plants as antioxidant and antibacterial agents: from traditional medicine to biotechnological applications. *Phytotherapy Res* (2018) **32**(9):1653–63. doi:10.1002/ptr.6101

48. Yang D, Yang Y, Zhao Y. Ibudilast, a Phosphodiesterase-4 inhibitor, ameliorates acute respiratory distress syndrome in neonatal mice by alleviating inflammation and apoptosis. *Med Sci Monit* (2020) **26**:e922281. doi:10.12659/MSM.922281

EBM Experimental Biology and Medicine

TYPE Original Research
PUBLISHED 01 October 2025
DOI 10.3389/ebm.2025.10756

OPEN ACCESS

*CORRESPONDENCE
Xuefang Wang,
202010109503@mail.scut.edu.cn
Ting Song,
flair@gzhmu.edu.cn

RECEIVED 18 July 2025
ACCEPTED 08 September 2025
PUBLISHED 01 October 2025

CITATION
Wang X, Li Y, Liang Z, Du R and Song T (2025) High-fidelity, personalized cardiac modeling via AI-driven 3D reconstruction and embedded silicone rubber printing.
Exp. Biol. Med. 250:10756.
doi: 10.3389/ebm.2025.10756

High-fidelity, personalized cardiac modeling via AI-driven 3D reconstruction and embedded silicone rubber printing

Xuefang Wang[1]*, Yixin Li[1], Zhiqi Liang[2], Ruxu Du[3] and Ting Song[2]*

[1]Shien-Ming Wu School of Intelligent Engineering, South China University of Technology, Guangzhou, China, [2]Department of Radiology, Guangdong Provincial Key Laboratory of Major Obstetric Diseases, Guangdong Provincial Clinical Research Center for Obstetrics and Gynecology, The Third Affiliated Hospital, Guangzhou Medical University, Guangzhou, China, [3]Guangzhou Janus Biotechnology Co., Ltd., Guangzhou, China

Abstract

The burgeoning clinical demand for patient-specific cardiac modeling encounters significant challenges. The current clinical cardiac models are either difficult to manufacture or lack of detailed geometric structures and hence, often fail to incorporate important patient-specific characteristics. Moreover, most 3D-printable soft materials, such as Thermoplastic Poly-Urethane (TPU) or elastic resins, exhibit insufficient flexibility and biocompatibility to accurately mimic cardiac tissues, therefore limiting their ability to truly replicate patient-specific cardiac conditions. To address these limitations, we propose an innovative method for patient-specific cardiac substructure reconstruction based on the integration of Artificial Intelligence (AI) and embedded 3D printing. First, by combining medical imaging data (CT scan) with AI-driven high-precision 3D reconstruction algorithms, the new method segments the patient-specific cardiac structure into 10 substructures. The average Dice coefficient across the ten substructures is 0.87. Second, it uses an embedded 3D printing technique which utilizes silicone rubber matrix as supporting structure and uses diluted catalyst ink to extrude onto the supporting matrix. Through precise regulation of the matrix composition, material deposition rate and curing time, it can fabricate high-fidelity, complex 3D patient-specific silicone heart models with the average dimensional error less than 0.5 mm. The proposed method can substantially reduce manual intervention and post-processing time. The fabricated models provide valuable morphological insights for cardiovascular diagnosis and treatment planning. It is believed that many clinic applications will follow.

KEYWORDS

cardiac 3D reconstruction, embedded 3D printing, cardiac segmentation, silicone rubber matrix, deep learning

Impact statement

We propose a novel framework integrating artificial intelligence (AI) and embedded 3D printing for personalized cardiac substructure reconstruction through two primary contributions: High-precision 3D reconstruction algorithm: Utilizing medical imaging data (CT scans), we developed a cardiac substructure segmentation framework incorporating anatomical priors with correlated spatial-channel co-attention mechanisms. This system enables automatic identification and precise segmentation of cardiac substructures, significantly enhancing image resolution and data fidelity during the 3D printing preprocessing stage, thereby generating high-quality 3D printable files. Embedded 3D printing of silicone rubber matrix: By precisely modulating the composition ratio of base materials within the supporting matrix, we achieved on-demand printing-curing synchronization. This innovative approach effectively addresses the rheological challenges associated with pre-cured silicone, enabling the fabrication of complex three-dimensional cardiac models with exceptional anatomical fidelity. This approach yields high-fidelity 3D silicone cardiac models (dimensional error <0.5 mm), accurately replicating patient-specific anatomy to support precise diagnosis and treatment planning.

Introduction

Cardiovascular diseases (CVDs) represent 33% of worldwide deaths (20.5 million/year), with persistently rising mortality rates (WHF [1]). Effective treatment requires not only targeted interventions but also personalized medical care. Developing accurate human heart models is crucial for understanding cardiac pathology and guiding diagnosis and treatment. The heart is an intricately complex and multifunctional organ, encompassing a sophisticated vascular network and atrial and ventricular structures. Accurately replicating the complex structures of the heart remains a significant challenge, primarily manifested in three critical aspects. First, the initial and most crucial step involves utilizing high-resolution medical imaging technologies combined with advanced algorithms to precisely capture the intricate details of cardiac structures. Second, the selection of an appropriate 3D printing technology is essential, as it must provide high resolution and detail fidelity to ensure the accuracy of the models. Third, identifying suitable printing materials that can mimic the softness and elasticity of the heart while maintaining sufficient strength and stability during the fabrication process is vital.

High-resolution imaging and advanced algorithms form the foundation for precise cardiac modeling, with substructure segmentation remaining a core research focus. While deep learning has revolutionized this field through automated feature extraction and nonlinear modeling [2–9], current approaches still face significant challenges: (1) The U-Net model proposed by Ronneberger et al. [10], a convolutional neural network architecture for biomedical image segmentation, achieved groundbreaking results in medical image segmentation. However, U-Net-based frameworks [11, 12] and their variants (e.g., dense U-Net for multi-scale features [13]): often struggle with cardiac substructures' scale variations and topological complexity. (2) Most methods neglect inherent cardiac anatomy, reducing effectiveness. (3) Many algorithms require high-performance hardware and extensive labeled data, leading to poor performance on fine substructures. Despite multi-stage solutions [14–16] that decompose segmentation into region-of-interest (ROI) localization and refinement, significant gaps remain in precision and robustness for clinical application.

Recent advances in 3D-printed cardiac models show promise for improving cardiac care, yet challenges remain. While integration of deep learning has enhanced segmentation accuracy (e.g., coronary artery identification [17]) and streamlined clinical workflows [18], current approaches often lack comprehensive solutions. Three major limitations persist: (1) manufacturing complexity and limited geometric fidelity hinder high-precision applications [19–21]; (2) commercially available soft materials (e.g., TPU, elastic resins); fail to adequately replicate cardiac tissue properties; (3) conventional 3D printing struggles with soft materials due to flowability, support requirements, and precision constraints.

In conclusion, the current limitations of existing models fail to meet the essential requirements for personalized and accurate replication of cardiac structures. To address these challenges, this study focuses on two dimensions: (1) enhancing data accuracy during the pre-processing stage of 3D printing to improve the precision of cardiac substructure replication; (2) exploring the optimal printing technologies and materials that can simultaneously mimic the soft elasticity of cardiac tissue while ensuring structural integrity during the manufacturing process. We propose a new solution leveraging advanced imaging data (e.g., CT scans) and high-precision 3D reconstruction algorithms to automatically identify and segment cardiac substructures from medical imaging data, thereby generating high-quality 3D printable files. By harnessing the capabilities of embedded 3D printing technology, we have engineered a specialized 3D printing system for fabricating silicone rubber-based constructs. This system enables the deposition of soft materials within a temporary support matrix, which is subsequently removed to yield intricate, patient-specific structures. This methodology simultaneously addresses challenges related to material flowability, support structure requirements, and printing precision, thereby enabling the production of highly customized cardiac models.

These patient-specific silicone cardiac models are designed for direct clinical translation. As tangible, anatomically accurate replicas, they facilitate the understanding of cardiac pathology,

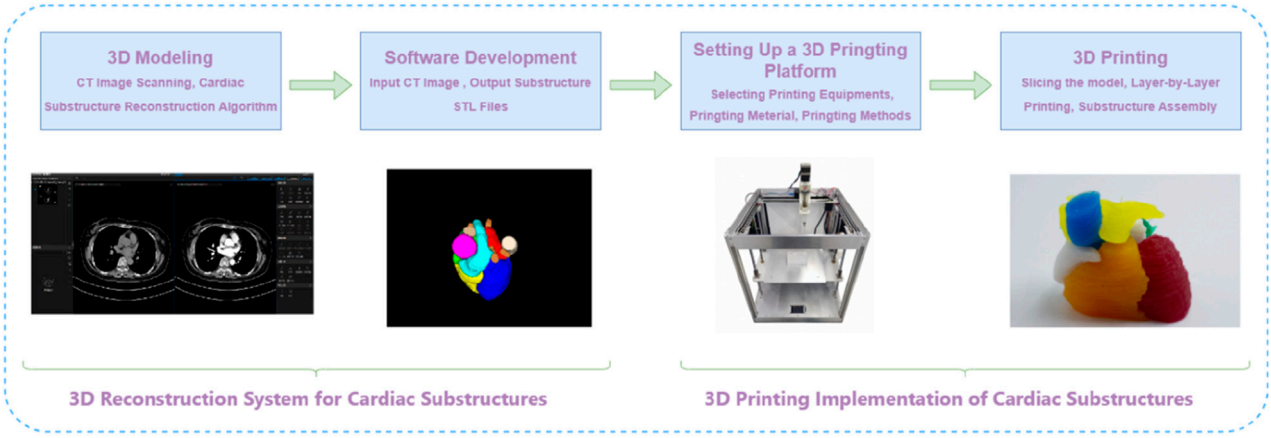

FIGURE 1
The integrated framework for 3D reconstruction of cardiac substructures.

aid in diagnostic decision-making, and support preoperative planning by allowing surgeons to visualize spatial anatomical relationships, assess procedural feasibility, and simulate surgical interventions (e.g., resection, implantation, or repair) prior to actual surgery. Additionally, the models provide a realistic tactile experience for training residents and fellows in cardiac anatomy and interventional techniques, reducing reliance on cadavers and live procedures. By bridging imaging, engineering, and clinical practice, this platform can enhances training efficacy while offering support for the development of personalized therapeutic strategies.

Methodology

To achieve precise reconstruction of the cardiac anatomical structure, we propose an integrated framework for 3D reconstruction of cardiac substructures, comprising two core subsystems: a 3D reconstruction system for cardiac substructures and an embedded 3D printing system for silicone rubber-based constructs, as depicted in Figure 1. This framework systematically addresses multiple critical stages, including the 3D modeling of ten cardiac substructures derived from medical CT images using advanced reconstruction algorithms, the development of specialized 3D reconstruction software, and the design and implementation of optimized 3D printing materials and a robust printing platform.

Three-dimensional reconstruction system for cardiac substructures

The three-dimensional (3D) reconstruction system for cardiac substructures was developed based on a proprietary algorithm specifically designed for cardiac imaging. This integrated system streamlines the entire workflow from cardiac computed tomography (CT) image acquisition to the generation of stereolithography (STL) files suitable for 3D printing applications, enabling automated and intelligent reconstruction of cardiac substructures.

High-precision reconstruction algorithm for cardiac substructures

Cardiac substructures present several technical challenges in CT imaging, including heterogeneous grayscale intensities, poorly defined boundaries, irregular morphological features, and positional variability. Adjacent substructures often have similar grayscale values, resulting in low contrast, while some are connected via blood inflow pathways and differ significantly in size. Moreover, cardiac morphology and spatial orientation vary considerably across individuals, and even within the same subject over time or across imaging planes (as illustrated in Figure 2). Due to the inherent limitations of medical imaging modalities and tissue-specific properties, images are susceptible to artifacts such as noise and motion-induced distortions. These intrinsic challenges pose significant difficulties for accurate reconstruction of cardiac substructures.

The experimental data were acquired from the Third Affiliated Hospital of Guangzhou Medical University, with prior approval from the Institutional Review Board (IRB). Cardiac CT imaging data from 117 clinical cases were collected for this study. Non-contrast CT scans were used in this study. All included cases had normal cardiac anatomy, with no significant pathological conditions or anatomical variants. Cases were selected via random sampling from the institutional database to ensure representativeness and minimize selection bias. These cases include precise contour annotations of ten key

FIGURE 2
CT slice sequence of cardiac substructures.

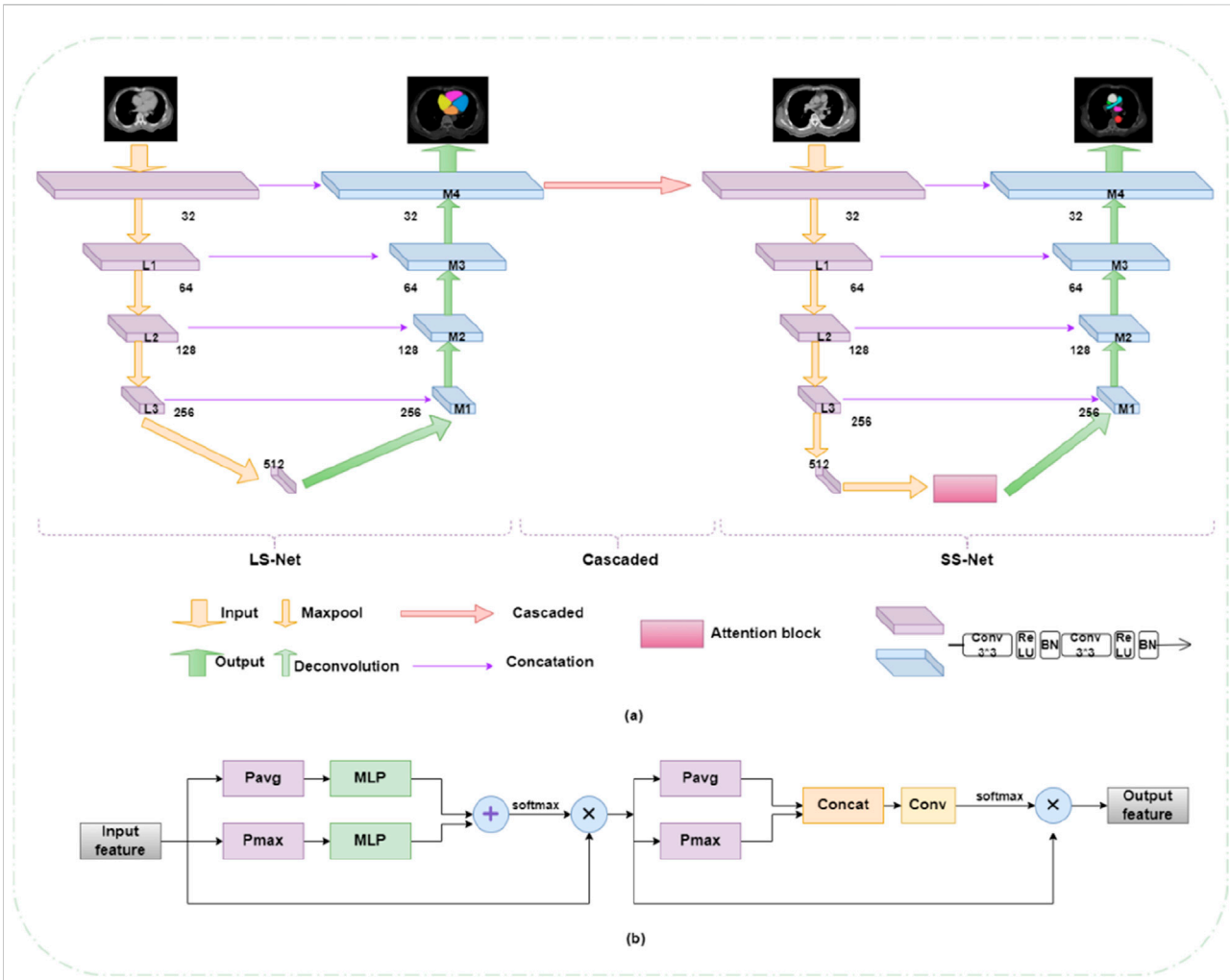

FIGURE 3
(a) Cardiac substructure segmentation framework integrating anatomical priors with collaborative spatial-channel attention mechanisms. **(b)** Collaborative attention module.

cardiac structures: the left and right atria (LA and RA), left and right ventricles (LV and RV), superior and inferior vena cava (SVC and IVC), pulmonary artery (PA), pulmonary vein (PV), and ascending and descending aorta (AA and DA). The annotation task was collaboratively performed by three experienced radiologists, with two intermediate-level

physicians performing the initial delineation, which was subsequently reviewed and confirmed by a senior physician.

In addressing the challenges associated with reconstructing substructures in cardiac CT images and the inherent limitations of current deep learning segmentation models, our approach is inspired by the meticulous delineation techniques employed by medical professionals. We have developed a cardiac substructure segmentation framework that synergistically combines anatomical prior knowledge with a spatial-channel co-attention mechanism (as depicted in Figure 3). This architecture represents an advanced iteration of a segmentation framework predicated on anatomical structure priors, as delineated in the seminal work [22]. This framework employs a sequential two-step segmentation process, utilizing a coarse-to-fine cascade network. The initial step involves coarse segmentation (Large substructure segmentation network LS-Net, depicted on the left side of Figure 3a) of more readily identifiable substructures (such as the quartet of atrial and ventricular formations), followed by fine segmentation (Small substructure segmentation network SS-Net, illustrated on the right side of Figure 3a) of more complex substructures (such as the quartet of atrial and ventricular formations). To augment the segmentation accuracy of small-scale substructures, the outcomes of the coarse segmentation are utilized as prior information, which, in conjunction with the original image, constitutes the model's input. The anatomical knowledge pertaining to large-scale substructures is embedded within the fine segmentation network to guide and refine the training of small-scale substructures. At the interface between the encoder and decoder in the fine segmentation network, a spatial-channel co-attention module is strategically designed to adaptively compute the region of interest based on the channel and spatial distribution information of the features themselves (illustrated in pink block in Figure 3a, with detailed architecture shown in Figure 3b). This module adeptly extracts spatial and channel data from feature maps across diverse scales, assimilates long-range dependencies among features of varying magnitudes, and computes the weighting of target features across multiple dimensions. Consequently, it captures the long-range dependencies and multi-scale global contextual information of cardiac CT images, enabling the segmentation network to assimilate both local and global information at each feature scale, thereby achieving efficient and precise segmentation of cardiac substructures. Segmentation performance was quantitatively assessed using the Dice similarity coefficient (DSC) [10], which is commonly used metrics in medical image segmentation tasks.

Software system based on cardiac substructure reconstruction algorithm

Building upon the aforementioned cardiac substructure segmentation algorithm, we have further developed a software system that facilitates the process from uploading cardiac CT imaging cases to outputting STL format files compatible with 3D printing systems, comprising the following functional modules: (1) a multi-modal image import module supporting standard formats (e.g., DICOM, NIFTI) with metadata extraction; (2) an intelligent preprocessing module integrating image normalization, hybrid denoising, and multi-modal registration algorithms; (3) a cardiac substructure segmentation module employing deep learning for automated segmentation of ten anatomical structures; (4) a 3D visualization module providing multiplanar reconstruction and volume rendering capabilities; (5) a data export module supporting parameter-adjustable STL file generation; (6) a security module implementing RBAC-based access control and data security compliance with clinical privacy standards; (7) a system monitoring module with comprehensive logging and exception handling mechanisms; and (8) a user interface module featuring a clinically optimized GUI design.

Embedded 3D printing system with silicone rubber matrix

The selection of appropriate 3D printing technology and materials is crucial for manufacturing heart models through 3D printing. These materials must be able to replicate the softness and elasticity of the heart while maintaining sufficient strength and stability during the fabrication process. Silicone rubber is considered particularly suitable for this application due to its exceptional elasticity, excellent thermal and chemical stability. Room temperature vulcanizing (RTV) silicone, in particular, offers ease of handling and can be chemically modified to achieve specific mechanical, optical, or electrical properties. These modified silicone rubbers have been widely used in fields such as soft robotics, flexible sensors, biomedical devices, and wearable technologies [23–25]. Based on these advantageous properties, we selected silicone rubber as the primary material for 3D printing cardiac substructures. The silicone rubber used in this study is an electrical insulator with very low electrical conductivity (typically on the order of 10^{-12} to 10^{-15} S/cm). This property ensures the models are electrically non-conductive, which is relevant for safety considerations in potential applications involving electrical stimulation or near electronic medical devices.

Conventional 3D printing techniques encounter substantial limitations when processing soft materials, particularly in the fabrication of complex geometric structures. These limitations include issues with material rheology, the necessity for support structures, and compromised printing precision. Embedded 3D printing technology [26] enables researchers to circumvent the limitations of traditional 3D printing techniques when processing soft materials, demonstrating great potential in the fabrication of complex structures and soft material-based products. However, the printing materials typically used in

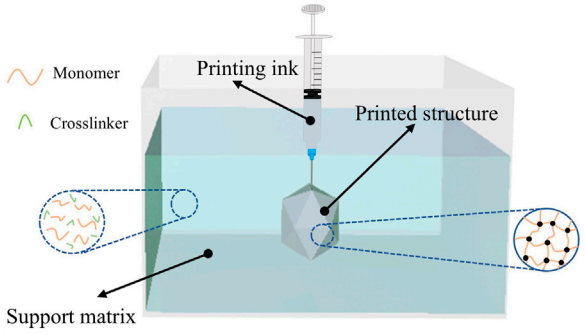

FIGURE 4
Printing principle.

embedded 3D printing, such as silicone and hydrogels, exhibit high fluidity and moldability. The most challenging aspect of the printing process involves precise control of the support matrix's curing parameters, particularly in terms of temporal and proportional adjustments. Silicone-based 3D printing of cardiac models faces two limitations. First, material supply is limited by reservoir capacity, typically less than 100 mL in most studies, necessitating frequent refilling during large-scale printing and continuous operator supervision to prevent print failure. Second, the printable time window is constrained, as most extrusion-based methods require pre-mixing of commercial two-part room-temperature vulcanizing (RTV) silicone, and printing must be completed before gelation. Even with curing inhibitors, the ink remains workable for only a few hours, making prolonged printing of large-volume models difficult. Furthermore, precise control of nozzle extrusion is challenging; high print speeds may lead to surface heterogeneity, compromising print quality, and most soft materials require extended curing times on the build platform.

To address these technical challenges, we have developed a silicone-embedded 3D printing system [27]. This system employs an advanced silicone printing methodology wherein diluted catalyst ink is continuously and uniformly extruded into a silicone polymer-containing support matrix. Through precise adjustment of the fundamental material ratios in the support matrix, we have successfully fabricated three-dimensional silicone cardiac models with complex features and high dimensional fidelity, as illustrated in the schematic diagram of the printing working principle (Figure 4) [27].

In comparison to conventional manufacturing methodologies, the advanced printing technology elucidated herein facilitates the versatile modulation of the mechanical properties of silicone rubber in response to diverse application demands. This is achieved through the precise calibration of the constituent ratios within the supporting matrix, obviating the necessity for molds or ancillary support structures. Diverging from the direct deposition of pre-cured silicone compounds, our innovative printing paradigm refines the procedural workflow by segregating the crosslinking agent from the catalyst. The methodology entails the incorporation of the crosslinking agent within the supporting matrix, whilst the catalyst is embedded within the printing ink.

During the extrusion process, the diluted catalyst-laden ink is dispensed into the supporting matrix, which is replete with the foundational silicone rubber precursors. This instigates a localized crosslinking and solidification of the adjacent matrix, thereby enabling a bespoke printing-curing sequence that augments material cohesion. Owing to the superlative catalytic efficacy, a minuscule quantity of the catalyst suffices to induce the solidification of the proximate supporting matrix. Empirical printing assays have corroborated that an ink extrusion rate of 4% engenders optimal fusion between successive printing trajectories. Consequently, the volumetric ratio of the resultant printed construct to the consumed ink approximates 25:1, indicative of an exemplary ink utilization efficiency. This innovation ameliorates the constraints imposed by finite ink reservoir capacities and protracted printing durations. The architectural schematics of the silicone-embedded 3D printing system are delineated in Figure 5.

Experiments and results

Experimental dataset and environment

The experimental data used in this study were provided by the Third Affiliated Hospital of Guangzhou Medical University. The dataset comprises 117 cardiac CT image samples, all acquired using a Siemens SOMATOM Force third-generation dual-source dual-energy spiral CT scanner. The constructed dataset has dimensions of 117 × 130 × 512 × 512, where 117 represents the number of cases, 130 denotes the number of slices per case, and 512 × 512 corresponds to the size of each slice. The cases were randomly divided into training, validation, and test sets in a ratio of 6:2:2.

The hardware environment for the experiments included an Intel® Xeon® E5-2678 v3 CPU and an NVIDIA GTX-1080Ti GPU with 11 GB of memory. The operating system was Ubuntu 18.04, and the programming language used was Python 3.7. All programs were implemented under the Pytorch open-source framework.

Experimental results of 3D reconstruction algorithm for cardiac substructures

In this chapter, the segmentation accuracy was quantitatively evaluated using the Dice coefficient [10], which is calculated as:

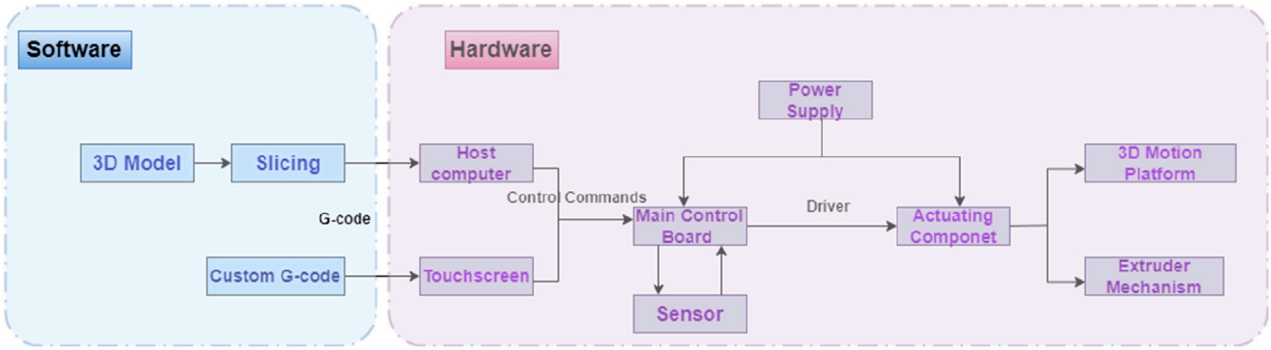

FIGURE 5
Silicone embedded 3D printing system.

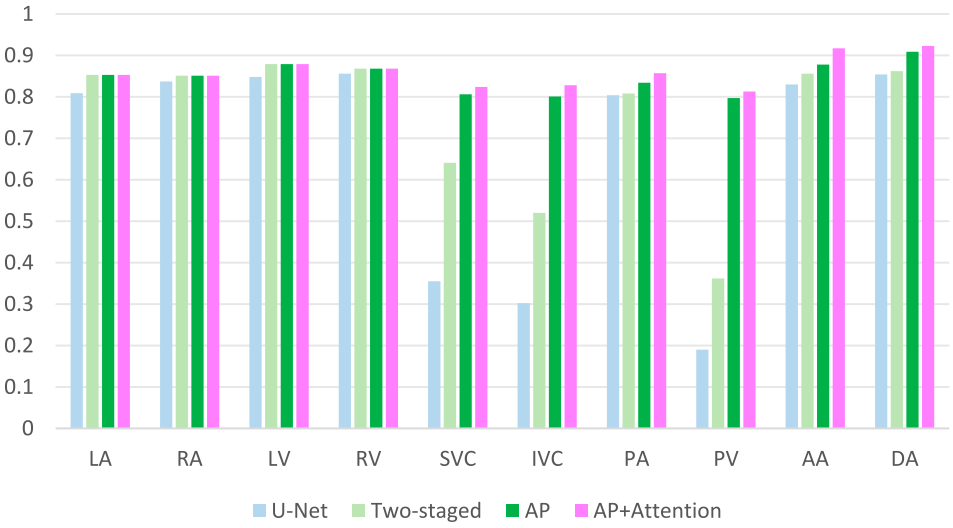

FIGURE 6
Ablation study:DSC comparison results.

$$\text{Dice}(X, Y) = \frac{2|G \cap P|}{|G| \cup |P|} \quad (1)$$

where G and P denote the manually segmented mask and the prediction mask, respectively, using binary tags. Dice calculates the ratio of twice the intersection of the two masks to their union, which reflects the similarity between the target region of segmentation and the annotated target region. The higher the similarity, the better the segmentation effect. Dice ranges from 0 to 1, where 1 represents the best segmentation, and 0 represents the worst segmentation.

To evaluate the impact of our method on segmentation performance, we compared the baseline U-Net, a two-stage U-Net, incorporating anatomical priors into a cascaded framework (AP), and our proposed framework that synergistically combines anatomical prior knowledge with a spatial-channel co-attention mechanism (AP+Attention). Results are shown in Figure 6 (The mean values calculated across all subjects in the independent test set). U-Net achieved reasonable Dice scores on large, high-contrast structures—including the four cardiac chambers (LA, RA, LV, RV) and three major arteries (AA, DA, PA)—but failed to segment small veins (SVC, IVC, PV), resulting in severe under-segmentation. The two-stage U-Net improved venous segmentation by grouping structures according to size, yielding visibly better delineation of SVC, IVC, and PV. The AP model further enhanced performance, with DSC increasing to 0.806 (SVC), 0.801 (IVC), and 0.797 (PV), demonstrating the benefit of anatomical prior integration in improving shape consistency and boundary accuracy. Our proposed

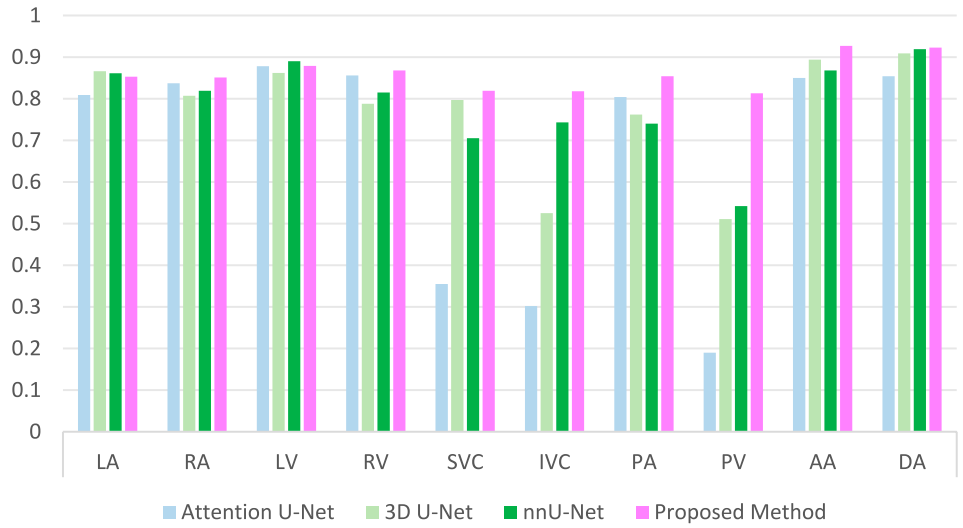

FIGURE 7
Comparison of DSC results with other methods.

AP+Attention framework achieved the highest DSC across all substructures. It showed the most significant gains in the most challenging small vessels—SVC (0.824), IVC (0.828), PV (0.813)—and attained state-of-the-art performance on the aorta (AA: 0.917, DA: 0.923). These results highlight the effectiveness of attention mechanisms in refining feature representation and enhancing segmentation accuracy, particularly for fine-grained cardiac structures.

To validate the performance of the proposed method, we conducted a comparative analysis with several prominent deep learning methods in the field of segmentation, including Attention U-Net [28], 3D U-Net [29], and nnU-Net [30]. The comparison is graphically illustrated in Figure 7. As evident from the comparative outcomes depicted in the figures, our method yielded modest yet consistent improvements in the traditional segmentation of cardiac chambers, specifically in RA, LV, LA and RV. Notably, our approach demonstrated a significant advantage in the segmentation of PA, DA and AA. Most strikingly, our method excelled in the challenging categories of SVC, IVC and PV, which are characterized by small sizes and low sample counts. Particularly for PV, neither 3D U-Net nor nnU-Net achieved a Dice score exceeding 0.6, indicating inadequate segmentation. This highlights the superior capability of our method to achieve accurate and comprehensive segmentation of these structures.

Experimental design for embedded 3D printing

The experimental platform for this study is illustrated in Figure 8, which is an XYZ frame 3D printing system using silicone as the support matrix and equipped with a motor-lead screw fluid extrusion mechanism.

The specific steps of the printing process are as follows:

1. Export the 3D model in STL format from the software system based on the heart substructure reconstruction algorithm described in Section *Software system based on cardiac substructure reconstruction algorithm* (as shown in Figure 9).
2. Use slicing software such as Ultimaker Cura or IdeaMaker to convert the STL format model into G-code, which the 3D printing system can understand and execute, and then send it to the 3D printing system (as shown in Figure 10).

G-code is a crucial part of the printing system, as it directly determines the structure and quality of the printed object. The designed 3D model is imported into the slicing software in STL format. First, the position, size, and orientation of the model are adjusted to achieve the optimal printing direction. The slicing software then layers the model based on the set printing parameters and uses built-in slicing algorithms to plan the printing path and control the speed for each layer, ultimately generating the G-code instruction file. The printer interprets these instructions and constructs the 3D object layer by layer along a specific path and speed.

The slicing software contains numerous parameters, with the most critical printing parameters including printing speed, layer height, line width, extrusion rate, infill density, and infill pattern. Only a combination of printing parameters that match the material and structural characteristics can achieve the best printing quality. For different printing materials and processes, parameter optimization experiments are necessary

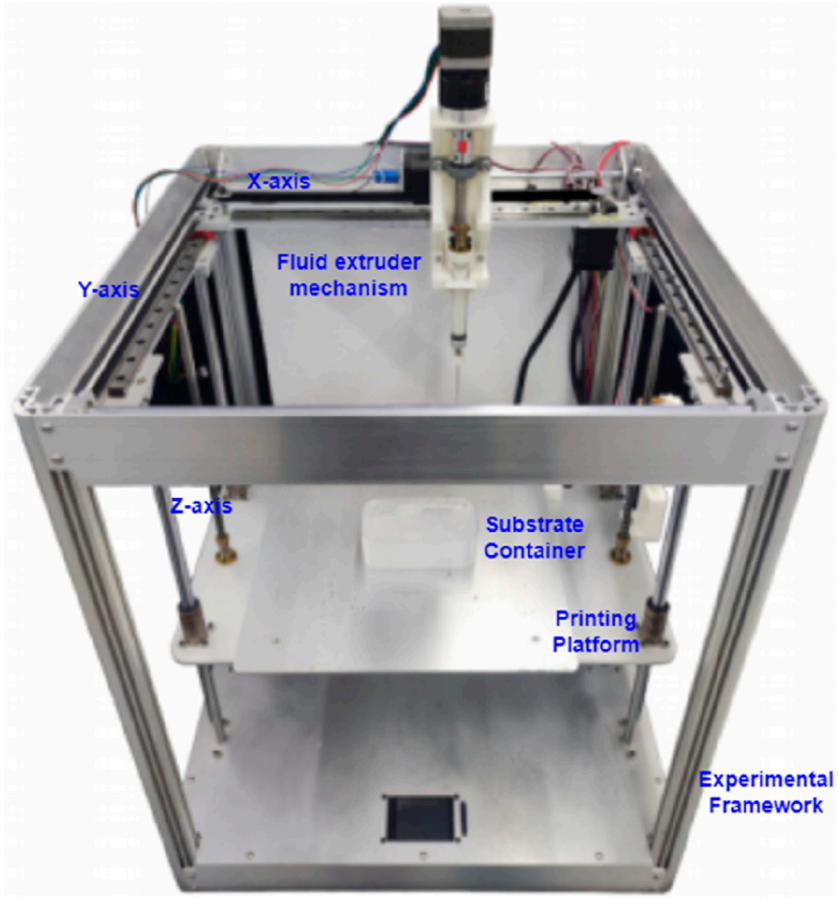

FIGURE 8
Silicone embedded 3D printing experimental platform.

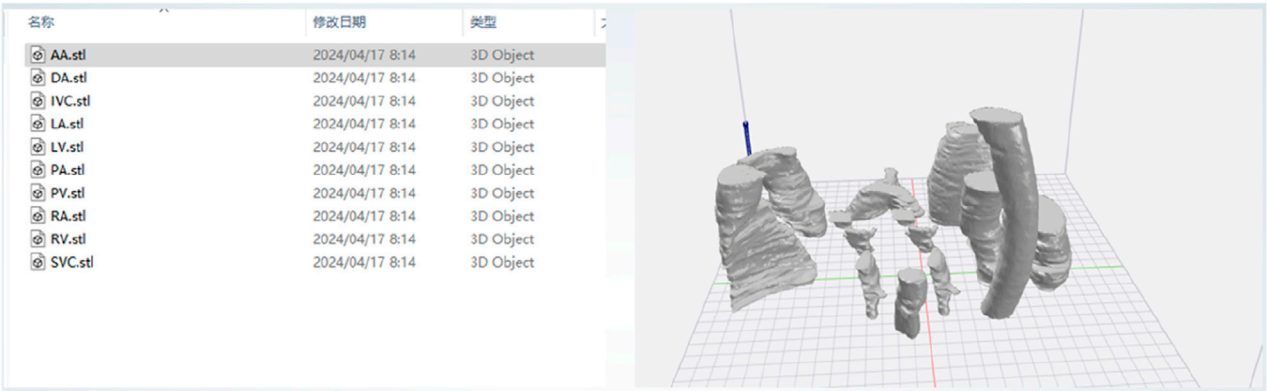

FIGURE 9
3D model in STL format.

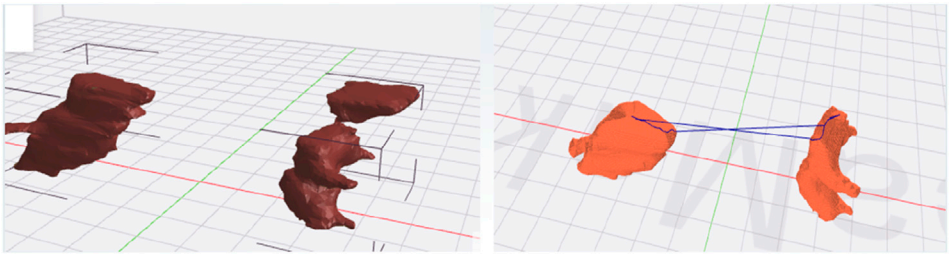

FIGURE 10
Conversion of STL format model to G-Code format model.

to improve printing quality. Through experimental testing, the printing parameters for this study are set as follows: layer height 0.4mm, line width 0.3mm, infill density 100%, extrusion rate 4%, printing speed 15 mm/s, and infill pattern: concentric circles.

After processing the model with the slicing software to obtain the G-code for layer-by-layer printing, additional lines of G-code are added before and after the start and end of the G-code generated by the slicing software. These lines control the lifting of the printing platform, aiming to lower the platform to a position where the needle tip does not overlap with the matrix container in the Z-axis direction. This prevents the needle from colliding with the container during the homing process, which could damage the system.

3. Preparation of Printing Materials: Prepare the support matrix and printing ink.

The main materials used for the support matrix include high-viscosity vinyl silicone oil MP5000, hydrogen-containing silicone oil MH180, hydrogen-containing silicone oil MDH50, and fumed silica A380. Among these, MP5000 and MH180 are the primary reactants, MDH50 adjusts the crosslinking density of the network to modify the mechanical properties of the printed silicone rubber material, and A380 acts as a rheological modifier to regulate the rheological properties of the support matrix. The printing ink is a platinum catalyst diluted with vinyl silicone oil MP450. Additionally, to enhance the visualization of the printing paths, a small amount of color paste or fluorescent powder in different colors is mixed into the ink for different substructures of the heart.

The support matrix is poured into a container, degassed, and then placed on the printing platform. The printing ink is loaded into the reservoir of the material supply system, ready for printing.

4. After all materials have been printed, heat is applied to accelerate curing. The printed structures are placed in a heating chamber at 70 °C to speed up the curing process, and they are removed after approximately 2 h. The printing results are shown in Figure 11.

3D printing results

The printed cardiac substructures were assembled by a radiologist using a minimal amount of adhesive (silicone adhesive J-527S) to precisely align and bond the components, ensuring tight junctions without significant material buildup. The adhesive cures rapidly at room temperature, forming a strong and durable connection. Anatomical landmarks were carefully referenced during alignment to maintain spatial relationships and overall morphological accuracy. The 3D heart model is shown in Figure 12. The measurement results of the pre-printed digital model and post-printed physical model are presented in Table 1, with comparative data illustrated in Figure 13. The data were derived from a single, representative patient-specific 3D-printed cardiac model. To assess fidelity, each anatomical landmark was measured by the physicians. The values reported are the means of these measurements, with the ± indicating the standard deviation (SD), reflecting variability due to measurement technique and minor surface irregularities. All SDs for the physical measurements were less than 0.5 mm, indicating measurement consistency, while the mean absolute differences (MADs) ranging from 0.15 to 0.46 mm demonstrate dimensional accuracy within clinically acceptable limits.

Discussion

In this study, we developed a comprehensive 3D reconstruction framework for cardiac substructures, enabling the precise replication of patient-specific cardiac anatomy and the creation of highly personalized heart models. This framework integrates two subsystems: a 3D reconstruction system for cardiac substructures and an embedded 3D printing system

FIGURE 11
3D models of printed cardiac substructures.

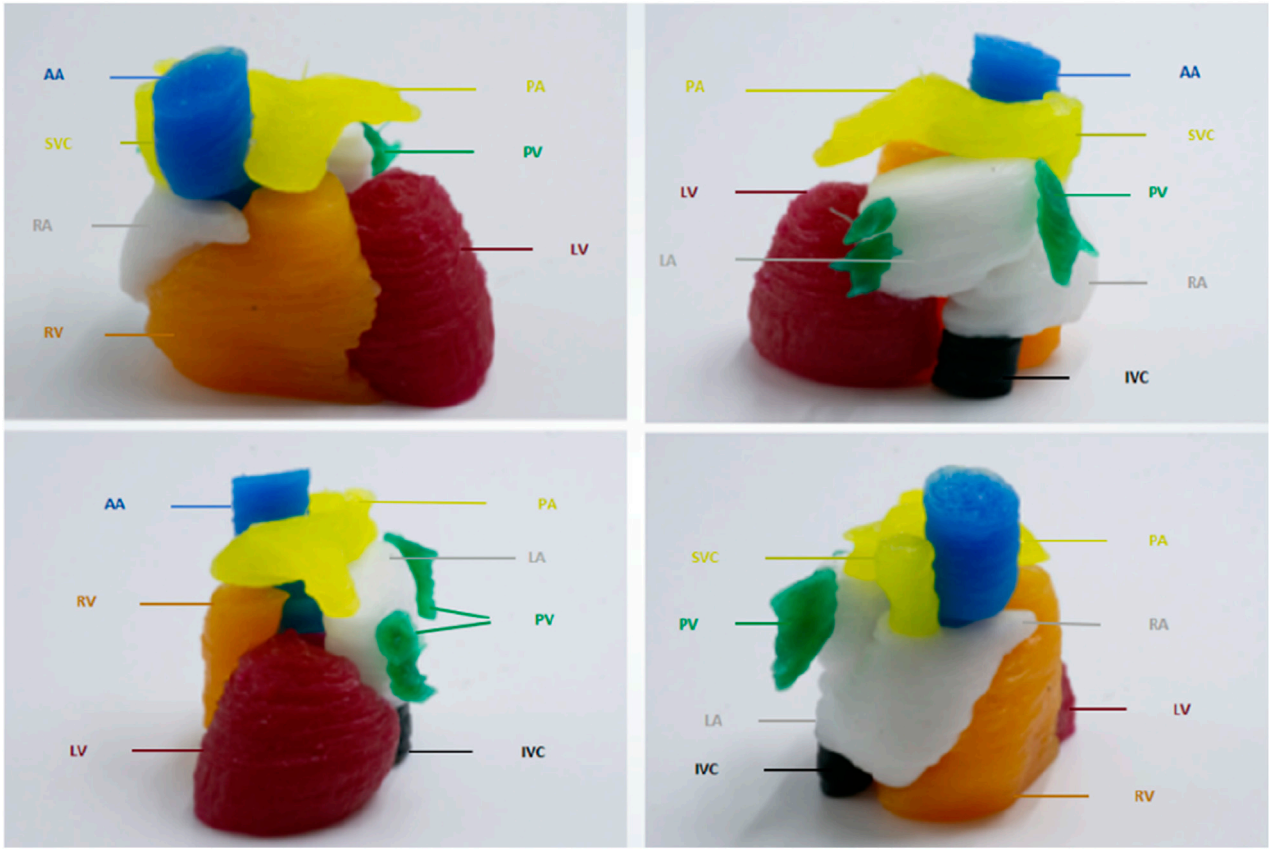

FIGURE 12
3D models of cardiac substructures.

TABLE 1 The measurement results of the digital model before printing and the physical model after printing.

Substructures	Measurement	Pre-printed digital model (mm)	Post-printed physical model (mm)	Mean absolute difference (mm)
LA	The maximum transverse diameter, measured at the level of the middle of the atrium, perpendicular to the interatrial septum	35.75 ± 0.22	35.41 ± 0.37	0.35
RA	The maximum transverse diameter, measured at the level of the middle of the atrium, from the lateral wall to the interatrial septum	33.15 ± 0.18	33.0 ± 0.26	0.15
LV	The short-axis diameter, measured at the level of the papillary muscles in the short-axis view, from the interventricular septum to the lateral wall	45.63 ± 0.22	45.21 ± 0.20	0.42
RV	The short-axis diameter, measured at the basal short-axis view, from the free wall to the interventricular septum	36.15 ± 0.19	36.38 ± 0.18	0.23
SVC	Diameter, measured at a transverse Section *Introduction* cm above the entrance of the right atrium	18.38 ± 0.18	17.92 ± 0.45	0.46
IVC	Diameter, measured at the transverse section at the level of the diaphragm	21.5 ± 0.14	21.78 ± 0.32	0.28
PA	Diameter, measured at a transverse Section *Introduction* cm above the valve level	24.95 ± 0.19	24.54 ± 0.40	0.41
PV	Diameter, measured at the transverse section at the junction of the left atrium (at the thickest point of the left superior pulmonary vein)	12.2 ± 0.14	11.82 ± 0.37	0.38
AA	Diameter, measured perpendicular to the direction of blood flow	30.48 ± 0.22	30.32 ± 0.21	0.16
DA	Diameter, measured at the transverse section above the diaphragm	20.33 ± 0.19	20.5 ± 0.24	0.17

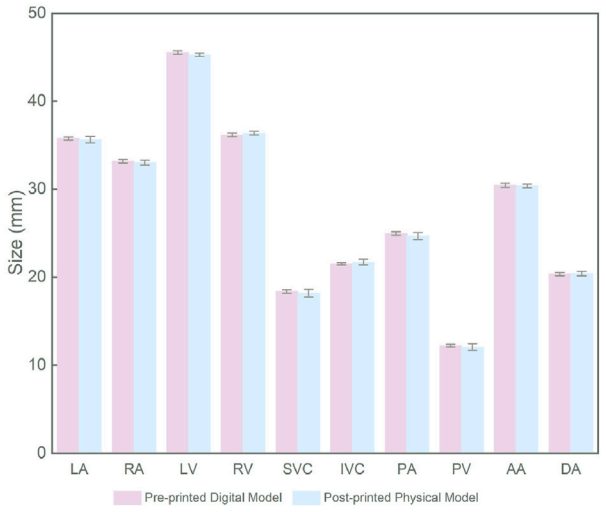

FIGURE 13
Comparison of pre-printed and post-printed models.

utilizing a silicone rubber matrix. The workflow encompasses the entire process, from uploading cardiac CT imaging data to generating STL files compatible with 3D printing systems, followed by embedded 3D printing with silicone rubber. This approach achieves automated and intelligent 3D reconstruction of cardiac substructures, addressing two critical challenges in the field: (1) enhancing data accuracy during the pre-processing phase through a novel cardiac substructure reconstruction algorithm that incorporates anatomical prior knowledge and a collaborative spatial-channel attention mechanism, and (2) enabling high-fidelity fabrication of complex 3D silicone heart models without the need for molds or support structures by optimizing the composition of the support matrix.

Accurate segmentation of cardiac substructures in CT remains challenging due to large variations in size, shape, intensity, and spatial location—e.g., the left ventricle is approximately ten times larger in volume than the superior vena cava. Conventional end-to-end models underperform on small, low-contrast structures like the SVC, IVC, and PV, especially with limited training data. To address this, we propose a two-stage framework integrating anatomical priors with a spatial-channel co-attention mechanism. The first stage segments large substructures (e.g., ventricles, atria), whose outputs are fused with the original image to guide the second-stage refinement network. This grouped strategy improves small-structure accuracy, increasing Dice scores for SVC, IVC, and PV by 20%–30%. By embedding spatial, morphological, and scale

priors from larger substructures, boundary delineation and shape consistency are enhanced, raising DSC to 0.806 (SVC), 0.801 (IVC), and 0.797 (PV). A spatial-channel collaborative attention module at the encoder-decoder interface further improves feature discrimination by fusing channel and spatial attention, strengthening global-local fusion and suppressing background noise—critical for resolving small, blurred vessels. As shown in Figure 6, the full model achieves peak performance on the most challenging targets: DSC = 0.824 (SVC), 0.828 (IVC), 0.813 (PV), and 0.917/0.923 (AA/DA). Compared to mainstream models (Figure 7), our method elevates Dice scores for small substructures from <0.35 to >0.82, demonstrating accuracy in handling scale disparity and low contrast for comprehensive cardiac segmentation.

Material selection is critical for achieving biomimetic fidelity in 3D-printed cardiac models. In this study, we selected silicone rubber as the primary printing material due to its superior mechanical properties and biocompatibility, enabling realistic cardiac simulation. Compared to common alternatives, silicone offers distinct advantages: thermoplastics such as polylactic acid (PLA) are accessible and suitable for rapid prototyping of basic anatomical structures [31], but lack the softness; thermoplastic polyurethane (TPU) improves flexibility for soft-tissue simulation [32], yet its mechanical behavior may deviate from the nonlinear elasticity of heart muscle; photopolymer resins enable high-resolution printing with excellent surface finish, making them ideal for detailed anatomical models in preoperative planning and education [33], although many commercial formulations do not meet medical-grade standards; while cell-laden bioinks hold promise for tissue engineering [34], they remain challenging for fabricating structurally robust and dimensionally stable models for surgical training. In contrast, silicone exhibits exceptional elasticity, tunable mechanical properties, and high thermal and chemical stability, closely mimicking the viscoelastic behavior of native cardiac tissue, with proven safety for clinical handling and repeated use [35]. Furthermore, advances in embedded 3D printing enable the precise fabrication of complex, multi-chambered cardiac models with silicone, overcoming limitations of traditional molding or layer-based rigid printing.

Silicone-based cardiac printing faces two limitations: (1) limited reservoir capacity (typically <100 mL), necessitating frequent material refilling and continuous supervision to prevent print failure during large-scale fabrication; and (2) constrained working time, as most extrusion-based methods require pre-mixing two-part RTV silicone, with printing completed before gelation. Even with inhibitors, ink usability lasts only a few hours, limiting prolonged printing of large constructs. This study presents an advanced embedded 3D printing method in which a diluted catalytic ink is extruded into a silicone polymer-laden support matrix. This approach enables mold-free, support-free fabrication of complex 3D cardiac models with high fidelity. By tuning the composition of the support matrix, the mechanical properties of the printed silicone can be precisely tailored to specific applications. Unlike conventional methods that deposit pre-mixed silicone, our system decouples the crosslinking agent (in the matrix) from the catalyst (in the ink). During printing, localized curing is triggered upon ink deposition, enabling on-demand, layer-by-layer solidification. This strategy enhances material integration and overcomes limitations in ink reservoir capacity and working time, facilitating extended, uninterrupted printing of large-scale, anatomically accurate cardiac structures.

This study has several limitations. First, although the segmentation algorithm integrating anatomical priors and attention fusion demonstrates promising performance, its accuracy for small or low-contrast structures could be further improved; future work will explore advanced techniques to enhance segmentation of challenging substructures. Second, we plan to evaluate the adaptability of our method to other biomedical imaging modalities, such as MRI and ultrasound, to assess its robustness and generalizability. Despite these limitations, our integrated framework holds significant potential for personalized clinical applications. The cardiac models enable preoperative planning for heart diseases, allowing surgeons to visualize anatomical relationships and simulate procedures, while also serving as an auxiliary platform for surgical training. The modular design facilitates extension to biomimetic modeling of other soft tissues—such as liver and kidney—by adapting the algorithm and tuning material mechanics, with applications in oncologic surgery planning. Future efforts will focus on incorporating micro-sensors for dynamic functional simulation, developing biodegradable or bioactive silicones, and automating the entire pipeline to reduce turnaround time and enhance clinical translation, ultimately supporting surgical innovation, patient-physician communication and medical education.

Conclusion

To address limitations in manufacturing complexity, geometric fidelity, and personalization of existing cardiac models, this study presents an innovative approach integrating artificial intelligence (AI) and embedded 3D printing for reconstructing patient-specific cardiac substructures. The proposed framework leverages medical imaging data (e.g., CT scans) and advanced 3D reconstruction algorithms to automatically segment and model cardiac anatomy, significantly enhancing image resolution and accuracy during preprocessing and generating high-quality 3D printable files. Furthermore, an embedded 3D printing technique based on a silicone rubber matrix enables on-demand printing and curing through precise modulation of the support matrix composition, facilitating the fabrication of highly complex, high-fidelity silicone heart models. These models accurately replicate patient-specific cardiac anatomy, providing valuable morphological insights for diagnosis and treatment. The

framework shows strong potential for personalized preoperative planning and training, with a modular design adaptable to other soft tissues for broader biomedical applications. Future efforts will focus on improving printing precision and efficiency to enhance clinical translation, ultimately supporting surgical innovation, patient-physician communication, and medical education.

Author contributions

XW designed the study, was responsible for medical image data processing, implementation and optimization of the 3D reconstruction algorithm, and prepared all related figures and tables. XW also wrote and revised the main text of the manuscript. YL primarily developed the embedded 3D printing technology and conducted experimental validation, while also participating in the proofreading of technical details. ZL provided annotations for the imaging data and assisted with data analysis. RD reviewed and revised the manuscript. TS provided data resources and clinical support. All authors contributed to the article and approved the submitted version.

Data availability

The data analyzed in this study is subject to the following licenses/restrictions: The datasets generated during this study are property of the participating hospital and are not publicly available due to institutional data governance policies. Data access requires approval from the hospital ethics committee. Requests to access these datasets should be directed to TS flair@gzhmu.edu.cn.

Ethics statement

The studies involving humans were approved by the Third Affiliated Hospital of Guangzhou Medical University Ethics Committee (No. 124-2023). For retrospective analysis of anonymized imaging data, the requirement for informed consent was waived. The studies were conducted in accordance with the local legislation and institutional requirements. The participants provided their written informed consent to participate in this study.

Funding

The author(s) declare that no financial support was received for the research and/or publication of this article.

Acknowledgments

We are grateful to Professor Yao Lu for providing computing server resources and guidance on model training, and to Professor Yong Zhong for offering access to the 3D printing experimental platform and technical resources.

Conflict of interest

Author RD was employed by Guangzhou Janus Biotechnology Co., Ltd.

The remaining author(s) declared no potential conflicts of interest with respect to the research, authorship, and/or publication of this article.

Generative AI statement

The author(s) declare that no Generative AI was used in the creation of this manuscript.

Any alternative text (alt text) provided alongside figures in this article has been generated by Frontiers with the support of artificial intelligence and reasonable efforts have been made to ensure accuracy, including review by the authors wherever possible. If you identify any issues, please contact us.

References

1. World Heart Federation (WHF)[EB/OL]. World heart Federation. Available online at: https://world-heart-federation.org/ (Accessed September 17, 2025).

2. Payer C, Štern D, Bischof H. Multilabel whole heart segmentation using cnns and anatomical label configurations. In: *International workshop on statistical atlases and computational models of the heart*. Springer (2017).190198

3. Wang C, Smedby Ö. Automatic whole heart segmentation using deep learning and shape context. In: *International workshop on statistical atlases and computational models of the heart*. Springer (2017).242249

4. Yang X, Bian C, Yu L. 3d convolutional networks for fully automatic finegrained whole heart partition. In: *International workshop on statistical atlases and computational models of the heart*. Springer (2017).181189

5. Savaashe AK, Dharwadkar NV. A review on cardiac image segmentation. In: *2019 3rd international conference on computing methodologies and communication (ICCMC)*. India: Erode (2019). p. 545–50.

6. Zhuang X. Evaluation of algorithms for multi-modality whole heart segmentation: an open-access grand challenge. *Med Image Anal* (2019) **55**: 92–102. doi:10.1016/j.media.2019.101537

7. Yang X, Zhang Y, Lo B, Wu D, Liao H, Zhang Y -T. DBAN: adversarial network with multi-scale features for cardiac MRI segmentation. *IEEE J Biomed Health Inform* (2021) **25**(6):2018–28. doi:10.1109/jbhi.2020.3028463

8. Slobodzian V, Radiuk P, Barmak O, Krak I. Multi-stage segmentation and cascade classification methods for improving cardiac MRI analysis. *J Med Imaging Health Inform* (2023) **13**(4):567–78. doi:10.48550/arXiv.2412.09386

9. Bui V, Hsu L-Y, Chang L-C, Sun A-Y, Tran L, Shanbhag SM, et al. DeepHeartCT: a fully automatic artificial intelligence hybrid framework based on convolutional neural network and multi-atlas segmentation for multi-structure cardiac computed tomography angiography image segmentation. *J Med Imaging Health Inform* (2023) **13**(5):789–801. doi:10.3389/frai.2022.1059007

10. Ronneberger O, Fischer P, Brox T. U-Net: Convolutional networks for biomedical image segmentation. *Lecture Notes Computer Sci* (2015) 234–41. doi:10.1007/978-3-319-24574-4_28

11. Diniz JOB, Dias Júnior DA, da Cruz LB, da Silva GLF, Ferreira JL, Pontes DBQ, et al. Heart segmentation in planning CT using 2.5D U-Net++ with attention gate. *Computer Methods Biomech Biomed Eng Imaging & Visualization* (2023) **11**(3):317–25. doi:10.1080/21681163.2022.2043779

12. Qiao J, Wang X, Chen J, Liu M. MBUTransNet: multi-branch U-shaped network fusion transformer architecture for medical image segmentation. *Int J Computer Assisted Radiol Surg* (2023) **18**(10):1895–902. doi:10.1007/s11548-023-02879-1

13. Jégou S, Drozdzal M, Vazquez D, Romero A, Bengio Y. The one hundred layers tiramisu: fully convolutional densenets for semantic segmentation. In: *2017 IEEE conference on computer vision and pattern recognition workshops (CVPRW)* (2017). p. 1175–83.

14. Roth HR, Lu L, Farag A, Shin H-C, Liu J, Turkbey EB, et al. DeepOrgan: multi-level deep convolutional networks for automated pancreas segmentation. In: *International conference on medical image computing and computer-assisted intervention (MICCAI)* (2015). p. 556–64.

15. Zhao Y, Wang X, Che T, Bao G, Li S. Multi-task deep learning for medical image computing and analysis: A review. *Comput Biol Med* (2023) **153**: 106496. doi:10.1016/j.compbiomed.2022.106496

16. Singh KR, Sharma A, Singh GK. MADRU-Net: multiscale attention-based cardiac MRI segmentation using deep residual U-Net. *IEEE Trans Instrum Meas* (2024) **73**: 1–13. doi:10.1109/TIM.2023.3332340

17. Song Y, Lu Y, Fu X, Wong KKL. Deep learning-based automatic segmentation of images in cardiac radiography: a promising challenge. *Comput Methods Programs Biomed* (2022) **220**: 106821. doi:10.1016/j.cmpb.2022.106821

18. Gharleghi R, Dessalles CA, Lal R, McCraith S, Sarathy K, Jepson N, et al. 3D printing for cardiovascular applications: from end-to-end processes to emerging developments. *Ann Biomed Eng* (2021) **49**: 1598–1618. doi:10.1007/s10439-021-02784-1

19. Valverde I. Three-dimensional printed cardiac models: applications in the field of medical education, cardiovascular surgery, and structural heart interventions. *Revista Española de Cardiología (English Edition)* (2017) **70**(4): 282–91. doi:10.1016/j.rec.2017.01.012

20. Noor N, Shapira A, Edri R, Gal I, Wertheim L, Dvir T. 3D printing of personalized thick and perfusable cardiac patches and hearts. *Adv Sci* (2019) **6**(11): 1900344. doi:10.1002/advs.201900344

21. Sun Z, Wee C. 3D printed models in cardiovascular disease: an exciting future to deliver personalized medicine. *Micromachines (Basel).* (2022) **13**(10):1575. doi:10.3390/mi13101575

22. Wang X, Li X, Du R, Zhong Y, Lu Y, Song T. Anatomical prior-based automatic segmentation for cardiac substructures from computed tomography images. *Bioengineering* (2023) **10**:1267–85. doi:10.3390/bioengineering10111267

23. Truby RL, Lewis JA. Printing soft matter in three dimensions. *Nature* (2016) **540**(7633):371–8. doi:10.1038/nature21003

24. Yuk H, Lin S, Ma C, Takaffoli M, Fang NX, Zhao X. Hydraulic hydrogel actuators and robots optically and sonically camouflaged in water. *Nat Commun* (2017) **8**(1):14230. doi:10.1038/ncomms14230

25. Wehner M, Truby RL, Fitzgerald DJ, Mosadegh B, Whitesides GM, Lewis JA, et al. An integrated design and fabrication strategy for entirely soft, autonomous robots. *Nature* (2016) **536**(7617):451–5. doi:10.1038/nature19100

26. Brown AL, Gaston AP, Truby RL, Lewis JA. Embedded 3D printing for complex geometry and soft materials. *Adv Mater Tech* (2018). doi:10.1038/nature19100

27. Li Y, Wu Z, Chen Y, Xian S, Hong Z, Wang Q, et al. Multi-material embedded 3D printing for one-step manufacturing of multifunctional components in soft robotics. *Additive Manufacturing* (2024) **85**:104178. doi:10.1016/j.addma.2024.104178

28. Oktay O. Attention U-Net: learning where to look for the pancreas. arXiv preprint arXiv:1804.03999 (2018).

29. Çiçek Ö, Abdulkadir A, Lienkamp SS. 3D U-net: learning dense volumetric segmentation from sparse annotation. In: *International conference on medical image computing and computerassisted intervention* (2016). p. 424–32.

30. Isensee F, Jaeger PF, Kohl SAA, Petersen J, Maier-Hein KH. nnU-Net: a self-configuring method for deep learning-based biomedical image segmentation. *Nat Methods* (2021) **18**:203–11. doi:10.1038/s41592-020-01008-z

31. Wei J, Oyunbaatar N-E, Jeong Y-J, Park J, Kim S-H, Kwon K, et al. Enhancing flexibility of smart bioresorbable vascular scaffolds through 3D printing using polycaprolactone and polylactic acid. *Sensors Actuators B: Chem* (2025) **422**: 136667. doi:10.1016/j.snb.2024.136667

32. Gasparotti E, Vignali E, Losi P, Scatto M, Fanni BM, Soldani G, et al. A 3D printed melt-compounded antibiotic loaded thermoplastic polyurethane heart valve ring design: an integrated framework of experimental material tests and numerical simulations. *Int J Polymeric Mater Polymeric Biomater* (2018) **68**(1–3):1–10. doi:10.1080/00914037.2018.1525717

33. Ertas A, Farley-Talamantes E, Cuvalci O, Gecgel O. 3D-Printing of artificial aortic heart valve using UV-Cured silicone: design and performance analysis. *Bioengineering* (2025) **12**(1):94. doi:10.3390/bioengineering12010094

34. Zhu K, Shin SR, van Kempen T, Li Y, Ponraj V, Nasajpour A, et al. Gold nanocomposite bioink for printing 3D cardiac constructs. *Adv Funct Mater* (2017) **27**(12):1605352. doi:10.1002/adfm.201605352

35. Dehnou KH, Hadianfard MJ. Enhancing thermal, viscoelastic, and mechanical properties of silicone rubber matrix through reinforcements for use as a medical implant. *Recent Prog Mater* (2024) **6**(2):011. doi:10.21926/rpm.2402011

EBM Experimental Biology and Medicine

TYPE Original Research
PUBLISHED 13 November 2025
DOI 10.3389/ebm.2025.10540

OPEN ACCESS

*CORRESPONDENCE
Zhenghui Wang,
ehui4298@163.com

†These authors share first authorship

RECEIVED 23 February 2025
REVISED 15 July 2025
ACCEPTED 07 October 2025
PUBLISHED 13 November 2025

CITATION
Guo R, Zhang Y, Chen Y, Sha W, Kou W, Xu C, Lei Y, Zhang N, Yang L, Guo Y, Zhang H and Wang Z (2025) The causal relationship between obstructive sleep apnea and otitis media: a bidirectional Mendelian randomization study. *Exp. Biol. Med.* 250:10540. doi: 10.3389/ebm.2025.10540

The causal relationship between obstructive sleep apnea and otitis media: a bidirectional Mendelian randomization study

Ruixin Guo[1†], Yifan Zhang[1†], Yijie Chen[1], Wenqi Sha[1], Wanyi Kou[1], Chensi Xu[1], Yuran Lei[1], Ningrui Zhang[1], Liu Yang[1], Yun Guo[1], Huihui Zhang[1] and Zhenghui Wang[1,2]*

[1]Department of Otolaryngology-Head and Neck Surgery, The Second Affiliated Hospital of Xi'an Jiaotong University, Xi'an, China, [2]Shaanxi Provincial Key Laboratory for Precision Diagnosis and Treatment of Otorhinolaryngology, The Second Affiliated Hospital of Xi'an Jiaotong University, Xi'an, China

Abstract

Obstructive sleep apnea (OSA) is manifested as periodic collapse of the upper airway during sleep. Otitis media is a spectrum of infectious and inflammatory diseases involving the middle ear. In this study, we sought to determine the causal effect of OSA on otitis media using a bidirectional, two-sample Mendelian randomization (MR) analysis. We analyzed the data from two different, extensive genome-wide association studies (GWAS) and selected OSA-related single-nucleotide polymorphisms (SNPs) as instrumental variables (IVs). Bidirectional MR analysis was conducted using the inverse-variance weighted (IVW) method. To ensure the robustness of the results, alternative sensitivity analysis procedures were performed, including MR-Egger, the MR pleiotropy residual sum and outlier (MR-PRESSO), and leave-one-out analysis. In the forward MR analysis, OSA was correlated with an increased risk of acute suppurative otitis media (odds ratio, 1.164; 95% confidence interval, 1.056–1.283; P = 0.002) and suppurative and unspecified otitis media (odds ratio, 1.150; 95% confidence interval, 1.059–1.249; P < 0.001). All reverse MR analyses showed that otitis media had no causal effect on OSA (P > 0.05). The MR analysis supports that OSA contributes to the development of otitis media. Thus, managing OSA may be beneficial in treating otitis media.

KEYWORDS

obstructive sleep apnea, otitis media, mendelian randomization, sleep disorder, twosample mendelian randomization

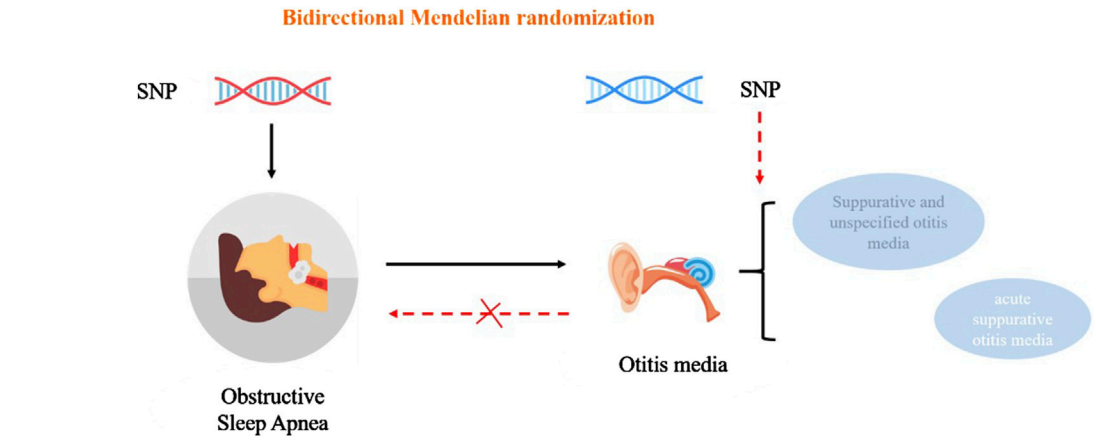

GRAPHICAL ABSTRACT

Impact statement

Several other studies have linked OSA to the development of otitis media, and similar pathological changes occur during the pathogenesis of both OSA and otitis media, such as the presence of systemic inflammation. Accordingly, we speculate that there may be a connection between OSA and otitis media, which confirmed by the result of the bidirectional MR analysis. Our finding may be exploited to improve the detection and management of otitis media.

Introduction

Obstructive sleep apnea (OSA) is a common type manifested as periodic collapse of the upper airway during sleep [1]. The sleep disorder is related to intermittent hypoxia, which elicits systemic inflammatory responses by promoting the release of inflammatory mediators such as nuclear factor-κB (NF-κB), interleukin (IL)-6, and IL-1β [2]. Accordingly, OSA may lead to serious complications affecting the cardiovascular, endocrine, and neurological systems [3–5].

Otitis media is a spectrum of infectious and inflammatory diseases involving the middle ear [6]. Risk factors for otitis media include bacterial or pathogenic infections, allergies, nasal congestion (sinusitis, adenoid hypertrophy, nasal or nasopharyngeal tumors), ciliary dysfunction, and possibly gastroesophageal reflux disease (GERD) [7]. Otitis media can cause a variety of pathological consequences, such as meningitis, acute mastoiditis, and hearing loss. Identification of the causal factors for otitis media is essential to improve the prognosis of patients with otitis media [7].

The relationship between OSA and otitis media is still controversial. On the one hand, from a macro-disease perspective, a previous study suggests no link between OSA and otitis media [8]. However, several other studies have linked OSA to the development of otitis media [9, 10]. OSA-related adenoid hypertrophy contributes to eustachian tube dysfunction, thus resulting in the development of secretory otitis media, particularly in children [9, 10]. Similar pathological changes occur during the pathogenesis of both OSA and otitis media, such as the presence of systemic inflammation [7, 11] and endoplasmic reticulum stress [12]. On the other hand, genetics play a role in both OSA and otitis media. Research had revealed that families with a history of chronic and recurrent otitis media have a higher incidence of otitis media than the general population [13]. A GWAS on OM was conducted at the University of Pittsburgh (UPitt), and significant duplication of rs10497394 on chromosome 2 was shown in a population of OM families. It is thought that this SNP plays a role in regulation by altering the binding of transcription factors, epigenetic markers, or lamellipodia-associated structural domains [14]. Similarly, OSA is a genetically complex disease that may result from the interaction of multiple genetic and environmental factors [15]. The role of genetic factors in OSA susceptibility is also supported by the studies of familial aggregation [16]. In addition, inflammation-related SNPs are associated with otitis media and OSA. Studies have shown that the risk of OM may be increased by SNPs for the IL-6 (−174) and proinflammatory cytokines tumor necrosis factor (TNF) [17]. It was also shown that polymorphisms in the TNF-α gene were associated with obstructive sleep apnoea (OSA) [18]. Therefore, we hypothesized that OSA may be associated with the development of otitis media. However, there is still a lack of appropriate clinical studies to explore this causal relationship further.

Mendelian randomisation (MR) analysis is an approach to investigate the causal link between illness exposure and outcome using an instrumental variable (IV) - genetic variation [3]. MR is based on the idea that genetic variation is randomly distributed to

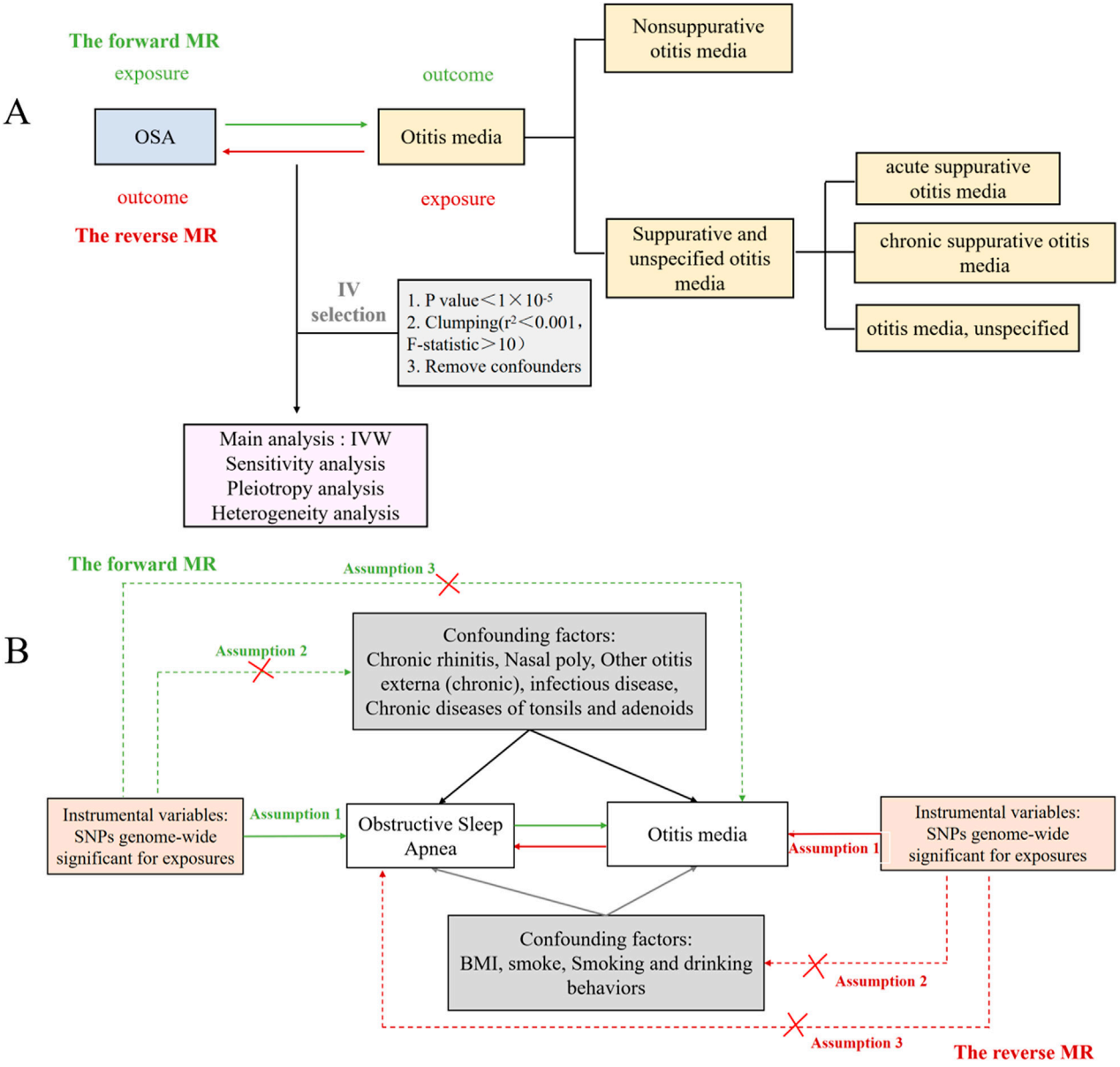

FIGURE 1
The Mendelian randomization study aims and assumptions. **(A)** The Mendelian randomization study aims. **(B)** The Mendelian randomization study assumptions.

offspring and has an advantage over traditional observational research in reducing confounding effects and reverse causation [19]. In this study, we analyzed the data from two large genome-wide association studies (GWAS) and chose OSA-related single-nucleotide polymorphisms (SNPs) as IVs. We aimed to determine the causal relationship between OSA and otitis media using a bidirectional MR analysis. Understanding the risk factors associated with otitis media can be beneficial for early diagnosis and treatment.

Materials and methods

MR research design

To determine the causal relationship between OSA and otitis media, we performed a bidirectional MR analysis (Figure 1A). SNPs were separately selected as IVs for the datasets of OSA and otitis media with their subtypes, while confounders were removed based on a review of the literature. There are three

hypotheses for the MR analysis: (1) IVs are strongly associated with exposure; (2) IVs are not associated with confounders that may affect exposure or outcome; (3) IVs affect otitis media only through the exposed pathway rather than other pathways (Figure 1B).

Data sources

We extracted the clinical and laboratory data on OSA and otitis media from FinnGen Study[1] and GWASs databases. This data was collected when all participants gave informed consent in their original studies. There is no requirement for additional ethical approval since reliance is only on summary-level statistics. Considering that bias can be caused in the estimates by population mixing, the genetic background of the population in the MR study was restricted to those of European descent.

Genetic summary-level data of OSA

Genetic predictors of OSA were obtained from FinnGen Study (G6_SLEEPAPNO). This dataset was built by the Finnish National Gene Research Project and contained 217,955 Europeans (16761 cases and 201,194 controls) with 16,380,465 SNPs. The case group comprised 10,557 males and 6,204 females. The average age at the first event was 54.91 years for males and 56 years for females. The overall unadjusted incidence rate was 7.72%, with 11.21% and 5.05% for males and females, respectively. The population diagnosis for the case group was based on ICD codes, all of which were ICD-10: G473. According to the American Academy of Sleep Medicine guidelines, diagnostic testing for OSA should be performed in conjunction with a comprehensive sleep evaluation and adequate follow-up, and polysomnography is the standard diagnostic test for the diagnosis of OSA in adult patients in whom there is a concern for OSA based on a comprehensive sleep evaluation [20]. The apnea-hypopnea index (AHI) is the primary measure of OSA severity, as indicated by the PSG outcomes [1]. AHI of ≥5 events/h with symptoms of respiratory sleep disorders and associated conditions, or AHI of ≥15 events/h without associated symptoms or conditions, fits the diagnostic criteria for OSA [21].

Genetic summary-level data of otitis media

The classification of otitis media into suppurative and non-suppurative (ICD-10) has been standardized by the International Health Organization (IHO), and further classification of otitis media into acute and chronic according to the course of the disease and the type of exudate has been carried out. In 2002, Gates et al. made further adjustments to the classification standard [22]. They proposed that otitis media should be divided into acute and chronic according to the course of the disease. They also suggested that otogenic complications should be categorized. This classification standard is now widely used.

However, based on the Mendelian randomization analysis that we performed using data from the FinnGen Study[1] 和IEU openGWAS of GWAS database[2], the classification and diagnostic criteria for otitis media were dominated by the ICD-10. The ICD-10 staging criteria include Nonsuppurative otitis media and Suppurative and unspecified otitis media. The latter includes acute suppurative otitis media, chronic suppurative otitis media and otitis media, unspecified.

First, we chose the datasets of Suppurative and unspecified otitis media (H8_MED_SUPP). The datasets contained 213,184 Europeans (7245 cases and 205,939 controls) with 16,380,441 SNPs. The first subtype dataset of Suppurative and unspecified otitis media was acute suppurative otitis media (finn-b-H8_SUP_ACUTE), which contained 211,171 Europeans (5,232 cases and 205,939 controls) with 16,380,429 SNPs. The case group comprised 2328 males and 2904 females. The average age at the first event was 14.55 years for males and 16.94 years for females. The overall unadjusted incidence rate was 2.41%, with rates of 2.47% and 2.36% for males and females, respectively. The population diagnosis for the case group was based on ICD codes, all of which were ICD-10: H660, ICD-8: 3810. The next subtype was Chronic suppurative otitis media, which was obtained from a publicly available GWAS dataset (GWAS ID: ebi-a-GCST90018809) and statistically analyzed by Sakaue S (PMID: 34594039) [23], including 484,145 Europeans (1,108 cases and 483,037 controls) and 24,194,289 SNPs. The last subtype was otitis media, unspecified, and its source was the FinnGen Study (H8_OTIMEDNAS). The Finnish National Gene Research Project built this dataset and comprises 2,179,555 European individuals (1,832 cases and 205,939 controls), with a total of 16,380,419 SNPs. The case group comprised 745 males and 1,087 females. The average age at the first event was 24.24 years for males and 24.48 years for females. The overall unadjusted incidence rate was 0.84%. Rates for males and females were 0.79% and 0.88%, respectively. The population diagnosis for the case group was based on ICD codes, all of which were ICD-10: H669, ICD-8: 3819.

According to ICD-10 classification criteria, the next subtype of otitis media was nonsuppurative otitis media (H8_NONSUPPNAS). The dataset of nonsuppurative otitis media contained 210320 Europeans (4,381 cases and 205,939 controls) with 16,380,433 SNPs. The case group comprised 1854 males and 2527 females. The average age at the first event was 21.78 years for males and 21.19 years for females. The overall unadjusted incidence rate was 2.02%, with rates of 1.97% and 2.06% for

1 https://www.finngen.fi/en

2 https://gwas.mrcieu.ac.uk/

males and females, respectively. The population diagnosis for the case group was based on ICD codes, all of which were ICD-10: H65, ICD-9: 381.

IV selection

In our study, we initially used a stringent threshold of $P < 5 \times 10^{-8}$ to screen for SNPs that were strongly associated with OSA and Otitis media, but only a few SNPs could fit this criterion. Finally, we set the significance threshold to $P < 1 \times 10^{-5}$ in OSA-otitis media studies and Otitis media-OSA studies. To avoid bias caused by linkage disequilibrium, any SNP that met the significance requirement must also have a r^2 value <0.001 and a kb value >10,000. We then removed palindromic SNPs with moderate allele frequencies, significant outliers detected by the MR Pleiotropy REsidual Sum and Outlier (MR-PRESSO) analysis, and confounders indicated by the Ldlink tool[3]. F values were calculated using formula F = (β/SE) [2], where β is the SNP's impact value and SE is its standard deviation [24]. The weak IVs with the F value of <10 were excluded [25].

MR analysis

In this study, we used the R software (version 4.3.3), the TwoSampleMR software package (version 0.5.10) for MR analysis, and the MR-PRESSO software package (version 1.0) for outlier removal. The inverse variance weighted (IVW) approach was utilized as the primary analysis method, with the MR-Egger, weighted median, simple model, and weighted model serving as auxiliary methods.

Sensitivity analysis

We employed the IVW and MR-Egger methods to assess heterogeneity. The heterogeneity among IVs was investigated using Cochran's Q statistic. We utilized a random-effects model in the MR analysis to eliminate heterogeneity-related bias. The test threshold for heterogeneity was $P > 0.05$. The MR-Egger intercept and MR-PRESSO were used to assess pleiotropy. MR-Egger is an adaptation of Egger's regression model which considers horizontal pleiotropy by incorporating an intercept into the weighted regression model [26]. The MR-PRESSO method was used to improve the analysis by identifying and excluding outliers that could be due to pleiotropy. The MR-PRESSO outlier test required at least 50% of the variants to be valid instruments dependent on Instrumental Strength Independent of Direct Effects (InSIDE), meaning the effect size of a variant on exposure should not depend on a horizontal, multidirectional effect on the outcome [27]. Funnel plots were used to ensure the study results were consistent and reliable. A "leave-one-out" analysis was also implemented to test the robustness and consistency of the results. The MR results for the remaining instrumental variables were calculated by excluding individual SNPs on a one-by-one basis, in order to assess whether the SNPs influenced the association between OSA and the risk of otitis media. The test threshold for pleiotropy was $P > 0.05$.

Results

IV selection for MR analysis

In the OSA-otitis media investigation, 59 SNPs were obtained after chain imbalance screening, and 10 were excluded due to their association with otitis media. Finally, we chose 49 SNPs as the IV, with an F-value of >10 for each SNP. The SNPs selected are given in Supplementary Table S1. In the otitis media - OSA investigation, we utilized a similar strategy for SNP selection. The final SNPs used for MR analysis are provided in Supplementary Table S2.

Causal effects of OSA on otitis media

In the forward MR analysis (Figure 2), the IVW method indicated OSA as a risk factor for acute suppurative otitis media (odds ratio (OR), 1.164; 95% confidence interval (CI), 1.056–1.283; $P = 0.002$). The Weighted median method also revealed a significant causal relationship (OR, 1.208; 95% CI, 1.056–1.715; $P = 0.006$). The association of OSA with suppurative and unspecified otitis media was also uncovered by the IVW (OR, 1.150; 95% CI, 1.059–1.249; $P < 0.001$) and Weighted median (OR, 1.182; 95% CI, 1.056–1.249; $P = 0.004$) methods. Both Weighted median IVW methods displayed similar scatter plots and had no significant heterogeneity or pleiotropy ($P > 0.05$; Supplementary Figure S1). Leave-one-out sensitivity analysis revealed that removing any single SNP had no significant effect on the results (Supplementary Figure S2). In addition, the other three subtypes of otitis media, i.e., chronic suppurative otitis media, nonsuppurative otitis media, and unspecified otitis media, did not appear to be related to OSA.

Causal effects of suppurative otitis media on OSA

In the reverse MR analysis, none of the suppurative otitis media subtypes showed a causal relationship with OSA

3 https://ldlink.nih.gov/

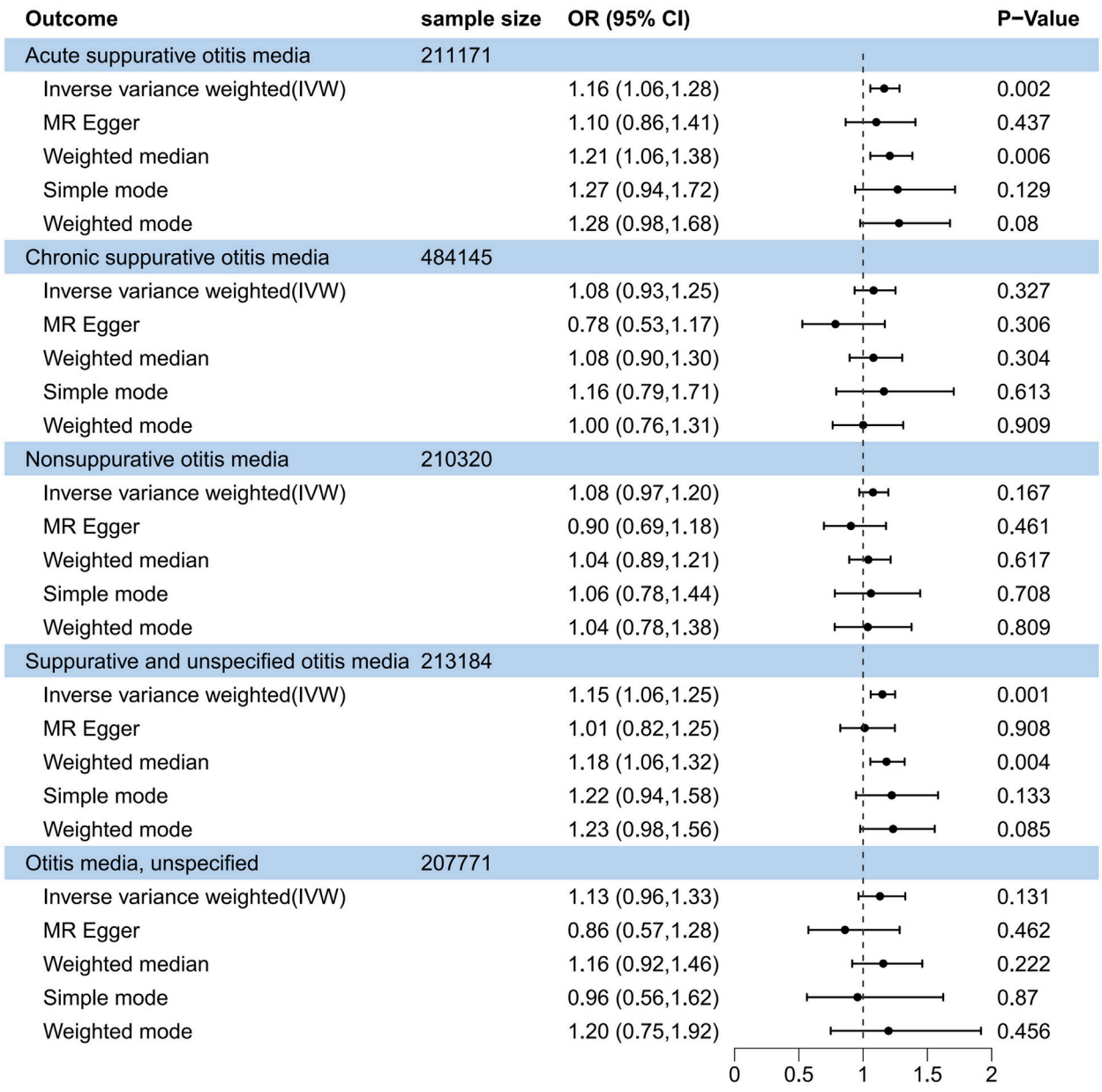

FIGURE 2
Forest plot of causal association between obstructive sleep apnea and suppurative otitis media in the forward MR analysis.

(Figure 3). The OR for the acute suppurative otitis media - OSA relationship was 0.984 (95% CI, 0.993–1.038; $P = 0.554$) in the IVW method, 1.015 (95% CI, 0.992–1.038; $P = 0.205$) for chronic suppurative media - OSA, 0.963 (95% CI, 0.897–1.034; $P = 0.302$) for nonsuppurative otitis media - OSA, 1.046 (95% CI, 0.988–1.109; $P = 0.125$) for suppurative and unspecified otitis media - OSA, and 0.978 (95% CI, 0.932–1.026; $P = 0.361$) for otitis media, unspecified - OSA. Similar results were obtained when the Weighted median method was used.

Discussion

In this work, we performed the MR analysis based on a large GWAS dataset to evaluate the causal relationship between OSA and otitis media. Our findings support the idea that OSA is significantly related to the development of otitis media, but otitis media has no causal effect on OSA.

Although our results show that the threshold for selecting SNPs is 1×10^5, the F statistics of the selected SNPs are all >10. Furthermore, the F statistics of the final 49 SNPs from positive

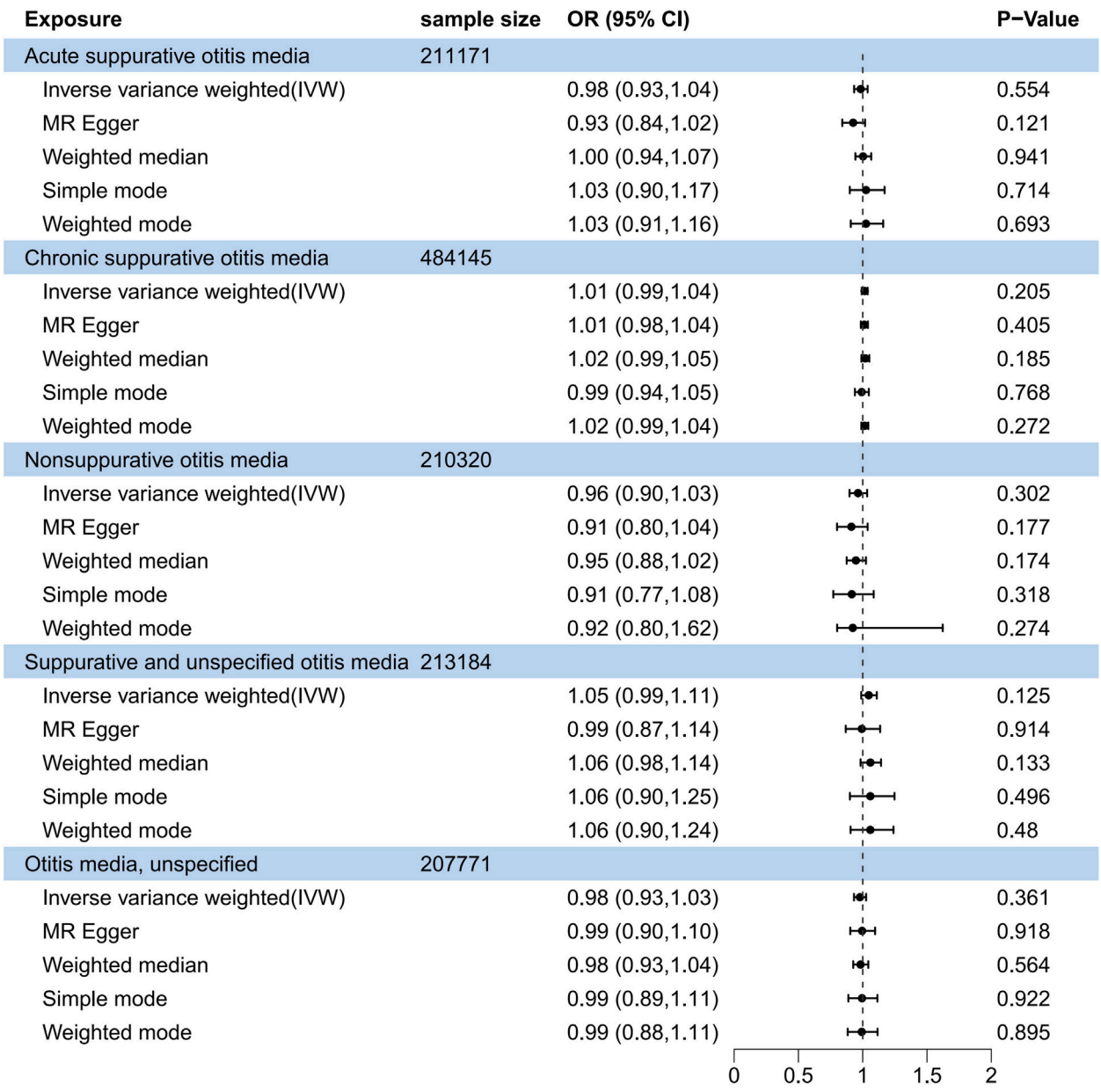

FIGURE 3
Forest plot of causal association between obstructive sleep apnea and suppurative otitis media in the reverse MR analysis.

Mendelian randomization after removing the confounders are all >19. This indicates that all our selected SNPs are strong instrumental variables, which provides a solid basis for conducting correlation analyses. Then, SNPs that were strongly associated with otitis media, including chronic rhinitis, nasal polyps, other otitis externa (chronic), infectious disease, and chronic diseases of tonsils and adenoids, were selected to avoid the influence of confounding factors. The final results show that the selected SNPs can only cause otitis media through OSA, and the forward MR results indicate that OSA can cause otitis media. Our results suggest that OSA is a risk factor for otitis media. This may be explained by the involvement of inflammatory and/or infectious processes in the pathogenesis of both OSA and otitis media. Abnormalities in nasopharyngeal anatomy contribute to the development of OSA. It has been documented that children with AOM had a reduced nasopharyngeal height and a small nose angle [28]. Newborns with OSA present an increased incidence of pharyngeal and eustachian tube dysfunction [29]. The angle

between the anterior and medial skull bases, the depth of the maxilla, and the height of the upper face are associated with the development of otitis media in adults [30]. Functional defects in the nasopharynx play an important role in the development of suppurative otitis media, which may arise from aberrant opening of the eustachian tube and bacterial colonization of the nasopharynx [31]. OSA is associated with pressure changes in the upper respiratory tract. The Eustachian tube not only protects the middle ear from bacterial infection, but also regulates pressure balance in the middle ear cavity [7]. OSA-induced pressure change in the upper respiratory tract may lead to the dysfunction of the Eustachian tube, consequently facilitating the development of suppurative otitis media [32].

In addition, our study shows no significant relationship between OSA and persistent suppurative otitis media. Recurrent middle ear infection has been suggested to contribute to chronic suppurative otitis media [33]. It has been documented that patients with chronic otitis media have a higher abundance of *Haemophilus* influenzae than patients with OSA [34]. Thus, rather than OSA, chronic suppurative otitis media may be caused by bacterial infection.

There are some limitations in this study. Firstly, our analysis was performed on only the European population. On the one hand, the prevalence of obstructive sleep apnoea (OSA) and otitis media varies across populations. Studies have shown that the prevalence of OSA is highest in China, followed by the United States, Brazil, and India [35]. A review of the literature has shown that the prevalence of OSA in Asian adults ranges from 3% to 97% [36]. In contrast, the prevalence of OSA in the general adult population in Europe ranges from 9% to 38% [37]. Significant differences in these results may be related to differences in geography, ethnicity, and research design. As for otitis media, it has also been shown that in Asia-Pacific countries, the prevalence of OM in schoolchildren ranges between 3.25% (Thailand) and 12.23% (Philippines) [38]; Auinger et al. showed that the prevalence of OM in children younger than 6 years of age in the United States was 68.2% (95% CI: 66.3%, 70.1%) during the period 1988–1994 [39]. Furthermore, there are discrepancies in the pathogens that cause acute otitis media. Research conducted in the United States, Finland and the Netherlands has demonstrated that in children between 4 weeks and 18 years of age, the predominant pathogens of AOM are *Streptococcus* pneumoniae (23%–48%) and *Haemophilus* influenzae (41%–57%) [40]; nevertheless, one study has shown that the predominant pathogens of AOM in Chinese children under 18 years of age are *Streptococcus* pneumoniae (47.2%; 108/229) and *Staphylococcus aureus* (18.8%; 43/229) [41]. These imply that the progression of OSA and otitis media is connected to a variety of elements, among which ethnic variations play a significant role. On the other hand, studies in a single population are insufficient to reveal all disease variants in different populations. GWA studies have been successful in identifying genetic variants that contribute to complex human traits, but they have mainly focused on European populations. The results of GWA studies may be affected by differences between populations, such as variations in disease allele frequencies, linkage disequilibrium (LD) patterns, phenotypic prevalence, effect sizes and rare variants [42]. To achieve a more comprehensive understanding of human genetic variation, it is essential to expand GWA studies to include more non-European populations. Secondly, the study subjects were adults. Since otitis media is more common in children, a validation study should be performed in Children. It is also necessary to include a wider range of people, including individuals of various age groups, in the GWA studies.

Conclusion

Our bidirectional MR analysis reveals a causal link between OSA and otitis media. This finding may be exploited to improve the detection and management of otitis media. The particular mechanism underlying the relationship between OSA and otitis media deserves further investigation.

Author contributions

RG and YZ completed majority of research, participated in conception and design, original draft. YC, WS, WK, and CX carried out conception, design and manuscript preparation. YL, NZ, and LY provide assistance for data acquisition and analysis. YG and HZ performed manuscript editing and review. The corresponding authors ZW, are major contributors in funding acquisition, designed experiments, writing-review and editing. All authors contributed to the article and approved the submitted version.

Data availability

The original contributions presented in the study are included in the article/Supplementary Material, further inquiries can be directed to the corresponding author.

Funding

The author(s) declare that financial support was received for the research and/or publication of this article. This work was

supported by the Funds for Shaanxi Province Zhong Dian Yan Fa Project (2025SF-YBXM-439) and Medical development fund of Xi'an Jiaotong University (XJYG2025-SFJJ030).

Conflict of interest

The author(s) declared no potential conflicts of interest with respect to the research, authorship, and/or publication of this article.

Generative AI statement

The author(s) declare that no Generative AI was used in the creation of this manuscript.

Any alternative text (alt text) provided alongside figures in this article has been generated by Frontiers with the support of artificial intelligence and reasonable efforts have been made to ensure accuracy, including review by the authors wherever possible. If you identify any issues, please contact us.

Supplementary material

The Supplementary Material for this article can be found online at: https://www.ebm-journal.org/articles/10.3389/ebm.2025.10540/full#supplementary-material

SUPPLEMENTARY FIGURE S1
The scatter plots of OSA on suppurative otitis media (Acute suppurative otitis media and suppurative and unspecified otitis media).

SUPPLEMENTARY FIGURE S2
The Leave-one-out sensitivity analysis plots of OSA on suppurative otitis media (Acute suppurative otitis media and suppurative and unspecified otitis media).

SUPPLEMENTARY TABLE S1
The final snp of OSA database.

SUPPLEMENTARY TABLE S2
The final snp of five subtype of otitis media.

References

1. Malhotra A, White DP. Obstructive sleep apnoea. *The lancet* (2002) **360**: 237–45. doi:10.1016/S0140-6736(02)09464-3

2. de Lima FFF, Mazzotti DR, Tufik S, Bittencourt L. The role inflammatory response genes in obstructive sleep apnea syndrome: a review. *Sleep and breathing* (2016) **20**:331–8. doi:10.1007/s11325-015-1226-7

3. Mi Z, Meng N, Zhang Y, Wang Q, Song S, Cheng R, et al. Genetically predicted obstructive sleep apnea is causally associated with an increased risk for periodontitis. *BMC Oral Health* (2023) **23**:723. doi:10.1186/s12903-023-03338-8

4. Gottlieb DJ, Punjabi NM. Diagnosis and management of obstructive sleep apnea: a review. *Jama* (2020) **323**:1389–400. doi:10.1001/jama.2020.3514

5. Abbasi A, Gupta SS, Sabharwal N, Meghrajani V, Sharma S, Kamholz S, et al. A comprehensive review of obstructive sleep apnea. *Sleep Sci* (2021) **14**:142–54. doi:10.5935/1984-0063.20200056

6. Principi N, Esposito S. Unsolved problems and new medical approaches to otitis media. *Expert Opin Biol Ther* (2020) **20**:741–9. doi:10.1080/14712598.2020.1740677

7. Schilder AG, Chonmaitree T, Cripps AW, Rosenfeld RM, Casselbrant ML, Haggard MP, et al. Otitis media. *Nat Rev Dis primers* (2016) **2**:16063–18. doi:10.1038/nrdp.2016.63

8. Dreher A, Patscheider M, Braun T. Pediatric obstructive sleep apnea and otitis media with effusion. *Otolaryngology—Head Neck Surg* (2011) **145**:P242–P42. doi:10.1177/0194599811415823a350

9. Liu C-B, Shi Y-H, Li X-Y, Fan Z-T. Prevalence and risk factors of otitis media with effusion in children with obstructive sleep apnea. *Eur Rev Med Pharmacol Sci* (2023) **27**:5445–52. doi:10.26355/eurrev_202306_32780

10. Huang C-C, Wu P-W, Chiu C-H, Lee T-J, Chen C-L. Assessment of sleep-disordered breathing in pediatric otitis media with effusion. *Pediatr and Neonatal* (2022) **63**:25–32. doi:10.1016/j.pedneo.2021.06.013

11. Pau MC, Zinellu A, Mangoni AA, Paliogiannis P, Lacana MR, Fois SS, et al. Evaluation of inflammation and oxidative stress markers in patients with obstructive sleep apnea (OSA). *J Clin Med* (2023) **12**:3935. doi:10.3390/jcm12123935

12. Jung SY, Kim SS, Yeo SG. Impact of endoplasmic reticulum stress in otorhinolaryngologic diseases. *Int J Mol Sci* (2020) **21**:4121. doi:10.3390/ijms21114121

13. Daly KA, Rich SS, Levine S, Margolis RH, Le CT, Lindgren B, et al. The family study of otitis media: design and disease and risk factor profiles. *Genet Epidemiol* (1996) **13**:451–68. doi:10.1002/(SICI)1098-2272(1996)13:5<451::AID-GEPI2>3.0.CO;2-5

14. Allen EK, Chen W-M, Weeks DE, Chen F, Hou X, Mattos JL, et al. A genome-wide association study of chronic otitis media with effusion and recurrent otitis media identifies a novel susceptibility locus on chromosome 2. *J Assoc Res Otolaryngol* (2013) **14**:791–800. doi:10.1007/s10162-013-0411-2

15. Mukherjee S, Saxena R, Palmer LJ. The genetics of obstructive sleep apnoea. *Respirology* (2018) **23**:18–27. doi:10.1111/resp.13212

16. Kump K, Browner I, Ferrette V, Krejci P. The familial aggregation of obstrurtive sleep apnea. *Am J Respircrit Caremed Vallsl* (1995) **682**:687. doi:10.1164/ajrccm/151.3_Pt_1.682

17. Patel JA, Nair S, Revai K, Grady J, Saeed K, Matalon R, et al. Association of proinflammatory cytokine gene polymorphisms with susceptibility to otitis media. *Pediatrics* (2006) **118**:2273–9. doi:10.1542/peds.2006-0764

18. Zhong A, Xiong X, Xu H, Shi M. An updated meta-analysis of the association between tumor necrosis factor-α-308G/A polymorphism and obstructive sleep apnea-hypopnea syndrome. *PLoS One* (2014) **9**:e106270. doi:10.1371/journal.pone.0106270

19. Emdin CA, Khera AV, Kathiresan S. Mendelian randomization. *Jama* (2017) **318**:1925–6. doi:10.1001/jama.2017.17219

20. Kapur VK, Auckley DH, Chowdhuri S, Kuhlmann DC, Mehra R, Ramar K, et al. Clinical practice guideline for diagnostic testing for adult obstructive sleep apnea: an American academy of sleep medicine clinical practice guideline. *J Clin Sleep Med* (2017) **13**:479–504. doi:10.5664/jcsm.6506

21. Berry RB, Budhiraja R, Gottlieb DJ, Gozal D, Iber C, Kapur VK, et al. Rules for scoring respiratory events in sleep: update of the 2007 AASM manual for the scoring of sleep and associated events: deliberations of the sleep apnea definitions task force of the American academy of sleep medicine. *J Clin Sleep Med* (2012) **08**:597–619. doi:10.5664/jcsm.2172

22. Bluestone CD, Gates GA, Klein JO, Lim DJ, Mogi G, Ogra PL, et al. 1. Definitions, terminology, and classification of otitis media. *Ann Otology, Rhinology and Laryngol* (2002) **111**:8–18. doi:10.1177/00034894021110S304

23. Sakaue S, Kanai M, Tanigawa Y, Karjalainen J, Kurki M, Koshiba S, et al. A cross-population atlas of genetic associations for 220 human phenotypes. *Nat Genet* (2021) **53**:1415–24. doi:10.1038/s41588-021-00931-x

24. Hu Y, Zou Y, Zhang M, Yan J, Zheng Y, Chen Y. The relationship between major depressive disorder and dementia: a bidirectional two-sample Mendelian

randomization study. *J Affective Disord* (2024) **355**:167–74. doi:10.1016/j.jad.2024.03.149

25. Burgess S, Dudbridge F, Thompson SG. Combining information on multiple instrumental variables in Mendelian randomization: comparison of allele score and summarized data methods. *Stat Med* (2016) **35**:1880–906. doi:10.1002/sim.6835

26. Bowden J, Davey Smith G, Burgess S. Mendelian randomization with invalid instruments: effect estimation and bias detection through egger regression. *Int J Epidemiol* (2015) **44**:512–25. doi:10.1093/ije/dyv080

27. Verbanck M, Chen C-Y, Neale B, Do R. Detection of widespread horizontal pleiotropy in causal relationships inferred from Mendelian randomization between complex traits and diseases. *Nat Genet* (2018) **50**:693–8. doi:10.1038/s41588-018-0099-7

28. Renko M, Kristo A, Tapiainen T, Koivunen P, Ilkko E, Alho O-P, et al. Nasopharyngeal dimensions in magnetic resonance imaging and the risk of acute otitis media. *The J Laryngol and Otology* (2007) **121**:853–6. doi:10.1017/S002221510700268X

29. Robison JG, Wilson C, Otteson TD, Chakravorty SS, Mehta DK. Increased eustachian tube dysfunction in infants with obstructive sleep apnea. *The Laryngoscope* (2012) **122**:1170–7. doi:10.1002/lary.22473

30. Di Francesco RC, Sampaio PL, Bento RF. Correlation between otitis media and craniofacial morphology in adults. *Ear, Nose and Throat J* (2007) **86**:738–43. doi:10.1177/014556130708601210

31. Cayé-Thomasen P, Hermansson A, Bakaletz L, Hellstrøm S, Kanzaki S, Kerschner J, et al. Panel 3: recent advances in anatomy, pathology, and cell biology in relation to otitis media pathogenesis. *Otolaryngology-head neck Surg official J Am Acad Otolaryngology-Head Neck Surg* (2013) **148**:E37–E51. doi:10.1177/0194599813476257

32. Zhang Q, Qiang Y, Xie M, Liu X, Guo R, Shi Y, et al. The effect of OSA on the negative pressure and acoustic compliance of middle ear cavity in children. *Int J Pediatr Otorhinolaryngol* (2023) **165**:111457. doi:10.1016/j.ijporl.2023.111457

33. Bhutta MF, Leach AJ, Brennan-Jones CG. Chronic suppurative otitis media. *The Lancet* (2024) **403**:2339–48. doi:10.1016/S0140-6736(24)00259-9

34. Nistico L, Kreft R, Gieseke A, Coticchia J, Burrows A, Khampang P, et al. Adenoid reservoir for pathogenic biofilm bacteria. *J Clin Microbiol* (2011) **49**:1411–20. doi:10.1128/JCM.00756-10

35. Benjafield AV, Ayas NT, Eastwood PR, Heinzer R, Ip MS, Morrell MJ, et al. Estimation of the global prevalence and burden of obstructive sleep apnoea: a literature-based analysis. *The Lancet Respir Med* (2019) **7**:687–98. doi:10.1016/S2213-2600(19)30198-5

36. Niu Y, Sun S, Wang Y, Chen L, Shao Y, Zhang X. Spatiotemporal trends in the prevalence of obstructive sleep apnoea across China: a multilevel meta-analysis incorporating geographic and demographic stratification (2000-2024). *Nat Sci Sleep* (2025) **Vol. 17**:879–903. doi:10.2147/NSS.S525547

37. Senaratna CV, Perret JL, Lodge CJ, Lowe AJ, Campbell BE, Matheson MC, et al. Prevalence of obstructive sleep apnea in the general population: a systematic review. *Sleep Med Rev* (2017) **34**:70–81. doi:10.1016/j.smrv.2016.07.002

38. Mahadevan M, Navarro-Locsin G, Tan H, Yamanaka N, Sonsuwan N, Wang P-C, et al. A review of the burden of disease due to otitis media in the Asia-Pacific. *Int J Pediatr Otorhinolaryngol* (2012) **76**:623–35. doi:10.1016/j.ijporl.2012.02.031

39. Auinger P, Lanphear BP, Kalkwarf HJ, Mansour ME. Trends in otitis media among children in the United States. *Pediatrics* (2003) **112**:514–20. doi:10.1542/peds.112.3.514

40. Coker TR, Chan LS, Newberry SJ, Limbos MA, Suttorp MJ, Shekelle PG, et al. Diagnosis, microbial epidemiology, and antibiotic treatment of acute otitis media in children: a systematic review. *Jama* (2010) **304**:2161–9. doi:10.1001/jama.2010.1651

41. Ding Y, Geng Q, Tao Y, Lin Y, Wang Y, Black S, et al. Etiology and epidemiology of children with acute otitis media and spontaneous otorrhea in suzhou, China. *Pediatr Infect Dis J* (2015) **34**:e102–e106. doi:10.1097/INF.0000000000000617

42. Rosenberg NA, Huang L, Jewett EM, Szpiech ZA, Jankovic I, Boehnke M. Genome-wide association studies in diverse populations. *Nat Rev Genet* (2010) **11**:356–66. doi:10.1038/nrg2760

EBM Experimental Biology and Medicine

TYPE Original Research
PUBLISHED 15 October 2025
DOI 10.3389/ebm.2025.10610

OPEN ACCESS

*CORRESPONDENCE
Chengfang Li,
lichengfang1228@163.com

†These authors have contributed equally to this work and share first authorship

RECEIVED 31 March 2025
ACCEPTED 29 September 2025
PUBLISHED 15 October 2025

CITATION
Jin D, Sun J, Zhang W, Zhang M and Li C (2025) Glaucoma and cardiovascular disease: a bidirectional two-sample Mendelian randomization analysis. *Exp. Biol. Med.* 250:10610. doi: 10.3389/ebm.2025.10610

Glaucoma and cardiovascular disease: a bidirectional two-sample Mendelian randomization analysis

Dongdong Jin[1†], Jie Sun[2†], Wei Zhang[3], Mingxuan Zhang[4] and Chengfang Li[5*]

[1]Department of Anesthesiology, Qingdao Traditional Chinese Medicine Hospital (Qingdao Hiser Hospital), Qingdao, Shandong, China, [2]Operating Room Nursing Department, Qingdao Traditional Chinese Medicine Hospital (Qingdao Hiser Hospital), Qingdao, Shandong, China, [3]Disinfection Supply Center, Qingdao Traditional Chinese Medicine Hospital (Qingdao Hiser Hospital), Qingdao, Shandong, China, [4]Department of Anesthesia Surgery, Qingdao Traditional Chinese Medicine Hospital (Qingdao Hiser Hospital), Qingdao, Shandong, China, [5]Department of Ophthalmology, Qingdao Traditional Chinese Medicine Hospital (Qingdao Hiser Hospital), Qingdao, Shandong, China

Abstract

Many studies reported that glaucoma is associated with cardiovascular disease (CVD). This study aims to investigate the potential causal relationship between glaucoma and CVD using a bidirectional two-sample Mendelian randomization (MR) analysis. The genome-wide association studies (GWAS) of glaucoma and CVD were downloaded from the IEU OpenGWAS project. The CVD included unstable angina pectoris (UAP), coronary artery disease (CAD), high blood pressure (HBP), myocardial infarct (MI), heart failure (HF), ischemic stroke (IS), atrial fibrillation (AF), and pulmonary embolism (PE). The inverse variance weighting (IVW) analysis was the primary method in MR analysis. Meanwhile, sensitivity analysis and statistical power tests were performed. The random effects IVW method showed a causal relationship between glaucoma and a decreased risk of MI (Odds ratio (OR): 0.94, 95% confidence interval (CI): 0.89–0.99; P = 0.012). In the reverse MR analysis, genetic susceptibility of UAP (OR: 1.12, 95% CI: 1.02–1.23; P = 0.022), CAD (OR: 1.1, 95% CI: 1–1.21; P = 0.041), and HBP (OR: 1.83, 95% CI: 1.25–2.67; P = 0.002) was significantly linked to an increased risk of glaucoma. MR-Egger (P = 0.005) and IVW (P = 0.005) methods found that HBP presented different degrees of heterogeneity. The random effects IVW method also demonstrated that HBP is the risk factor for glaucoma (P = 0.0017). Although reverse MR initially suggested a potential association between CAD and glaucoma, MVMR showed no causal relationship after adjusting for obesity and BMI. The MR analysis found that glaucoma serves

as a protective factor for MI, while UAP and HBP were risk factors for glaucoma in the European population, which may contribute to preventing and managing glaucoma and CVD.

KEYWORDS

glaucoma, cardiovascular disease, causal relationship, Mendelian randomization analysis, genetic correlation

Impact statement

Many studies reported that glaucoma is associated with CVD. However, the causal relationship between glaucoma and CVD is not clear. This discovery bridges the gap between basic research and clinical care, providing genetic-based evidence. This evidence could potentially guide the development of prevention strategies in the clinical practice of glaucoma and CVD, such as early screening for at-risk patients with specific cardiovascular conditions for glaucoma and *vice versa*, and tailoring treatment plans considering the identified causal relationships. The MR analysis found that glaucoma serves as a protective factor for MI, while UAP and HBP were risk factors for glaucoma in the European population, which may contribute to preventing and managing glaucoma and CVD.

Introduction

Glaucoma is a chronic, progressive optic neuropathy, characterized by optic nerve damage and visual field loss, leading to irreversible blindness [1]. In 2020, glaucoma (3.6 million cases) is the second leading cause of blindness in people aged 50 and older worldwide, after cataracts (15.2 million cases) [2]. The global prevalence of glaucoma is 3.54%, and patients with glaucoma are expected to reach 111 million by 2040 [3]. Based on the anatomical state of the anterior chamber angle, glaucoma can be categorized into open-angle and closed-angle types [4]. Each type can be further divided into primary and secondary glaucoma [4]. An increase in intraocular pressure (IOP) is closely associated with the development of glaucoma, and lowering IOP is the only feasible way to treat glaucoma [1, 5]. However, the IOP of nearly 50% of glaucoma patients falls within the normal range [1]. Many studies have reported that there are associations between gut microbiota, body mass index, and waist circumference with glaucoma [6, 7]. Noteworthily, some cardiovascular diseases (CVD) have also been associated with glaucoma [8, 9].

CVD are various diseases that affect the heart and blood vessels, such as unstable angina pectoris (UAP), coronary artery disease (CAD), high blood pressure (HBP), myocardial infarction (MI), heart failure (HF), ischemic stroke (IS), atrial fibrillation (AF), and pulmonary embolism (PE) [10, 11]. CVD poses a heavy medical burden in China [12]. Several large population studies have reported CVD as a risk factor for open-angle glaucoma (OAG) [13, 14]. Bennion et al. demonstrated that heart disease was the leading cause of death in glaucoma-related mortality in the United States, followed by malignant neoplasms and cerebrovascular disease [15]. Similarly, patients with OAG are about 1.5 times more likely to develop CVD than non-glaucoma individuals [16]. However, the causal relationship between glaucoma and CVD is not clear.

Mendelian randomization (MR) analysis is applied to explore the potential causal relationship between exposure and outcome through single-nucleotide polymorphisms (SNPs) as the instrumental variable (IV) [17]. Since the selected SNPs were randomly assigned through meiosis, MR results are not influenced by confounders between exposure and outcome and reverse causation [18]. Meng et al. reported that ankylosing spondylitis was the risk factor for both primary OAG and primary angle-closure glaucoma [19]. In addition, getting up easily in the morning and sleep duration were demonstrated as risk factors for POAG through MR analysis [20]. Therefore, the potential causal effects between glaucoma and CVD, including MI, HBP, HF, PE, CAD, UAP, IS, and AF, are explored using bidirectional two-sample MR analysis in this study.

Materials and methods

Data source and study design

Summary statistics data for glaucoma- and CVD-associated SNPs were collected from the IEU OpenGWAS project[1]. The GWAS of glaucoma[2] included 8,591 cases and 210,201 controls. For the CVD datasets, summary data for UAP[3] included 9,481 cases and 446,987 controls [21], summary data for CAD[4] comprised 42,096 cases and 361 controls [22], summary data for HBP[5] included 124,227 cases and 337,653 controls, summary data for MI[6] comprised 20,917 cases and 440,906 controls [21], summary data for HF[7]

1 https://gwas.mrcieu.ac.uk
2 https://gwas.mrcieu.ac.uk/datasets/finn-b-H7_GLAUCOMA/
3 https://gwas.mrcieu.ac.uk/datasets/ebi-a-GCST90018932/
4 https://gwas.mrcieu.ac.uk/datasets/ebi-a-GCST003116/
5 https://gwas.mrcieu.ac.uk/datasets/ukb-b-14177/
6 https://gwas.mrcieu.ac.uk/datasets/ebi-a-GCST90018877/
7 https://gwas.mrcieu.ac.uk/datasets/ebi-a-GCST009541/

TABLE 1 Detailed information on the GWAS datasets included in this study.

Exposure or outcomes	GWAS ID	Sample size (case/controls)	SNPs	Year
Glaucoma	finn-b-H7_GLAUCOMA	8,591/210,201	16,380,466	2021
Unstable angina pectoris	ebi-a-GCST90018932	9,481/446,987	24,179,929	2021
Coronary artery disease	ebi-a-GCST003116	42,096/361	8,597,751	2015
High blood pressure	ukb-b-14177	124,227/337,653	9,851,867	2018
Myocardial infarct	ebi-a-GCST90018877	20,917/440,906	24,172,914	2021
Heart failure	ebi-a-GCST009541	47,309/93,0014	7,773,021	2020
Ischemic stroke	ebi-a-GCST90018864	11,929/472,192	24,174,314	2021
Atrial fibrillation	ebi-a-GCST006414	60,620/970,216	11,039,197	2018
Pulmonary embolism	ebi-a-GCST90013887	407,746	33,519,037	2021

SNPs: Single Nucleotide Polymorphisms.

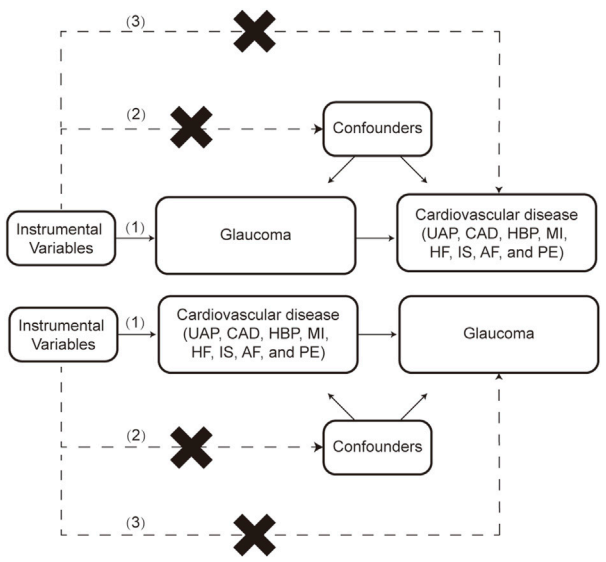

FIGURE 1
The flow chart of this study. The MR method is based on 3 hypotheses: (1) Instrumental variables (IVs) must be closely related to the exposure; (2) IVs independent from confounders; (3) IVs only affect outcomes through exposure, not through other pathways. UAP: Unstable angina pectoris, CAD: Coronary artery disease, HBP: High blood pressure, MI: Myocardial infarction, HF: Heart failure, IS: Ischemic stroke, AF: Atrial fibrillation, PE: Pulmonary embolism.

included 47,309 cases and 930,014 controls [23], summary data for IS[8] comprised 11,929 cases and 472,192 controls [21], and summary data for AF[9] contained 60,620 cases and 970,216 controls [24]. The summary data for PE[10] included 407,746 samples [25]. The detailed information of all the GWAS is demonstrated in Table 1. All statistical data were gathered from the descendants of Europeans, reducing the potential bias due to racial differences. Notably, no overlap was observed, given that samples of glaucoma and CVD originated from distinct study groups.

Two-sample MR analysis was utilized to explore the potential causal association between glaucoma and CVD risks. An overview of the study design is shown in Figure 1. SNPs served as IVs must satisfy the following conditions: (1) IVs must be closely related to the exposure; (2) IVs independent from confounders; (3) IVs only affect outcomes through exposure, not through other pathways.

Selection of IVs

First, the SNPs with p-value $< 5 \times 10^{-8}$ were selected as the IVs. Then, the parameters ($r^2 < 0.001$ and clump window = 10,000 kb) were utilized to remove the linkage disequilibrium bias. Next, SNPs with F-statistic >10, strongly correlated with exposure, were obtained [26].

Statistical analysis

This study used three methods (fixed-effects inverse variance weighted (IVW), weighted median, and MR-Egger) to perform MR analysis. The fixed-effects IVW method is the primary analysis to assess the causal associations between glaucoma

8 https://gwas.mrcieu.ac.uk/datasets/ebi-a-GCST90018864/

9 https://gwas.mrcieu.ac.uk/datasets/ebi-a-GCST006414/

10 https://gwas.mrcieu.ac.uk/datasets/ebi-a-GCST90013887/

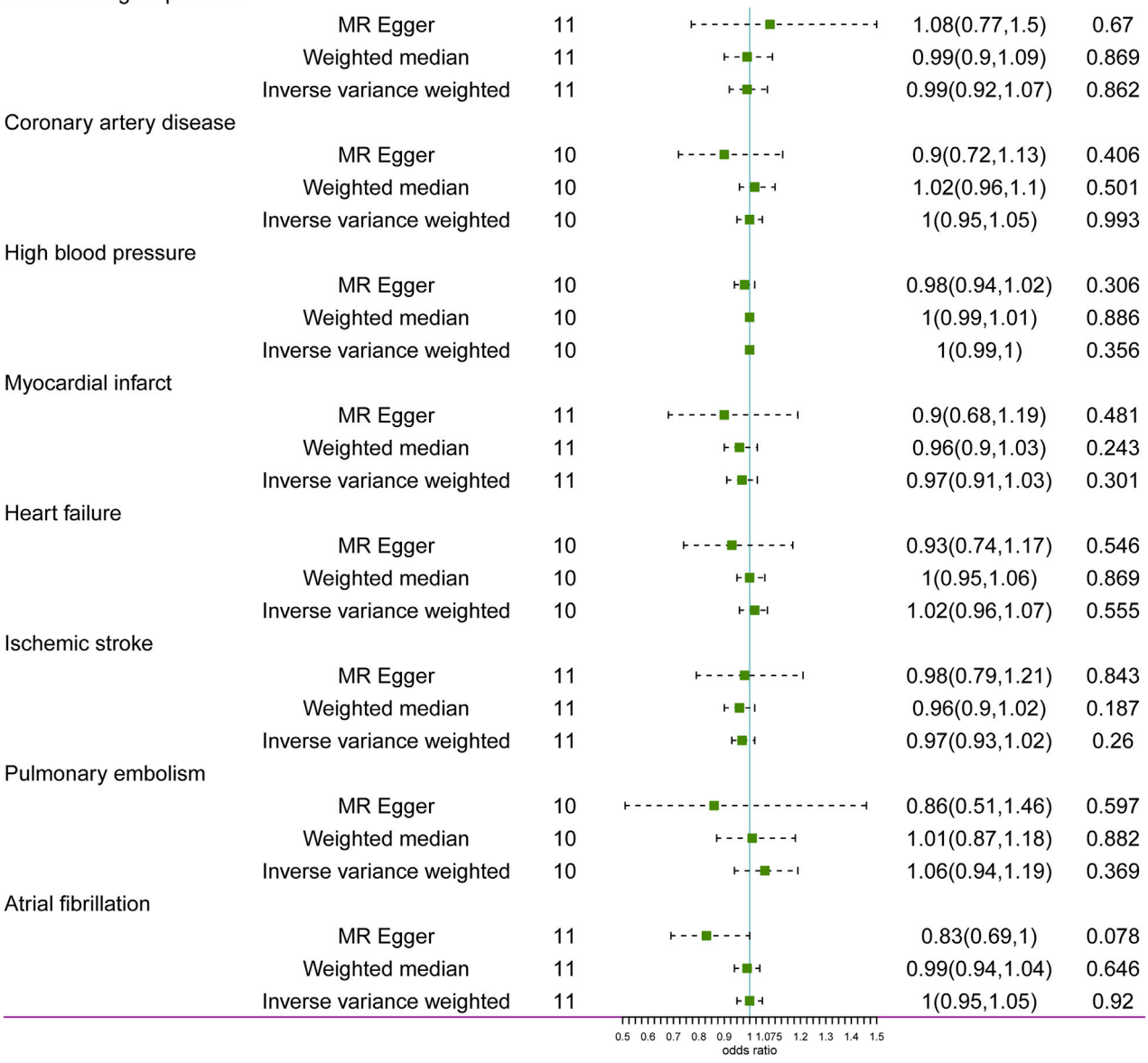

FIGURE 2
Associations between glaucoma and risk of cardiovascular disease using Mendelian randomization analysis. SNPs: Single-nucleotide polymorphisms, OR: Odds ratio, CI: Confidence interval.

and CVD according to heterogeneity [27]. Weighted median and MR-Egger methods were applied as supplementary analyses. The weighted median method can provide reliable causal estimates when at least half of the IVs are valid [28]. MR-Egger regression can discern horizontal pleiotropy and offer causal estimates after correction for horizontal pleiotropy [28].

For sensitivity analysis, firstly, MR-Egger regression and IVW methods were used to detect heterogeneity [28]. Cochrane's Q-derived p-value < 0.05 indicated that heterogeneity existed between IVs, and then random effects IVW was carried out to calculate causal estimates [29]. Second, for the horizontal pleiotropy analysis, the MR-Egger intercept was performed. The p-value > 0.05 was considered a weak possibility of genetic pleiotropy, and its impact may be discarded [30]. The MR-PRESSO method was utilized to remove outliers and then calculate causal estimates [31]. Finally, leave-one-out was performed to evaluate whether the results were caused by a single SNP [32]. The "TwoSampleMR" and "MR-PRESSO" packages in R (v 4.2.3) were utilized to perform statistical analysis.

TABLE 2 Heterogeneity and pleiotropy test for the associations of glaucoma with CVD.

Outcome	Heterogeneity test						Pleiotropy test		
	MR-Egger			Inverse variance weighted			MR-Egger		
	Q	Q_df	Q_pval	Q	Q_df	Q_pval	Egger intercept	se	pval
UAP	12.731	9	0.175	13.073	10	0.220	−0.012	0.025	0.634
CAD	9.306	8	0.317	10.245	9	0.331	0.015	0.017	0.395
HBP	31.092	8	1.35E-04	34.297	9	7.92E-05	0.003	0.003	0.390
MI	18.341	9	0.031	18.900	10	0.042	0.011	0.021	0.613
HF	14.607	8	0.067	15.730	9	0.073	0.013	0.017	0.455
IS	9.799	9	0.367	9.801	10	0.458	−0.001	0.016	0.971
PE	4.929	8	0.765	5.531	9	0.786	0.030	0.038	0.460
AF	14.090	9	0.119	20.431	10	0.025	0.027	0.013	0.075

UAP: unstable angina pectoris; CAD: coronary artery disease; HBP: high blood pressure; MI: myocardial infarct; HF: heart failure; IS: ischemic stroke; PE: pulmonary embolism; AF: atrial fibrillation; Q: Heterogeneity static Q; df: Degree of freedom; se: Standard error.

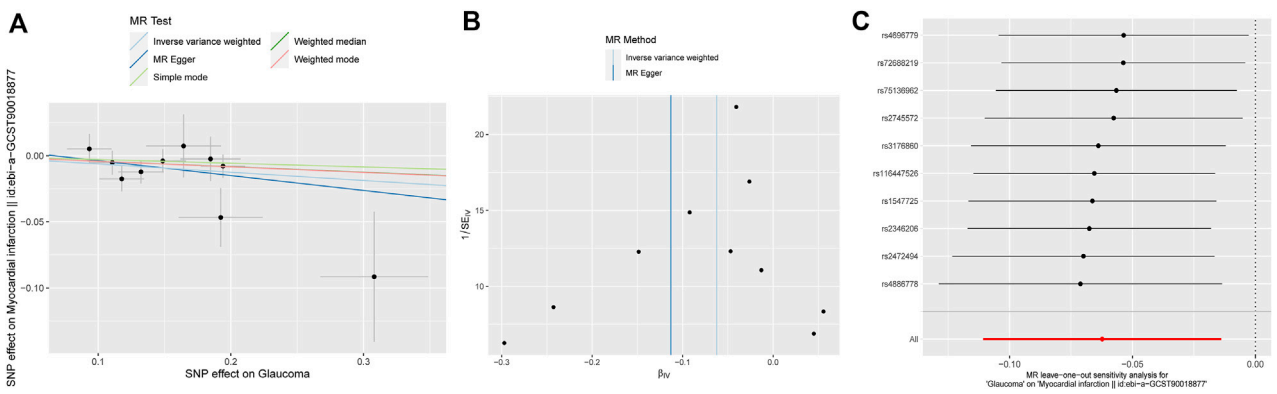

FIGURE 3
Associations between glaucoma and risk of MI using Mendelian randomization analysis. **(A)** Scatter plot for the associations between glaucoma and MI. **(B)** Funnel plots for the relationship between glaucoma and MI. **(C)** Leave-one-out for the relationship between glaucoma and MI. MI: Myocardial infarction; SNP: Single nucleotide polymorphism.

Summary data-based mendelian randomization (SMR) analysis

Using the summary statistics of eQTL and GWAS, the association between gene expression and HBP and glaucoma was tested by SMR analysis. Gene expression was used as the exposure factor, and HBP and glaucoma were the outcome factors. The SNPs of cis-eQTL were used as IVs. The analysis was performed using Rstudio and SMR software, with default settings applied during the analysis. Genes with significant loci were selected using P_SMR less than 0.05, and the heterogeneity in dependent instruments (HEIDI) test was used to evaluate the heterogeneity of the results (p_HEIDI > 0.05). Subsequently, GO and KEGG enrichment analysis (P < 0.05) was performed and a Protein-Protein Interaction (PPI) network was constructed to explore the possible molecular mechanisms involved in potential pathogenic genes.

Results

Information of IVs

A total of 11 SNPs associated with glaucoma were obtained. For SNPs linked to CVD, there were 14 for UAP, 31 for CAD, 187 for HBP, 67 for MI, 9 for HF, 13 for IS, 7 for PE, and 97 for AF. All SNPs were satisfied the following criteria: $p < 5 \times 10^{-8}$, $r^2 < 0.001$, and clump window = 10,000 kb. Simultaneously, palindromic SNPs were removed. The range of SNPs associated

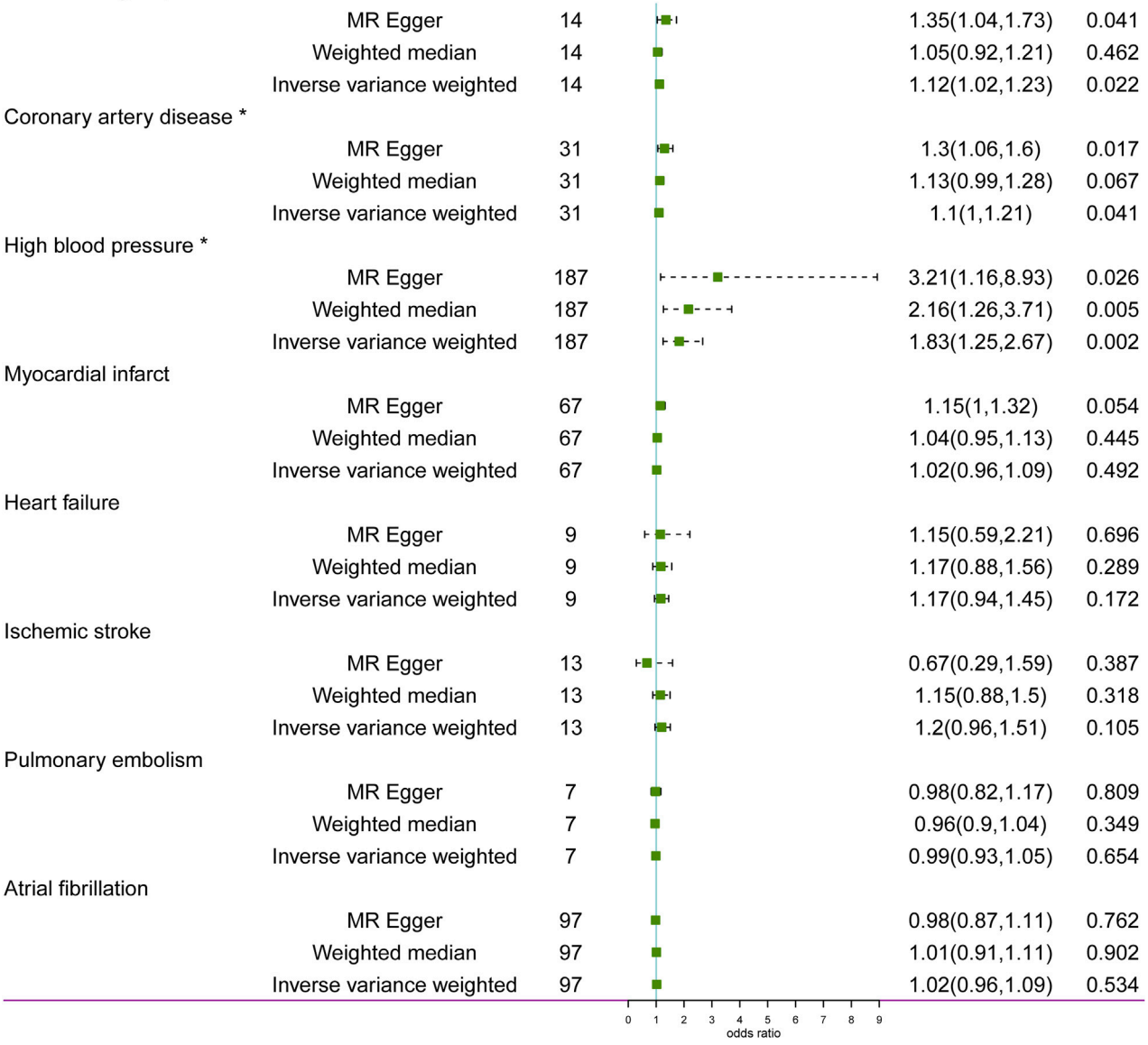

FIGURE 4
Associations between cardiovascular disease and risk of glaucoma using Mendelian randomization analysis. SNPs: Single-nucleotide polymorphisms, OR: Odds ratio, CI: Confidence interval.

with glaucoma based on F-statistic was 30.91–135.09, while the range of SNPs linked to CVD was 29.50–2039.47.

Causal effects of glaucoma on CVD

The results of MR analysis do not support a causal relationship between glaucoma and CVD risks (Figure 2). The *p*-values of Cochran's Q test were less than 0.05 for both MR-Egger and IVW methods in HBP and MI, demonstrating that the IVs of HBP and MI presented different degrees of heterogeneity (Table 2). Additionally, IVW analysis showed that IVs in AF (P = 0.025) also have heterogeneity (Table 2). Meanwhile, the MR-Egger regression intercept test found that IVs among CVD were not present with horizontal pleiotropy (Table 2). Then, random effects IVM analysis was carried out, and we found that no causal associations existed between glaucoma and HBP (P = 0.356), MI (P = 0.301), and AF (P = 0.92). MR-PRESSO analysis showed that HBP (P < 0.001), MI (P = 0.049), and AF (P = 0.021) existed horizontal pleiotropy. After removing outliers, causal relationships between glaucoma and

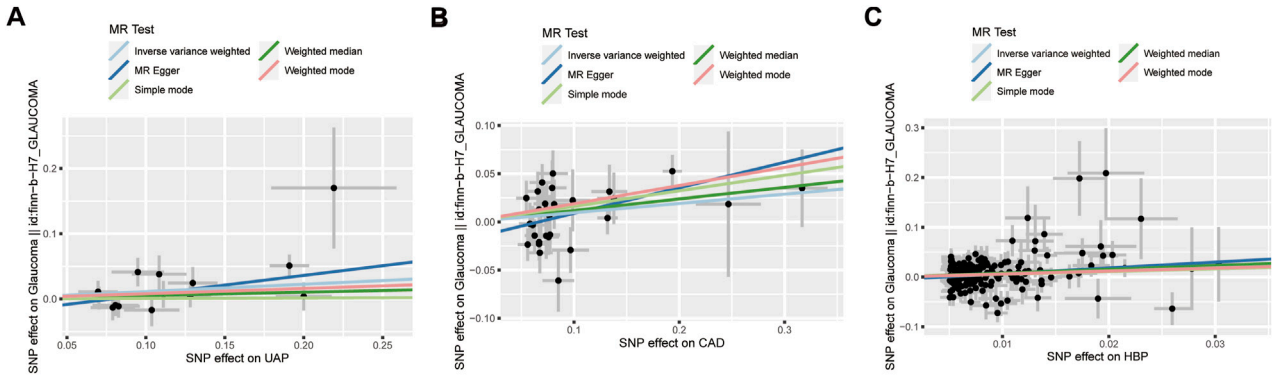

FIGURE 5
Scatter plot for the associations between UAP **(A)**, CAD **(B)**, as well as HBP **(C)** and glaucoma. UAP: Unstable angina pectoris; CAD: Coronary artery disease; HBP: High blood pressure; SNP: Single nucleotide polymorphism.

TABLE 3 Heterogeneity and pleiotropy test for the associations of CVD with glaucoma.

Exposure	Heterogeneity test						Pleiotropy test		
	MR-Egger			Inverse variance weighted			MR-Egger		
	Q	Q_df	Q_pval	Q	Q_df	Q_pval	Egger intercept	se	pval
UAP	12.569	12	0.401	15.020	13	0.306	−0.023	0.015	0.152
CAD	35.806	29	0.179	39.748	30	0.110	−0.018	0.010	0.084
HBP	238.149	185	0.005	239.889	186	0.005	−0.005	0.004	0.246
MI	79.118	65	0.112	83.277	66	0.074	−0.012	0.006	0.069
HF	2.686	7	0.912	2.689	8	0.952	0.001	0.022	0.958
IS	16.348	11	0.129	19.144	12	0.085	0.036	0.026	0.197
PE	2.736	5	0.741	2.747	6	0.840	0.003	0.026	0.921
AF	154.450	95	0.000	155.349	96	0.000	0.004	0.005	0.459

UAP: unstable angina pectoris; CAD: coronary artery disease; HBP: high blood pressure; MI: myocardial infarct; HF: heart failure; IS: ischemic stroke; PE: pulmonary embolism; AF: atrial fibrillation; Q: Heterogeneity static Q; df: Degree of freedom; se: Standard error.

HBP, as well as AF, were not present. However, there was a causal relationship between glaucoma and MI (P = 0.028). Subsequently, MR analysis was performed again after removing outliers, and the results showed that glaucoma was linked to a decreased risk of MI (OR: 0. 94, 95% CI: 0.89–0.99; P = 0.012). The effect estimates of glaucoma on MI by different MR methods are displayed in Figure 3A. The funnel plots is displayed in Figure 3B. The leave-one-out method revealed that no SNPs strongly affected the potential causal association between glaucoma and MI risk (Figure 3C).

Causal effects of CVD on glaucoma

The statistical results of reverse-direction MR between CVD and glaucoma are depicted in Figure 4. We found that genetic susceptibility of UAP, CAD, and HBP was significantly linked to glaucoma (Figure 4). The Odds ratios (ORs) of UAP, CAD, and HBP were 1.12 (95% confidence interval (CI): 1.02–1.23; P = 0.022), 1.1 (95% CI: 1–1.21; P = 0.041), and 1.83 (95% CI: 1.25–2.67; P = 0.002), respectively, in the IVW model. However, no evidence was supported for the causal association between MI (OR: 1.02, 95% CI: 0.96–1.09; P = 0.492), HF (OR: 1.17, 95% CI: 0.94–1.45; P = 0.172), IS (OR: 1.2, 95% CI: 0.96–1.51; P = 0.105), PE (OR: 0.99, 95% CI: 0.93–1.05; P = 0.654), AF (OR: 1.02, 95% CI: 0.96–1.09; P = 0.534) and glaucoma. Noteworthily, the result of MR-Egger in HBP was consistent with the IVW method (Figure 5).

MR-Egger regression and IVW analysis for UAP, CAD, MI, HF, IS, and PE revealed no heterogeneity among IVs. However, both MR-Egger regression (P = 0.005) and IVW analysis (P = 0.005) of HBP indicated the presence of heterogeneity among IVs (Table 3).

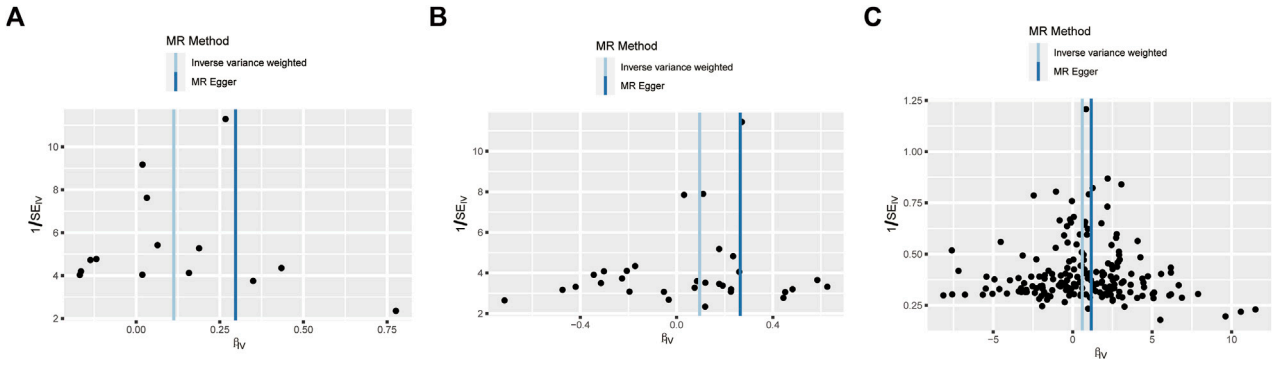

FIGURE 6
Funnel plot to assess the robustness. Unstable angina pectoris **(A)**, Coronary artery disease **(B)**, and High blood pressure **(C)**. MR: mendelian randomization; SE: standard error; IV: instrument variable.

The IVs in AF also exhibited heterogeneity (P = 0.0001). The MR-Egger regression intercept test indicated no horizontal pleiotropy among the IVs for CVD. Then, random effects IVM analysis demonstrated a causal association between HBP and glaucoma (P = 0.0017). After eliminating outliers (rs2032915 and rs73046792) in the MR-PRESSO analysis, genetic susceptibility of HBP was also significantly associated with glaucoma (P = 0.00015). The funnel plots of UAP, CAD, and HBP are displayed in Figure 6. Additionally, random effects IVM analysis showed that glaucoma susceptibility was unrelated to AF (P = 0.086). Furthermore, leave-one-out analysis demonstrated that the causal relationships between UAP, CAD, and HBP and glaucoma were not driven by any single SNP (Supplementary Figure S1).

Multivariable MR (MVMR) analysis

Based on the observed causal association between UAP, CAD, and HBP and glaucoma, further MVMR was performed to evaluate the causal effect of UAP, CAD, and HBP on glaucoma after adjusting for the underlying risk factors. The selected common risk factors of smoking, obesity, body mass index (BMI), and physical activity were validated whether there was the presence of causality with glaucoma in using MR analysis, and results showed that obesity and BMI were causally associated with glaucoma (Supplementary Table S1). Subsequently, obesity and BMI were included in the MVMR analysis, and the results showed that UAP and HBP were causally associated with glaucoma after controlling for the effects of obesity and BMI (Supplementary Table S2).

SMR analysis

Through SMR analysis and filtering by P_SMR and P_HEIDI, 1800 and 1055 potential pathogenic genes (potential drug targets) related to HBP and glaucoma were identified, respectively. Among them, 146 genes were common potential pathogenic genes for HBP and glaucoma (Figure 7A). The GO enrichment analysis revealed that the common potential pathogenic genes were associated with 5 biological processes, 9 cellular component and 2 molecular functions (Figure 7B). Furthermore, only one pathway intestinal immune network for IgA production was enriched in KEGG (Figure 7C). The pathogenic genes enriched in the intestinal immune network for IgA production signaling pathway include HLA-DMA, TNFSF13 and CCL28. Subsequently, the PPI network was used to analyze the interactions among the proteins encoded by the common potential pathogenic genes (Figure 8). The number of interacting proteins for IRF1, IFI30, NR3C1 and LRRC14 was relatively abundant, suggesting that they may play a key role in the regulatory pathways of HBP and glaucoma.

Discussion

In a longitudinal prospective study from UK Biobank, multivariable Cox regression analyses demonstrated that individuals with glaucoma were more susceptible to develop CVD than healthy controls [9]. In the population-based cohort study, cardiovascular mortality is elevated in individuals with glaucoma among 3,654 persons aged 49–97 years [33]. A meta-analysis indicated that MI, chronic ischemic heart disease, angina, and HBP were related to pseudoexfoliation, which is the common cause of OAG [34]. In an epidemiological study of patients with diabetes, glaucoma was positively correlated with MI and arterial hypertension [35]. Our study showed that glaucoma was associated with a lower risk of MI after removing outliers, while no evidence supported the causal effects between glaucoma and other CVDs. Previous MR studies have shown that the results are different before and after

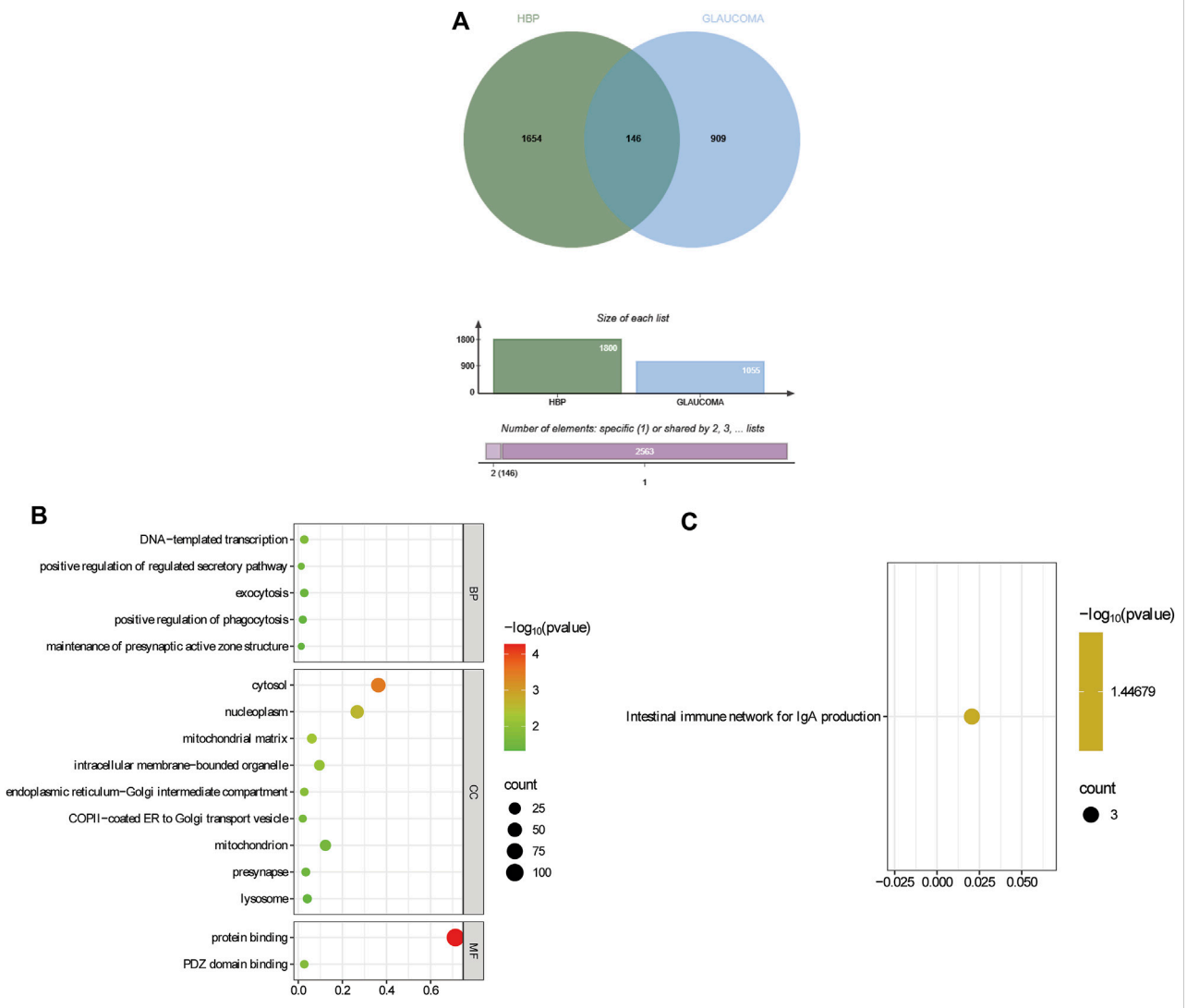

FIGURE 7
Identification and functional enrichment of common potential pathogenic genes for HBP and glaucoma. **(A)** Identification of common potential pathogenic genes. **(B)** GO enrichment of common potential pathogenic genes. **(C)** KEGG enrichment of common potential pathogenic genes.

removing outliers [36–38]. Eliminating abnormal instrumental variables can optimize causal inference [39].

The precise mechanism through which glaucoma reduces the risk of MI remains unclear. Impaired ocular blood flow regulation is one of the factors affecting glaucomatous optic neuropathy [40, 41]. The self-regulating system of arteries, arterioles, and capillaries is essential for maintaining steady blood flow within the eye [40]. Nitric oxide (NO) and renin-angiotensin system (RAS) are one way to regulate the stabilization of intraocular blood flow [40, 42]. Polak et al. found that NO was increased in endothelial cells of glaucoma [43]. In the cardiovascular system, NO, acting on vascular smooth muscle, serves as a significant vasodilator and protector against MI-reperfusion injury [44]. RAS is an important fluid regulatory system in the body, playing a crucial role in regulating vascular tone and blood pressure [45]. High concentrations of angiotensin II (ANG-II), a major active peptide of the RAS, were observed in the aqueous humor of patients with POAG [46]. However, the conversion of ANG-(1–7) from ANG-II has been reported to have protective effects on the cardiovascular system [47]. Additionally, timolol, a nonselective beta-blocker, can not only alleviate OAG but also be used to prevent MI [48]. Therefore, we speculate that NO and RAS may be a bridge between glaucoma and MI.

Reverse MR analysis showed that UAP, CAD, and HBP were associated with an increased risk of glaucoma in our study. A prospective longitudinal study supported by Marshall et al. reported that CVD significantly increases the risk of glaucoma

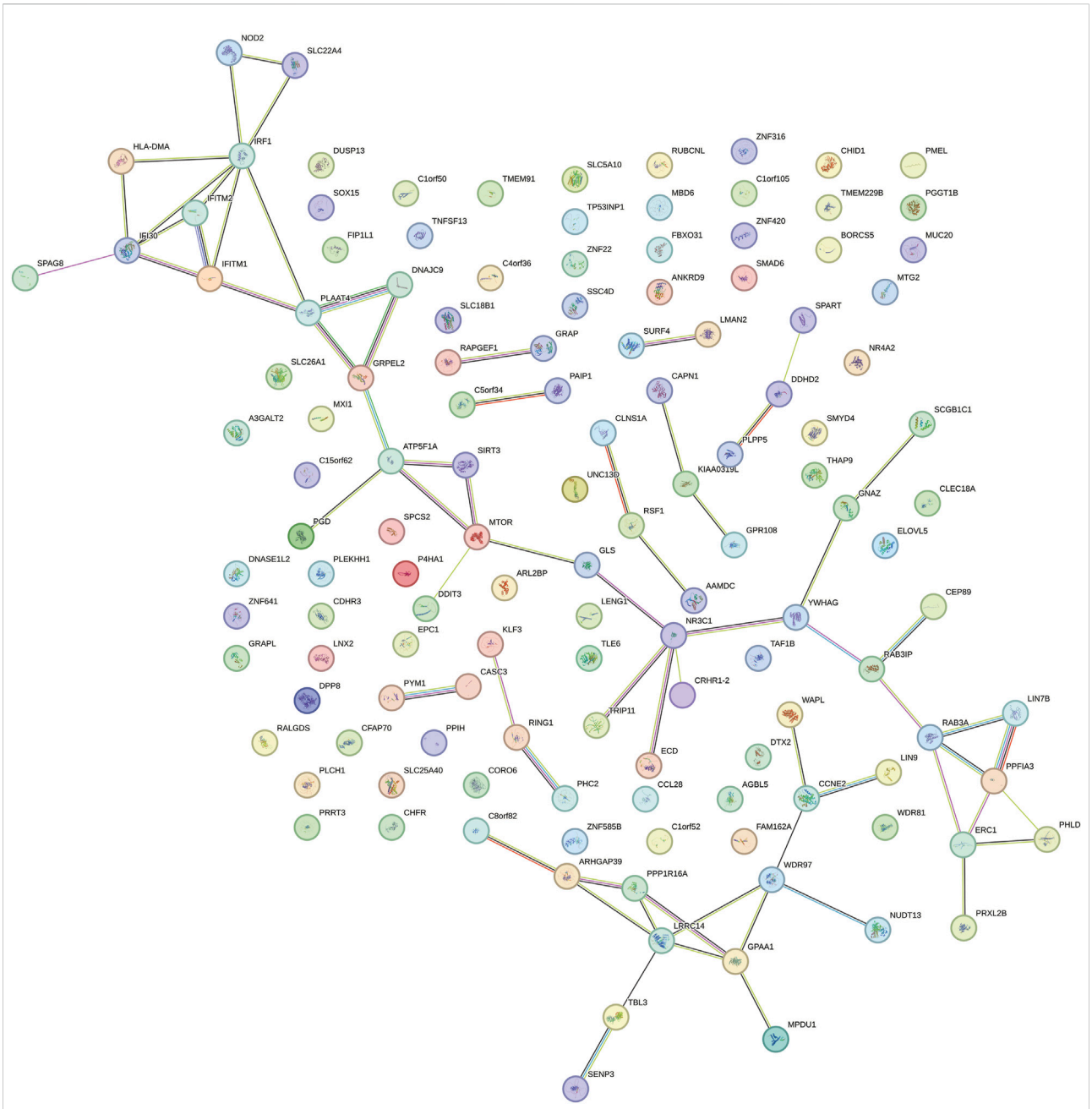

FIGURE 8
PPI network of proteins encoded by common potential pathogenic genes.

progression [8]. Moreover, having cardiovascular risk factors/disease is associated with higher risk of developing POAG [13]. The relationships among UAP, CAD, and glaucoma were not reported, while many studies were consistent with our findings in HBP. In a retrospective cohort study, Baek et al. reported that higher morning blood pressure surge was a significant independent predictor of visual field progression in normal-tension glaucoma patients with hypertension [49]. Another retrospective study demonstrated that HBP (HR: 1.056), stage 1 hypertension (HR: 1.101), and stage 2 hypertension (HR: 1.114) were associated with an elevated risk of glaucoma [50]. A regression discontinuity study found that HBP positively correlates with glaucoma, and antihypertensive therapy can significantly reduce the risk of glaucoma progression in a nationwide survey covering >2.6 million individuals [51]. Mechanically, increased IOP was the leading risk factor for

glaucoma, and IOP is controlled by aqueous humor homeostasis [1, 40]. HBP could elevate IOP through increased secretion of aqueous humor and decreased outflow of aqueous humor to cause glaucoma [52]. While reverse MR suggested an association, our MVMR (adjusting for obesity/BMI) did not detect a robust causal effect of CAD on glaucoma. This indicates that the initial association observed in MR was likely mediated by shared metabolic risk factors. Furthermore, this discrepancy may also stem from residual confounding—CAD often clusters with complex cardiovascular comorbidities (dyslipidemia, endothelial dysfunction) not fully captured by our selected covariates (obesity, BMI). Notably, the lack of prior literature on the causal relationship between CAD and glaucoma, which further highlights the necessity of conducting in-depth research.

Through SMR analysis, 146 common potential pathogenic genes for HBP and glaucoma were identified. The enrichment of these genes in the intestinal immune network for IgA production pathway (involving HLA-DMA, TNFSF13, and CCL28) is particularly intriguing, as it hints at a potential crosstalk between gut immunity and ocular/vasculature homeostasis. Additionally, PPI network analysis showed that IRF1, IFI30, NR3C1 and LRRC14 have relatively abundant interacting proteins, suggesting that these genes might act as key regulatory nodes in the molecular pathways underlying HBP and glaucoma. Collectively, these findings may provide new insights into the shared pathogenic mechanisms of HBP and glaucoma, and the identified common genes and pathways might serve as potential therapeutic targets for further investigation.

The present study has several advantages. First, for the first time, the causal effects between glaucoma and CVD, including MI, HBP, CAD, UAP, HF, IS, PE, and AF, were investigated using bidirectional two-sample MR analysis. Secondly, IVW was used to assess the causal association, and weighted median and MR-Egger methods were utilized as the supplementary analysis. Thirdly, the evaluations of IV strength and sensitivity analysis were carried out to ensure the accuracy and reliability of the results. Some limitations should be noticed in this study. The subtypes of glaucoma and different stages of CVD were not classified, and the relationships need to be further explored. Then, this study included only European populations and may not be applied to other populations. In addition, stratified analysis, such as the subgroups based on sex, age, could not be conducted with aggregated information from the GWAS. In the future, we will collect a large number of clinical samples to verify the results of this study and conduct further stratified analyses.

Conclusion

Conclusively, we found a causal effect between glaucoma and MI. In addition, reverse MR and MVMR suggested that UAP and HBP were the risk factors for glaucoma. However, the potential mechanisms among glaucoma, MI, UAP, and HBP require further investigation.

Author contributions

Significant contribution to conception and design: DJ and CL; Data Acquisition: DJ and JS; Data Analysis and Interpretation: DJ, JS, and WZ; Manuscript Drafting: DJ and JS; Significant intellectual content revision of the manuscript: DJ, JS, and CL; Have given final approval of the submitted manuscript: DJ, JS, WZ, MZ, and CL; Statistical analysis: DJ, JS, and MZ; Supervision of administrative, technical, or material support: CL. All authors contributed to the article and approved the submitted version.

Data availability

Publicly available datasets were analyzed in this study. This data can be found here: The datasets presented in this study can be found in the IEU OpenGWAS project[1]. The accession numbers are finn-b-H7_GLAUCOMA, ebi-a-GCST90018932, ebi-a-GCST003116, ukb-b-14177, ebi-a-GCST90018877, ebi-a-GCST009541, ebi-a-GCST90018864, ebi-a-GCST006414 and ebi-a-GCST90013887, respectively.

Ethics statement

We obtained publicly available summarized results from published studies, which have obtained institutional review board approval in their respective studies.

Funding

The author(s) declare that no financial support was received for the research and/or publication of this article.

Conflict of interest

The author(s) declared no potential conflicts of interest with respect to the research, authorship, and/or publication of this article.

Generative AI statement

The author(s) declare that no Generative AI was used in the creation of this manuscript.

Any alternative text (alt text) provided alongside figures in this article has been generated by Frontiers with the support of artificial intelligence and reasonable efforts have been made to ensure accuracy, including review by the authors wherever possible. If you identify any issues, please contact us.

Supplementary material

The Supplementary Material for this article can be found online at: https://www.ebm-journal.org/articles/10.3389/ebm.2025.10610/full#supplementary-material

References

1. Jayaram H, Kolko M, Friedman DS, Gazzard G. Glaucoma: now and beyond. *The Lancet* (2023) **402**:1788–801. doi:10.1016/s0140-6736(23)01289-8

2. Steinmetz JD, Bourne RRA, Briant PS, Flaxman SR, Taylor HRB, Jonas JB, et al. Causes of blindness and vision impairment in 2020 and trends over 30 years, and prevalence of avoidable blindness in relation to VISION 2020: the right to sight: an analysis for the global burden of disease study. *The Lancet Glob Health* (2021) **9**: e144–e160. doi:10.1016/s2214-109x(20)30489-7

3. Jerrome S, Joseph S, Niranjana B, Arkaprava M, Lakshmanan P, Balagiri S, et al. Agreement and reliability of transpalpebral tonometers with goldmann applanation tonometer: a systematic review and meta-analysis. *Ophthalmol Glaucoma* (2025) **8**: 242–56. doi:10.1016/j.ogla.2024.11.001

4. Kang JM, Tanna AP. Glaucoma. *Med Clin North America* (2021) **105**:493–510. doi:10.1016/j.mcna.2021.01.004

5. Hakim A, Guido B, Narsineni L, Chen D-W, Foldvari M. Gene therapy strategies for glaucoma from IOP reduction to retinal neuroprotection: progress towards non-viral systems. *Adv Drug Deliv Rev* (2023) **196**:114781. doi:10.1016/j.addr.2023.114781

6. Zhou X, Xu J, Zhang X, Zhao Y, Duan X. Causal relationships between gut microbiota and primary open-angle glaucoma: a Mendelian randomization and mediation analysis of glaucoma endophenotypes. *Exp Eye Res* (2024) **240**:109788. doi:10.1016/j.exer.2024.109788

7. Yuan R, Liu K, Cai Y, He F, Xiao X, Zou J. Body shape and risk of glaucoma: a Mendelian randomization. *Front Med* (2022) **9**:999974. doi:10.3389/fmed.2022.999974

8. Marshall H, Mullany S, Qassim A, Siggs O, Hassall M, Ridge B, et al. Cardiovascular disease predicts structural and functional progression in early glaucoma. *Ophthalmology* (2021) **128**:58–69. doi:10.1016/j.ophtha.2020.06.067

9. Choi JA, Lee SN, Jung SH, Won HH, Yun JS. Association of glaucoma and lifestyle with incident cardiovascular disease: a longitudinal prospective study from UK biobank. *Sci Rep* (2023) **13**:2712. doi:10.1038/s41598-023-29613-w

10. Deng Y, Li Q, Zhou F, Li G, Liu J, Lv J, et al. Telomere length and the risk of cardiovascular diseases: a Mendelian randomization study. *Front Cardiovasc Med* (2022) **9**:1012615. doi:10.3389/fcvm.2022.1012615

11. Lüscher TF. Cardiovascular diseases outside the heart: novel recommendations for pulmonary embolism and peripheral arterial disease. *Eur Heart J* (2020) **41**:487–9. doi:10.1093/eurheartj/ehaa019

12. Zhang J, Tong H, Jiang L, Zhang Y, Hu J. Trends and disparities in China's cardiovascular disease burden from 1990 to 2019. *Nutr Metab Cardiovasc Dis* (2023) **33**:2344–54. doi:10.1016/j.numecd.2023.07.039

13. Jung KI, Kim YC, Shin HJ, Park CK. Nationwide cohort study of primary open angle glaucoma risk and cardiovascular factors among in Korean glaucoma suspects. *Sci Rep* (2025) **15**:1952. doi:10.1038/s41598-025-85505-1

14. Cho HK, Han JC, Choi JA, Chae JE, Kim RB. Association between atrial fibrillation and the risk of glaucoma development: a 12-year nationwide cohort study. *Eye (Lond)* (2023) **37**:2033–41. doi:10.1038/s41433-022-02274-1

15. Bennion JR, Wise ME, Carver JA, Sorvillo F. Analysis of glaucoma-related mortality in the United States using death certificate data. *J Glaucoma* (2008) **17**: 474–9. doi:10.1097/IJG.0b013e318163bdbd

16. Lin HC, Chien CW, Hu CC, Ho JD. Comparison of comorbid conditions between open-angle glaucoma patients and a control cohort: a case-control study. *Ophthalmology* (2010) **117**:2088–95. doi:10.1016/j.ophtha.2010.03.003

17. Chen B, Yan Y, Wang H, Xu J. Association between genetically determined telomere length and health-related outcomes: a systematic review and meta-analysis of Mendelian randomization studies. *Aging Cell* (2023) **22**:e13874. doi:10.1111/acel.13874

18. Carter AR, Sanderson E, Hammerton G, Richmond RC, Davey Smith G, Heron J, et al. Mendelian randomisation for mediation analysis: current methods and challenges for implementation. *Eur J Epidemiol* (2021) **36**:465–78. doi:10.1007/s10654-021-00757-1

19. Meng Y, Tan Z, Su Y, Li L, Chen C. Causal association between common rheumatic diseases and glaucoma: a Mendelian randomization study. *Front Immunol* (2023) **14**:1227138. doi:10.3389/fimmu.2023.1227138

20. Zhang J, Chen X, Zhu Y, Wan S, Hu S, Yang Y. Investigating the causal relationship between sleep behaviors and primary open-angle glaucoma: a bidirectional two-sample Mendelian randomization study. *Nat Sci Sleep* (2024) **16**:143–53. doi:10.2147/nss.S439274

21. Sakaue S, Kanai M, Tanigawa Y, Karjalainen J, Kurki M, Koshiba S, et al. A cross-population atlas of genetic associations for 220 human phenotypes. *Nat Genet* (2021) **53**:1415–24. doi:10.1038/s41588-021-00931-x

22. The CARDIoGRAMplusC4D Consortium, Goel A, Won HH, Hall LM, Willenborg C, Kanoni S, et al. A comprehensive 1,000 Genomes-based genome-wide association meta-analysis of coronary artery disease. *Nat Genet* (2015) **47**: 1121–30. doi:10.1038/ng.3396

23. Shah S, Henry A, Roselli C, Lin H, Sveinbjörnsson G, Fatemifar G, et al. Genome-wide association and Mendelian randomisation analysis provide insights into the pathogenesis of heart failure. *Nat Commun* (2020) **11**:163. doi:10.1038/s41467-019-13690-5

24. Nielsen JB, Thorolfsdottir RB, Fritsche LG, Zhou W, Skov MW, Graham SE, et al. Biobank-driven genomic discovery yields new insight into atrial fibrillation biology. *Nat Genet* (2018) **50**:1234–9. doi:10.1038/s41588-018-0171-3

25. Mbatchou J, Barnard L, Backman J, Marcketta A, Kosmicki JA, Ziyatdinov A, et al. Computationally efficient whole-genome regression for quantitative and binary traits. *Nat Genet* (2021) **53**:1097–103. doi:10.1038/s41588-021-00870-7

26. Gan T, Hu J, Liu W, Li C, Xu Q, Wang Y, et al. Causal association between anemia and cardiovascular disease: a 2-Sample bidirectional mendelian randomization study. *J Am Heart Assoc* (2023) **12**:e029689. doi:10.1161/jaha.123.029689

27. Gao N, Kong M, Li X, Zhu X, Wei D, Ni M, et al. The association between psoriasis and risk of cardiovascular disease: a mendelian randomization analysis. *Front Immunol* (2022) **13**:918224. doi:10.3389/fimmu.2022.918224

28. Yang F, Hu T, He K, Ying J, Cui H. Multiple sclerosis and the risk of cardiovascular diseases: a mendelian randomization study. *Front Immunol* (2022) **13**:861885. doi:10.3389/fimmu.2022.861885

29. Gao N, Yu Z, Fan Y, Jiang X, Hu T. Impact of negative emotions on upper gastrointestinal diseases: a mendel randomization study. (2024) **19**:e0304121. doi:10.1371/journal.pone.0304121

30. Wang Z, Lai W, Zhong S. Investigating the causal relationship between human blood metabolites and coronary artery disease using two-sample Mendelian randomization. *Nan Fang Yi Ke Da Xue Xue Bao* (2021) **41**:272–8. doi:10.12122/j.issn.1673-4254.2021.02.16

31. Xiao X, Wu X, Yi L, You F, Li X, Xiao C. Causal linkage between type 2 diabetes mellitus and inflammatory bowel disease: an integrated Mendelian randomization study and bioinformatics analysis. *Front Endocrinol (Lausanne)* (2024) **15**:1275699. doi:10.3389/fendo.2024.1275699

32. Song D-J, Fan B, Li G-Y. Blood cell traits and risk of glaucoma: a two-sample Mendelian randomization study. *Front Genet* (2023) **14**:1142773. doi:10.3389/fgene.2023.1142773

33. Meyer NI. Open-angle glaucoma and cardiovascular mortality. *Ophthalmology* (2007) **114**:392. doi:10.1016/j.ophtha.2006.09.007

34. Siordia JA, Franco J, Golden TR, Dar B. Ocular pseudoexfoliation syndrome linkage to cardiovascular disease. *Curr Cardiol Rep* (2016) **18**:61. doi:10.1007/s11886-016-0738-5

35. Nielsen NV. The prevalence of glaucoma and ocular hypertension in type 1 and 2 diabetes mellitus. An epidemiological study of diabetes mellitus on the island of falster, Denmark. *Acta Ophthalmologica* (1983) **61**:662–72. doi:10.1111/j.1755-3768.1983.tb04357.x

36. Wei H, Ge H, Qian Y, Li B. Genetic determinants of inflammatory cytokines and their causal relationship with inflammatory disorders of breast: a two-sample

Mendelian randomization study. *Sci Rep* (2025) **15**:7300. doi:10.1038/s41598-025-91723-4

37. Jee Y, Ryu M, Sull JW. Alcohol consumption and cancer risk: two sample Mendelian randomization. *Epidemiologia* (2024) **5**:618–26. doi:10.3390/epidemiologia5030043

38. Lee SH, Lee JY, Kim G, Jung KJ, Lee S, Kim HC, et al. Two-sample mendelian randomization study of lipid levels and ischemic heart disease. *Korean Circ J* (2020) **50**:940–8. doi:10.4070/kcj.2020.0131

39. Verbanck M, Chen CY, Neale B, Do R. Detection of widespread horizontal pleiotropy in causal relationships inferred from Mendelian randomization between complex traits and diseases. *Nat Genet* (2018) **50**:693–8. doi:10.1038/s41588-018-0099-7

40. Ekici E, Moghimi S. Advances in understanding glaucoma pathogenesis: a multifaceted molecular approach for clinician scientists. *Mol Aspects Med* (2023) **94**:101223. doi:10.1016/j.mam.2023.101223

41. Wu X, Konieczka K, Liu X, Chen M, Yao K, Wang K, et al. Role of ocular blood flow in normal tension glaucoma. *Adv Ophthalmol Pract Res* (2022) **2**:100036. doi:10.1016/j.aopr.2022.100036

42. Kelly RA, Kuhn MS, Reina-Torres E, Balasubramanian R, Perkumas KM, Li G, et al. Endothelial cell-specific postnatal deletion of Nos3 preserves intraocular pressure homeostasis *via* macrophage recruitment and NOS2 upregulation. *J Clin Invest* (2025) **135**:e183440. doi:10.1172/jci183440

43. Polak K, Luksch A, Berisha F, Fuchsjaeger-Mayrl G, Dallinger S, Schmetterer L. Altered nitric oxide system in patients with open-angle glaucoma. *Arch Ophthalmol* (2007) **125**:494–8. doi:10.1001/archopht.125.4.494

44. Russo I, Barale C, Melchionda E, Penna C, Pagliaro P. Platelets and cardioprotection: the role of nitric oxide and carbon oxide. *Int J Mol Sci* (2023) **24**:6107. doi:10.3390/ijms24076107

45. Balakumar P, Orayj KM, Khan NA, Shanmugam K, Jagadeesh G. Impact of the local renin-angiotensin system in perivascular adipose tissue on vascular health and disease. *Cell Signal* (2024) **124**:111461. doi:10.1016/j.cellsig.2024.111461

46. Li H, Cui H, Ren J, Wang D, Zhao R, Zhu S, et al. Elevated Angiotensin-II levels contribute to the pathogenesis of open-angle glaucoma *via* inducing the expression of fibrosis-related genes in trabecular meshwork cells through a ROS/NOX4/SMAD3 axis. *Cell Transplant* (2023) **32**:09636897231162526. doi:10.1177/09636897231162526

47. Santos RAS, Oudit GY, Verano-Braga T, Canta G, Steckelings UM, Bader M. The renin-angiotensin system: going beyond the classical paradigms. *Am J Physiology-Heart Circulatory Physiol* (2019) **316**:H958–H970. doi:10.1152/ajpheart.00723.2018

48. Barnes J, Moshirfar M. Timolol. StatPearls [Internet]. Treasure Island (FL): StatPearls Publishing (2024).

49. Baek MS, Song WK, Kim KE, Lee A, Lee JY, Shin JW, et al. Morning blood pressure surge and glaucomatous visual field progression in normal-tension glaucoma patients with systemic hypertension. *Am J Ophthalmol* (2023) **254**:161–76. doi:10.1016/j.ajo.2023.06.014

50. Lee JS, Kim YJ, Kim S, Bae HW, Kim SS, Lee SW, et al. Increased risks of open-angle glaucoma in untreated hypertension. *Am J Ophthalmol* (2023) **252**:111–20. doi:10.1016/j.ajo.2023.03.032

51. Horwitz A, Klemp M, Jeppesen J, Tsai JC, Torp-Pedersen C, Kolko M. Antihypertensive medication postpones the onset of glaucoma: evidence from a nationwide study. *Hypertension* (2017) **69**:202–10. doi:10.1161/hypertensionaha.116.08068

52. Leeman M, Kestelyn P. Glaucoma and blood pressure. *Hypertension* (2019) **73**:944–50. doi:10.1161/hypertensionaha.118.11507

EBM Experimental Biology and Medicine

TYPE Original Research
PUBLISHED 15 October 2025
DOI 10.3389/ebm.2025.10533

OPEN ACCESS

*CORRESPONDENCE
Marya Obeidat,
mmobeidat82@just.edu.jo

†These authors have contributed equally to this work

RECEIVED 18 February 2025
ACCEPTED 02 October 2025
PUBLISHED 15 October 2025

CITATION
Obeidat M, Tadros S, Ismail B and Al-Khaldi A (2025) TIMAP downregulation in Burkitt's lymphoma reveals key molecules and signaling pathways in B-cell lymphomagenesis. *Exp. Biol. Med.* 250:10533. doi: 10.3389/ebm.2025.10533

TIMAP downregulation in Burkitt's lymphoma reveals key molecules and signaling pathways in B-cell lymphomagenesis

Marya Obeidat*†, Saleh Tadros†, Batool Ismail and Ayah Al-Khaldi

Department of Medical Laboratory Sciences, Faculty of Applied Medical Sciences, Jordan University of Science and Technology, Irbid, Jordan

Abstract

Burkitt's lymphoma (BL) is an aggressive subtype of B-cell non-Hodgkin's lymphoma, known for its rapid tumor growth and poor prognosis. Transforming growth factor beta-inhibited membrane-associated protein (TIMAP) is a regulatory subunit of protein phosphatase 1 catalytic subunit, enriched in lymphoid tissues, and upregulated in various cancers. Despite suggestions that TIMAP promotes lymphomagenesis in a *c-myc*-driven model, its precise role remains unclear. This study aimed to investigate the contribution of TIMAP to B-cell lymphomagenesis by examining transcriptomic changes upon TIMAP downregulation in BL cells. Raji BL cells were transfected with 2′Fluoro Arabinonucleic acid (FANA)-antisense oligonucleotides (ASO) targeting TIMAP (FANA-ASO-TIMAP) or a scramble control (FANA-ASO-Scramble). TIMAP expression was significantly reduced at the mRNA (0.70 $\pm$ 0.04, $p = 0.001$) and protein levels (median = 0.73, IQR = 0.13, $p = 0.002$). RNA sequencing identified 2,368 differentially expressed genes (DEGs), of which 1,326 were upregulated, and 1,042 were downregulated. Gene Ontology analysis revealed that the DEGs were primarily involved in cellular processes, DNA replication, intracellular signal transduction, and apoptosis. Pathways related to lymphoma progression, such as B-cell receptor signaling, p53 signaling, and mTOR signaling, were notably affected. Key genes such as *PAK3*, *LINC00487*, *AID*, *PURPL*, and *BCL2* were among the most dysregulated, highlighting TIMAP's role in critical oncogenic pathways in B-cell Lymphoma. These findings suggest that TIMAP is a key regulator of gene expression and signaling pathways in B-cell lymphomagenesis and could serve as a potential therapeutic target for novel treatments.

KEYWORDS

TIMAP, PPP1R16B, RNA sequencing, B-cell lymphoma, transcriptome

Impact statement

This manuscript contributes to the growing body of research on Burkitt's lymphoma (BL) by investigating the role of TIMAP, a protein implicated in cancer progression. The study reveals that even a partial reduction in TIMAP expression causes significant changes in the behavior of BL cells, particularly in genes and pathways linked to cell survival, proliferation, and apoptosis. Through transcriptomic analysis, the research identifies over 2,300 differentially expressed genes and highlights the disruption of critical signaling pathways like B-cell receptor signaling and mTOR, essential in lymphoma development. These findings deepen our understanding of how TIMAP regulates key processes in B-cell lymphomagenesis and suggest that TIMAP could be a promising target for new lymphoma therapies. By positioning TIMAP as a central player in lymphoma biology, the study opens new avenues for targeted treatments and offers insights into the disease's molecular mechanisms. Future research can further explore TIMAP's therapeutic potential in clinical applications.

Introduction

Blood cancers, which account for 6% of all malignancies [1], are a group of neoplastic illnesses that primarily involve bone marrow, blood, and lymphatic tissue [2]. Based on the site of involvement, hematological malignancies are divided into leukemia, lymphoma, and myeloma [3]. Lymphoma is caused by the abnormal proliferation of blood lymphocytes (B, T, and Natural Killer (NK) cells) at various stages of maturation [4] and accounts for 5% of all cancer cases [5]. These malignant cells accumulate in the lymphatic system (lymph nodes, spleen, thymus, and bone marrow) and other parts of the body [3]. Hodgkin Lymphoma (HL) and Non-Hodgkin Lymphoma (NHL) are two subtypes of lymphoma distinguished by the presence of Reed-Sternberg cells in the biopsies of HL patients [6]. Approximately 90% of lymphoma cases are NHL, which is more common among men than women [7]. NHL is further subdivided into subgroups based on the kind of malignant lymphocyte (B-cells, T-cells, or natural killer (NK)-cells), clinical presentation, aggressiveness, prognosis, and treatment response [8]. Most cases of NHL are B-cell lymphomas, which are further divided into indolent (low-grade), such as follicular lymphoma (FL), and aggressive (high-grade), such as diffuse large B-cell lymphoma (DLBCL) and Burkitt's Lymphoma (BL).

Burkitt's lymphoma (BL) is an aggressive B-cell subtype of NHL that often affects children and, to a lesser extent, young individuals in malaria-endemic areas [9]. BL is distinguished by rapid cell division, as seen by cell-cycle markers like Ki-67 (>95% of cells are positive) [10]. Additionally, it is one of the neoplasms that has been connected to Epstein-Barr Virus (EBV), Human Immunodeficiency Virus (HIV), and chromosomal translocations that lead to overexpression of *c-Myc* oncogene [11–13]. While *c-Myc* overexpression enhances B-cell proliferation, it also promotes cell death [14]. As a result, lymphoma development requires extra genes that support cell survival.

The World Health Organization (WHO) classifies BL into three types: endemic, sporadic, and immunodeficiency-related [15], all have the same morphology, genetic features, and immunostaining results. Physical examination, laboratory tests (Complete Blood Count (CBC), Blood Film Examination (BFE), and assessment of bone marrow and lymph node biopsies), radiography, and cytogenetic analysis are all required for a clear diagnosis of BL [10]. Treatment must begin as soon as a diagnosis is made since BL is fatal if left untreated. BL is often treated with chemotherapeutic and immune-targeted medicines for months [16]. Even though BL is susceptible to chemotherapy [16, 17], chemotherapy-related toxicity and infections can develop, especially in immunocompromised patients [18]. Targeting molecules involved in BL pathogenesis as a treatment option against BL reduces non-specific damage to normal cells and minimizes side effects from conventional therapies [19].

TIMAP (Transforming Growth Factor Beta 1 (TGF-ß1) Inhibited Membrane-Associated Protein) is a member of the Myosin Phosphatase Targeting subunits (MYPT) family that forms a holoenzyme complex with Ser/Thr Protein Phosphatase 1 catalytic subunit (PP1c) to regulate its substrate specificity, activity, and localization [20]. TIMAP is predominantly expressed in endothelial cells, white blood cells (B, T, NK, and Dendritic cells), and several tissues, including the central nervous system (CNS), bone marrow, and lymphoid organs [21–23]. TIMAP has been reported to be upregulated in a variety of solid cancers [23], including breast cancer [24] and head and neck cancer [23]. *TIMAP* transcript was identified among the upregulated genes in diffuse DLBCL and peripheral T-cell lymphoma not otherwise specified (PTCL-NOS) [25], BL cell lines, and leukemia cell lines [23]. It is a prognostic biomarker in HER-2-negative breast cancer [24], head and neck cancer [23, 26], liver cancer, renal cancer [23], and glioblastoma multiform [27]. Furthermore, a large-scale study in a c-*Myc* mice lymphoma model sensitive to apoptosis found two deregulated oncogenes, TIMAP and histone deacetylase isoform 6 (HDAC6), demonstrating their significance in lymphomagenesis [28]. Nonetheless, to date, the functional role of TIMAP in lymphoma is underexplored.

Numerous protein partners for the TIMAP-PP1c complex have been identified, mainly in studies on endothelial cells (EC), which are involved in pathways that regulate cell growth, adhesion, and migration [20]. Among TIMAP partners in EC is a small nuclear ribonucleoprotein U5 (U5 snRNP) that is involved in RNA splicing [29]. Additionally, a recent study in neuroblastoma cells found multiple nuclear protein partners for TIMAP, including splicing factor proline- and glutamine-rich

TABLE 1 AUM*silence*^{TM} sequences and their target regions on the TIMAP transcript.

AUM*silence* ASOs	AUM*silence*^{TM} sequence (5′- 3′)	Target region in TIMAP transcript (NM_015568.4)
AUM*scr*^{TM}	CCTTCCCTGAAGGTTCCTCC	No target
AUM*silence*^{TM}1	AATATACCGAGGTCCCATTGC	1 AATATACCGAGGTCCCATTGC 21 1806 AATATACCGAGGTCCCATTGC 1786
AUM*silence*^{TM}2	ACCTAACGTAGAGGCTGGCAT	1 ACCTAACGTAGAGGCTGGCAT 21 4599 ACCTAACGTAGAGGCTGGCAT 4579
AUM*silence*^{TM}3	GAGACTAGGAGATACGGCAAC	1 GAGACTAGGAGATACGGCAAC 21 1905 GAGACTAGGAGATACGGCAAC 1885
AUM*silence*^{TM}4	TAGATCATCCTGTCCTGTTCC	1 TAGATCATCCTGTCCTGTTCC 21 4082 TAGATCATCCTGTCCTGTTCC 4062

(SFPQ) proteins and heterogeneous nuclear ribonucleoprotein A1 (hnRNPA1) [27]. These findings strongly suggest that TIMAP may play a role in the regulation of gene transcription.

Cumulative evidence strongly indicates the role of TIMAP in cell transformation, likely through transcriptional regulation. Despite this, studies explaining how TIMAP works in malignant cells and identifying its target genes are still lacking. Since TIMAP is implicit in lymphomagenesis and its expression is upregulated in various lymphoma cell lines [23]. We sought to identify transcripts whose expression is deregulated following TIMAP knockdown in BL cells, to gain insight into the cellular pathways that might be influenced by TIMAP expression. Ultimately, these findings will help researchers understand the pathogenic role of TIMAP in lymphomagenesis, particularly in BL.

Materials and methods

Cell lines and cell culture

Raji (ATCC CCL-86™) and Daudi (ATCC CCL-213™) BL cell lines were purchased from the American Type Culture Collection (ATCC) and cultured in sterile RPMI 1640 w/L-Glutamine (Euro Clone, Cat. No. ECB 2000L) supplemented with 10% heat-inactivated fetal bovine serum (FBS) (PAN BIOTECH, Cat. No. P30-3306 and Gibco, Cat. No.10500-064) and 1% penicillin/streptomycin (Euro Clone, Cat. No. ECB 3001D). Cell cultures were maintained at 37 °C in a humidified 5% CO2 incubator and used at passages 4–7. Cell growth and morphology were monitored daily using an inverted microscope, and the growth media were replaced every 2-3 days or as needed.

RNA extraction

Total RNA was extracted from cells using Qiagen RNeasy® Micro kit (Cat. No. 74004) as directed by the manufacturer. A Thermo Fisher ND-2000 nanodrop™ spectrophotometer was used to determine the quality of extracted RNA. RNA samples were stored at −80 °C for further analysis.

Reverse transcriptase-polymerase chain reaction (RT-PCR)

A total mass of 500 µg RNA was reverse transcribed into cDNA using a two-step QuantiTect® Reverse Transcription Kit (Qiagen, Cat. No. 205311). The PCR mixture was prepared of 2 µL 5x HOT FIREPol Blend Master Mix (Solis BioDyne, Cat. No. 04-25-00S25), 0.5 µL forward (F) and reverse (R) primers (Table 2), 1 µL of cDNA template, and 6 µL of nuclease-free water. The PCR cycles were as follows: 95 °C for 12 min, followed by 35 cycles of 95 °C for 30 s, 61 °C for 30 s, 72 °C for 2 min, and 72 °C for 10 min. Using a UV transilluminator, the PCR products were visualized on a 2% agarose gel.

Immunofluorescence

The expression of TIMAP protein was examined in Raji and Daudi BL cells seeded on glass coverslips in a 24-well plate containing 1 mL complete growth media/well for 24 h at 37 °C in a humidified 5% CO2 incubator. Afterward, the plate was centrifuged at 250 × g for 7 min at room temperature (RT), and cells were rinsed with 1x phosphate-buffered saline (PBS) and fixed in 10% formalin for 15 min at RT. The cells were then permeabilized with 0.1% Triton X 100 in PBS for 15 min in the

dark, blocked with 1 mL of 2% bovine serum albumin (BSA) in PBS for 1 h at RT on a shaker to block non-specific binding, and incubated overnight at 4 °C with 1: 500 primary rabbit polyclonal anti-PPP1R16B antibody (MyBioSource, Cat. No. MBS417306) in 1% BSA. The following day, the plate was further incubated for 20 min on ice on a shaker, followed by three washes with PBS for 5 min. Then 500 µL of secondary goat anti-rabbit antibody (Alexa Fluor® 488) (Abcam Cat# ab150077, RRID:AB_2630356) diluted at 1: 1000 in 1% BSA was added and incubated for 40 min on a shaker in the dark. Finally, the plate was rinsed three times with PBS, and coverslips were placed on a drop of mounting media with DAPI counterstain (Abcam, Cat. No. ab104139) on frosted glass slides and sealed with nail polish to avoid drying. The Nikon Eclipse E600 microscope was used to capture images at ×100 magnification.

Immunohistochemistry (IHC)

Archived paraffin-embedded lymph node tissue samples from a healthy control, a BL patient, a DLBCL patient, and an FL patient were sectioned to a thickness of 4 µm and mounted on Superfrost Plus glass slides for IHC processing using the BenchMark ULTRA system (Roche Diagnostics, Risch-Rotkreuz, Switzerland). To assess TIMAP protein expression, an anti-PPP1R16 B rabbit polyclonal antibody (MyBioSource, Inc, San Diego, United States) was used at a 1:400 dilution [24, 26].

TIMAP knockdown

Four different constructs of 2′-Deoxy-2′-fluoro-arabinoguanosine-Antisense Oligonucleotides (FANA-ASOs) targeting TIMAP mRNA [FANA-ASO-TIMAP (AUM*silence*^{TM} ASO)], and a scramble negative control [FANA-ASO-scramble (AUM*scr*^{TM} ASO)] were purchased from AUM Bio Tech, LLC (PA, United States) (Table 1). FANA ASOs are 2′-deoxy-2′-fluoroarabinonucleotides that mimic DNA [30]. These ASOs form FANA: RNA hybrids, like native DNA: RNA hybrids, and can trigger RNase H-mediated RNA cleavage. Due to their chemical modifications, FANA ASOs are self-delivered into cells, including hard-to-transfect cells [31], without a need for transfection reagents, reducing cell toxicity and enabling targeted mRNA degradation. Raji cells were plated in complete growth media at a density of 50% in 12-well or 24-well plates as directed by the manufacturer. Afterward, the cells were gently mixed with 2 µM of FANA-ASO diluted in the growth media, and the growth media was refreshed 48 h after treatment. A soup of 4 FANA-ASO-TIMAP constructs was used to knock down TIMAP. RNA and protein extractions were conducted 72 h after treatment.

In each experiment, equal numbers of cells were seeded following viable cell counting by trypan blue exclusion using a hemocytometer [32]. This method involves mixing a cell suspension with trypan blue dye, where viable cells exclude the dye and remain unstained, while non-viable cells take up the dye and appear blue under a light microscope. The mixture is then loaded onto a hemocytometer, and cells are counted to determine cell concentration and viability as follows: Cells/mL = (total cells counted/number of squares counted) × dilution factor × 10,000

$$\text{Total cells in sample} = \text{cells/mL x total sample volume.}$$

After 72 h of treatment with FANA-ASO, viable cells were again quantified, and cell counts were compared between groups to evaluate changes in growth.

Real-time qPCR

Real-time qPCR was carried out using QuantiNova SYBR Green PCR Kit (Qiagen, Cat. No. 208054) according to the manufacturer's instructions. Briefly, a total volume of 10 µL reaction mixture was prepared from 5 µL of 1x Master Mix, 1 µL of F and R primer (Table 2), 2 µL of cDNA (6 ng/µL), and 1 µL of RNase-free water. PCR cycling conditions: 95 °C for 2 min followed by 40 cycles of 95 °C for 5 s, and 61-63 °C for 30 s. All reactions were performed in duplicate. *GAPDH* was employed as an internal control. The $2^{-\Delta\Delta CT}$ formula was used to calculate changes in expression level.

Protein extraction and quantification

Total protein was extracted using M-PER®Mammalian Protein Extraction Reagent (Thermo Scientific™, Cat. No. 75801) supplemented with protease inhibitors mini tablets (Thermo Scientific™, Cat. No. A32953) according to the manufacturer's instructions. Briefly, cells were centrifuged at 2500 g for 10 min at 4 °C, washed with 1x PBS, and the cell pellets were incubated for 20 min on ice with M-PER reagent (200 µL per $1*10^6$ cells). Afterward, the cells were centrifuged at 14000 g for 15 min at 4 °C, and the supernatants were transferred to new tubes and stored at −80 for further investigation. Protein concentration was determined using the Bicinchoninic acid (BCA) (Pierce™ BCA) kit (Thermo Scientific™, Cat. No. 23225) according to the kit's instructions. TIMAP protein levels were quantified using a human PPP1R16B sandwich ELISA Kit (ELK Biotechnology, Cat. No. ELK0855) according to the manufacturer's instructions, and measurements were normalized based on the total protein concentration obtained from the BCA assay in corresponding samples.

RNA sequencing and data analysis

The Qubit RNA assay was used to assess the quality of RNA samples before proceeding with RNA-seq. Azenta Biotech's RNA sequencing service (Chelmsford, Massachusetts) was used to

TABLE 2 Primer sequences.

Gene	Primers	Primer sequences (5′-3′)	Gene entry
TIMAP	TIMAP-F	GCCGCAAGAAAGTGTCCTTC	NM_015568.4
	TIMAP-R	ACAAATCAGGGCTGACCTTATTC	
GAPDH	GAPDH-F	GGAGCGAGATCCCTCCAAAAT	NM_001357943.2
	GAPDH-R	GGCTGTTGTCATACTTCTCATGG	
AICDA	AICDA-F	CGCATCCTTTTGCCCCTGT	NM_020661.4
	AICDA-R	ACAGAGAAGACTTGAAGGACTGT	
PAK3	PAK3-F	CGCTGTCTTGAGATGGATGTGG	NM_002578
	PAK3-R	CAGTCTTAGCGGCTGCTGTTCT	
BCL-2	BCL2-F	ATCGCCCTGTGGATGACTGAGT	NM_000633
	BCL2-R	GCCAGGAGAAATCAAACAGAGGC	

analyze all samples. Poly(A) selection method was applied before sequencing, and RNA sequencing was then conducted on the Illumina platform in a paired-end fashion with 2 × 150 bp reads. The RNA-seq data were received as Fastq files.

The FastQC and MultiQC tools (Galaxy Version 0.74), (RRID: SCR_014583) were used to evaluate the quality of reads [33–35]. The RNA-seq data were run through the Trim Galore tool (RRID: SCR_011847) to remove the adapter sequences from the reads before further analysis [36]. Following this, RNA-seq data were aligned to the human genome (GRCh38) using an ultrafast universal aligner RNA STAR tool (Galaxy Version 2.7.10b), (RRID: SCR_004463) [37]. The feature counts tool (Galaxy Version 2.0.3) was then applied to the alignment BAM output file to count RNA-seq reads [38]. After that, the Limma-Voom tool (Galaxy Version 3.50.1) was employed to identify the differentially expressed genes (DEGs) (adjusted p-value <0.05) between FANA -ASO-scramble treated and FANA -ASO- TIMAP treated samples [39, 40]. A volcano plot (Galaxy Version 0.0.5) and heatmap2 (Galaxy Version 3.1.3), (RRID:SCR_006281) were used to display the differentially expressed genes [34]. Furthermore, using the DAVID server (RRID:SCR_001881) and Enrichr tool (RRID: SCR_001575), we performed functional enrichment analysis to establish the gene categories and signaling pathways the differentially expressed genes belong to [41, 42].

Statistical analysis

IBM SPSS Statistics 26 software (RRID:SCR_002865) was used to analyze the q-RT-PCR, ELISA, and cell counting data. Before performing statistical tests, a normality test was conducted to determine the distribution of the data. The unpaired, two-tailed Student's t-test for independent samples, with equal variances assumed, was utilized for normally distributed data. At the same time, the Mann-Whitney U or Kruskal-Wallis test was used for non-normally distributed data. The data was presented as Mean ± SEM for normally distributed data and median with interquartile range (IQR) for non-normally distributed data. P-values of less than 0.05 were considered significant.

Results

TIMAP expression in B-cell NHL

TIMAP protein expression was evaluated in lymph tissue sections from a healthy control, a BL patient, a DLBCL patient, and an FL patient by IHC. As shown in Figure 1A, TIMAP expression was upregulated in the lymphoma tissues compared to the normal lymph tissue. Notably, its expression was particularly high in DLBCL tissue. We next investigated TIMAP expression at both mRNA and protein levels in Raji and Daudi cell lines before knocking it down. Figures 1B,C show that TIMAP is expressed at both the protein and mRNA levels in Raji and Daudi cells, respectively.

TIMAP knockdown analysis

TIMAP knockdown effectiveness was assessed at the mRNA and protein levels in the Raji cells after 72 h of FANA-ASO treatment using qPCR and ELISA, respectively. TIMAP mRNA was considerably decreased in cells treated with FANA-ASO-TIMAP (0.70 ± 0.04, $p = 0.001$, n = 4) compared to FANA-ASO-scramble control (0.97 ± 0.02) (Figure 2A), and TIMAP protein levels were decreased in FANA-ASO-TIMAP-treated cells (median = 0.73, IQR = 0.13, $p = 0.002$, n = 6) compared to FANA-ASO-scramble (median = 1.00, IQR = 0.00) (Figure 2B).

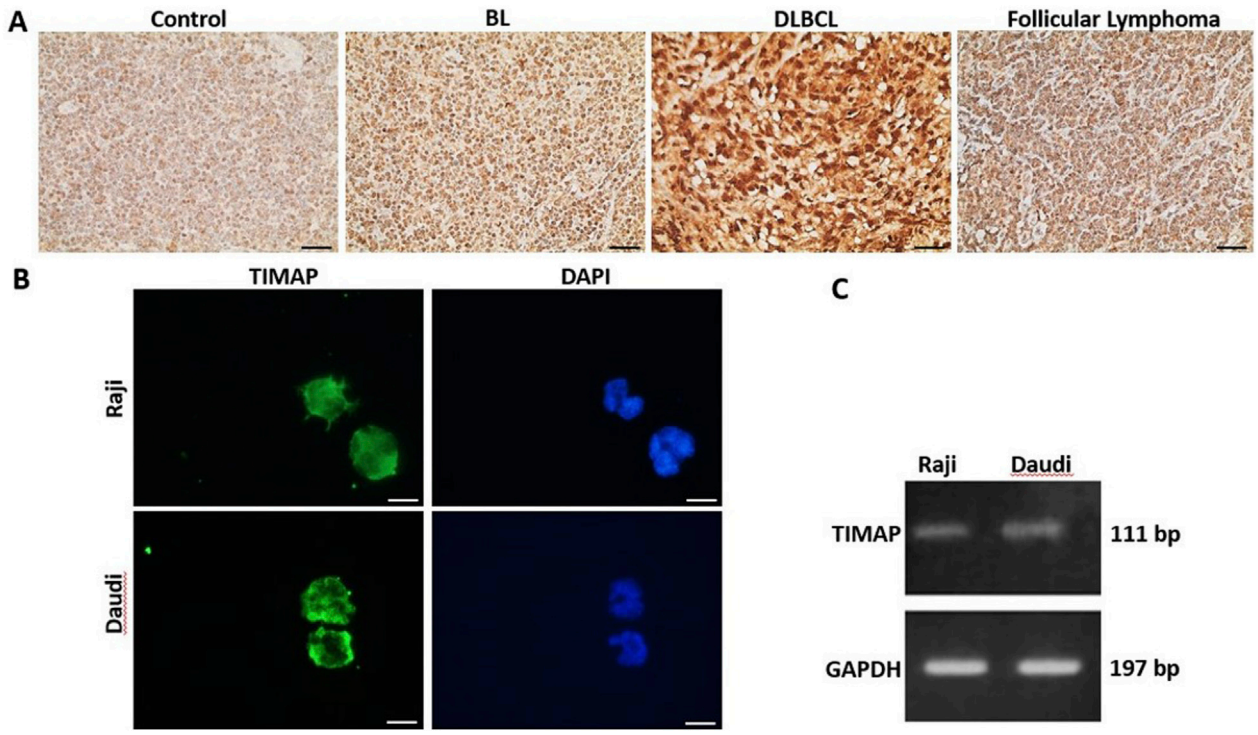

FIGURE 1
TIMAP expression in B-cell NHL. **(A)** IHC images captured at ×40 magnification of TIMAP expression in normal lymph node tissue (control), BL patient, DLBCL patient, and follicular lymphoma patient lymph node tissues. Scale bar 50μm. **(B)** Immunofluorescence images captured at ×100 magnification of TIMAP protein (green) in Raji and Daudi cell lines. Cell nuclei are depicted by DAPI staining (blue). Scale bar 50μm. **(C)** RT-PCR gel-electrophoresis demonstrates TIMAP and GAPDH expression in Raji and Daudi cell lines.

These results indicate that FANA-ASO technology decreased TIMAP expression at the transcriptional and translational levels.

TIMAP knockdown has been previously shown to reduce endothelial cell growth [43]. Therefore, we further validated the efficiency of its knockdown by examining the impact on BL cell growth. An equal number of Raji cells was seeded and counted at baseline and after 72 h of transfection. While no significant difference was detected between scramble and TIMAP knockdown groups at baseline (H = 0.0, df = 1, p = 1.0), a Kruskal–Wallis test revealed a significant reduction in cell numbers following TIMAP knockdown compared with scramble-treated controls (H = 4.71, df = 1, p = 0.03) (Figure 2C). These findings indicate that TIMAP silencing impairs BL cell growth.

Gene expression profile after TIMAP knockdown

To uncover the transcriptome profile after TIMAP knockdown, a paired-end Illumina RNA-seq was performed on FANA-ASO-scramble and FANA-ASO-TIMAP-treated cells from 3 independent experiments. In total, 39,470,217, 33,222,502, and 35,556,701 clean reads were obtained from three FANA-ASO-scramble-treated samples, while 43,443,071, 36,557,909, and 35,812,052 clean reads were obtained from three FANA-ASO-TIMAP-treated samples. All samples successfully mapped over 80% of reads to the current version of the human genome (GRCh38.p14) and met the quality standards required for downstream analysis.

Using the Ensembl annotation reference file, read counts were summarized at the gene level using featureCounts. A cutoff of 1 Count per Million (CPM) was used to select genes for differential expression analysis, resulting in 11,631 genes. Limma-Voom was then used to determine accurate DEGs based on the count tables generated from featureCounts. RNA-seq data were further evaluated through a Principal Component Analysis (PCA), which clustered samples with similar characteristics together (Figure 2D), indicating significant differences between control and knockdown samples.

A total of 2,368 genes were substantially dysregulated (adjusted $P < 0.05$ as the threshold), with 1,326 upregulated genes (log2FC > 0) and 1,042 downregulated genes (log2FC < 0). The distinct expression patterns in various samples were visualized by a volcano plot and hierarchical clustering, as illustrated in Figures 3A,B, respectively. The top

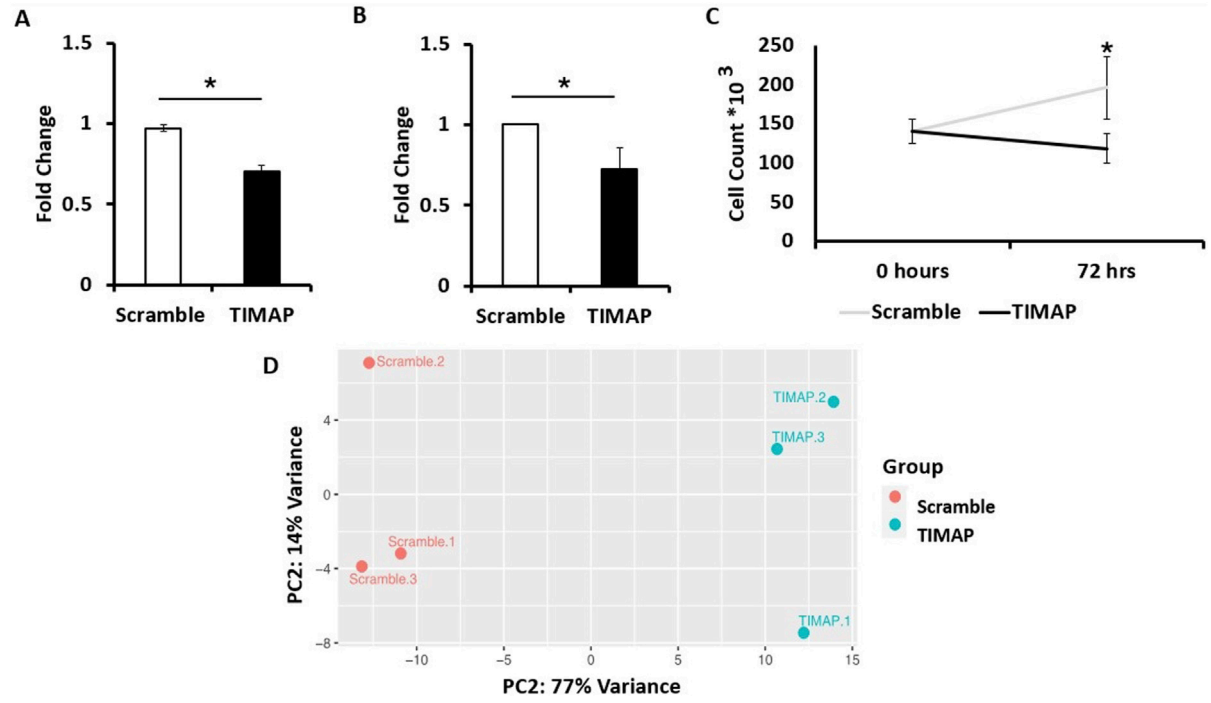

FIGURE 2
TIMAP Knockdown Analysis. **(A)** qPCR analysis of TIMAP mRNA expression (fold change) between FANA-ASO-scramble and FANA-ASO-TIMAP-treated cells. Data represent Mean ± SEM, * ($P \leq 0.05$), n = 4 **(B)** ELISA analysis of TIMAP protein expression (fold change) between FANA-ASO-scramble and FANA-ASO-TIMAP-treated cells. Data represent Median ± IQR, * ($P \leq 0.05$), n = 6. **(C)** Effect of TIMAP knockdown on cell growth. An equal number of Raji cells was seeded (0 h). After 72 h, viable cells were counted using trypan blue exclusion and a hemocytometer. TIMAP knockdown significantly reduced Raji cell growth compared with scramble-treated cells. Data represent Mean ± SEM. Statistical significance was determined using an independent-samples Kruskal-Wallis test, * ($P \leq 0.05$), n = 9. **(D)** Principal component analysis (PCA) plot for FANA-ASO-TIMAP and FANA-ASO-Scramble treated samples. A two-dimensional PCA was conducted using normalized counts of genes between TIMAP and scramble samples. On the plot, each point represents a sample. The principal components (PC1, PC2) demonstrate the degree of variation between the groups.

50 differentially up-and down-regulated genes are summarized in Tables 3, 4, respectively.

Validation of key DEGs by qPCR

To validate key DEGs relevant to BL pathogenesis, qPCR was performed for *PAK3*, *AICDA*, and *BCL-2*. As shown in Figure 4A, *PAK3* expression was absent in FANA-ASO-Scramble–treated cells but induced upon TIMAP knockdown; this expression was also undetectable at baseline in Raji BL cells (data not shown). Because *PAK3* was not measurable in the scramble control, expression is shown as normalized Ct values relative to *GAPDH* in knockdown samples. Figure 4B demonstrates that *AICDA* expression was downregulated in FANA-ASO-TIMAP–treated cells (0.53 ± 0.16, $P = 0.07$, n = 4) compared to the scramble control (1.1 ± 0.2). While TIMAP knockdown induced *BCL-2* expression (1.35 ± 0.12, $P = 0.03$, n = 4) compared to scramble (0.75 ± 0.16), as shown in Figure 4C. These results are consistent with the RNA-seq analysis and confirm that even partial TIMAP silencing alters the expression of genes central to BL pathogenesis.

Gene ontology (GO) analysis of DEGs

Using the DAVID server, the molecular functions (MF), biological processes (BP), and cellular components (CC) of the DEGs were clustered to reveal the significantly enriched GO terms (adjusted $p < 0.05$) (Figure 5). According to the results, biological processes are primarily involved in the positive regulation of cellular processes (GO: 0048522), cell communication (GO: 0010646), intracellular signal transduction (GO: 0035556), DNA metabolic process (GO: 0006259), and leukocyte activation (GO: 0045321). Cellular components include the cytoplasm (GO: 0005737) and cytosol (GO: 0005829), intracellular organelles (GO: 0043229), nucleoplasm (GO: 0005654), and cytoskeleton (GO: 0005856). Among the molecular functions of DEGs are kinase activity (GO: 0016301) and kinase binding (GO:

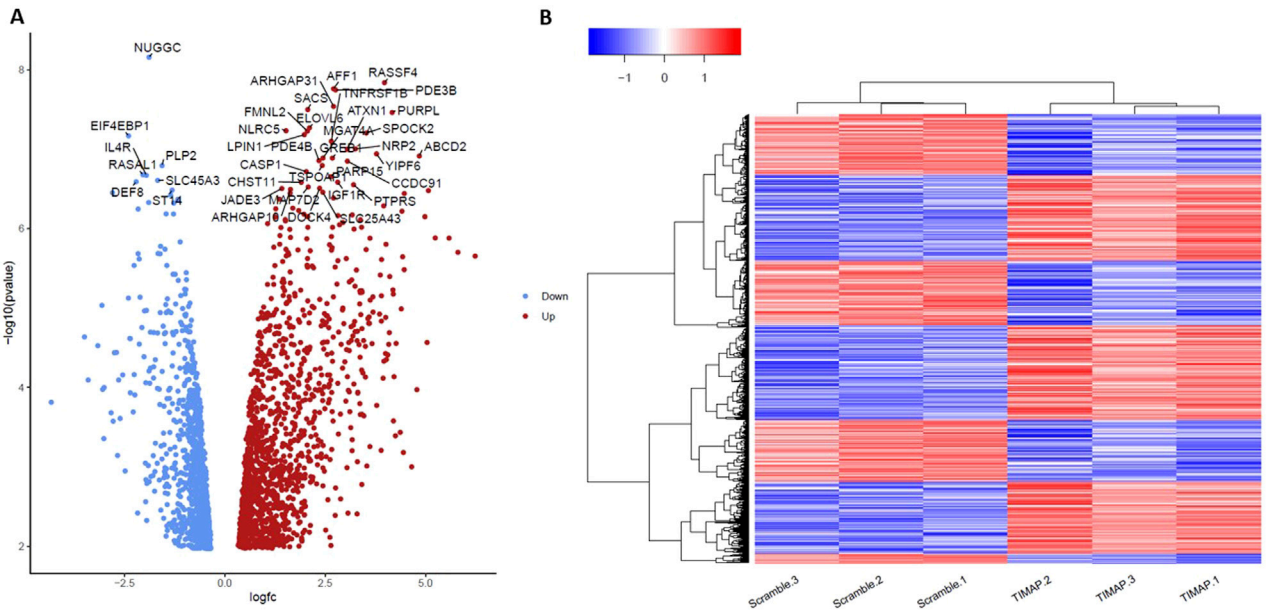

FIGURE 3
Evaluation of TIMAP Expression Patterns using Volcano plot and hierarchical clustering of DEGs. **(A)** A volcano plot showing all the genes with log2FC in TIMAP-knockdown and scramble samples on the X-axis, while the -log10 adjusted p-value is presented on the Y-axis. The grey dots indicate genes that are not statistically significant (using 0.05 of the adjusted p-value as a threshold), the red points represent genes that are considerably overexpressed (log2FC > 0), and the blue points represent significantly under-expressed genes (log2FC < 0). **(B)** A Heatmap of the normalized counts for the DEGs in Scramble 1-3 samples and TIMAP-knockdown 1–3 samples. The blue color indicates low expression of certain genes in the sample, while the red color indicates high expression of those genes. Hierarchical clustering by heatmap has successfully differentiated the DEGs between scramble and TIMAP knockdown samples.

0019900), phosphor-transferase activity; alcohol group as acceptor (GO: 0016773), nucleotide binding (GO: 0000166), phospholipid binding (GO: 0005543), and phosphatidylinositol binding (GO: 0035091).

KEGG analysis of DEGs

Based on the KEGG pathway database, the Enrichr tool was used to find the most significantly enriched pathways to which the DEGs belong. The findings in Figure 6 demonstrate that DEGs were clustered in several significant KEGG pathways (adjusted $p < 0.05$), including the p53 signaling pathway (hsa04115), apoptosis (hsa04210), B-cell receptor (BCR) signaling pathway (hsa04662), homologous recombination (hsa03440), mTOR signaling pathway (hsa04150), and DNA replication (hsa03030).

Discussion

TIMAP is highly expressed in several solid tumors and blood cancer cells, including BL [23]. However, its molecular function in cancer has not been fully investigated. Many previous studies convincingly demonstrated TIMAP's role in regulating various cellular processes that are known to be implicated in tumor pathogenesis through its interaction with key complicit molecules [20]. Among those are several nuclear proteins involved in the RNA splicing mechanism, such as U5 snRNP, SFPQ, and hnRNPA1 [27, 29], indicating a possible function of TIMAP in transcriptional regulation. In this study, RNA-seq was conducted to identify the transcriptome profile of BL cells after TIMAP silencing. Our analysis revealed 2,368 DEGs and 20 signaling pathways dysregulated in BL.

RNA-seq is one of the most sensitive and widely used methods for observing how cells respond to treatment and eventually identifying the dysregulated genes and pathways [44, 45]. In this first-of-its-kind work, RNA-seq was performed on Raji BL cells treated with FANA-ASO-TIMAP, and the gene expression profile was compared to that of the cells treated with FANA-ASO-Scramble control to discover TIMAP-responsive genes. The PCA plot highlighted considerable similarities between the TIMAP knockdown samples and distinguished them from the control. A total of 2,368 genes were found to be differentially expressed in response to TIMAP downregulation, of which 1,326 were upregulated and 1,042 were downregulated. On the heatmap, the clustering of those DEGs provided consistent expression patterns for each treatment group, further confirming the distinguished transcriptome profile of TIMAP knockdown cells.

TABLE 3 Top 50 up-regulated DEGs after TIMAP knockdown.

GeneID	Gene name	Description	Feature	Log2FC	Adj.P.Val
ENSG00000077264	*PAK3*	p21 (RAC1) activated kinase 3	protein coding	6.23699785	0.00025039
ENSG00000186297	*GABRA5*	gamma-aminobutyric acid type A receptor subunit alpha5	protein coding	5.807702811	0.000240473
ENSG00000163362	*INAVA*	innate immunity activator	protein coding	5.587054181	0.000189518
ENSG00000172296	*SPTLC3*	serine palmitoyl transferase long chain base subunit 3	protein coding	5.242882496	0.000189518
ENSG00000152128	*TMEM163*	transmembrane protein 163	protein coding	5.039945964	0.001050781
ENSG00000099282	*TSPAN15*	tetraspanin 15	protein coding	4.985660189	0.000131879
ENSG00000173208	*ABCD2*	ATP binding cassette subfamily D member 2	protein coding	4.846412503	7.51E-05
ENSG00000257261	*SLC38A4-AS1*	SLC38A4 Antisense RNA 1	lncRNA	4.655443681	0.010921537
ENSG00000104177	*MYEF2*	myelin expression factor 2	protein coding	4.47245795	9.81E-05
ENSG00000235831	*BHLHE40-AS1*	BHLHE40 antisense RNA 1	lncRNA	4.470596306	0.000318507
ENSG00000111249	*CUX2*	cut like homeobox 2	protein coding	4.450363672	0.008324052
ENSG00000092051	*JPH4*	junctophilin 4	protein coding	4.431012223	0.000252779
ENSG00000204161	*TMEM273*	transmembrane protein 273	protein coding	4.414377442	0.000128125
ENSG00000137491	*SLCO2B1*	solute carrier organic anion transporter family member 2B1	protein coding	4.397003908	0.00064369
ENSG00000142347	*MYO1F*	myosin IF	protein coding	4.371096523	0.005564985
ENSG00000250358	*LINC02200*	long intergenic non-protein coding RNA 2200	lncRNA	4.268124613	0.001068858
ENSG00000078018	*MAP2*	microtubule associated protein 2	protein coding	4.251541511	0.005947381
ENSG00000071909	*MYO3B*	myosin IIIB	protein coding	4.216609343	0.001940389
ENSG00000215386	*MIR99AHG*	mir-99a-let-7c cluster host gene	lncRNA	4.201310683	0.004459451
ENSG00000198216	*CACNA1E*	calcium voltage-gated channel subunit alpha1 E	protein coding	4.197890373	0.000503653
ENSG00000162714	*ZNF496*	zinc finger protein 496	protein coding	4.189331705	0.00047376
ENSG00000250337	*PURPL*	p53 upregulated regulator of p53 levels	lncRNA	4.169379922	5.75E-05
ENSG00000146950	*SHROOM2*	shroom family member 2	protein coding	4.110414976	0.000366862
ENSG00000114646	*CSPG5*	chondroitin sulfate proteoglycan 5	protein coding	4.100209392	0.00087828
ENSG00000113946	*CLDN16*	claudin 16	protein coding	4.084168866	0.001070074
ENSG00000165868	*HSPA12A*	heat shock protein family A (Hsp70) member 12A	protein coding	4.060589474	0.00127637
ENSG00000276231	*PIK3R6*	phosphoinositide-3-kinase regulatory subunit 6	protein coding	4.026197817	0.001413494
ENSG00000136531	*SCN2A*	sodium voltage-gated channel alpha subunit 2	protein coding	4.008373053	0.000704814
ENSG00000179088	*C12orf42*	chromosome 12 open reading frame 42	protein coding	4.005637675	0.001250976
ENSG00000107551	*RASSF4*	Ras association domain family member 4	protein coding	3.978025743	5.24E-05
ENSG00000163518	*FCRL4*	Fc receptor like 4	protein coding	3.964185129	0.00145664
ENSG00000101255	*TRIB3*	tribbles pseudo kinase 3	protein coding	3.958941693	0.000120615
ENSG00000198933	*TBKBP1*	TBK1 binding protein 1	protein coding	3.94411888	0.00198347
ENSG00000173198	*CYSLTR1*	cysteinyl leukotriene receptor 1	protein coding	3.905841489	0.0002639
ENSG00000188487	*INSC*	INSC spindle orientation adaptor protein	protein coding	3.902938238	0.000518891
ENSG00000075651	*PLD1*	phospholipase D1	protein coding	3.901750708	0.000751531

(Continued on following page)

TABLE 3 (*Continued*) Top 50 up-regulated DEGs after TIMAP knockdown.

GeneID	Gene name	Description	Feature	Log2FC	Adj.P.Val
ENSG00000171016	*PYGO1*	pygopus family PHD finger 1	protein coding	3.895986603	0.008004992
ENSG00000135821	*GLUL*	glutamate-ammonia ligase	protein coding	3.87401119	0.000354305
ENSG00000154102	*C16orf74*	chromosome 16 open reading frame 74	protein coding	3.855659004	0.000679729
ENSG00000116833	*NR5A2*	nuclear receptor subfamily 5 group A member 2	protein coding	3.785153504	0.003323437
ENSG00000181704	*YIPF6*	Yip1 domain family member 6	protein coding	3.781298376	7.51E-05
ENSG00000149403	*GRIK4*	glutamate ionotropic receptor kainate type subunit 4	protein coding	3.693682798	0.000671969
ENSG00000064225	*ST3GAL6*	ST3 beta-galactoside alpha-2,3-sialyltransferase 6	protein coding	3.690727682	0.000522351
ENSG00000138771	*SHROOM3*	shroom family member 3	protein coding	3.668740688	0.001068858
ENSG00000124570	*SERPINB6*	serpin family B member 6	protein coding	3.623297993	0.000552965
ENSG00000237372	*LINC03062*	long intergenic non-protein coding RNA 3062	lncRNA	3.617369981	0.000189518
ENSG00000283526	*PRRT1B*	proline rich transmembrane protein 1B	protein coding	3.615650355	0.007432053
ENSG00000162654	*GBP4*	guanylate binding protein 4	protein coding	3.596555527	0.000701994
ENSG00000072840	*EVC*	EvC ciliary complex subunit 1	protein coding	3.584536839	0.000775413
ENSG00000163554	*SPTA1*	spectrin alpha, erythrocytic 1	protein coding	3.539517179	0.010756775

In our study, 2 μM FANA-ASO was used to target TIMAP in BL cells, achieving approximately 30% knockdown efficiency after 72 h. This result is notably lower than an earlier study, which used 8 μM FANA-ASO to knock down KCTD15 in B-cell leukemia cells, resulting in a much higher 80% knockdown efficiency on days 8–16 [31]. Additionally, previous research on silencing ABI1 in healthy $CD34^+$ cells using FANA-ASO achieved approximately 40% knockdown after 48 h of treatment [46]. These discrepancies may be attributed to differences in FANA-ASO concentration, treatment duration, cell type, and the target gene.

Despite achieving only a 30% knockdown of TIMAP, our study was still able to identify a significant number of DEGs with deregulated expression. This indicates that even partial silencing of TIMAP can lead to substantial alterations in the transcriptome of BL cells. The identified DEGs were associated with critical pathways involved in cell survival, proliferation, and apoptosis. Consistently, TIMAP knockdown attenuated cell growth, in line with previous findings [43] and the predicted impact on growth signaling pathways identified here. These results suggest that even a modest knockdown of TIMAP can have profound effects on the cellular processes driving tumorigenesis. Identifying key genes and pathways affected by TIMAP silencing provides valuable insights into potential therapeutic targets, despite the limited knockdown efficiency. Hence, future research that utilizes variable gene manipulation techniques is vital to elucidate the precise mechanisms through which TIMAP regulates these molecules and pathways in BL.

In addition to the transcriptomic alterations observed upon TIMAP silencing, our IHC and cell line data provide important evidence that TIMAP is upregulated in B-cell non-Hodgkin lymphomas. Specifically, TIMAP protein expression was markedly elevated in BL, DLBCL, and FL tissues compared to normal lymph tissue, with particularly strong expression in DLBCL. Notably, *TIMAP* transcript was also among the upregulated genes in a previous transcriptomic profiling study of DLBCL [25], providing independent support for our findings. Consistently, both Raji and Daudi BL cell lines exhibited detectable TIMAP expression at the mRNA and protein levels. These findings suggest that TIMAP overexpression may represent a common feature across multiple B-cell lymphoma subtypes, rather than being restricted to BL. This is consistent with its known role in regulating pathways central to cell survival and proliferation, including PI3K/Akt/mTOR [43]. The observation of particularly high TIMAP expression in DLBCL further raises the possibility that TIMAP may contribute to disease aggressiveness or heterogeneity in B-cell lymphomas. Future studies involving patient cohorts and subtype-specific analyses are necessary to clarify whether TIMAP expression has prognostic significance and to determine its potential as a biomarker or therapeutic target across B-cell malignancies.

Among the most upregulated genes in our study was *PAK3*, a member of the PAK family of serine/threonine kinases originally identified as downstream effectors of the Rho GTPases Cdc42 and Rac [47]. PAKs are divided into two groups based on the sequence and structure: Group I PAKs (PAK1, PAK2, and PAK3) and Group II PAKs (PAK4, PAK5, and PAK6) [48]. PAKs regulate various cellular processes that are often disrupted in cancer, including cell survival, cell growth, and cytoskeleton remodeling [49]. PAKs are frequently upregulated in various tumors and influence several oncogenic signaling pathways that

TABLE 4 Top 50 down-regulated DEGs after TIMAP knockdown.

GeneID	Gene name	Description	Feature	Log2FC	adj.P.Val
ENSG00000205837	*LINC00487*	long intergenic non-protein coding RNA 487	lncRNA	−4.320875734	0.003139371
ENSG00000188783	*PRELP*	proline and arginine rich end leucine rich repeat protein	protein coding	−3.493418349	0.000951158
ENSG00000162105	*SHANK2*	SH3 and multiple ankyrin repeat domains 2	protein coding	−3.401540724	0.002057955
ENSG00000130487	*KLHDC7B*	kelch domain containing 7B	protein coding	−3.160369721	0.00109221
ENSG00000143995	*MEIS1*	Meis homeobox 1	protein coding	−3.058968491	0.000604104
ENSG00000164694	*FNDC1*	fibronectin type III domain containing 1	protein coding	−3.041008069	0.002498708
ENSG00000163884	*KLF15*	KLF transcription factor 15	protein coding	−3.010938764	0.006295845
ENSG00000165457	*FOLR2*	folate receptor beta	protein coding	−3.003218524	0.002418629
ENSG00000203710	*CR1*	complement C3b/C4b receptor 1 (Knops blood group)	protein coding	−2.829643321	0.003776015
ENSG00000102098	*SCML2*	Scmpolycomb group protein like 2	protein coding	−2.795587703	9.81E-05
ENSG00000168491	*CCDC110*	coiled-coil domain containing 110	protein coding	−2.750088398	0.001241616
ENSG00000273018	*FAM106A*	family with sequence similarity 106 member A	lncRNA	−2.695369633	0.001241616
ENSG00000254030	*IGLC5*	immunoglobulin lambda constant 5 (pseudogene)	IG_C_pseudogene	−2.669444649	0.008864195
ENSG00000078114	*NEBL*	nebulette	protein coding	−2.605029011	0.00426347
ENSG00000211898	*IGHD*	immunoglobulin heavy constant delta	IG_C_gene	−2.479821045	0.011755158
ENSG00000182866	*LCK*	LCK proto-oncogene, Src family tyrosine kinase	protein coding	−2.398245479	0.000533898
ENSG00000187840	*EIF4EBP1*	eukaryotic translation initiation factor 4E binding protein1	protein coding	−2.395071203	6.10E-05
ENSG00000182168	*UNC5C*	unc-5 netrin receptor C	protein coding	−2.364945932	0.000986908
ENSG00000270959	*LPP-AS2*	LPP antisense RNA 2	lncRNA	−2.353260745	0.00262887
ENSG00000117020	*AKT3*	AKT serine/threonine kinase 3	protein coding	−2.350106042	0.000988183
ENSG00000224187	*LINC01991*	Long Intergenic Non-Protein Coding RNA 1991	lncRNA	−2.257073659	0.000295627
ENSG00000230426	*LINC01036*	long intergenic non-protein coding RNA 1036	lncRNA	−2.255122831	0.00187507
ENSG00000167995	*BEST1*	bestrophin 1	protein coding	−2.238896365	0.002732034
ENSG00000140995	*DEF8*	differentially expressed in FDCP 8 homolog	protein coding	−2.206241878	9.52E-05
ENSG00000125888	*BANF2*	BANF family member 2	protein coding	−2.168635127	0.025987585
ENSG00000082458	*DLG3*	discs large MAGUK scaffold protein 3	protein coding	−2.156337647	0.000124827
ENSG00000182963	*GJC1*	gap junction protein gamma 1	protein coding	−2.130493525	0.000261897
ENSG00000160505	*NLRP4*	NLR family pyrin domain containing 4	protein coding	−2.129066591	0.001070074
ENSG00000179750	*APOBEC3B*	apolipoprotein B mRNA editing enzyme catalytic subunit3B	protein coding	−2.10871196	0.000523548
ENSG00000167483	*NIBAN3*	niban apoptosis regulator 3	protein coding	−2.063615734	0.000814506
ENSG00000111344	*RASAL1*	RAS protein activator like 1	protein coding	−2.039040937	9.22E-05
ENSG00000146215	*CRIP3*	cysteine rich protein 3	protein coding	−2.010201596	0.001326338
ENSG00000132464	*ENAM*	enamelin	protein coding	−1.976291645	0.010163259
ENSG00000246705	*H2AJ*	H2A.J histone	protein coding	−1.969529943	0.020995928
ENSG00000151322	*NPAS3*	neuronal PAS domain protein 3	protein coding	−1.966339059	0.002197977
ENSG00000077238	*IL4R*	interleukin 4 receptor	protein coding	−1.952740272	9.22E-05

(Continued on following page)

TABLE 4 (*Continued*) Top 50 down-regulated DEGs after TIMAP knockdown.

GeneID	Gene name	Description	Feature	Log2FC	adj.P.Val
ENSG00000107331	*ABCA2*	ATP binding cassette subfamily A member 2	protein coding	−1.950283708	0.000658604
ENSG00000185189	*NRBP2*	nuclear receptor binding protein 2	protein coding	−1.943895447	0.030072386
ENSG00000144331	*ZNF385B*	zinc finger protein 385B	protein coding	−1.904057567	0.010662957
ENSG00000145012	*LPP*	LIM domain containing preferred translocation partner in lipoma	protein coding	−1.893440473	0.000113202
ENSG00000232265	*LINC02805*	long intergenic non-protein coding RNA 2805	lncRNA	−1.886336509	0.001762078
ENSG00000189233	*NUGGC*	nuclear GTPase, germinal center associated	protein coding	−1.885608864	5.24E-05
ENSG00000116157	*GPX7*	glutathione peroxidase 7	protein coding	−1.881730165	0.014259455
ENSG00000171766	*GATM*	glycine amidino transferase	protein coding	−1.85258952	0.001675188
ENSG00000148175	*STOM*	stomatin	protein coding	−1.851974907	0.00087828
ENSG00000111732	*AICDA*	activation induced cytidine deaminase	protein coding	−1.83973866	0.013005594
ENSG00000212123	*PRR22*	proline rich 22	protein coding	−1.78860534	0.012811673
ENSG00000147437	*GNRH1*	gonadotropin releasing hormone 1	protein coding	−1.780287627	0.008879193
ENSG00000132744	*ACY3*	amino acylase 3	protein coding	−1.769829408	0.001632406
ENSG00000012779	*ALOX5*	arachidonate 5-lipoxygenase	protein coding	−1.768707059	0.00087828

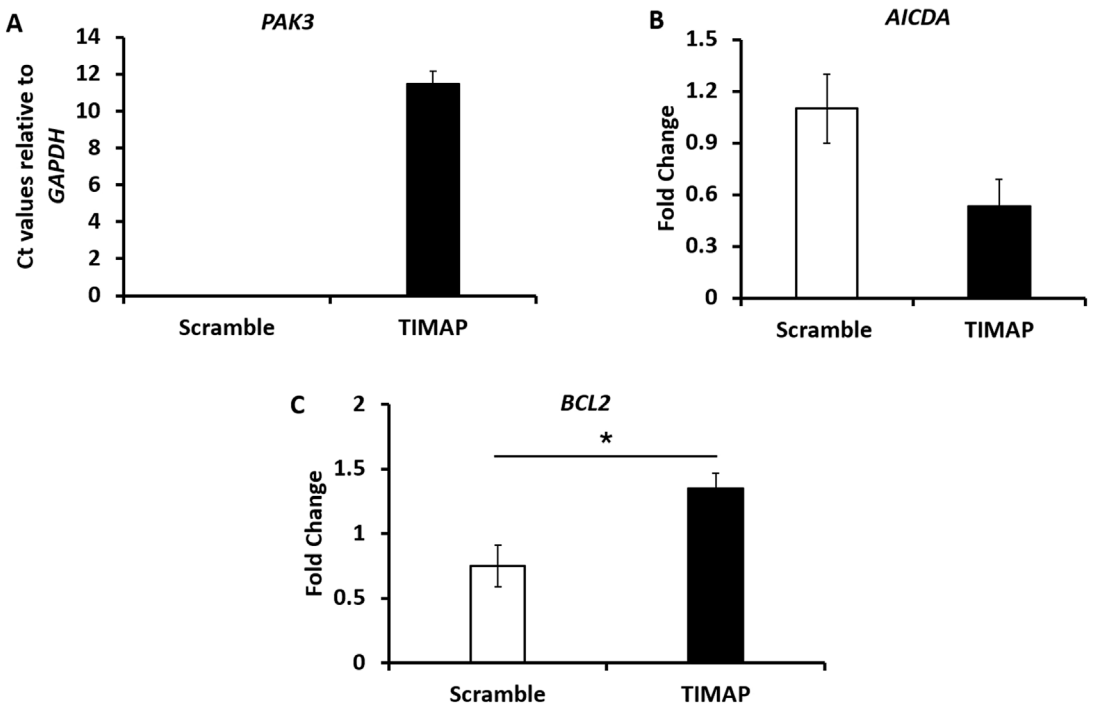

FIGURE 4
Validation of selected DEGs by qPCR. **(A)** qPCR analysis of *PAK3* mRNA expression between FANA-ASO-scramble and FANA-ASO-TIMAP-treated cells, as represented by the mean normalized Ct value relative to *GAPDH*, n = 3. **(B,C)** qPCR analysis of *AICDA* and *BCL2* mRNA expression (fold change) in FANA-ASO-scramble and FANA-ASO-TIMAP-treated cells. Data represent mean ± SEM of three independent experiments, * ($P \leq 0.05$).

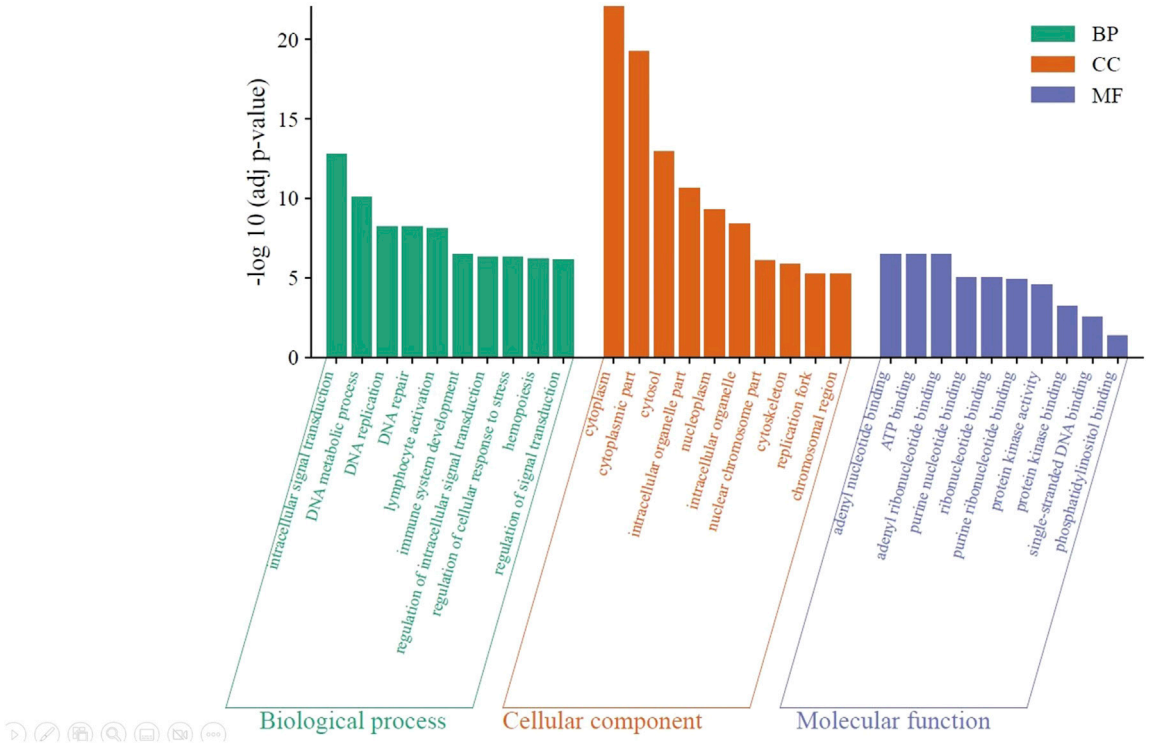

FIGURE 5
Significantly enriched GO terms in the identified DEGs. The green bars represent the top 10 biological processes, the orange bars represent the top 10 cellular components, and the violet bars represent the top 10 molecular functions. BP: biological processes; CC: cellular component; and MF: molecular function.

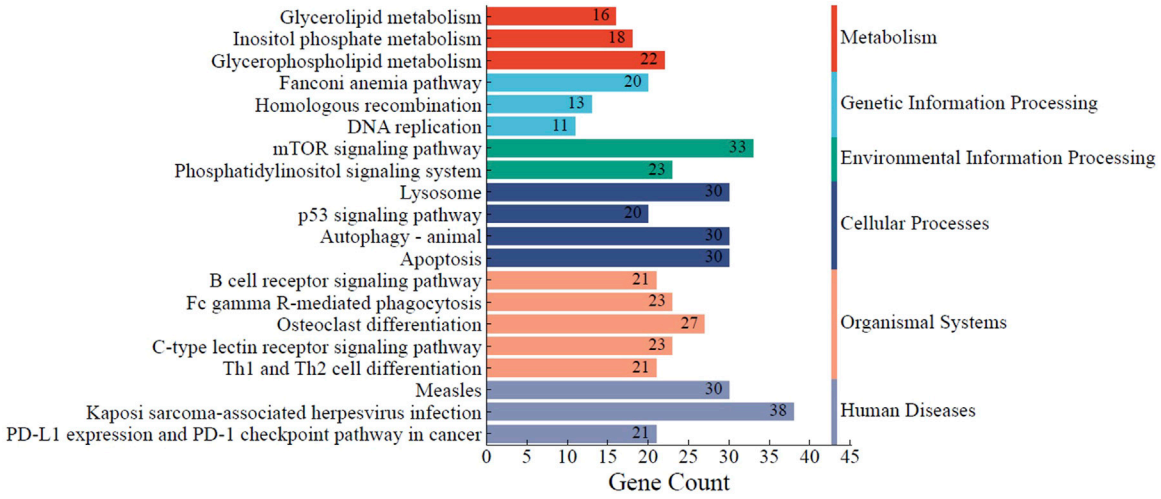

FIGURE 6
KEGG pathway analysis of the identified DEGs. The top 20 significantly enriched KEGG pathways to which DEGs belong are summarized. The functional KEGG pathways and the number of DEGs in each pathway are represented by the Y- and X-axes, respectively. * KEGG, Kyoto Encyclopedia of Genes and Genomes.

promote resistance to apoptosis, uncontrolled cell proliferation, and drug resistance, making them potential targets for therapy [48, 50]. Consequently, PAK inhibitors have recently been examined for their therapeutic activity in several cancers, including lymphoma [48, 50–52].

Previous studies have revealed a negative impact of high PAK1 and PAK2 expression on relapse-free survival in T-cell lymphoblastic lymphoma (T-LBL) patients, and PAK inhibitors were shown to attenuate T-LBL growth and enhance chemosensitivity to doxorubicin [48, 50]. To date, the role of PAK3 in cancer remains elusive. It is upregulated in head and neck squamous cell carcinoma and is considered a prognostic marker in glioblastoma multiforme [23]. However, it is best known for its biological function in the nervous system, where it is predominantly expressed and plays an important role in synaptic plasticity [53]. Since TIMAP is also predominantly expressed in the nervous system [21, 23] and is a prognostic marker in glioblastoma multiform [27] and head and neck cancer [23, 26], it is plausible that it might be associated with PAK3 regulation. Interestingly, our qPCR analysis revealed that while PAK3 expression was undetectable in FANA-ASO-scramble–treated cells and in untreated cells, it was induced upon TIMAP knockdown. Hence, our findings suggest the importance of the TIMAP-PAK3 axis in BL, which prompts future investigations to address this relationship.

In contrast to *PAK3*, *LINC00487*, a long intergenic non-coding RNA (lncRNA), was the most downregulated gene in our study. *LINC00487* is one of the core genes in the germinal center B cells, contributing to B-cell development [54] and a key gene for predicting prognosis in DLBCL [55]. Research has shown that LINC00487 and other lncRNAs are linked to the enzyme activation-induced cytidine deaminase (AICDA), also known as AID [56]. AICDA is a DNA-modifying enzyme and one of the key genes in germinal center B cells [54, 57]. It plays a crucial role in generating diversity in immunoglobulins by converting cytosine to uracil in the variable and switch regions of immunoglobulin genes. This process leads to C: G mismatches, promoting class switching from IgM and IgD to other isotypes [57].

AICDA has been identified as an oncogene due to its ability to modify DNA, which enhances chromosomal translocations between the *c-myc* oncogene and immunoglobulin genes, induces point mutations in oncogenes, alters DNA methylation, and activates translocations of non-immunoglobulin genes [57–62]. It is also overexpressed in DLBCL [63] where TIMAP showed the most upregulation in our study. A recent study suggests that upregulation of AICDA significantly promotes cell proliferation, migration, genomic instability, and resistance to chemotherapy in B-cell lymphoma, indicating that AICDA could be a potential therapeutic target [64]. Furthermore, AICDA was identified as a driver of epigenetic heterogeneity in B-cell lymphoma, and its overexpression aggravates the disease [65].

Interestingly, AICDA was also downregulated in our study, suggesting that reduced TIMAP expression negatively impacts AICDA transcription. This may, in turn, decrease its effect on BL cell growth. This finding is consistent with previous reports that TIMAP downregulation adversely affects cell growth [43, 66], as well as with the reduced cell growth observed in FANA-ASO-TIMAP-treated cells in our study. Moreover, since *AICDA* and *LINC00487* are predominantly expressed in the germinal center B-cells, which are the precursors of BL, and downregulated in BL cells by TIMAP knockdown in the current study, this suggests that they might be associated with TIMAP in regulating normal and cancer B-cell development.

Another upregulated gene in our study involved in cell survival regulation is the p53 upregulated regulator of p53 levels (*PURPL*). Normally, P53 activation drives cells with translocations to undergo apoptosis [67]. However, P53 is inhibited in numerous types of cancer, resulting in the survival of aberrant cells that eventually develop into malignant cells [68–70]. PURPL has been shown to deplete P53 levels in colorectal cancer cells through its interaction with the Myb-binding protein 1A (MYBBP1A), a protein that binds to and stabilizes p53, and PURPL-deficient cells exhibit impaired tumor growth [71]. Furthermore, PURPL is overexpressed in gastric cancer, where it promotes cell growth, migration, survival, and invasion [72]. Therefore, our findings indicate a potential regulatory role of TIMAP in the p53 pathway.

An important gene that was also found to be upregulated in our RNA-seq and validated by qPCR is *BCL2*, a central regulator of apoptosis in B cells. BCL2 is an anti-apoptotic protein that promotes cell survival by inhibiting mitochondrial outer membrane permeabilization, thereby blocking caspase activation [73]. Dysregulated expression of BCL2 is a hallmark of several B-cell malignancies, including FL and DLBCL, where it often arises from the characteristic t(14; 18) (q32; q21) translocation [74]. Although BL is classically considered BCL2-negative, subsets of BL can display BCL2 expression [75], which may contribute to treatment resistance and disease heterogeneity. Raji cells, on the other hand, express BCL2 [76], which is consistent with our results. *BCL2* was not among the top 50 upregulated genes in our RNA-seq analysis. Still, we validated its expression due to its well-established critical role in B-cell lymphoma biology, especially since TIMAP protein expression was upregulated in different B-cell lymphoma cases in the current study, suggesting it might play a common role in these malignancies. The induction of *BCL2* expression following TIMAP knockdown in our study implies a potential compensatory mechanism by which BL cells may counterbalance the pro-apoptotic stress induced by reduced TIMAP expression. This aligns with our observed reduction in cell growth, indicating that despite *BCL2* upregulation, TIMAP silencing may override survival signals and shift the balance toward apoptosis. These findings raise the possibility that

TIMAP may be indirectly linked to apoptotic regulation through its influence on *BCL2* expression, a hypothesis that warrants further mechanistic investigation.

Through GO analysis using the DAVID server, the DEGs revealed by TIMAP knockdown were categorized into three categories (biological processes (BP), cellular components (CC), and molecular functions (MF)). DEGs were associated with various GO terms, including signal transduction via intracellular signaling cascades, cytoskeleton organization, apoptosis, replication, repair, hemopoiesis, leukocyte activation, cell communication regulation, and kinase activity. These pathways are consistent with previously published research on TIMAP [20]. Ultimately, prospective research dissecting these significantly enriched GO terms could help us precisely understand how TIMAP is implicated in B-cell lymphomagenesis.

Among the signaling pathways impacted by TIMAP silencing in our study are mTOR and BCR. The survival of malignant B cells in BL depends on the tonic BCR signaling pathway, as evidenced by the death of BL cell lines when BCR components are knocked down [77, 78]. BCR activates PI3K/Akt/mTOR signaling pathways to overcome the pro-apoptotic effect of *c-myc* overexpression and stimulate B cell proliferation; thus, inhibition of PI3K and mTOR pathways was associated with BL cell death and increased sensitivity to chemotherapy [79–81]. In support of our findings, Obeidat et al reported that TIMAP downregulation inhibits cellular proliferation and survival in EC by attenuating the PI3K/Akt signaling pathway [43]. Further research is recommended to expand TIMAP's molecular mechanism regarding these pathways in the context of B-cell lymphoma pathogenesis. This may, eventually, facilitate its incorporation into diagnostic and therapeutic approaches.

While our study focused on BL, TIMAP has been reported to be expressed in several solid tumors [23, 24, 26]. Extending transcriptomic profiling of TIMAP knockdown to other malignancies could uncover both shared and cancer–type–specific targets. Such comparative analyses may reveal whether TIMAP regulates universal oncogenic pathways or acts through lineage-restricted mechanisms.

Conclusion

This study highlights TIMAP as a potential therapeutic target in B-cell lymphoma by demonstrating that even partial silencing in Raji BL cells induces profound transcriptomic and phenotypic changes. TIMAP suppression altered the gene expression of key regulators, including *PAK3*, *AICDA, and BCL2*, and impacted critical pathways such as BCR and PI3K/Akt/mTOR, confirming its role in cell growth. Although limited by the lack of siRNA or single-oligonucleotide validation, our findings establish a foundation for future work to dissect the TIMAP–PAK3, TIMAP–BCL2, and TIMAP–AICDA axes and to evaluate the functional impact of TIMAP silencing *in vivo*. Importantly, TIMAP overexpression in BL, DLBCL, and FL tissues suggests a broader role in B-cell lymphomagenesis, which prompts the investigation of its clinical significance as a prognostic marker and therapeutic target across lymphoma subtypes.

Author contributions

Conceptualization, MO; Data analysis and curation, MO and ST; Conducted experiments, ST, BI, and AA-K; Resources, MO; Writing – original draft, MO and ST; Validation, MO, ST, BI, and AA-K. Review-writing, MO. All authors contributed to the article and approved the submitted version.

Data availability

The datasets presented in this study can be found in online repositories. The names of the repository/repositories and accession number(s) can be found below: https://www.ncbi.nlm.nih.gov/, PRJNA1172000.

Ethics statement

Ethical approval was not required for the studies on humans in accordance with the local legislation and institutional requirements because only commercially available established cell lines were used.

Funding

The author(s) declare that financial support was received for the research and/or publication of this article. This study received funding from the Deanship of Research at Jordan University of Science and Technology (grant# 2022/0338).

Acknowledgments

The authors thank Dr. Sohaib Alkhatib (Department of Pathology, Jordan University of Science and Technology) for providing the lymph node tissues.

Conflict of interest

The author(s) declared no potential conflicts of interest with respect to the research, authorship, and/or publication of this article.

Generative AI statement

The author(s) declare that Generative AI was used in the creation of this manuscript. The authors declare that Grammarly and ChatGPT were used to enhance readability and language. The authors thoroughly reviewed and edited the content as necessary, taking full responsibility for the accuracy and content of the publication.

Any alternative text (alt text) provided alongside figures in this article has been generated by Frontiers with the support of artificial intelligence and reasonable efforts have been made to ensure accuracy, including review by the authors wherever possible. If you identify any issues, please contact us.

References

1. Tietsche de Moraes Hungria V, Chiattone C, Pavlovsky M, Abenoza LM, Agreda GP, Armenta J, et al. Epidemiology of hematologic malignancies in real-world settings: findings from the hemato-oncology Latin America observational registry study. *J Glob Oncol* (2019) **5**(5):1–19. doi:10.1200/JGO.19.00025

2. CDC. Hematologic cancer incidence, survival, and prevalence (2025). Available online at: www.cdc.gov/uscs (Accessed November, 2023).

3. Rosmarin A. Leukemia, lymphoma, and myeloma. In: *Cancer*. Wiley (2019). p. 299–316. doi:10.1002/9781119645214.ch16

4. Mugnaini EN, Ghosh N. Lymphoma. *Prim Care Clin Off Pract* (2016) **43**(4): 661–75. doi:10.1016/j.pop.2016.07.012

5. Jamil A, Mukkamalla SKR. Lymphoma. (2022).

6. Aggarwal P, Limaiem F. *Reed Sternberg Cells* (2022).

7. Shankland KR, Armitage JO, Hancock BW. Non-hodgkin lymphoma. *The Lancet* (2012) **380**(9844):848–57. doi:10.1016/S0140-6736(12)60605-9

8. Parihar A, Singh R, Shaik S, Negi B, Rajguru J, Patil P, et al. Non-Hodgkin's lymphoma: a review. *J Fam Med Prim Care* (2020) **9**(4):1834. doi:10.4103/jfmpc.jfmpc_1037_19

9. God JM, Haque A. Burkitt lymphoma: pathogenesis and immune evasion. *J Oncol* (2010) **2010**:1–14. doi:10.1155/2010/516047

10. Molyneux EM, Rochford R, Griffin B, Newton R, Jackson G, Menon G, et al. Burkitt's lymphoma. *The Lancet* (2012) **379**(9822):1234–44. doi:10.1016/S0140-6736(11)61177-X

11. Epstein MA, Achong BG, Barr YM. Virus particles in cultured lymphoblasts from burkitt's lymphoma. *The Lancet* (1964) **283**(7335):702–3. doi:10.1016/s0140-6736(64)91524-7

12. Zech L, Haglund U, Nilsson K, Klein G. Characteristic chromosomal abnormalities in biopsies and lymphoid-cell lines from patients with burkitt and non-Burkitt lymphomas. *Int J Cancer* (1976) **17**(1):47–56. doi:10.1002/ijc.2910170108

13. Schulz TF, Boshoff CH, Weiss RA. HIV infection and neoplasia. *The Lancet* (1996) **348**(9027):587–91. doi:10.1016/S0140-6736(95)11033-X

14. Jacobsen KA, Prasad VS, Sidman CL, Osmond DG. Apoptosis and macrophage-mediated deletion of precursor B cells in the bone marrow of E mu-myc transgenic mice. *Blood* (1994) **84**(8):2784–94. doi:10.1182/blood.v84.8.2784.2784

15. Noy A. Burkitt lymphoma — subtypes, pathogenesis, and treatment strategies. *Clin Lymphoma Myeloma Leuk* (2020) **20**:S37–S38. doi:10.1016/S2152-2650(20)30455-9

16. Dozzo M, Carobolante F, Donisi PM, Scattolin A, Maino E, Sancetta R, et al. Burkitt lymphoma in adolescents and young adults: management challenges. *Adolesc Health Med Ther* (2016) **8**:11–29. doi:10.2147/AHMT.S94170

17. Wästerlid T, Brown PN, Hagberg O, Hagberg H, Pedersen L, D'Amore F, et al. Impact of chemotherapy regimen and rituximab in adult burkitt lymphoma: a retrospective population-based study from the nordic lymphoma group. *Ann Oncol* (2013) **24**(7):1879–86. doi:10.1093/annonc/mdt058

18. Opanga L, Mulaku MN, Opanga SA, Godman B, Kurdi A. Adverse effects of chemotherapy and their management in pediatric patients with non-hodgkin's lymphoma in Kenya: a descriptive, situation analysis study. *Expert Rev Anticancer Ther* (2019) **19**(5):423–30. doi:10.1080/14737140.2019.1606717

19. Zayac AS, Olszewski AJ. Burkitt lymphoma: bridging the gap between advances in molecular biology and therapy. *Leuk & Lymphoma* (2020) **61**(8): 1784–96. doi:10.1080/10428194.2020.1747068

20. Boratkó A, Csortos C. TIMAP, the versatile protein phosphatase 1 regulator in endothelial cells. *IUBMB life* (2017) **69**:918–28. doi:10.1002/iub.1695

21. Magdaleno S, Northcutt GM, Curran T, Kurschner C. mPPP1R16B is a novel mouse protein phosphatase 1 targeting subunit whose mRNA is located in cell bodies and dendrites of neurons in four distinct regions of the brain. *Gene Expr Patterns* (2002) **1**:143–9. doi:10.1016/S1567-133X(02)00010-8

22. Cao W, Mattagajasingh SN, Xu H, Kim K, Fierlbeck W, Deng J, et al. TIMAP, a novel CAAX box protein regulated by TGF-β1 and expressed in endothelial cells. *Am J Physiology-Cell Physiol* (2002) **283**(1):C327–37. doi:10.1152/ajpcell.00442.2001

23. The human protein atlas. (2025).

24. Obeidat M, Bodoor K, Alqudah M, Masaadeh A, Barukba M, Almomani R. TIMAP upregulation correlates negatively with survival in HER2- negative subtypes of breast cancer. *Asian Pac J Cancer Prev* (2021) **22**(6):1899–905. doi:10.31557/APJCP.2021.22.6.1899

25. Mahadevan D, Spier C, Della Croce K, Miller S, George B, Riley C, et al. Transcript profiling in peripheral T-cell lymphoma, not otherwise specified, and diffuse large B-cell lymphoma identifies distinct tumor profile signatures. *Mol Cancer Ther* (2005) **4**(12):1867–79. doi:10.1158/1535-7163.MCT-05-0146

26. Obeidat M, Algargaz W, Barukba M, Bodoor K, Mohamad I, Barakat F, et al. Clinical and molecular characteristics of Jordanian oropharyngeal cancer patients according to P16 expression: a retrospective study and a report of a novel biomarker. *Med Mol Morphol* (2024) **57**(2):136–46. doi:10.1007/s00795-024-00383-2

27. Fonódi M, Thalwieser Z, Csortos C, Boratkó A. TIMAP, a regulatory subunit of protein phosphatase 1, inhibits *in vitro* neuronal differentiation. *Int J Mol Sci* (2023) **24**(24):17360. doi:10.3390/ijms242417360

28. Mendrysa SM, Akagi K, Roayaei J, Lien WH, Copeland NG, Jenkins NA, et al. An integrated genetic-genomic approach for the identification of novel cancer loci in mice sensitized to c-Myc-Induced apoptosis. *Genes & Cancer* (2010) **1**(5):465–79. doi:10.1177/1947601910374875

29. Adyshev DM, Kolosova IA, Verin AD. Potential protein partners for the human TIMAP revealed by bacterial two-hybrid screening. *Mol Biol Rep* (2006) **33**(2):83–9. doi:10.1007/s11033-005-2311-y

30. Pelisch N, Rosas Almanza J, Stehlik KE, Aperi BV, Kroner A. Use of a self-delivering anti-ccl3 fana oligonucleotide as an innovative approach to target inflammation after spinal cord injury. *eNeuro* (2021) **8**(2):ENEURO.0338–20.2021. doi:10.1523/ENEURO.0338-20.2021

31. Smaldone G, Beneduce G, Incoronato M, Pane K, Franzese M, Coppola L, et al. KCTD15 is overexpressed in human childhood B-cell acute lymphoid leukemia. *Sci Rep* (2019) **9**(1):20108. doi:10.1038/s41598-019-56701-7

32. Cadena-Herrera D, Esparza-De Lara JE, Ramírez-Ibañez ND, López-Morales CA, Pérez NO, Flores-Ortiz LF, et al. Validation of three viable-cell counting methods: manual, semi-automated, and automated. *Biotechnol Rep* (2015) **7**:9–16. doi:10.1016/j.btre.2015.04.004

33. Afgan E, Baker D, Batut B, van den Beek M, Bouvier D, Čech M, et al. The galaxy platform for accessible, reproducible and collaborative biomedical analyses: 2018 update. *Nucleic Acids Res* (2018) **46**(W1):W537–W544. doi:10.1093/nar/gky379

34. Batut B, van den Beek M, Doyle MA, Soranzo N. RNA-seq data analysis in galaxy. *Methods Mol Biol* (2021) **2284**:367–92. doi:10.1007/978-1-0716-1307-8_20

35. Ewels P, Magnusson M, Lundin S, Käller M. MultiQC: summarize analysis results for multiple tools and samples in a single report. *Bioinformatics* (2016) **32**(19):3047–8. doi:10.1093/bioinformatics/btw354

36. Lindgreen S. AdapterRemoval: easy cleaning of next-generation sequencing reads. *BMC Res Notes* (2012) **5**(1):337. doi:10.1186/1756-0500-5-337

37. Dobin A, Davis CA, Schlesinger F, Drenkow J, Zaleski C, Jha S, et al. STAR: ultrafast universal RNA-Seq aligner. *Bioinformatics* (2013) **29**(1):15–21. doi:10.1093/bioinformatics/bts635

38. Liao Y, Smyth GK, Shi W. featureCounts: an efficient general purpose program for assigning sequence reads to genomic features. *Bioinformatics* (2014) **30**(7):923–30. doi:10.1093/bioinformatics/btt656

39. Law CW, Chen Y, Shi W, Smyth GK. Voom: precision weights unlock linear model analysis tools for RNA-seq read counts. *Genome Biol* (2014) **15**(2):R29. doi:10.1186/gb-2014-15-2-r29

40. Ritchie ME, Phipson B, Wu D, Hu Y, Law CW, Shi W, et al. Limma powers differential expression analyses for RNA-sequencing and microarray studies. *Nucleic Acids Res* (2015) **43**(7):e47. doi:10.1093/nar/gkv007

41. Huang D, Sherman BT, Tan Q, Collins JR, Alvord WG, Roayaei J, et al. The DAVID gene functional classification tool: a novel biological module-centric algorithm to functionally analyze large gene lists. *Genome Biol* (2007) **8**(9):R183. doi:10.1186/gb-2007-8-9-r183

42. Kuleshov MV, Jones MR, Rouillard AD, Fernandez NF, Duan Q, Wang Z, et al. Enrichr: a comprehensive gene set enrichment analysis web server 2016 update. *Nucleic Acids Res* (2016) **44**(W1):W90–W97. doi:10.1093/nar/gkw377

43. Obeidat M, Li L, Ballermann BJ. TIMAP promotes angiogenesis by suppressing PTEN-Mediated Akt inhibition in human glomerular endothelial cells. *Am J Physiology-Renal Physiol* (2014) **307**:F623–F633. doi:10.1152/ajprenal.00070.2014

44. Hong M, Tao S, Zhang L, Diao LT, Huang X, Huang S, et al. RNA sequencing: new technologies and applications in cancer research. *J Hematol Oncol* (2020) **13**(1):166. doi:10.1186/s13045-020-01005-x

45. Whitley SK, Horne WT, Kolls JK. Research techniques made simple: methodology and clinical applications of RNA sequencing. *J Invest Dermatol* (2016) **136**(8):e77–e82. doi:10.1016/j.jid.2016.06.003

46. Chorzalska A, Morgan J, Ahsan N, Treaba DO, Olszewski AJ, Petersen M, et al. Bone marrow-specific loss of ABI1 induces myeloproliferative neoplasm with features resembling, human myelofibrosis. *Blood* (2018) **132**(19):2053–66. doi:10.1182/blood-2018-05-848408

47. Zhao ZS, Manser E. PAK and other rho-associated kinases - effectors with surprisingly diverse mechanisms of regulation. *Biochem J* (2005) **386**(2):201–14. doi:10.1042/BJ20041638

48. Su N, Fang Y, Chen X, Chen X, Xia Z, Huang H, et al. Targeting P21-activated kinase suppresses proliferation and enhances chemosensitivity in T-cell lymphoblastic lymphoma. *Blood Sci* (2023) **5**(4):249–57. doi:10.1097/BS9.0000000000000169

49. Liu H, Liu K, Dong Z. The role of p21-Activated kinases in cancer and beyond: where are we heading? *Front Cell Dev Biol* (2021) **9**:641381. doi:10.3389/fcell.2021.641381

50. Cai Q, Su N, Fang Y, Chen X, Tian X, Ma S, et al. The expression of paks and its clinical significance in T-Cell lymphoblastic lymphoma. *Blood* (2020) **136**(Suppl. 1):14–6. doi:10.1182/blood-2020-136975

51. Wu A, Jiang X. p21-Activated kinases as promising therapeutic targets in hematological malignancies. *Leukemia* (2022) **36**(2):315–26. doi:10.1038/s41375-021-01451-7

52. Chung EY, Mai Y, Shah UA, Wei Y, Ishida E, Kataoka K, et al. PAK kinase inhibition has therapeutic activity in novel preclinical models of adult T-Cell leukemia/lymphoma. *Clin Cancer Res* (2019) **25**(12):3589–601. doi:10.1158/1078-0432.CCR-18-3033

53. Kumar R, Sanawar R, Li X, Li F. Structure, biochemistry, and biology of PAK kinases. *Gene* (2017) **605**:20–31. doi:10.1016/j.gene.2016.12.014

54. Petri A, Dybkær K, Bøgsted M, Thrue CA, Hagedorn PH, Schmitz A, et al. Long noncoding RNA expression during human B-cell development. *PLoS One* (2015) **10**(9):e0138236. doi:10.1371/journal.pone.0138236

55. Wang X, Lu Y, Liu Z, Zhang Y, He Y, Sun C, et al. A 9-LncRNA signature for predicting prognosis and immune response in diffuse large B-Cell lymphoma. *Front Immunol* (2022) **13**:813031. doi:10.3389/fimmu.2022.813031

56. Baghdadi H, Heidari R, Zavvar M, Ahmadi N, Shakouri Khomartash M, Vahidi M, et al. Long non-coding RNA signatures in lymphopoiesis and lymphoid malignancies. *Noncoding RNA* (2023) **9**(4):44. doi:10.3390/ncrna9040044

57. Park SR. Activation-induced cytidine deaminase in B cell immunity and cancers. *Immune Netw* (2012) **12**(6):230. doi:10.4110/in.2012.12.6.230

58. Jiao J, Lv Z, Wang Y, Fan L, Yang A. The off-target effects of AID in carcinogenesis. *Front Immunol* (2023) **14**:1221528. doi:10.3389/fimmu.2023.1221528

59. Robbiani DF, Bothmer A, Callen E, Reina-San-Martin B, Dorsett Y, Difilippantonio S, et al. AID is required for the chromosomal breaks in c-myc that lead to c-myc/IgH translocations. *Cell* (2008) **135**(6):1028–38. doi:10.1016/j.cell.2008.09.062

60. Álvarez-Prado ÁF, Pérez-Durán P, Pérez-García A, Benguria A, Torroja C, de Yébenes VG, et al. A broad atlas of somatic hypermutation allows prediction of activation-induced deaminase targets. *J Exp Med* (2018) **215**(3):761–71. doi:10.1084/jem.20171738

61. Robbiani DF, Bunting S, Feldhahn N, Bothmer A, Camps J, Deroubaix S, et al. AID produces DNA double-strand breaks in non-Ig genes and mature B cell lymphomas with reciprocal chromosome translocations. *Mol Cell* (2009) **36**(4):631–41. doi:10.1016/j.molcel.2009.11.007

62. Jiao J, Jin Y, Zheng M, Zhang H, Yuan M, Lv Z, et al. AID and TET2 co-operation modulates FANCA expression by active demethylation in diffuse large B cell lymphoma. *Clin Exp Immunol* (2019) **195**(2):190–201. doi:10.1111/cei.13227

63. Liu Z, Meng J, Li X, Zhu F, Liu T, Wu G, et al. Identification of hub genes and key pathways associated with two subtypes of diffuse large B-Cell lymphoma based on gene expression profiling *via* integrated bioinformatics. *Biomed Res Int* (2018) **2018**:1–14. doi:10.1155/2018/3574534

64. Godsmark G, De Souza Rios LA, Mowla S. Activation-induced cytidine deaminase promotes proliferation and enhances chemoresistance and migration in B-cell lymphoma. *Anticancer Res* (2021) **41**(1):237–47. doi:10.21873/anticanres.14770

65. Teater M, Dominguez PM, Redmond D, Chen Z, Ennishi D, Scott DW, et al. AICDA drives epigenetic heterogeneity and accelerates germinal center-derived lymphomagenesis. *Nat Commun* (2018) **9**(1):222. doi:10.1038/s41467-017-02595-w

66. Király N, Csortos C, Boratkó A. Ser69 phosphorylation of TIMAP affects endothelial cell migration. *Exp Lung Res* (2021) **47**(7):334–43. doi:10.1080/01902148.2021.1960651

67. Brady CA, Attardi LD. p53 at a glance. *J Cell Sci* (2010) **123**(Pt 15):2527–32. doi:10.1242/jcs.064501

68. Mantovani F, Collavin L, Del Sal G. Mutant p53 as a guardian of the cancer cell. *Cell Death Differ* (2019) **26**(2):199–212. doi:10.1038/s41418-018-0246-9

69. Kandoth C, McLellan MD, Vandin F, Ye K, Niu B, Lu C, et al. Mutational landscape and significance across 12 major cancer types. *Nature* (2013) **502**(7471):333–9. doi:10.1038/nature12634

70. Xu P, Liu X, Ouyang J, Chen B. TP53 mutation predicts the poor prognosis of Non-Hodgkin lymphomas: evidence from a meta-analysis. *PLoS One* (2017) **12**(4):e0174809. doi:10.1371/journal.pone.0174809

71. Li XL, Subramanian M, Jones MF, Chaudhary R, Singh DK, Zong X, et al. Long noncoding RNA PURPL suppresses basal p53 levels and promotes tumorigenicity in colorectal cancer. *Cell Rep* (2017) **20**(10):2408–23. doi:10.1016/j.celrep.2017.08.041

72. Cheng Z, Hong J, Tang N, Liu F, Gu S, Feng Z. Long non-coding RNA p53 upregulated regulator of p53 levels (PURPL) promotes the development of gastric cancer. *Bioengineered* (2022) **13**(1):1359–76. doi:10.1080/21655979.2021.2017588

73. Kapoor I, Bodo J, Hill BT, Hsi ED, Almasan A. Targeting BCL-2 in B-cell malignancies and overcoming therapeutic resistance. *Cell Death Dis* (2020) **11**(11):941. doi:10.1038/s41419-020-03144-y

74. Li S, Lin P, Fayad LE, Lennon PA, Miranda RN, Yin CC, et al. B-cell lymphomas with MYC/8q24 rearrangements and IGH@BCL2/t(14;18) (Q32;q21): an aggressive disease with heterogeneous histology, germinal center B-cell immunophenotype and poor outcome. *Mod Pathol* (2012) **25**(1):145–56. doi:10.1038/modpathol.2011.147

75. Masqué-Soler N, Szczepanowski M, Kohler CW, Aukema SM, Nagel I, Richter J, et al. Clinical and pathological features of burkitt lymphoma showing expression of BCL2 - an analysis including gene expression in formalin-fixed paraffin-embedded tissue. *Br J Haematol* (2015) **171**(4):501–8. doi:10.1111/bjh.13624

76. Lin P, Zhou B, Yao H, Guo YP. Effect of carboplatin injection on BCL-2 protein expression and apoptosis induction in raji cells. *Eur J Histochem : EJH* (2020) **64**(3):3134. doi:10.4081/ejh.2020.3134

77. Young RM, Staudt LM. Targeting pathological B cell receptor signalling in lymphoid malignancies. *Nat Rev Drug Discov* (2013) **12**(3):229–43. doi:10.1038/nrd3937

78. Schmitz R, Young RM, Ceribelli M, Jhavar S, Xiao W, Zhang M, et al. Burkitt lymphoma pathogenesis and therapeutic targets from structural and functional genomics. *Nature* (2012) **490**(7418):116–20. doi:10.1038/nature11378

79. Ferreira ACd S, de-Freitas-Junior JCM, Morgado-Díaz JA, Ridley AJ, Klumb CE. Dual inhibition of histone deacetylases and phosphoinositide 3-kinases: effects on burkitt lymphoma cell growth and migration. *J Leukoc Biol* (2016) **99**(4):569–78. doi:10.1189/jlb.2A0415-162R

80. Li C, Xin P, Xiao H, Zheng Y, Huang Y, Zhu X. The dual PI3K/mTOR inhibitor NVP-BEZ235 inhibits proliferation and induces apoptosis of burkitt lymphoma cells. *Cancer Cell Int* (2015) **15**(1):65. doi:10.1186/s12935-015-0213-1

81. Bhatti M, Ippolito T, Mavis C, Gu J, Cairo MS, Lim MS, et al. Pre-clinical activity of targeting the PI3K/Akt/mTOR pathway in burkitt lymphoma. *Oncotarget* (2018) **9**(31):21820–30. doi:10.18632/oncotarget.25072

EBM Experimental Biology and Medicine

TYPE Brief Communication
PUBLISHED 03 December 2025
DOI 10.3389/ebm.2025.10638

OPEN ACCESS

*CORRESPONDENCE
Reinaldo B. Oriá,
oria@ufc.br

RECEIVED 24 April 2025
REVISED 27 September 2025
ACCEPTED 27 October 2025
PUBLISHED 03 December 2025

CITATION
de Azevedo OGR, Shin JH, Freire RS, Ciurleo GCV, Brito GAC, Vitek MP, Guerrant RL, Oriá RB and Warren CA (2025) ApoE COG 133 mimetic peptide improves survival, infection burden, and *Clostridioides difficile* toxin-A-induced intestinal damage in mice.
Exp. Biol. Med. 250:10638.
doi: 10.3389/ebm.2025.10638

ApoE COG 133 mimetic peptide improves survival, infection burden, and *Clostridioides difficile* toxin-A-induced intestinal damage in mice

Orleâncio G. R. de Azevedo[1], Jae H. Shin[2], Rosemayre S. Freire[3], Gabriella C. V. Ciurleo[1], Gerly A. C. Brito[4], Michael P. Vitek[5], Richard L. Guerrant[2], Reinaldo B. Oriá[1]* and Cirle A. Warren[2]

[1]Laboratory of the Biology of Tissue Healing, Ontogeny and Nutrition, Department of Morphology and Institute of Biomedicine, School of Medicine, Federal University of Ceara, Fortaleza, Brazil, [2]Division of Infectious Diseases and International Health, School of Medicine, University of Virginia, Charlottesville, VA, United States, [3]Analytical Core Facility, Federal University of Ceara, Fortaleza, Brazil, [4]Department of Morphology, Faculty of Medicine, Federal University of Ceara, Fortaleza, Brazil, [5]Department of Neurology, Duke University Medical Centre, Durham, NC, United States

Abstract

Apolipoprotein E (ApoE = protein; APOE = gene), a lipid carrier that modulates inflammatory responses, may influence *Clostridioides difficile* (*C. difficile*) infection (CDI) outcomes. We explored the role of the APOE gene using apoE-deficient mice challenged by *C. difficile* toxin A (TcdA)-induced enteritis, and the potential use of the ApoE mimetic peptide in repairing the intestinal damage induced by TcdA. 4-cm ileal loops from C57BL/6 wild-type and APOE knockout (–/–) were ligated and injected with either PBS or TcdA (50 μg). After 4 h of incubation, the intestinal loops were harvested for measurement of length, weight, volume of secretion, and histopathology scores. In mouse ileal loops, TcdA induced a significant increase in weight/ileal loop length in the wild-type mice. When $APOE^{-/-}$ mice were infected with 1×10^4–10^5 CFUs of *C. difficile*, they had higher deaths and diarrhea scores compared to wild-type. $APOE^{-/-}$ mice under the toxin A (TcdA) had worse inflammatory changes in the ileal loop. $APOE^{-/-}$ mice treated with COG133 (3 mg/kg) showed fewer deaths, and lower diarrhea scores, but no change in *C. difficile* shedding. This suggests a potential anti-inflammatory role of COG133 in CDI. More studies are neede to these intial findings in depth.

KEYWORDS

***C. difficile* infection, toxin a, apolipoprotein E mimetic peptide, ApoE knockout, intestinal inflammation**

Impact statement

This short communication brings new data that fills a gap in the scientific literature, showing that apoE deficiency during *C. difficile* infection worsens intestinal inflammation. We have also shown that this is partially rescued by COG 133 treatment, an ApoE mimetic peptide COG 133. It was able to reduce the inflammation pattern in *C. difficile*-infected mice and improve survival rates. The mechanism of action of these effects is underway in our research group labs.

Introduction

Clostridioides difficile is a Gram-positive anaerobic *bacillus* [1], associated with 15–20% of antibiotic-associated diarrhea in the United States [2]. Clinical manifestations range from asymptomatic to severe pseudomembranous colitis and death. There has been an increase in *C. difficile* infection (CDI)-related hospitalizations in the USA over time [3]. In addition, the death rate was higher in hospitalizations due to CDI compared to other diseases [3]. The excess costs for CDI-related inpatient healthcare are estimated at $ 4.8 billion and are likely will rise in the upcoming years [4, 5].

C. difficile pathogenic strains produce two high molecular weight exotoxins: toxin A (TcdA) and toxin B (TcdB), which both induce epithelial cell death and loss of cytoskeletal structure in the cell, contributing to colitis by induction of pro-inflammatory cytokines, disruption of cell-to-cell junctions, increased intestinal permeability, and luminal fluid accumulation [6, 7]. TcdA is a 308-kDa cytotoxin and enterotoxin that induces intestinal epithelial injury, leading to the release of inflammatory mediators [7]. In addition, TcdA has pro-inflammatory and pro-secretory activities [4, 5, 8, 9].

Brayan et al., study the effects of TcdA and TcdB in murine model of intoxication where the subjects had their polymorphonuclears depleted by 100ug of Ly6G/Ly6C and then murine-ligated-ileal loop model [10]. The mice with a regular number of PMN was given TcdA and TcdB showed high levels of IL-1β, IL-6 and TNF-α production. However, the study showed a reduction in cytokine production when TcdA + TcdB were administered together. IL-1β and Il-8 are produced in higher levels, as innate immune inflammatory mediators, in patients with CDI [11]. In general, both toxins induce inflammatory cytokines entering the host cells through endocytosis and then translocating the glucosyltransferase domain and glycosylates proteins such as Rho proteins leading to a disruption of cytoskeleton inducing cell death activating immune cells which synthesizes and release pro-inflammatory cytokines [12]. TcdA is cytotoxic to the intestinal epithelial lining, leading to cytoskeletal protein disruption, loss of epithelial tight junctions, and consequently increased intestinal permeability. Intestinal epithelial barrier damage contributes to a proinflammatory state, activating immune cells to release IL-1β, IL-6, TNF-α, and IL-8, with tissue infiltration of neutrophils and mast cells, initiating a mucosal inflammatory response. TcdA induces COX-2 and PGE2-associated secretory response in the gut by increasing CFTR and calcium-activated chloride channel activity [13].

Apolipoprotein E (ApoE) is a lipid carrier shown to modulate inflammatory and immune responses. ApoE delivers cholesterol to the liver to be metabolized, playing a pivotal role in lipid homeostasis [14]. The ApoE COG133 (133–149) mimetic peptide lacks a lipid-binding role, but it has potent anti-inflammatory properties in models of brain injury and retains the ApoE holoprotein's neuroprotective roles [15, 16]. According to the study of Li et al., the treatment of mice under a murine experimental autoimmune encephalomyelitis with the administration of COG 133 significanlty reduced the activation of macrophages, production of nitric oxide and pro-inflammatory cytokines, and lymphocyte proliferation [14]. Prior studies have shown that ApoE mimetic peptides inhibited the nitric oxide synthase (iNOS), chemokines, and the NF-KB pathway in a colitis murine model of *C. rodentium* [17] and reduced LPS-induced vascular adhesion molecule-1 and monocyte adhesion to endothelial cells [18]. Our group has documented these COG 133 beneficial effects in reducing intestinal inflammation in mice and hastening IEC-6 cell monolayers' restitution following 5-fluorouracil-induced challenge [19].

In this report, we investigate whether ApoE deficiency could worsen CDI outcomes and whether COG 133 could reverse these effects in mice. In this study, we evaluated the effect of TcdA on fluid accumulation and inflammation in the ileal loop mouse model and the effect of infection by *C. difficile* on animal survival, weight loss, and diarrhea in APOE knockout (APOE $^{-/-}$) and wild-type mice. No studies have yet evaluated the effects of ApoE deficiency and the COG 133 following CDI.

Materials and methods

Reagents and materials

The ApoE mimetic peptide (COG133) was provided courtesy of Michael P. Vitek, (Cognosci Inc., Duke University (Durham, NC) [20]. ApoE COG133 mimics residues 133–149 of the receptor-binding component of the apolipoprotein that binds to ApoE receptors. The ApoE COG 133 amino terminus was acetylated, and the carboxyl terminus was blocked with an amide moiety. The ApoE COG 133 was frozen and reconstituted in sterile PBS for administration during experiments.

Intravenous solutions of vancomycin hydrochloride (Hospira, Inc., Lake Forest, IL), colistimethate (Colistin) (X-GEN Pharmaceuticals, Inc., Big Flats, NY), gentamicin sulfate (Hospira), metronidazole (Flagyl) (Baxter Healthcare

Corporation, Deerfield, IL), and cleocin phosphate (clindamycin) (Pfizer New York, NY). *C. difficile* strain VPI10463 was purchased from the American Type Culture Collection (Manassas, VA). Purified Toxin A from *Clostridioides difficile* (strain # 10463; molecular weight 308 kDa) was kindly provided by Dr. David Lyerly (Tech Lab, Blacksburg, VA) [21] and used diluted in PBS (pH≅7.4). Chopped Meat Broth (CM, catalog AS-811) was purchased from Anaerobe Systems (Morgan Hill, CA).

Mouse ileal loops

C57BL/6 wild type (WT) and APOE knockout (APOE $^{-/-}$) underwent midline laparotomy, and one 4 cm-ileal loop per mouse was ligated and injected with either 0.1 mL PBS or TcdA (50 μg) (TechLab, Blacksburg, VA) [21]. The abdomen was surgically closed for incubation. Ileal loop ligation was subsequently performed on WT mice, which were injected with ApoE peptide (3 mg/kg) either intraperitoneally or intraluminally, in addition to TcdA, to determine which administration route would improve the TcdA-induced ileal secretion. After 4 h of incubation, the mice were euthanized, and the ileal loops were harvested for measurement of length, weight, and histopathology, which was measured on a scale of 0–3 based on the presence of inflammatory cells, vascular congestion, architectural destruction, and edema [22].

Infection model

Preparation of inoculum

C. difficile was grown for 20 h in chopped meat broth (37 °C), transferred to a fresh tube of chopped meat broth, and incubated for 5 h to achieve log-phase growth before infection. Bacteria were centrifuged at 10,000 rpm for 2 min, washed three times with BHI, and then reconstituted in BHI medium. Using spectrophotometry, an OD reading of 1.0 was calculated to be equivalent to 5×10^7 CFU *C. difficile*/mL. The final concentration of *C. difficile* (CFU/mL) was validated by hemocytometer reading under light microscopy. Unless the dose was specifically stated, 1×10^4–10^5 of *C. difficile* was given by gavage to each mouse in the infected groups, and BHI medium only was given to mice in the uninfected groups.

The infection model is a modification of the published protocol by Chen et al [23]. This protocol has been approved by the Center for Comparative Medicine at the University of Virginia. Approximately 8-week-old C57BL/6 and APOE $^{-/-}$ mice from Jackson Laboratory (Bar Harbor, ME) were used. APOE $^{-/-}$ mice were generated from the B6.129APOE $^{-/-}$ mice at the N10 backcross and constructed from B6.129APOE$^{-/-}$ mice. Sterilized food and water were given *ad libitum* to all mice. Between 4 and 6 days before infection, mice were given an antibiotic cocktail containing vancomycin (0.0045 mg/g), colistin (0.0042 mg/g), gentamicin (0.0035 mg/g), and metronidazole (0.0215 mg/g) by gavage. One day before infection, clindamycin (32 mg/kg) was injected subcutaneously. This antibiotic cocktail was used to facilitate *C. difficile* toxin effect in mice that underwent antibiotic pre-treatment designed to deplete the resident gut microbiota. This combination targets both Gram-positive/negative bacteria and effectively reduces microbial diversity in the intestinal tract. On the day preceding *C. difficile* challenge, mice were administered a single subcutaneous injection of clindamycin (32 mg/kg), a well-established antibiotic in murine models of antibiotics against *C. difficile* infection, and a critical step known to suppress residual microbial populations further and enhance susceptibility to *C. difficile* toxins.

Infection was performed with *C. difficile* strain VPI 10463 inoculum given by gavage. In the first experiment, mice were divided into 4 groups consisting of control uninfected WT mice, control uninfected APOE KO mice, infected WT mice, and infected APOE$^{-/-}$ mice. The mice were observed for 5 days post-inoculation and euthanized. In the next experiment, the mice were divided into the following groups: control uninfected, control infected, infected treated with vancomycin (50 mg/kg), infected treated with ApoE mimetic peptide-COG 133 (3 mg/kg by ip, given 2 x/day), and infected treated with vancomycin and ApoE peptide. One day post-infection, treated mice were given either vancomycin (50 mg/kg) daily with or without ApoE peptide or ApoE peptide alone for 5 days. The very sick animals were euthanized daily, and all surviving mice were euthanized at day 14.

The ApoE mimetic peptide dose for the ileal loop and the infection model was based on the findings from Pane et al., who evaluated the antimicrobial effect *in vitro* against *S. aureus* ATCC 6538P and a clinical isolate of *P. aeruginosa* strain KK27 [24], who investigated the antimicrobial activity of different ApoE-mimetic peptides. A significant COG 133 antimicrobial activity was seen at a concentration of 3.12 μM (~0.065 mg/kg); However, to improve bioavailability to mice, we decided to use a higher dose. Other study found good results with 2 mg/kg of the ApoE COG 1410 [25].

Animal handling and endpoints

As described in a prior study, experimental animals were weighed and scored. Daily stool specimens were collected at regular intervals [22]. The diarrhea scores were assessed according to the following scale of 0–3: 0—well-formed pellets; 1—stick stools adhering to the microtube wall or color change; 2—pasty stools with or without mucus; and 3—watery stools. This scoring method was described elsewhere [20] with some modifications. Cecal and colonic tissues were harvested from all animals at autopsy. Tissues were fixed overnight with

Bouin's solution and stored in 70% ethanol. Hematoxylin & Eosin (HE) staining of samples was performed by the University of Virginia Research Histology Core. Slides were examined using a Leica DFC425 digital camera equipped microscope with Leica Application Suite Version 3.6.0.488 imaging software (Leica Microsystems Inc., Buffalo Grove, IL 60089). Histopathology was scored based on inflammation, mucosal disruption, mucosal hypertrophy, exudate, and submucosal edema, as we have previously described [26].

DNA extraction and quantification

All stool samples were weighed for sample normalization. Stool DNA was extracted under the modified protocol provided in the QIAamp DNA Stool Mini Kit. Briefly, frozen stool was added to 400 µL of ASL buffer, homogenized by grinding with a wooden stick, vortexed for 15 s before and after heating in a water bath at 82.5 °C for 5 min, centrifuged at 14,000 rpm for 2 min. The remaining steps followed the manufacturer's directions. Extracted stool DNA was stored at −20 °C before PCR testing.

C. difficile DNA was analyzed from extracted stool DNAs with iQ SYBR Green Supermix in a 96-well plate performed at CFX96™ Real-Time PCR Detection System (Bio-Rad). A PCR master mix was prepared with a 23 µL aliquot containing 1 µL each of TcdA forward and reverse primers, 12.5 µL iQ SYBR Green Supermix, and 8.5 µL of H2O purified by the Milli-Q Integral Water Purification System (Millipore Corporation, Billerica, MA). 2 µL of each sample was then added to each well filled with PCR master mix aliquot in a 96-well plate. The PCR parameters were sequentially set for 3 stages: 1× cycle for 5 min at 94.0 °C, 40 × cycle for 30 s each from 94.0 °C to 55.0 °C–72.0 °C, 64 °C × cycle at 62.0 °C for 15 s, and 1× cycle for hold at 25.0 °C. Melt curve data collection and analysis were enabled. Copy numbers of the unknown sample were extrapolated from the standard curve that was generated with the extracted DNA prepared from a known *C. difficile* inoculum. The sequence of the TcdB forward primer was 5′-GGAGAGTCA TCCAACTTATATG-3′, and the reverse primer was 5′-CCA CCAATTTCTTTTAATGCAG-3′.

Statistical analysis

Statistical analyses were conducted using GraphPad Prism Version 5.02 software. When a mouse was either found dead or sacrificed due to severe distress, the last recorded body weight was continuously plotted against the body weights of surviving mice. Differences between groups for the entire experimental period were analyzed by 2-Way ANOVA with Bonferroni *post hoc* testing. Survival curves were analyzed using the Log-rank (Mantel-Cox) or Log-rank test for mortality trend.

Results

ApoE deficiency and ApoE COG 133 peptide modulated histopathology in TcdA-challenged ileal loops

As expected, in wild-type mice, injection of TcdA into the ileal loop caused marked worse intestinal mucosal injury (Figure 1B) and increased weight/length ratio (secretion) (Figure 1E), as compared to wild-type control (Figures 1A,E). These effects were markedly improved by ApoE COG 133 peptide treatment with lower weight/length ratio ($p = 0.003$) (Figures 1C,E), markedly reducing inflammatory cell infiltrates, and preserving villus and crypt architecture. APOE $^{-/-}$ mice that received TcdA intraluminally also showed worse histopathology and increased intestinal weight/length ratio ($p < 0.0001$) (Figure 1D), with marked inflammation, vascular congestion, submucosal edema, and epithelial disruption. However, this beneficial effect was only seen when the peptide was administered intraluminally (Figure 1E).

ApoE deficiency and ApoE COG 133 peptide influenced the outcome of CDI

CDI in APOE$^{-/-}$ mice resulted in an absolute number of more deaths than in wild-type infected mice (Figure 2A). Survival in APOE $^{-/-}$ mice was 57.14% compared to 85.71% in the wild-type infected mice. When treated with COG 133 (3 mg/kg), wild-type and APOE $^{-/-}$ mice showed survival rates of 87.5% and 85.7%, respectively. These findings suggest that ApoE may confer protection against *C. difficile* infection, leading to a decrease in survival in APOE $^{-/-}$ mice, which was reversed when ApoE was replaced with COG 133. However, the addition of COG 133 to wild-type mice did not further improve survival. When the weights were compared, APOE $^{-/-}$ mice did not differ significantly from wild-type mice in weight loss (Figure 2B). When COG 133 was administered in wild-type mice, there were no statistically significant changes in weight changes. When diarrhea scores were compared, APOE $^{-/-}$ infected mice had significantly higher diarrhea scores, while COG 133 administration significantly improved the diarrhea scores of the APOE $^{-/-}$ mice on day 10 ($p = 0.0096$) (Figure 2C).

APOE $^{-/-}$ mice did not have any significant difference from wild-type mice in *C. difficile* shedding as measured by qPCR. The administration of COG 133 did not show a significant difference in the *C. difficile* shedding in wild-type and APOE$^{-/-}$ mice,

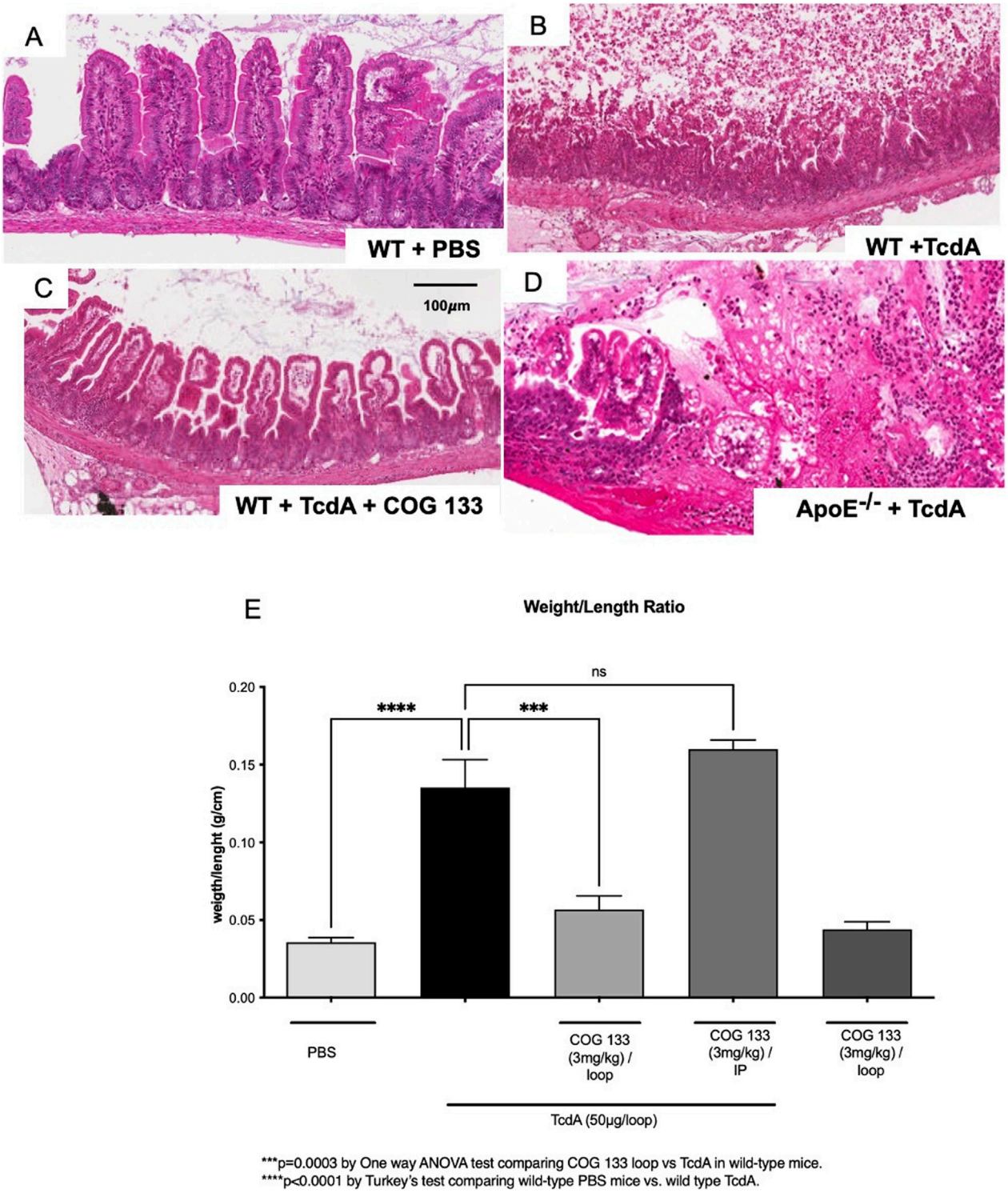

FIGURE 1
Apolipoprotein E (ApoE) deficiency and COG 133 modulate histopathology in TcdA-challenged ileal loops. Representative histopathology of the intestinal injury of ileal loops from experimental mice. Compared to unchallenged controls **(A)**, *C. difficile*-toxin A (TcdA), 50μg/loop, induced severe intestinal mucosal damage with marked features of inflammation and disrupted villi and crypt glands in wild-type **(B)** and APOE knockout (–/–) mice **(D)**. ApoE COG 133 (COG 133) treatment, at 3 mg/kg, partially rescues intestinal injury following TcdA in wild-type mice **(C)**. Hematoxylin-Eosin
(*Continued*)

FIGURE 1 (Continued)
staining. Scale bar: 100 μm. TcdA significantly induced an increase in the ileal loop weight/length ratio (g/cm) in wild-type mice compared with intraperitoneal COG 133 treatment **(E)**. Results are expressed by mean ± SD. N = 7 mice per group.

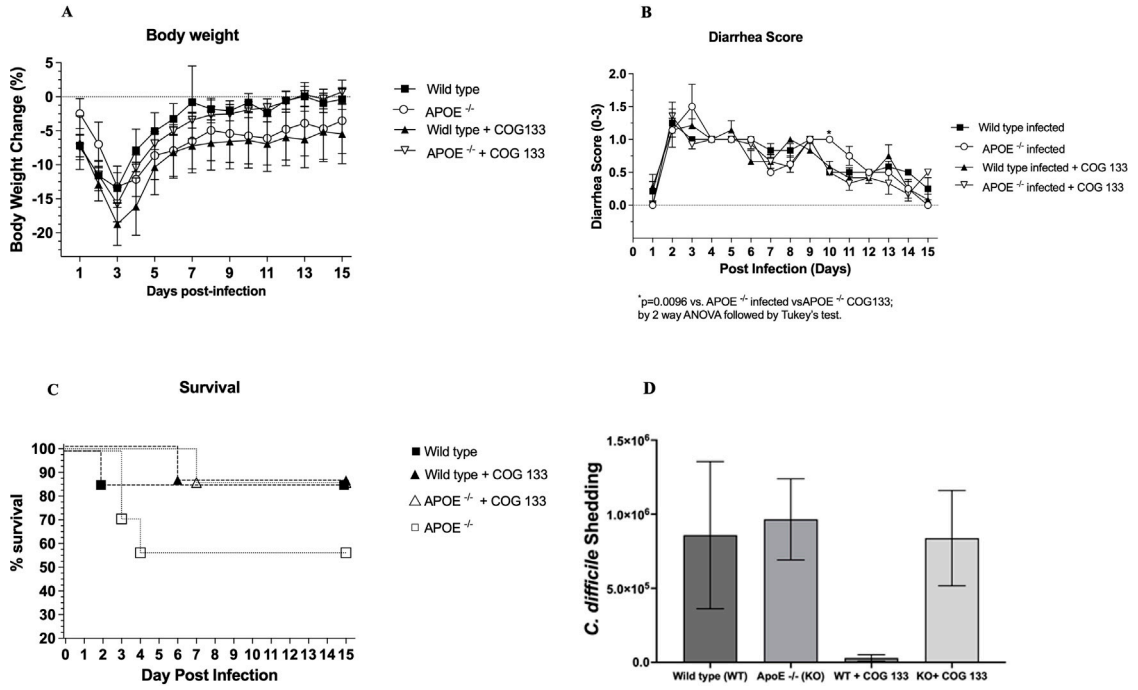

FIGURE 2
The administration of the ApoE mimetic COG133 peptide (3 mg/kg i.p.) did not affect weight loss **(A)**, however, it significantly reduced diarrhea scores ($p = 0.0096$) on day 10 post-infection in APOE knockout (−/−) mice subjected to *C. difficile* infection (CDI) with the VPI10463 strain (10^5 CFU by oral gavage) **(B)**. In addition, infected APOE (−/−) mice exhibited absolute less survival rate (57.14%) compared to infected APOE (−/−) treated with COG 133 (85.71%) **(C)**. The *C. difficile* burden measured through qRT-PCR did not document any significant differences between the experimental groups **(D)**. *C. difficile* shedding was expressed in log of C. diff. DNA shedding.

suggesting that the peptide COG 133 (3 mg/kg) may have inconsistent activity on *C. difficile* growth (Figure 2D).

Discussion

This study suggests that ApoE has a modulatory role in the pathogenesis of CDI. The mouse model demonstrated more severe CDI in $APOE^{-/-}$ compared to WT mice, that were partially improved when ApoE mimetic peptide was given. In the mouse ileal loop model utilizing toxin A (TcdA) injection, ApoE deficiency worsened the inflammation patterns on histology and worsened the edema as measured by the weight/length ratio. However, the intraluminal treatment with COG 133 peptide improved weight/length ratios in animals challenged by TcdA, suggesting that the role of ApoE may be cell or tissue-specific and may be affected by the presence or absence of other inflammatory cells.

The critical role of ApoE in affecting susceptibility to infection was demonstrated using $APOE^{-/-}$ mice in a model of *Mycobacterium smegmatis, Klebsiella pneumoniae,* and *Cryptosporidium parvum* infection [27–29]. In a study evaluating the effect of ApoE against gram-negative bacteria, ApoE exhibited anti-bacterial activity against *P. aeruginosa* and *E. coli in vitro* and an anti-inflammatory activity against *P. aeruginosa and E. coli* infection in a mouse model, mediated by binding LPS and reducing the inflammation in those infected mice [29]. ApoE has been shown to directly regulate the type 1 inflammatory response, with significantly greater proinflammatory cytokines such as TNF-α, IL-6, IL-12, and IFN-γ in $APOE^{-/-}$ mice than in WT mice following LPS challenge [30].

The importance of ApoE was also demonstrated by studies utilizing ApoE mimetic peptides [30]. In a *Citrobacter rodentium* infection mouse model, ApoE mimetic peptide COG

112 demonstrated inhibition of NF-κB pathway, blocking chemokines, nitric oxide, and p53 release [17]. The anti-inflammatory activity of COG 112 in *C. rodentium* colitis reduced the inflammatory pattern in ileal samples of APOE $^{-/-}$ and wild-type infected mice. APOE23, a new combination of two fragments of ApoE 141–148 and ApoE 135–149, demonstrated anti-bacterial activity against *E. coli*, *P. aeruginosa*, *S. aureus*, *Enterococcus faecalis,* and *Acinetobacter baumannii* (MDR). These ApoE peptides also showed anti-inflammatory effects, reducing the levels of expression of TNF-α and IL-6 in THP-1 cells treated with LPS [32].

Another study demonstrated the antimicrobial effect of COG 1410 ApoE mimetic peptide against pan-drug-resistant *A. baumannii.* The mimetic peptide exhibited biofilm inhibition and eradication activity; the peptide induces a lesion in the bacterial membrane. In addition, the COG 1410 controlled the oxidation-reduction processes [33].

ApoE COG 133 has demonstrated protective activity in infection and inflammation models. A study investigating the CM-A (cecropin-A and melittin) that showed antimicrobial activity *in vitro* experiments. The authors demonstrated the biological role of the peptides in inducing breaks in the cell membrane, leading to an efflux of the internal contents [34]. In a murine model of intestinal mucositis induced by 5-FU, the COG 133 led to a significant reduction in levels of IL-1β and TNF-α and a significant reduction in mRNA levels of iNOS, as well as improvement in intestinal repair and integrity of tight junctions in intestinal cell lines [19]. In another model, ApoE COG133 significantly reduced TNF after 1 h and IL-6 serum levels after 1 and 3 h of LPS challenge [35].

Conclusion

This study suggest the potential benefit of ApoE COG 133 in ameliorating the effect of TcdA and CDI, which may have clinical implications either as a stand-alone treatment or as an adjunctive intervention with other gut-trophic protective nutrients. Future studies to examine the interplay of these molecules in cell viability mechanism are needed.

Author contributions

OA: Formal analysis, Methodology, Visualization, Writing – original draft, Writing – review and editing. JS: Formal analysis, Methodology, Visualization, Writing – original draft, Writing – review and editing. RF: Data curation, Formal analysis, Investigation, Methodology, Software, Validation, Visualization, Writing – original draft. GC: Formal analysis, Visualization, Writing – original draft, Writing – review and editing. GB: Conceptualization, Funding acquisition, Investigation, Methodology, Project administration, Resources, Supervision, Writing – original draft, Writing – review and editing. MV: Conceptualization, Data curation, Funding acquisition, Investigation, Methodology, Project administration, Resources, Supervision, Validation, Writing – original draft, Writing – review and editing. RG: Conceptualization, Data curation, Formal analysis, Funding acquisition, Investigation, Methodology, Project administration, Resources, Software, Supervision, Validation, Visualization, Writing – original draft, Writing – review and editing. RO: Conceptualization, Data curation, Formal analysis, Funding acquisition, Investigation, Methodology, Project administration, Resources, Supervision, Writing – original draft, Writing – review and editing. CW: Conceptualization, Data curation, Formal analysis, Funding acquisition, Investigation, Methodology, Project administration, Resources, Software, Supervision, Validation, Visualization, Writing – original draft, Writing – review and editing. All authors contributed to the article and approved the submitted version.

Data availability

The raw data supporting the conclusions of this article will be made available by the authors, without undue reservation.

Ethics statement

The animal study was approved by Center for Comparative Medicine at the University of Virginia. The study was conducted in accordance with the local legislation and institutional requirements.

Funding

The author(s) declare that financial support was received for the research and/or publication of this article. This research was funded by Projeto Universal, grant number 402738/2021-7 Research call CNPq/MCTI/FNDCT No. 18/2021.

Acknowledgements

The authors would like to acknowledge the support from the Brazilian funding agencies Fundação Cearense de Apoio ao Desenvolvimento Científico e Tecnológico (FUNCAP) and Coordenação de Aperfeiçoamento de Pessoal de Nível Superior (CAPES) Brazilian funding agencies for their financial support.

Conflict of interest

Vitek M.P. is currently a principal in Cognosci Inc., which has ownership rights to selected ApoE-mimetic peptides.

The remaining authors declare that the research was conducted in the absence of any commercial or financial relationships that could be construed as a potential conflict of interest.

Generative AI statement

The author(s) declare that no Generative AI was used in the creation of this manuscript.

Any alternative text (alt text) provided alongside figures in this article has been generated by Frontiers with the support of artificial intelligence and reasonable efforts have been made to ensure accuracy, including review by the authors wherever possible. If you identify any issues, please contact us.

References

1. Voth DE, Ballard JD. *Clostridium difficile* toxins: mechanism of action and role in disease. *Clin Microbiol Rev* (2005) **18**:247–63. doi:10.1128/CMR.18.2.247-263.2005

2. Bartlett JG, Gerding DN. Clinical recognition and diagnosis of *Clostridium difficile* infection. *Clin Infect Dis* (2008) **46**:S12–S18. doi:10.1086/521863

3. Solanki D, Kichloo A, El-Amir Z, Dahiya DS, Singh J, Wani F, et al. *Clostridium difficile* infection hospitalizations in the United States: insights from the 2017 national inpatient sample. *Gastroenterol Res* (2021) **14**:87–95. doi:10.14740/gr1371

4. Hippenstiel S, Schmeck B, N'Guessan PD, Seybold J, Krüll M, Preissner K, et al. Rho protein inactivation induced apoptosis of cultured human endothelial cells. *Am J Physiology-Lung Cell Mol Physiol* (2002) **283**:L830–L838. doi:10.1152/ajplung.00467.2001

5. Alcantara C, Stenson WF, Steiner TS, Guerrant RL. Role of inducible cyclooxygenase and prostaglandins in *Clostridium difficile* toxin A–Induced secretion and inflammation in an animal model. *J Infect Dis* (2001) **184**:648–52. doi:10.1086/322799

6. Pruitt RN, Lacy DB. Toward a structural understanding of *Clostridium difficile* toxins A and B. *Front Cell Infect Microbiol* (2012) **2**:28. doi:10.3389/fcimb.2012.00028

7. Chandrasekaran R, Lacy DB. The role of toxins in *Clostridium difficile* infection. *FEMS Microbiol Rev* (2017) **41**:723–50. doi:10.1093/femsre/fux048

8. Brito G., Fujji J, Carneiro-Filho BA, Lima A., Obrig T, Guerrant RL. Mechanism of *Clostridium difficile* toxin A–Induced apoptosis in T84 cells. *J Infect Dis* (2002) **186**:1438–47. doi:10.1086/344729

9. Bobo LD, El Feghaly RE, Chen Y-S, Dubberke ER, Han Z, Baker AH, et al. MAPK-activated Protein kinase 2 contributes to clostridium difficile-Associated inflammation. *Infect Immun* (2013) **81**:713–22. doi:10.1128/IAI.00186-12

10. Brayan MT, Alejandro AA, Quesada-Gómez C, Chaves-Olarte E, Elías BC. Polymorphonuclear neutrophil depletion in ileal tissues reduces the immunopathology induced by Clostridioides difficile toxins. *Anaerobe* (2025) **92**:102947. doi:10.1016/j.anaerobe.2025.102947

11. Steiner TS, Flores CA, Pizarro TT, Guerrant RL. Fecal lactoferrin, interleukin-1beta, and interleukin-8 are elevated in patients with severe *Clostridium difficile* colitis. *Clin Diagn Lab Immunol* (1997) **4**:719–22. doi:10.1128/cdli.4.6.719-722.1997

12. Yu H, Chen K, Sun Y, Carter M, Garey KW, Savidge TC, et al. Cytokines are markers of the clostridium difficile-induced inflammatory response and predict disease severity. *Clin Vaccin Immunol : CVI* (2017) **24**:e00037-17. doi:10.1128/CVI.00037-17

13. Kim H, Rhee SH, Kokkotou E, Na X, Savidge T, Moyer MP, et al. *Clostridium difficile* toxin A regulates inducible Cyclooxygenase-2 and prostaglandin E2 synthesis in colonocytes *via* reactive oxygen species and activation of p38 MAPK. *J Biol Chem* (2005) **280**:21237–45. doi:10.1074/jbc.M413842200

14. Rebeck GW. The role of APOE on lipid homeostasis and inflammation in normal brains. *J Lipid Res* (2017) **58**:1493–9. doi:10.1194/jlr.R075408

15. Li F-Q, Sempowski GD, McKenna SE, Laskowitz DT, Colton CA, Vitek MP. Apolipoprotein E-Derived peptides ameliorate clinical disability and inflammatory infiltrates into the spinal cord in a murine model of multiple sclerosis. *The J Pharmacol Exp Ther* (2006) **318**:956–65. doi:10.1124/jpet.106.103671

16. Wang H, Durham L, Dawson H, Song P, Warner DS, Sullivan PM, et al. An apolipoprotein E-based therapeutic improves outcome and reduces Alzheimer's disease pathology following closed head injury: evidence of pharmacogenomic interaction. *Neuroscience* (2007) **144**:1324–33. doi:10.1016/j.neuroscience.2006.11.017

17. Singh K, Chaturvedi R, Asim M, Barry DP, Lewis ND, Vitek MP, et al. The apolipoprotein E-mimetic peptide COG112 inhibits the inflammatory response to Citrobacter rodentium in colonic epithelial cells by preventing NF-κB activation. *J Biol Chem* (2008) **283**:16752–61. doi:10.1074/jbc.M710530200

18. Datta G, White CR, Dashti N, Chaddha M, Palgunachari MN, Gupta H, et al. Anti-inflammatory and recycling properties of an apolipoprotein mimetic peptide, Ac-hE18A-NH2. *Atherosclerosis* (2010) **208**:134–41. doi:10.1016/j.atherosclerosis.2009.07.019

19. Azevedo OGR, Oliveira RAC, Oliveira BC, Zaja-Milatovic S, Araújo CV, Wong DVT, et al. Apolipoprotein E COG 133 mimetic peptide improves 5-fluorouracil-induced intestinal mucositis. *BMC Gastroenterol* (2012) **12**:35. doi:10.1186/1471-230X-12-35

20. Warren CA, van Opstal EJ, Riggins MS, Li Y, Moore JH, Kolling GL, et al. Vancomycin treatment's association with delayed intestinal tissue injury, clostridial overgrowth, and recurrence of *Clostridium difficile* infection in mice. *Antimicrob Agents Chemother* (2013) **57**:689–96. doi:10.1128/AAC.00877-12

21. Li Y, Figler RA, Kolling G, Bracken TC, Rieger J, Stevenson RW, et al. Adenosine A2A receptor activation reduces recurrence and mortality from clostridium difficileinfection in mice following vancomycin treatment. *BMC Infect Dis* (2012) **12**:342. doi:10.1186/1471-2334-12-342

22. Buffie CG, Jarchum I, Equinda M, Lipuma L, Gobourne A, Viale A, et al. Profound alterations of intestinal microbiota following a single dose of clindamycin results in sustained susceptibility to clostridium difficile-Induced colitis. *Infect Immun* (2012) **80**:62–73. doi:10.1128/IAI.05496-11

23. Chen X, Katchar K, Goldsmith JD, Nanthakumar N, Cheknis A, Gerding DN, et al. A mouse model of clostridium difficile–Associated disease. *Gastroenterology* (2008) **135**:1984–92. doi:10.1053/j.gastro.2008.09.002

24. Pane K, Sgambati V, Zanfardino A, Smaldone G, Cafaro V, Angrisano T, et al. A new cryptic cationic antimicrobial peptide from human apolipoprotein E with antibacterial activity and immunomodulatory effects on human cells. *The FEBS J* (2016) **283**:2115–31. doi:10.1111/febs.13725

25. Laskowitz DT, Lei B, Dawson HN, Wang H, Bellows ST, Christensen DJ, et al. The apoE-mimetic peptide, COG1410, improves functional recovery in a murine model of intracerebral hemorrhage. *Neurocrit Care* (2012) **16**:316–26. doi:10.1007/s12028-011-9641-5

26. Pawlowski S., Calabrese G, Kolling G., Freire R, AlcantaraWarren C, Liu B, et al. Murine model of *Clostridium difficile* infection with aged gnotobiotic C57BL/6 mice and a BI/NAP1 strain. *J Infect Dis* (2010) **202**:1708–12. doi:10.1086/657086

27. Zhao Y-Y, Wang C, Wang W-X, Han L-M, Zhang C, Yu J-Y, et al. ApoE mimetic peptide COG1410 exhibits strong additive interaction with antibiotics against Mycobacterium smegmatis. *Infect Drug Resist* (2023) **16**:1801–12. doi:10.2147/IDR.S403232

28. Azevedo OGR, Bolick DT, Roche JK, Pinkerton RF, Lima AAM, Vitek MP, et al. Apolipoprotein E plays a key role against cryptosporidial infection in transgenic undernourished mice. *PLoS One* (2014) **9**:e89562. doi:10.1371/journal.pone.0089562

29. Puthia M, Marzinek JK, Petruk G, Ertürk Bergdahl G, Bond PJ, Petrlova J. Antibacterial and anti-inflammatory effects of apolipoprotein E. *Biomedicines* (2022) **10**:1430. doi:10.3390/biomedicines10061430

30. Ali K, Middleton M, Puré E, Rader DJ. Apolipoprotein E suppresses the type I inflammatory response *in vivo*. *Circ Res* (2005) **97**:922–7. doi:10.1161/01.RES.0000187467.67684.43

31. Oriá RB, Freitas RS, Roque CR, Nascimento JCR, Silva AP, Malva JO, et al. ApoE mimetic peptides to improve the vicious cycle of malnutrition and enteric infections by targeting the intestinal and blood-brain barriers. *Pharmaceutics* (2023) **15**:1086. doi:10.3390/pharmaceutics15041086

32. Wang C, Yang C, Yang Y, Pan F, He L, Wang A. An apolipoprotein E mimetic peptide with activities against multidrug-resistant bacteria and immunomodulatory effects. *J Pept Sci* (2013) **19**:745–50. doi:10.1002/psc.2570

33. Wang B, Zhang F-W, Wang W-X, Zhao Y-Y, Sun S-Y, Yu J-H, et al. Apolipoprotein E mimetic peptide COG1410 combats pandrug-resistant Acinetobacter baumannii. *Front Microbiol* (2022) **13**:934765. doi:10.3389/fmicb.2022.934765

34. Arthithanyaroj S, Chankhamhaengdecha S, Chaisri U, Aunpad R, Aroonnual A. Effective inhibition of Clostridioides difficile by the novel peptide CM-A. *PLoS One* (2021) **16**:e0257431. doi:10.1371/journal.pone.0257431

35. Lynch JR, Tang W, Wang H, Vitek MP, Bennett ER, Sullivan PM, et al. APOE genotype and an ApoE-mimetic peptide modify the systemic and central nervous system inflammatory response. *J Biol Chem* (2003) **278**:48529–33. doi:10.1074/jbc.M306923200

EBM Experimental Biology and Medicine

TYPE Original Research
PUBLISHED 30 September 2025
DOI 10.3389/ebm.2025.10782

OPEN ACCESS

*CORRESPONDENCE
Simone Nunes de Carvalho,
simone.nunes.carvalho@uerj.br

RECEIVED 04 August 2025
ACCEPTED 15 September 2025
PUBLISHED 30 September 2025

CITATION
Martins ACRN, Silva KR, Pereira ACdS, Paris GC, Nascimento ALR, Aiceles V, Cortez EAC, Thole AA and de Carvalho SN (2025) Therapeutic effects of mesenchymal stromal cell secretome in liver fibrosis with acute lung injury.
Exp. Biol. Med. 250:10782.
doi: 10.3389/ebm.2025.10782

Therapeutic effects of mesenchymal stromal cell secretome in liver fibrosis with acute lung injury

Ane Caroline Ribeiro Novaes Martins[1,2], Karina Ribeiro Silva[1], Anna Carolina de Souza Pereira[1], Gustavo Claudino Paris[1,2], Ana Lúcia Rosa Nascimento[3], Verônica Aiceles[3], Erika Afonso Costa Cortez[1], Alessandra Alves Thole[1] and Simone Nunes de Carvalho[1]*

[1]Stem Cell Research Laboratory, Histology and Embryology Department, Rio de Janeiro State University (UERJ), Rio de Janeiro, Brazil, [2]Post-Graduation Program in Clinical and Experimental Pathophysiology (FISCLINEX), Rio de Janeiro State University (UERJ), Rio de Janeiro, Brazil, [3]Ultrastructure and Tissue Biology Laboratory, Histology and Embryology Department, Rio de Janeiro State University (UERJ), Rio de Janeiro, Brazil

Abstract

Chronic liver disease (CLD) is a widespread condition and liver fibrosis is a common hallmark. The COVID-19 pandemic has drawn awareness over emerging pathogens that pose severe risks for chronic disease patients, whose management is complicated because most drugs can overload liver metabolism, therefore therapeutic alternatives are needed. Aims: based on the difficulty of treating CLD patients during respiratory infections, this study focused on the therapeutic evaluation of adipose-derived mesenchymal stromal cell (ASC) secretome. Methods: the effects of ASC secretome were evaluated in a preclinical murine model of liver fibrosis induced by thioacetamide (TAA) and acute lung injury induced by lipopolysaccharide, using histological and cytokine profile analyses. ASC secretome exhibited therapeutic effects alleviating fibrogenesis and inflammation, decreasing plasmatic inflammatory markers (cytokines IL-6, IL-17A and TNF-α), and restoring immune homeostasis. The secretome reduced liver collagen accumulation and IL-6 levels and restored lung cytoarchitecture, decreasing levels of CD68 and TNF-α. These results provide a preclinical basis for potential clinical use of the ASC secretome and its products, advancing the concept of cell-free, systemically active interventions for complex tissue injuries, and reinforcing the potential of its paracrine factors to modify pathological responses and promote tissue regeneration in combined chronic-acute diseases.

KEYWORDS

liver fibrosis, acute lung injury, mesenchymal stromal cells, secretome, regenerative therapy

Impact statement

This study demonstrates the therapeutic efficacy of murine adipose-derived mesenchymal stromal cell (ASC) secretome in a dual-injury preclinical model combining liver fibrosis and acute lung injury. By showing histological and inflammatory improvements in both organs after systemic administration of minimally processed, cell-free preparation in a murine model, this work suggests the translational value of ASC-derived secretome in complex conditions offering a scalable strategy for regenerative interventions in translational pipelines, especially for real-world health systems seeking affordable, cell-free alternatives for chronic and acute inflammatory conditions. The findings contribute to new *in vivo* data confirming the systemic reach and multi-organ impact of stromal cell-derived soluble factors in comorbid diseases, providing a relevant foundation for future translational studies.

Introduction

Chronic liver disease (CLD) prevalence has been increasing in the later years, in a widespread pattern driven by metabolic diseases associated with industrialized food intake, as well as the consumption of pharmaceutical and recreational drugs and infection by hepatitis viruses [1]. The COVID-19 pandemic impacted mainly patients suffering with chronic diseases such as liver fibrosis or its more severe condition, cirrhosis, associated or not with the metabolic changes related to non-alcoholic fatty liver disease (NAFLD) and nonalcoholic steatohepatitis (NASH) [2–4]. This group had higher morbidity and mortality rates during the COVID-19 pandemic, in a predictable scenario, since acute lung infections by different pathogens of bacterial, fungal, or viral origins are one of the main causes of death in chronic patients [4–8]. Alternatively, respiratory infections may cause liver damage as a direct impact of the pathogenic agent and/or as a secondary effect of acute lung injury (ALI), as observed for the COVID-19 pathogen, the severe acute respiratory syndrome coronavirus 2 (SARS-CoV-2) [9–11]. This demonstrates that ALI is a major concern for chronic liver disease patients, and the clinical management of these patients when both diseases happen to coexist is complicated, because many medications such as antibiotics and anti-inflammatory drugs directly affect the impaired liver. Other situations like post-transplanted patients, the occurrence of ascites and paracentesis procedures also pose greater risk of nosocomial respiratory infections that are a major mortality factor in this group [12–17].

Mesenchymal stromal cells (MSCs) are found in diverse tissues, where they differentiate from mesenchymal stem cells. MSCs stand out for their therapeutic properties, including their ability to differentiate into distinct cell types, undergo targeted migration in response to injuries, modulate the immune system, and release tissue repair factors in a paracrine way via their well-known secretome [18–20]. They were originally characterized in bone marrow and can be found in various adult tissues especially in perivascular niches, with adipose tissue emerging as a prominent source due to its availability and minimally invasive collection capabilities. Adipose Stromal/Stem Cells (ASC) are a heterogenic cell population that comprehends mesenchymal stem cells and their progeny, isolated after enzymatic digestion of the unilocular (or white) adipose tissue obtained, for instance, from lipoaspirates [21].

Therapy using MSC secretome has shown benefits in treating conditions such as hepatic fibrosis [22–26] and ALI [27–31], but there is no data regarding the effectiveness of this approach in the combined diseases, which is increasingly a likely scenario. Therefore, our study aimed to investigate the potential therapeutic effects of ASC secretome in a murine model of concomitant hepatic fibrosis and ALI, exploring its impacts in histological features and cytokine profile in both systemic (plasma) and local (lung and liver) analyses.

Materials and methods

All animal experiments were conducted in compliance with international standards for the care and use of laboratory animals, following the ARRIVE guidelines and equivalent international recommendations, under approval of the institutional Ethics Committee (protocol IBRAG 031/2023).

Isolation of ASCs from mouse adipose tissue

ASC were obtained from the inguinal adipose tissue of healthy male C57BL/6 mice (n = 4), 8 weeks old, which were euthanized according to the protocol approved by the Ethics Committee. Inguinal subcutaneous adipose tissue was collected and kept in a solution containing antimicrobials penicillin 500IU/mL, streptomycin 0.5 mg/mL, gentamicin 0.25 mg/mL and amphotericin B 0.012 mg/mL in DMEM (Dulbecco's Modified Eagle Medium, Sigma-Aldrich) high-glucose at 4 °C for 2 h, and then dissociated with 0.2% type II collagenase solution (Sigma-Aldrich) in DMEM for 15 min at 4 °C followed by agitation for 45 min at 37 °C in an orbital shaker. Then DMEM with 10% Fetal Bovine Serum (FBS) (Gibco) was added to stop enzymatic dissociation. The suspension was filtered in a 100 μm cell strainer (BD Biosciences) and centrifuged at 300 *g* for 5 min. The cell pellet was resuspended in DMEM-F12 with 15% FBS and antimicrobials.

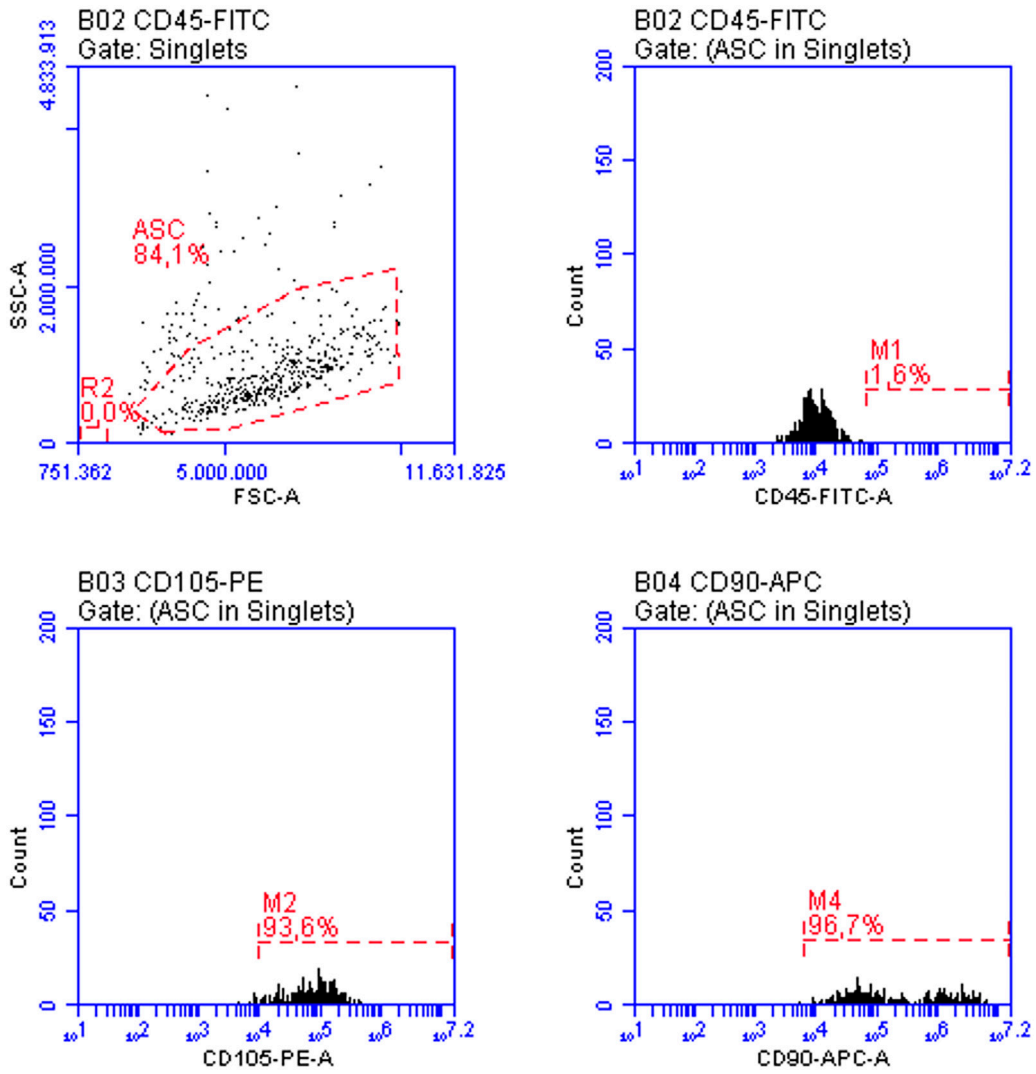

FIGURE 1
ASC characterization by flow cytometry in the third passage: more than 90% of the cells expressed varying levels of CD105 and higher levels of CD90, while CD45 expression was absent in more than 98% of the cells. These features align with the expected phenotype for these cultures.

The cells were plated in 25 cm^2 culture flasks at the rate of 1 bottle per animal used for cell isolation and maintained at 37 °C in a humidified atmosphere with 5% CO_2. After 48 h, non-adherent cells were removed by washing the cultures with buffered saline solution (PBS, phosphate buffer saline, pH 7.4) and adherent cells were maintained in complete culture medium. When the cells reached 70%–80% confluence, the passage or replating procedure was performed using Trypsin (Gibco), incubated for 5 min at 37 °C. After 7 days cells were counted by exclusion of trypan blue dye (0.4% in PBS) in a Neubauer chamber and replated in complete medium until growth and new confluence. The procedure was repeated until the third passage, when they were plated to obtain the secretome.

ASCs in the third passage were characterized using anti-mouse CD45-FITC, CD90-APC and CD105-PE primary antibodies (BD Biosciences) and analyzed in an Accuri C6 flow cytometer. To isolate the secretome, ASCs were plated in 24-well plates, at a concentration of 7.5×10^4 cells per well, in DMEM-F12 containing 15% FBS. The following day, cultures were maintained with 0.6 mL/well of DMEM-F12 without serum, to condition the supernatant with the ASC secretome. The supernatant was filtered through a 0.22 μm filter, aliquoted and stored at −80 °C for further analysis. Cell numbers at plating were adjusted to total medium volume proportions in order to maintain the same concentrations in secretome samples used in the study.

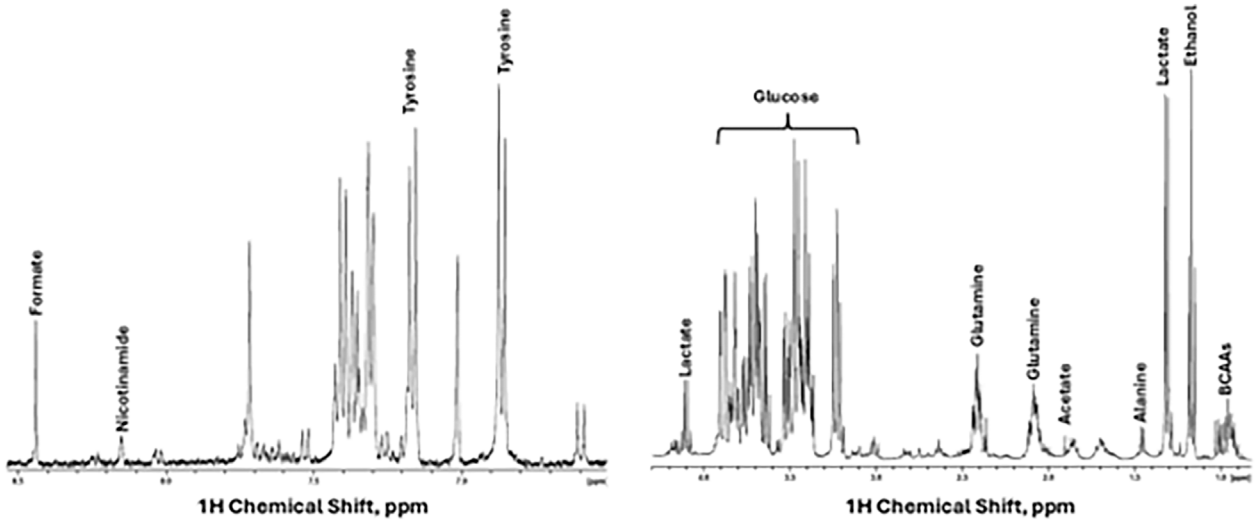

FIGURE 2
Secretome characterization. ^{1}H NMR spectra display some metabolites assigned in the secretome, in the spectra aliphatic (right) and aromatic region (left).

ASC secretome characterization with NMR-based metabolomics

Nuclear Magnetic Resonance (NMR)-based metabolomics were done by Metabogen Diagnostico® protocol.[1] Several metabolites could be assigned, as shown in Figure 2. In addition, by 2D NMR spectra we could assign 4-Hydroxybenyl alcohol, 4-hydroxyphenylacetonitrile, agmatine, alanine, cadaverine, D-glucose, D-glucuronate, D-xylose, ethanol, glycine, homoarginine, l-arginine, l-canavanine, l-glutamine, l-isoleucine, l-tyrosine, l-valine, lactic acid, leucine, malonic acid, maltose, pyruvic acid, rhamnose.

Experimental groups and induction of liver fibrosis and acute lung injury

In this work, 8-week-old male C57BL/6 mice were distributed into 3 experimental groups with n = 8 each. Except for the control group, all animals underwent peritoneal injection of thioacetamide (TAA) (Sigma-Aldrich) and nasal instillations of a single dose of lipopolysaccharide (LPS) to establish a model of concomitant chronic liver disease and ALI. To induce liver fibrosis, TAA (Sigma-Aldrich) was diluted in 0.6% sterile PBS and applied at a concentration of 100 mg/kg intraperitoneally, 3 times a week, for 6 weeks, in male C57BL mice, at 8 weeks of age [32]. The animals were transferred to cages with food and water *ad libitum* and monitored throughout the procedure. Histological analysis with Picrosirius (Sirius Red) confirmed that liver fibrosis was established after 6 weeks of TAA administration. For the induction of ALI, mice at the end of the sixth week of liver fibrosis induction (42nd day) received a single nasal instillation containing 30 µL of LPS solution in warm sterile PBS (LPS at 10 mg/mL, obtained from *Escherichia coli* O111:B4, 076K4020, Sigma-Aldrich) [33].

After 6 weeks of treatment with TAA followed by the administration of an intranasal dose of LPS, the secretome obtained from ASCs was administered in 2 doses of 0.4 mL each in the peritoneal region of the animals. Therefore, the groups of animals that made up this study were: (a) control group (CTRL), healthy animals that were not subjected to the procedures; (b) Liver fibrosis and ALI group (TAA+LPS), animals that received TAA for 6 weeks, 3 times a week, and intranasal LPS at the beginning of the sixth week (42nd day), being euthanized at the end of the seventh week (49 days); and (c) Liver fibrosis and ALI treated with ASCs secretome (namely ASC group), animals that received TAA for 6 weeks, 3 times a week, and intranasal LPS at the end of the sixth week (42nd day). After 48h, they received the first dose of 0.4 mL of ASC secretome (44th day) and the same dose on the 46th day, being euthanized on the 49th day.

On the day of euthanasia, blood samples were collected by cardiac puncture in syringes containing sodium heparin (anticoagulant, Cristalia), and transferred to an Eppendorf tube. Then, the blood was centrifuged at 2.000 rpm for

1 http://www.metabogen.com.br

10 min at room temperature to obtain plasma. The resulting plasma was then collected and stored at −80 °C for further analysis. Liver and lung samples were harvested, fixed with 4% buffered formaldehyde, dehydrated in ethanol, clarified in xylol and embedded in paraffin for histological analysis.

Cytokine profile analysis of the ASCs secretome, plasma, liver and lung

The presence and quantity of the cytokines IL-10, IL-17A, TNF-α, IFN-γ, IL-6, IL-2 and IL-4 were evaluated in the ASCs secretome and in plasma, livers and lungs from experimental groups using the CBA (Cytometric Bead Array) Mouse Th1/Th2/Th17 Kit (Catalog number 560485, BD Biosciences), according to the protocol recommended by the manufacturer. Liver and lung lysates protein contents were previously measured with BCA (bicinchoninic acid) protocol (Pierce, Thermo Scientific) for normalization. Samples were acquired on a flow cytometer (BD C6 Accuri) and analyzed using FCAP Array 3.0 software (BD Biosciences).

Liver analysis

The levels of liver enzyme Aspartate Aminotransferase (AST) (also called TGO, for glutamic-oxaloacetic transaminase) were measured in plasma using commercial kits following the manufacturer's protocol (Bioclin, Brazil), with absorbance reading performed on a spectrophotometer (INNO).

To quantify collagen accumulation as a measure of liver fibrosis, livers underwent routine histological processing for paraffin inclusion, and 5 μm thick deparaffinized sections were stained with Sirius Red (0.1% Direct Red 80 solution, Sigma-Aldrich) for 1 h, placed in a 0.1 N HCl solution for 1 min and washed with distilled water. Next, the sections were counterstained with hematoxylin for 1 min and dehydrated with increasing concentrations of alcohol, then clarified and mounted with Entellan (Merck). To quantify collagen, images of 5 fields of 3 non-serial sections per animal were obtained, totaling 15 fields per animal. The images were captured using a light microscope with a ×40 objective (Olympus BX53). Quantification of deposited collagen was performed using the segmentation tool, selecting the red-stained areas per field, and expressed in pixels per μm^2, using Image Pro Plus 7.0 software.

Lung analysis

Lung samples underwent routine histological processing for inclusion in paraffin and 5 μm thick sections were stained with Hematoxylin and Eosin, dehydrated with increasing concentrations of alcohol, clarified and mounted with Entellan (Merck). Lungs were evaluated under an Olympus BX53 light microscope, and quantification was performed to analyze alveolar and interstitial neutrophils and septal thickness, using a 0-4 scoring system designed to quantify the extent of lung injury histologically, based on 10 random high-power fields (magnification of 400), considering neutrophils in the alveolar space, neutrophils in the interstitial space and septal thickening, as previously described [33]. To assess lung inflammation, immunohistochemistry for CD68 and TNF-α was performed. Deparaffinized sections were immersed in hydrogen peroxide (%) for 20 min, washed in Phosphate Buffered Saline (PBS) and immersed in citrate buffer, pH 6.0 at 60 °C for 20 min. Sections were then incubated with 2.5% blocking solution (Vectastain Universal quick kit-Vector laboratories) for 20 min. Subsequently, the sections were incubated with primary antibodies anti-CD68 (Cell Signaling, E307v) and TNF-α (Santa Cruz Biotechnologies, sc-52746), diluted in PBS/BSA 1% overnight, followed by incubation with biotinylated secondary antibody, streptavidin-peroxidase and finally revealed with DAB (3,3′-diaminobenzidine tetrahydrochloride), under observation in a light microscope. Cell nuclei were stained with hematoxylin, and slides were dehydrated, clarified and mounted with Entellan (Merck). Finally, images were captured using the Olympus BX53 light microscope. To quantify CD68 and TNF-α staining, images of 10 fields of 2 non-serial sections per animal were obtained. The images were captured using a light microscope with a ×40 objective (Olympus BX53). Quantification was performed using the segmentation tool, selecting the brown-stained areas per field and expressed in pixels per μm^2, using Image Pro Plus 7.0 software.

Statistical analysis

Statistical data were presented in the results plotted as boxes with medians and whiskers from the minimum to the lower quartile, and from the upper quartile to the maximum, along with mean ± standard deviation of the mean (SD) of 8 animals per experimental group. The data were statistically analyzed using a one-way ANOVA (analysis of variance) test, followed by the chosen post-test. The Shapiro-Wilk test of normality was performed for all data as well as possible outliers, excluded using the ROUT test (Q = 1%). The tests and post-tests were selected according to the result obtained in the normality test regarding the nature of data distribution. Individual data points are shown for all animals. Statistical analysis was performed using the GraphPad Prism 8 software. The value of $p < 0.05$ was used to consider that the differences between groups were statistically significant.

TABLE 1 Analysis of cytokines in the ASC secretome using CBA kit.

Cytokines	IL-10	IL-17A	TNF-α	IFN-γ	IL-6	IL-4	IL-2
pg/mL	2.58	4.19	0.92	2.86	30.62	3.86	3.72

Interleukins 10, 17A, 6, 4 and 2, TNF-α and IFN-γ were present at varying concentrations.

Results

ASC phenotyping

The isolated cells were characterized in the 3rd passage by flow cytometry, according to the phenotypic criteria established for murine adipose-derived mesenchymal stem cells (mASCs). Following stringent exclusion of debris and subcellular events based on scatter parameters (FSC-A vs. SSC-A) and selection of singlets (FSC-A vs. FSC-H), a morphologically homogeneous population comprising 84.1% of events was identified (Figure 1). This population was predominantly negative for the hematopoietic marker CD45 (1.6%) and exhibited high expression of the mesenchymal markers CD105 (93.6%) and CD90 (96.7%), consistent with the expected mASC phenotype. These data confirm the mesenchymal identity of the isolated cells and validate the phenotypic purity of the culture for downstream applications.

Analysis of the ASC secretome

Based on the cytokine analysis by CBA, the results indicate that ASC secretome presents varying concentrations of each analyzed cytokine, and IL-6 showed the higher concentrations, while TNF-α had the lowest levels (Table 1). The metabolomic profiling of the ASC secretome after 48 h of culture in serum-free conditions revealed a complex array of bioactive metabolites (Figure 2). Analysis by NMR spectroscopy identified key components of glycolytic metabolism, including lactic acid and pyruvic acid, consistent with the well-described preference of ASC for aerobic glycolysis. Additionally, the presence of D-glucose, maltose, rhamnose, and D-xylose suggests both residual sugar content and potential metabolic interconversions in the extracellular milieu. A broad spectrum of amino acids—such as alanine, glycine, valine, isoleucine, leucine, tyrosine, arginine, and glutamine—was detected, reflecting active protein turnover and paracrine signaling capacity. The identification of metabolites such as homoarginine, agmatine, and L-canavanine further supports the well-known role for these cells in immunomodulation. Together, these findings indicate that even under serum deprivation, ASCs sustain a metabolically active and secretory phenotype, capable of releasing a diverse set of signaling molecules relevant to tissue repair and immunoregulation.

Liver analysis

The Picrosirius (Sirius Red) staining technique was used to evaluate fibrosis extension. The presence of collagen fiber deposits was found in a basal quantity in the livers of the control group (Figure 3a). However, the TAA+LPS group showed the presence of fibrous septa and excessive collagen deposition compared to the control group, indicating the establishment of liver fibrosis in animals subjected to TAA induction. Collagen fibers were observed spreading from portal areas and around hepatocyte plates, accumulating in the perisinusoidal space (Figure 3b). Statistical analysis revealed a significant reduction in collagen deposition in the ASC group, approaching the baseline levels observed in the control group (Figures 3c,d). The analysis of AST, a liver enzyme, in blood plasma demonstrated a significant increase in the TAA+LPS group compared to the control, and although no increase was observed in the treatment with the supernatant during the analyzed period, ASC group levels of AST in the plasma were similar to the control animals (Figure 3e).

Assessment of lung injury and inflammation

Using routine staining, it was possible to recognize and quantify three histological parameters of ALI using score counting: (1) thickening of the interalveolar septa; (2) the presence of interstitial leukocyte infiltration, especially of neutrophils and lymphocytes, both within the interalveolar septa and in the proximity of vessels and bronchioles; and (3) the presence of leukocytes, notably neutrophils, within bronchioles, alveolar ducts and alveoli. Regarding the formation of hyaline membrane and fibrin deposits, these characteristics were not identified during our analyses, at 24h, 48h and 4 days after the injury.

We observed that after injury with LPS, there is an abrupt and significant increase in the three parameters evaluated (Figure 4), and that treatment with ASC secretome was able to significantly reduce interstitial neutrophils and thickening of the interalveolar septum. The photomicrographs demonstrate the remodeling of the lung parenchyma, with recovery of the alveolar morphology lost after the injury, and a reduced amount of inflammatory infiltration.

The results of immunohistochemistry for CD68, a lung macrophage marker, confirmed the expected staining findings

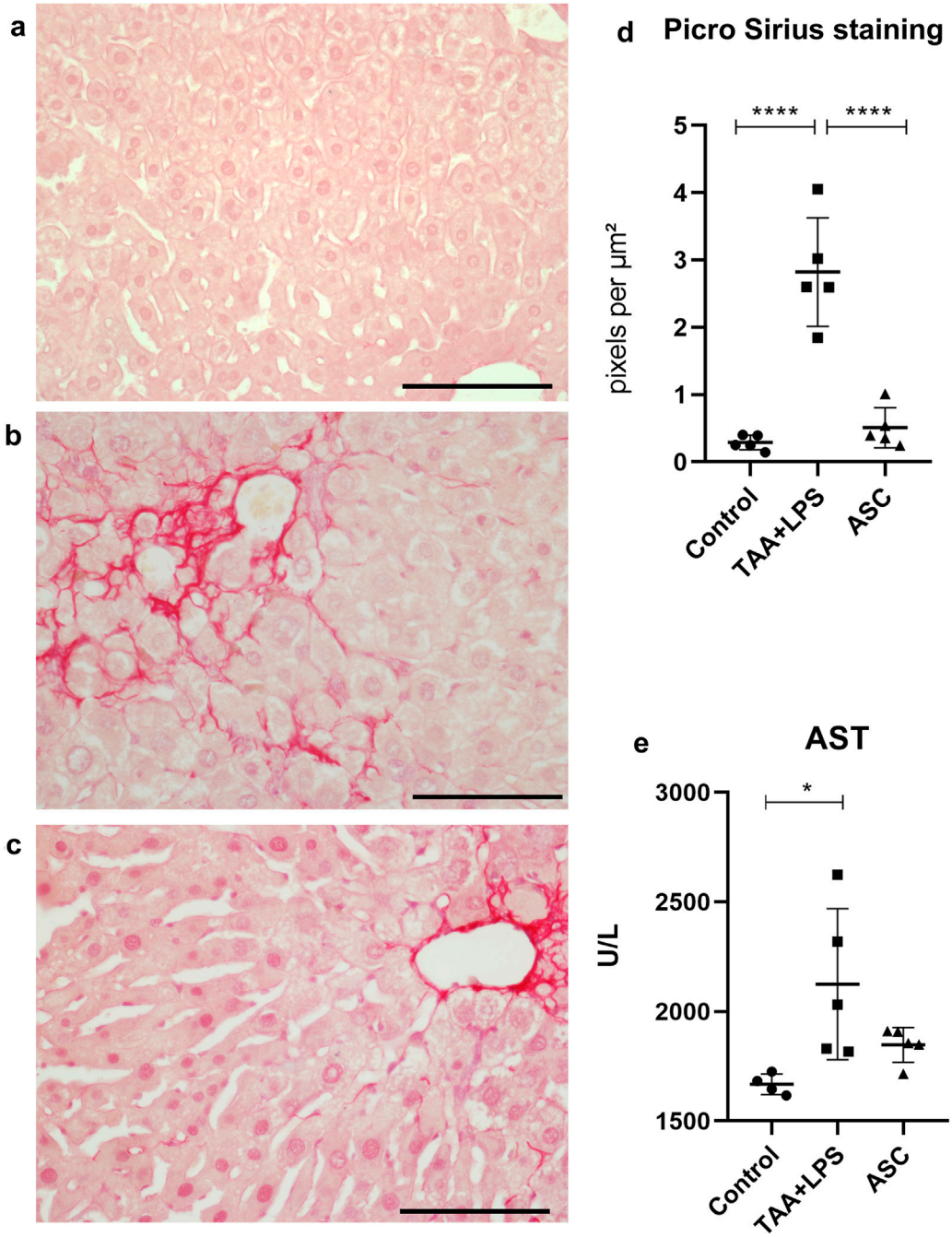

FIGURE 3
Picro Sirius was used to highlight collagen fibers in liver samples. **(a)** Control Group, with collagen restricted to portal spaces and vessels. **(b)** TAA+LPS group presented an increase in collagen fibers in red, demonstrating prominent fibrosis in the portal spaces and diffuse fibrosis in perisinusoidal areas. **(c)** ASC group, where there is a smaller amount of red-stained fibers. Bar size = 100 µm. ×40 objective. ×400 magnification. **(d)** Quantification of the stained area by densitometry: Control group (0.2884 ± 0.1087); TAA+LPS (2,822 ± 0.8072) and ASC (0.5086 ± 0.2993). **(e)** AST plasma levels: Control group (1668 ± 46.91), TAA+LPS (2124 ± 345.4) and ASC (1848 ± 79.37). Data are presented as mean ± SD; each point represents an individual animal. Statistical analysis performed with one-way ANOVA followed by Tukey's post-test, ****P < 0.0001, *P < 0.05.

related to tissue inflammation. There was a significant increase in expression after injury with LPS (Figure 5), and a reduction in labeling after treatment with ASC secretome. Furthermore, in the injured group, we observed a large number of macrophages clustered in areas of inflammation, while in control and treated animals,

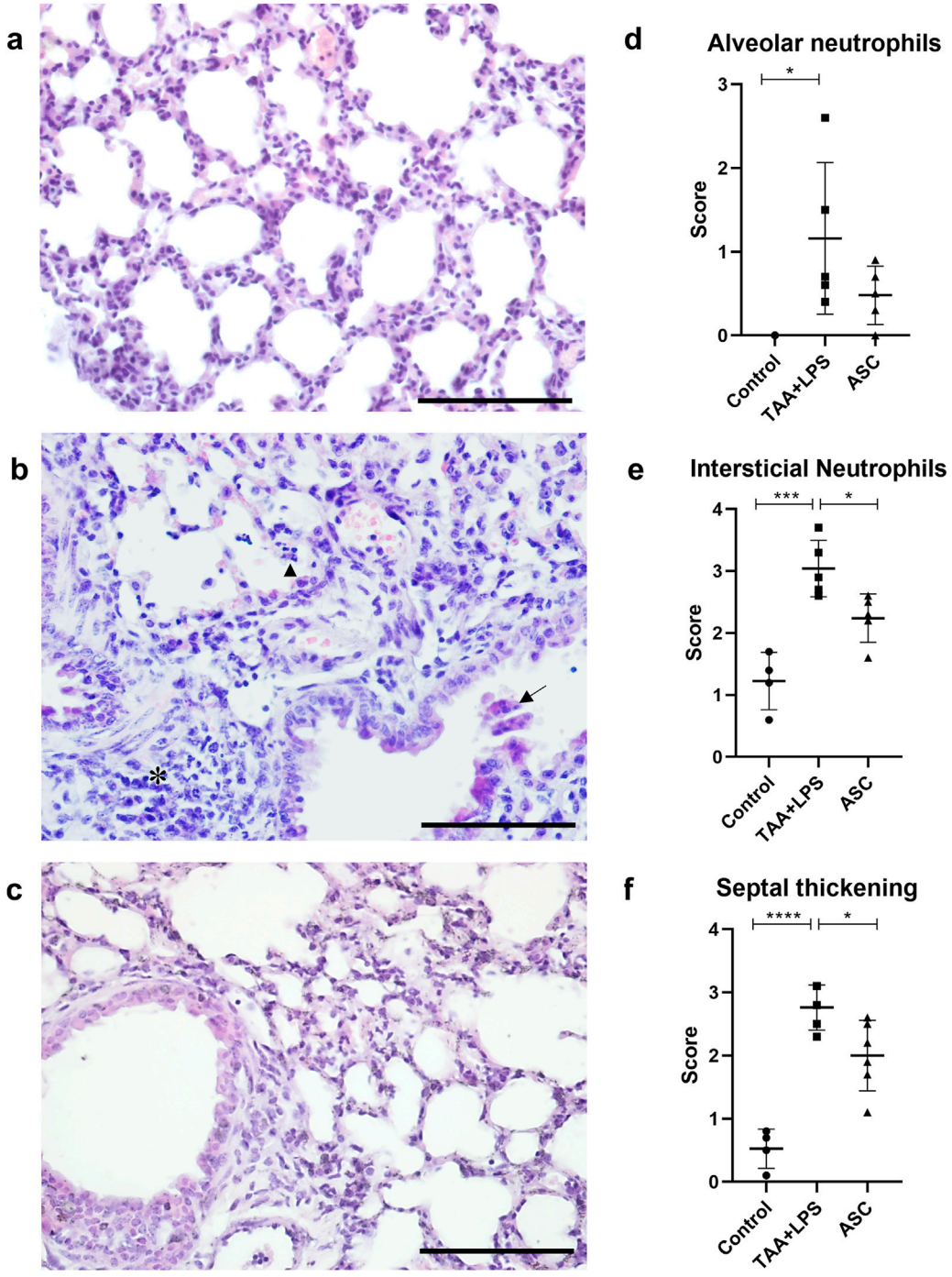

FIGURE 4
Histological analysis of the lung. **(a)** Control Group, with normal cytoarchitecture of the alveolar septa. **(b)** TAA+LPS group, diffuse thickening of the interalveolar septa, inflammatory infiltration (*), leukocytes in the bronchiolar space (arrow) and neutrophils in the alveolar space (arrowhead). **(c)** ASC group, where bronchioles without congestion were observed, and a significant reduction in the thickness of the interalveolar septa and the number of inflammatory cells. Bar size = 100 μm. ×40 objective. ×400 magnification. **(d–f)**, results of counting by scores of lung parameters, respectively: alveolar neutrophils (Control, 0.000 ± 0.000, TAA+LPS, 1,160 ± 0.9072 and ASC, 0.4800 ± 0.3493), interstitial neutrophils (Control, 1,225 ± 0.4646, TAA+LPS, 3,040 ± 0.4561 and ASC, 2,240 ± 0.3912) and thickening of the interalveolar septum (Control, 0.5250 ± 0.3096, TAA+LPS, 2,760 ± 0.3578 and ASC, 2,000 ± 0.5586). Data are presented as mean ± SD; each point represents an individual animal. Statistical analysis performed with one-way ANOVA followed by Tukey's post-test, ****P < 0.0001, ***P < 0.001, and *P < 0.05.

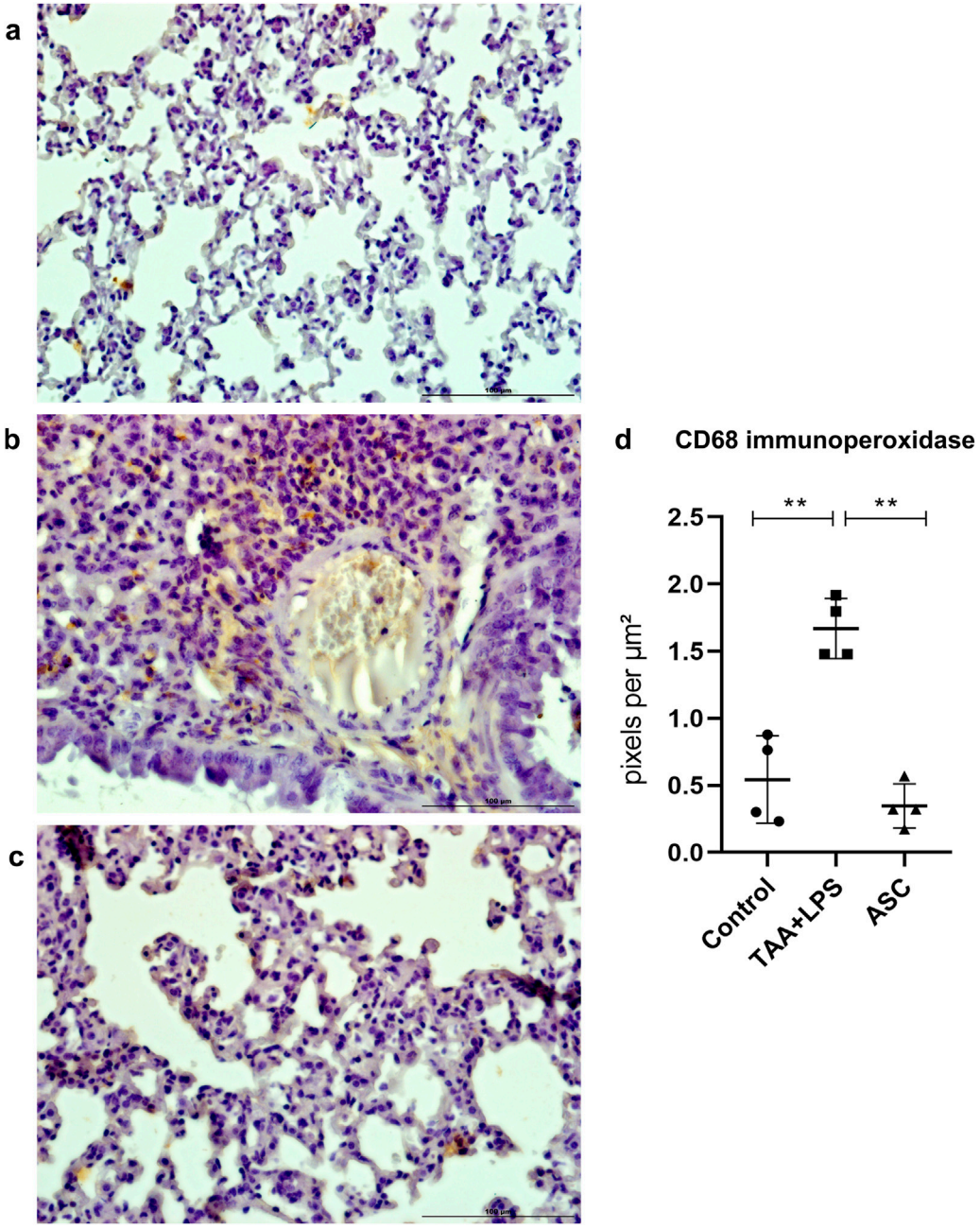

FIGURE 5
Immunoperoxidase to detect CD68 protein expression in the lung. **(a)** Control Group, with normal cytoarchitecture of the alveolar septa and basal levels of CD68 expression. **(b)** TAA+LPS group, with greater staining for CD68, especially in regions of inflammatory infiltration. **(c)** ASC group, reduction of inflammatory cells marked with CD68. Bar size = 100 µm. ×40 objective. ×400 magnification. **(d)** CD68 labeling quantification showed that ASC secretome is effective in reducing tissue macrophages. Control (0.5436 ± 0.3253), TAA+LPS (1,731 ± 0.2267), and ASC (0.3556 ± 0.2002). Data are presented as mean ± SD; each point represents an individual animal. Statistical analysis performed with one-way ANOVA followed by Tukey's post-test, **P < 0.01.

macrophages were found in the usual location, associated with the alveolar space.

TNF-α is an inflammatory cytokine of relevance as a predictor of loss of lung function and injury severity. Similar to CD68 labeling, marked and diffuse expression occurred after LPS injury, which was significantly reduced in animals treated with the ASC secretome (Figure 6).

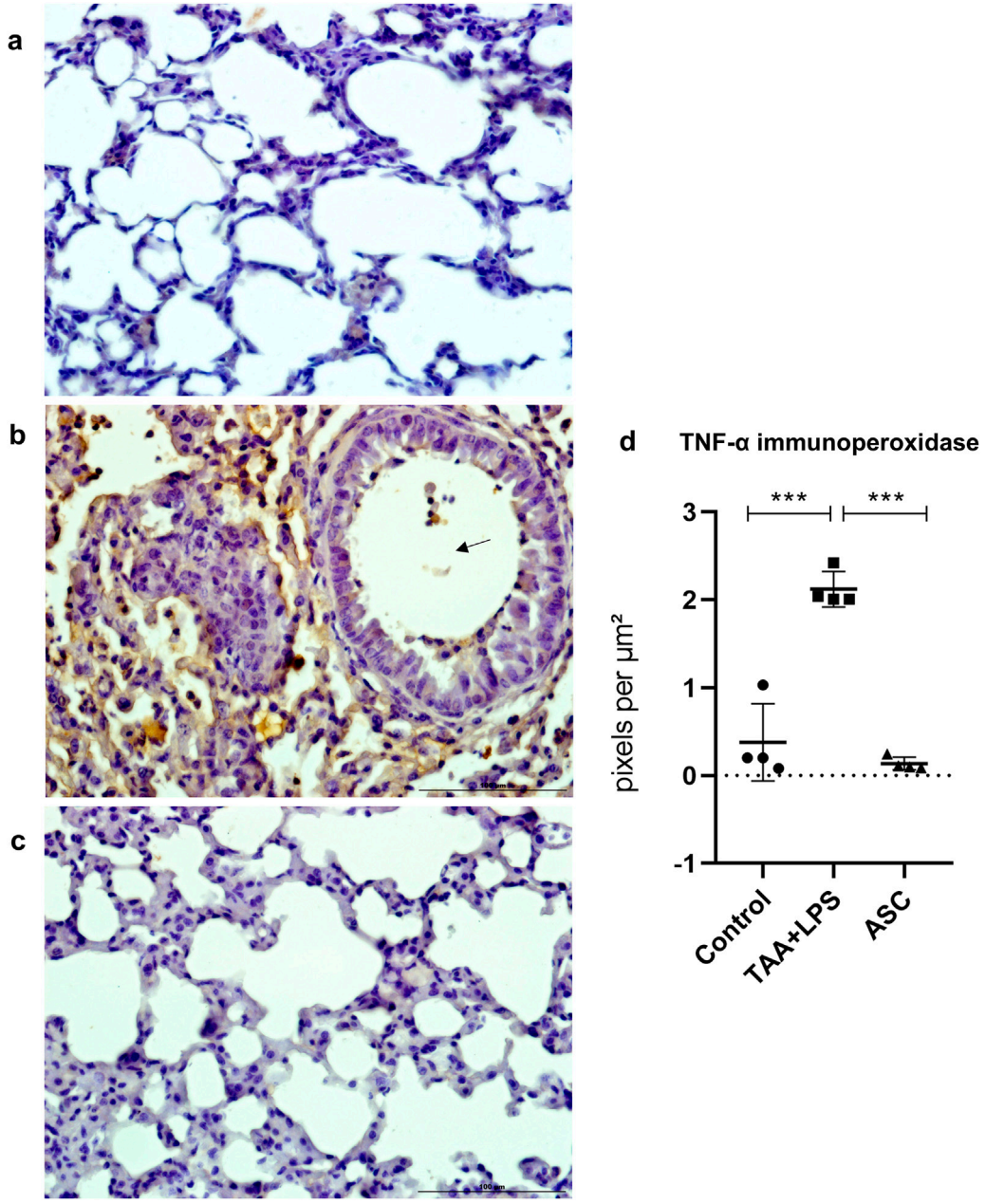

FIGURE 6
Immunoperoxidase to detect TNF-α protein expression in the lung. **(a)** Control Group, with normal cytoarchitecture of the alveolar septa and basal levels of TNF-α expression. **(b)** TAA+LPS group, with greater staining for TNF-α, diffusely around bronchioles and thickened interalveolar septa. Marking is also observed in leukocytes inside a bronchiole (arrow). **(c)** ASC group, with lower expression of TNF-α and preserved alveolar cytoarchitecture. Bar size = 100 µm. ×40 objective. ×400 magnification. **(d)** TNF-α labeling quantification showed that ASC secretome is effective in reducing inflammation sites in the lung parenchyma. Control (0.4378 ± 0.5174), TAA+LPS (2.157 ± 0.2296), and ASC (0.1367 ± 0.07313). Data are presented as mean ± SD; each point represents an individual animal. Statistical analysis performed with one-way ANOVA followed by Tukey's post-test, ***P < 0.001.

Plasma cytokine analysis

There was a significant increase in plasma levels of the cytokines IL-10, IL-17A, IFN-γ, TNF-α, IL-6, IL-4 in the TAA+LPS group when compared to the control group, and a marked reduction of all these cytokines was observed in the ASC group compared to the TAA+LPS group (Figure 7). As for IL-2, statistical tests did not reveal significant differences between

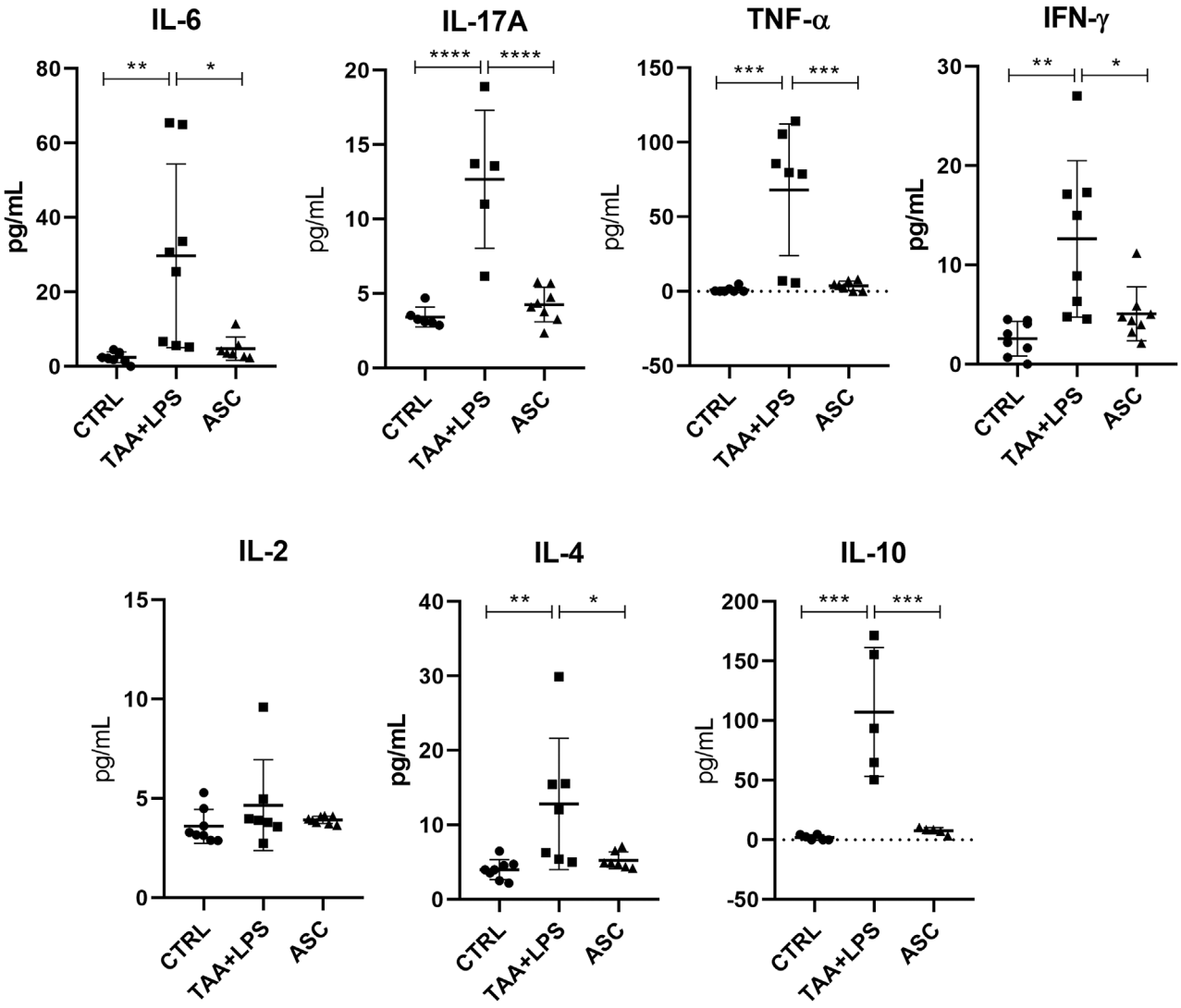

FIGURE 7
IL-6, IL-17A, TNF-α, IFN-γ, IL-2, IL-4, and IL-10 plasma levels were analyzed in a flow cytometer using the CBA kit (BD Biosciences) for Th1, Th2 and Th17 responses, and are expressed as a concentration of pg/mL. Data are presented as mean ± SD; each point represents an individual animal. Statistical analysis performed with one-way ANOVA followed by Tukey's post-test, ****P < 0.0001, ***P < 0.001, **P < 0.01, and *P < 0.05.

groups. All results obtained in animals treated with ASC secretome demonstrated a return of cytokine concentrations to levels close to control animals, indicating a systemic immunomodulatory effect from ASCs secretome.

Liver cytokine analysis

TAA administration was associated with an increase in IFN-γ, IL-4, IL-6 and IL-10 levels in liver tissues of the TAA+LPS group. However, ASC secretome correlated with decreased levels of these cytokines, especially IL-6, showing an improvement towards a decreased inflammatory activity (Figure 8).

Lung cytokine analysis

Results showed that ASC treatment correlated with significantly decreased TNF-α and IL-17A levels in the lung, 7 days after acute LPS-induced inflammation and 6-weeks chronic TAA exposure (Figure 9).

Discussion

In this work, ASC secretome effects in a model of concomitant liver fibrosis and ALI were assessed to evaluate its therapeutic potential in chronic-acute disease. Although there

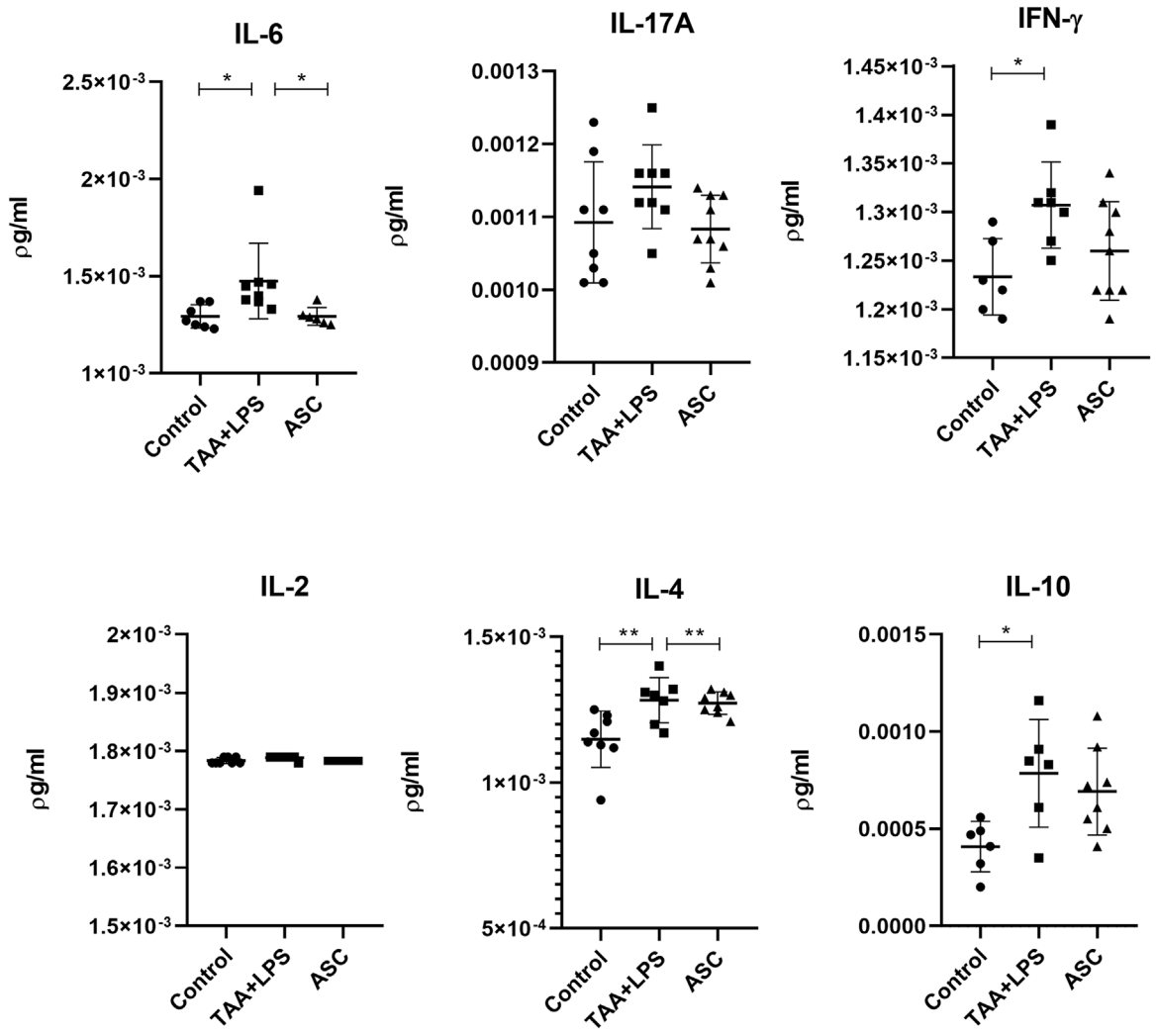

FIGURE 8
Levels of IL-6, IL-17A, IFN-γ, IL-2, IL-4, and IL-10 in liver lysates were quantified by flow cytometry using the CBA kit (BD Biosciences) to assess Th1, Th2, and Th17 responses, and are expressed as pg/mL. Data are presented as mean ± SD; each point represents an individual animal. Statistical analysis was performed using one-way ANOVA followed by Holm–Sidak's post-test. **P < 0.01, *P < 0.05.

is much data confirming that ASC paracrine modulation helps ameliorate both chronic and acute disorders, for the first time we demonstrated that this is also possible in a murine model of a CLD-ALI scenario, where both injured liver and lung were benefited for ASC secretome administration, as evidenced by a significant decrease in liver fibrosis and in inflammatory activity in the lung as well as in the systemic circulation. It is noteworthy that liver fibrosis by TAA and ALI by LPS have completely unique features, having in common a prominent inflammatory background, but in each case, different inflammatory cells and molecules are involved. Nevertheless, there is significant interchange between the liver and lung circulatory axis [34, 35], and this feature must also be considered when these organs are affected.

CLD is a condition characterized by continuous and sustained inflammation leading to fibrosis and structural liver changes. Liver fibrosis, triggered by various factors, poses a significant health challenge, as it can progress to cirrhosis and hepatocellular carcinoma. This process involves the activation of Kupffer cells and hepatic stellate cells, and abnormal extracellular matrix deposition [1, 22, 36]. Different chemical compounds like CCl_4, dimethylnitrosamine and TAA are used to induce liver fibrosis in animal models. Each model has unique characteristics and provides valuable insights for effective therapeutic strategies [32].

ALI, whether associated or not with acute respiratory distress syndrome (ARDS), has serious consequences and high mortality rates, and inflammation as well as oxidative stress play a

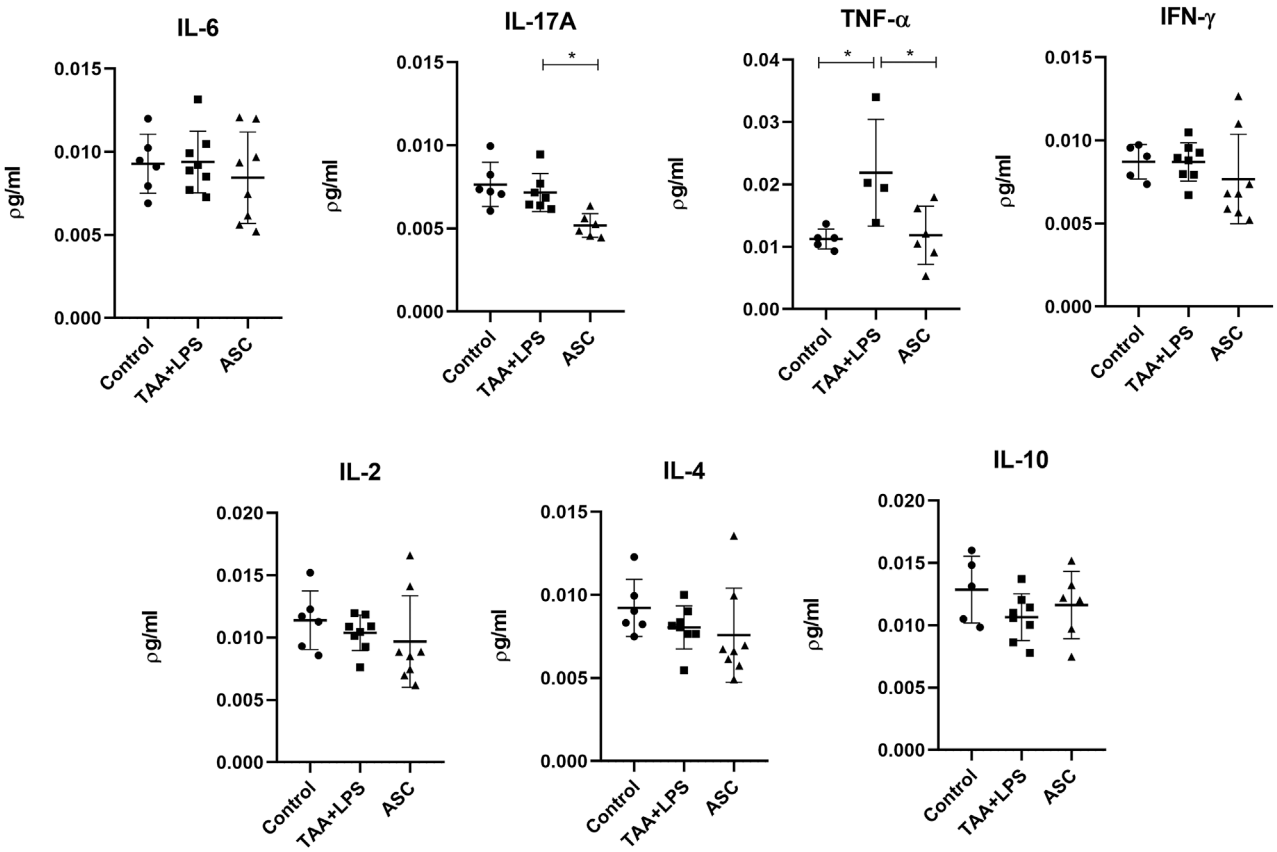

FIGURE 9
Levels of IL-6, IL-17A, TNF-α, IFN-γ, IL-2, IL-4, and IL-10 in lung lysates were analyzed in a flow cytometer using the CBA kit (BD Biosciences) for Th1, Th2 and Th17 responses, and are expressed as a concentration of pg/mL. Data are presented as mean ± SD; each point represents an individual animal. Statistical analysis performed with one-way ANOVA followed by Holm–Sidak's post-test, **P < 0.01, and *P < 0.05.

significant role [37, 38]. The liver-lung interplay is little explored, and bacterial endotoxins such as LPS - commonly found in the gut and a hallmark of severe bacterial infection and sepsis - are largely absorbed by the mesenteric veins, which carry the toxins to the liver, and further to systemic circulation, from which they can lead to severe lung damage [34, 39–41]. Therefore, LPS is widely used to study acute lung injuries, as it may mimic the histopathological features of human lung injury induced by respiratory pathogens. LPS can also potentially lead to hepatic compromise in cirrhotic individuals, increasing the severity and mortality rate of the disease [42–45].

MSC have been the focus of intensive research for clinical applications aimed at tissue regeneration, metabolic and musculoskeletal disorders, acute and chronic inflammatory and autoimmune diseases, with prospects for innovative discoveries. MSC secretome consists of diverse bioactive molecules, including small and large extracellular vesicles, cytokines, and growth factors [18, 20, 46]. These substances have the capability to influence processes such as tissue regeneration, immune response, angiogenesis and inflammation. They can modulate the inflammatory response and reduce fibrogenesis, affecting both the local and systemic environment when released by MSC. There is increasing interest in defining the content of exosomes in MSC secretome and in developing strategies to escalate its production, for use as a potential therapeutic treatment, with the advantage of being an acellular product, thus presenting greater safety for clinical use [27, 28, 47, 48].

The major concerns regarding cell therapies are defining the complex interactions between donor and recipient's cells and establishing the complete composition of the cell solution obtained in each therapeutic protocol. When secretome is applied, these concerns are more easily assessed, because the complexity is reduced from live cells to simply secreted molecules and vesicles, in a solution that is suitable for proteomic screenings [46, 48]. Bearing this in mind, this work aimed at the potential benefits of MSC secretome in multiple organs and pathological conditions after peritoneal administration and absorption, proving that this is an easy and effective way of delivering MSC derivatives, independently of the target organ.

An interesting aspect in this choice is that MSC molecules and exosomes are easily absorbed through the peritoneal membrane, and particularly exosomes possess surface receptors that help deliver them to injured and inflamed sites via circulation, after absorption [47]. Alternatively, if ASCs hole fraction was to be used, the best access pathway would be by vascular administration, implying a greater risk of thromboembolic events [46].

The effectiveness of MSC depends on several factors, and this is a sort of heterogeneous and complex population in terms of phenotypic characterization (such as a non-exclusive CD105, CD90, CD73 expression and exclusion of hematopoietic markers) and functional roles (the multipotent capacity to differentiate through fibrogenic, adipogenic, chondrogenic, or osteogenic processes under certain stimuli). Today, MSC are considered the progeny of *bona fide* mesenchymal stem cell precursors that are present in some tissues at an extremely low rate [19]. MSC therapeutic capacity is influenced by different aspects of the organism, namely the original tecidual source, age, general metabolic state and preexisting chronic conditions [46, 47]. There is evidence that MSC exert their beneficial roles through the paracrine way. This effect is observed in both animal and clinical studies, for a vast myriad of diseases of diverse etiologies [18, 20, 46, 47, 49]. Our group has published evidence on MSC therapeutic effect on liver fibrosis previously [25, 50], as well as many worldwide groups in different models and experimental designs, including acute liver injury [22, 24, 26]. This approach was proven true for different models of lung injury likewise [29, 51–55], however, for the first time we observed in a murine preclinical model that the ASCs secretome can exert its therapeutic effects simultaneously and systemically in both liver and lung disease, which points to a promising and safe strategy when conventional pharmacological therapy is complicated by multiorgan injury.

MSC secretome stimulates fibrosis regression through multiple pathways, leading to immunomodulation towards M2 phenotype in tecidual macrophages, which is a first kick towards fibrogenic cell deactivation and apoptosis, favoring tissue remodeling in a beneficial way. The common cytokine repertoire in this scenario may include unexpectedly high levels of interleukin IL-6 and low levels of IL-10, which stimulates hepatocyte proliferation and hepatic remodeling in CLD [22, 24, 26]. In the present study, we aimed to answer whether ASC could still be effective for liver regeneration in a severe lung injury situation, and histological as well as plasma analysis showed that the secretome maintained its effect in the liver during ALI, although we believe that liver regeneration appeared slower or in a lesser extent because we expected a more pronounced reduction in AST plasmatic levels in the ASC treated group. This underscores the need to assess durability and dosing frequency in future studies, as repeated administration has been shown to prolong therapeutic effects. In this respect, although repeated dosing has been shown to prolong therapeutic benefits in chronic injury models [27], our study focused on demonstrating that a minimal secretome dose was sufficient to achieve systemic and hepatic effects, and future work should address whether additional administrations could further enhance recovery. Several chronic conditions in the liver can lead to loss of pulmonary function even in the absence of a pathogenic infectious agent, such as hepatopulmonary syndrome observed in cases of severe cholestasis and/or portal hypertension, in NAFLD, decompensated cirrhosis and in chronic infections with hepatitis viruses [56–60]. This observation enhances the multiuse advantages of using MSC secretome in systemic delivery for CLD patients. In our study, LPS induction resulted in a massive injury to the lung parenchyma, with widespread disorganization of interalveolar septa and other inflammatory features such as a marked increase in CD68 and TNF-α levels, as observed by other authors [42–44]. All these features were obviously attenuated after ASC secretome treatment, disregarding the preexisting CLD condition, showing that the reduction in lung macrophages is associated with TNF-α decrease, in an overall decline of the inflammatory activity inflicted by LPS. This was even more encouraging by the observation that all plasmatic cytokines that were quite imbalanced in the TAA+LPS group returned to normal basal levels after the secretome therapy. In fact, the well-known cytokine storm is a common cause of severe and fatal lung and multiorgan injury, including acute liver failure [4, 13, 61], and LPS administration simulated a similar scenario detectable in the altered cytokine plasmatic levels in this study.

Of the seven cytokines related to Th1, Th2 and Th17 responses measured in the present work, only cytokine IL-2 was not affected in the plasma, nor by our experimental disease model, nor by the secretome treatment. This is because this protein is more related to lymphocyte activation in pathogenic infections, and although LPS is of bacterial origin, it does not lead to a complete immune response [44, 62]. It is noteworthy that the main cytokines elevated in our injury model are IL-10, IL-17A and TNF-α, what denotes the diverse nature of the inflammatory response in this case, since there are two different diseases involved, both in major organs that impact directly in systemic parameters, and of diverse cause (chronic and acute). Cytokines IL-6 and IL-10, although thought of generally having inflammatory and anti-inflammatory properties respectively, play very diverse roles in the local and systemic regulation of the immune response and bone marrow hematopoiesis [63–65]. These cytokines can promote both pro-inflammatory and anti-inflammatory responses according to the local microenvironment status and cell interactions influencing their production [64, 65]. The normalization of all plasmatic cytokines affected by chronic TAA and acute LPS administration to levels similar to the control group in the ASC group points to a significant immunomodulation capacity of the ASC secretome in regulation of the systemic immune response, confirming that this

therapy which may be benefic even in respiratory infectious diseases [66].

Further exploration of systemic immunomodulation remains essential to strengthen the translational relevance of our findings. While the observed normalization of circulating cytokines indicates broad immune rebalancing, more detailed analyses—such as longitudinal cytokine kinetics, flow cytometry of immune cell subsets, and functional assays of T cells, macrophages, and NK cells—would help delineate the mechanisms by which MSC-derived products exert their effects. Such approaches could clarify whether the modulation is transient or sustained, specific to certain pathways, or generalized across the immune network. Future studies integrating multi-omics profiling and temporal resolution will be critical to validate systemic immunomodulation as a core mechanism underlying therapeutic benefit [20].

Our metabolomic profiling of ASC secretome further supports a mechanistic link with the immunomodulatory effects observed. The presence of agmatine, reported to attenuate pro-inflammatory signaling and nitric oxide synthase activity [67], may have a role with the reduction in IL-6 and TNF-α detected in plasma and tissues. Likewise, homoarginine, which has been associated with endothelial protection and antifibrotic processes [68], may contribute to the tissue-repair context observed in the liver and lung. Beyond these specific metabolites, the abundance of amino acids and arginine-derived compounds suggests engagement of pathways linked to redox balance and immune regulation, which aligns with the systemic normalization of cytokines after treatment. While correlative, these findings reinforce the hypothesis that secretome bioactivity involves a coordinated metabolic–immune interface that merits further targeted validation.

Regarding liver and lung tissue levels of the measured cytokines, it is noteworthy that given the time point of analysis (7 days after injuries), early and minor local changes in the tissues were not scored. However, after ASC treatment, we observed a decrease in the main cytokines involved in inflammatory processes in each organ and model, as for TNF-α in acute lung injury (confirming immunoperoxidase results), and IL-6 in chronic liver fibrosis. These data show that ASC can attenuate different inflammatory processes in diverse organ systems, revealing a multifaceted effect which proved to be efficient in reverting injuries in the different pathological models applied in this study.

The differential cytokine responses observed in liver and lung allow us to hypothesize potential cellular and molecular pathways involved. The reduction of hepatic IL-6 may reflect modulation of Kupffer cells and hepatic stellate cells, consistent with a dampening of STAT3-driven inflammatory signaling. In parallel, the decrease in pulmonary TNF-α suggests inhibition of NF-κB activity, a central axis in alveolar macrophage–mediated inflammation [29]. While our data do not directly establish these mechanisms, proposing such links highlights plausible immune and stromal cell populations as targets of secretome activity and provides a framework for future mechanistic investigation.

In comparison with existing MSC-based therapies, our findings underscore key distinctions among live-cell administration, exosome-enriched products, and unfractionated secretome. Direct infusion of MSCs has been extensively tested and offers regenerative and immunomodulatory benefits, but concerns remain regarding engraftment efficiency, potential for ectopic differentiation, and risks such as microvascular occlusion [18]. Exosome-based strategies, in turn, provide mechanistic precision through well-defined vesicular cargo but are limited by complex and costly isolation procedures that challenge large-scale clinical translation. Unfractionated secretome integrates soluble proteins, metabolites, and extracellular vesicles, retaining broad therapeutic activity while offering advantages in manufacturing scalability and accessibility, which are particularly relevant in resource-limited health systems [69, 70]. This layered comparison highlights that secretome-based approaches may combine safety and feasibility benefits while reducing the risks associated with cell-based administration. In summary, our findings reinforce the therapeutic potential of ASC-derived secretome in a preclinical setting, suggesting it may represent a minimally processed, cell-free strategy applicable to inflammatory and fibrotic conditions. Importantly, the use of unfractionated secretome underscores its possible translational relevance in settings where advanced processing technologies for exosome or EV isolation are technically or economically prohibitive. This aligns with the urgent need for scalable and accessible regenerative interventions in real-world clinical systems [69].

Conclusion

In conclusion, this study provides evidence that ASC secretome therapy may be a helpful tool in the treatment of liver fibrosis and ALI. Its potential to modulate the inflammatory response both systemically and locally, promote tissue regeneration, and attenuate fibrosis makes it a promising approach for these conditions, although the mechanistic effects and protocol improvement demand further investigations.

Despite promising results, there are challenges to overcome before MSC secretome therapy is widely adopted in clinical practice. Additional studies are needed to define secretome composition and to understand the mechanisms of action involved in its regenerative and immunomodulating responses, before conducting controlled clinical trials to assess efficacy and safety in human patients.

Author contributions

AM conducted all the experiments and participated in manuscript writing, KP participated in experimental design and all cell culture proceedings and cytometric assays and analyses, AP helped in animal procedures, GP, AN, and VA conducted histological processing, staining and immunoperoxidase assays, EC and AT helped in funding

acquisition and manuscript revision, and SC participated in conception and experimental design, funding acquisition and manuscript writing. All authors contributed to the article and approved the submitted version.

Data availability

The original contributions presented in the study are included in the article/supplementary material, further inquiries can be directed to the corresponding author.

Ethics statement

The animal study was approved by Ethics Committee for the Care and Use of Experimental Animals of the institution (protocol IBRAG 031/2023). The study was conducted in accordance with the local legislation and institutional requirements.

Funding

The author(s) declare that financial support was received for the research and/or publication of this article. This study was supported by the following funding agencies: Conselho Nacional de Desenvolvimento Científico e Tecnológico (CNPq) (grant number 426916/2018-2); Fundação Carlos Chagas Filho de Amparo à Pesquisa do Estado do Rio de Janeiro (FAPERJ) (grants numbers E26/200.145/2023 and E-26/210.521/2019); and Coordenação de Aperfeiçoamento de Pessoal de Nível Superior (CAPES) (Master's scholarship).

Conflict of interest

The author(s) declared no potential conflicts of interest with respect to the research, authorship, and/or publication of this article.

Generative AI statement

The author(s) declare that no Generative AI was used in the creation of this manuscript.

Any alternative text (alt text) provided alongside figures in this article has been generated by Frontiers with the support of artificial intelligence and reasonable efforts have been made to ensure accuracy, including review by the authors wherever possible. If you identify any issues, please contact us.

References

1. Pellicoro A, Ramachandran P, Iredale JP, Fallowfield JA. Liver fibrosis and repair: immune regulation of wound healing in a solid organ. *Nat Rev Immunol* (2014) **14**:181–94. doi:10.1038/nri3623

2. Hu X, Sun L, Guo Z, Wu C, Yu X, Li J. Management of COVID-19 patients with chronic liver diseases and liver transplants. *Ann Hepatol* (2022) **27**:100653. doi:10.1016/j.aohep.2021.100653

3. Portincasa P, Krawczyk M, Smyk W, Lammert F, Di Ciaula A. COVID-19 and non-alcoholic fatty liver disease: two intersecting pandemics. *Eur J Clin Invest* (2020) **50**:e13338. doi:10.1111/eci.13338

4. Brozat JF, Hanses F, Haelberger M, Stecher M, Dreher M, Tometten L, et al. COVID-19 mortality in cirrhosis is determined by cirrhosis-associated comorbidities and extrahepatic organ failure: results from the multinational LEOSS registry. *United Eur Gastroenterol J* (2022) **10**:409–24. doi:10.1002/ueg2.12232

5. Saviano A, Wrensch F, Ghany MG, Baumert TF. Liver disease and coronavirus disease 2019: from pathogenesis to clinical care. *Hepatology* (2021) **74**:1088–100. doi:10.1002/hep.31684

6. Elhence A, Vaishnav M, Biswas S, Anand A, Gunjan D, Kedia S, et al. Predictors of in-hospital outcomes in patients with cirrhosis and coronavirus Disease-2019. *J Clin Exp Hepatol* (2022) **12**:S29–886. doi:10.1016/j.jceh.2021.10.052

7. Guerra Veloz MF, Cordero Ruiz P, Ríos-Villegas MJ, Del Pino Bellido P, Bravo-Ferrer J, Galvés Cordero R, et al. Liver manifestations in COVID-19 and the influence of pre-existing liver disease in the course of the infection. *Revista espanola de enfermedades digestivas* (2021) **113**:103–9. doi:10.17235/reed.2020.7627/2020

8. Rabiee A, Sadowski B, Adeniji N, Perumalswami PV, Nguyen V, Moghe A, et al. Liver injury in liver transplant recipients with coronavirus disease 2019 (COVID-19): U.S. multicenter experience. *Hepatology* (2020) **72**:1900–11. doi:10.1002/hep.31574

9. Nardo AD, Schneeweiss-Gleixner M, Bakail M, Dixon ED, Lax SF, Trauner M. Pathophysiological mechanisms of liver injury in COVID-19. *Liver Int* (2021) **41**:20–32. doi:10.1111/liv.14730

10. Parohan M, Yaghoubi S, Seraji A. Liver injury is associated with severe coronavirus disease 2019 (COVID-19) infection: a systematic review and meta-analysis of retrospective studies. *Hepatol Res* (2020) **50**:924–35. doi:10.1111/hepr.13510

11. Gupta A, Madhavan MV, Sehgal K, Nair N, Mahajan S, Sehrawat TS, et al. Extrapulmonary manifestations of COVID-19. *Nat Med* (2020) **26**:1017–32. doi:10.1038/s41591-020-0968-3

12. Nagarajan R, Krishnamoorthy Y, Rajaa S, Hariharan VS. COVID-19 severity and mortality among chronic liver disease patients: a systematic review and meta-analysis. *Prev Chronic Dis* (2022) **19**:210228. doi:10.5888/pcd19.210228

13. Premkumar M, Kedarisetty CK. Cytokine storm of COVID-19 and its impact on patients with and without chronic liver disease. *J Clin Transl Hepatol* (2021) **9**:256–64. doi:10.14218/JCTH.2021.00055

14. Li C, Chen Q, Wang J, Lin H, Lin Y, Lin J, et al. Clinical characteristics of chronic liver disease with coronavirus disease 2019 (COVID-19): a cohort study in Wuhan, China. *Aging* (2020) **12**:15938–45. doi:10.18632/aging.103632

15. Bajaj JS, O'Leary JG, Tandon P, Wong F, Garcia-Tsao G, Kamath PS, et al. Nosocomial infections are frequent and negatively impact outcomes in hospitalized patients with cirrhosis. *Am J Gastroenterol* (2019) **114**:1091–100. doi:10.14309/ajg.0000000000000280

16. Levesque E, Hoti E, Jiabin J, Dellamonica J, Ichai P, Saliba F, et al. Respiratory impact of paracentesis in cirrhotic patients with acute lung injury. *J Crit Care* (2011) **26**:257–61. doi:10.1016/j.jcrc.2010.08.020

17. Yang T, Zhang J, Lu J-H, Yang G-S, Wu M-C, Yu W-F. Risk factors influencing postoperative outcomes of major hepatic resection of hepatocellular carcinoma for patients with underlying liver diseases. *World J Surg* (2011) **35**:2073–82. doi:10.1007/s00268-011-1161-0

18. Galipeau J, Sensébé L. Mesenchymal stromal cells: clinical challenges and therapeutic opportunities. *Cell Stem Cell* (2018) **22**:824–33. doi:10.1016/j.stem.2018.05.004

19. Keating A. Mesenchymal stromal cells. *Curr Opin Hematol* (2006) **13**:419–25. doi:10.1097/01.moh.0000245697.54887.6f

20. Ouzin M, Kogler G. Mesenchymal stromal cells: heterogeneity and therapeutical applications. *Cells* (2023) **12**:2039. doi:10.3390/cells12162039

21. Cannavino J, Gupta RK. Mesenchymal stromal cells as conductors of adipose tissue remodeling. *Genes Dev* (2023) **37**:781–800. doi:10.1101/gad.351069.123

22. Roehlen N, Crouchet E, Baumert TF. Liver fibrosis: mechanistic concepts and therapeutic perspectives. *Cells* (2020) **9**:875. doi:10.3390/cells9040875

23. de Andrade DC, de Carvalho SN, Pinheiro D, Thole AA, Moura AS, de Carvalho L, et al. Bone marrow mononuclear cell transplantation improves mitochondrial bioenergetics in the liver of cholestatic rats. *Exp Cell Res* (2015) **336**:15–22. doi:10.1016/j.yexcr.2015.05.002

24. Ma C, Han L, Wu J, Tang F, Deng Q, He T, et al. Mesenchymal stem cell fates in murine acute liver injury and chronic liver fibrosis induced by carbon tetrachloride. *Drug Metab Disposition* (2022) **50**:1352–60. doi:10.1124/dmd.122.000958

25. Pinheiro D, Leirós L, Dáu JBT, Stumbo AC, Thole AA, Cortez EAC, et al. Cytokines, hepatic cell profiling and cell interactions during bone marrow cell therapy for liver fibrosis in cholestatic mice. *PLoS One* (2017) **12**:e0187970. doi:10.1371/journal.pone.0187970

26. Pinheiro D, Dias I, Ribeiro Silva K, Stumbo AC, Thole A, Cortez E, et al. Mechanisms underlying cell therapy in liver fibrosis: an overview. *Cells* (2019) **8**:1339. doi:10.3390/cells8111339

27. Sengupta V, Sengupta S, Lazo A, Woods P, Nolan A, Bremer N. Exosomes derived from bone marrow mesenchymal stem cells as treatment for severe COVID-19. *Stem Cells Development* (2020) **29**:747–54. doi:10.1089/scd.2020.0080

28. Rogers CJ, Harman RJ, Bunnell BA, Schreiber MA, Xiang C, Wang F-S, et al. Rationale for the clinical use of adipose-derived mesenchymal stem cells for COVID-19 patients. *J Transl Med* (2020) **18**:203. doi:10.1186/s12967-020-02380-2

29. Xiao K, He W, Guan W, Hou F, Yan P, Xu J, et al. Mesenchymal stem cells reverse EMT process through blocking the activation of NF-κB and hedgehog pathways in LPS-induced acute lung injury. *Cell Death Dis* (2020) **11**:863. doi:10.1038/s41419-020-03034-3

30. Paris GC, Azevedo AA, Ferreira AL, Azevedo YMA, Rainho MA, Oliveira GP, et al. Therapeutic potential of mesenchymal stem cells in multiple organs affected by COVID-19. *Life Sci* (2021) **278**:119510. doi:10.1016/j.lfs.2021.119510

31. Soliman AH, Abdellatif M. COVID-19 disease treatment: pivotal challenges in the arena of umbilical cord-mesenchymal stem cells (UC-MSCs). *Front Cell Dev Biol* (2023) **11**:1146835. doi:10.3389/fcell.2023.1146835

32. Wallace M, Hamesch K, Lunova M, Kim Y, Weiskirchen R, Strnad P, et al. Standard operating procedures in experimental liver research: thioacetamide model in mice and rats. *Lab Anim* (2015) **49**:21–9. doi:10.1177/0023677215573040

33. Du Z-A, Sun M-N, Hu Z-S. Saikosaponin a ameliorates LPS-induced acute lung injury in mice. *Inflammation* (2018) **41**:193–8. doi:10.1007/s10753-017-0677-3

34. Spagnolo P, Zeuzem S, Richeldi L, Du Bois RM. The complex interrelationships between chronic lung and liver disease: a review. *J Viral Hepat* (2010) **17**:381–90. doi:10.1111/j.1365-2893.2010.01307.x

35. Pai S, Njoku DB. The role of hypoxia-induced mitogenic factor in organ-specific inflammation in the lung and liver: key concepts and gaps in knowledge regarding molecular mechanisms of acute or immune-mediated liver injury. *Int J Mol Sci* (2021) **22**:2717. doi:10.3390/ijms22052717

36. Ju C, Tacke F. Hepatic macrophages in homeostasis and liver diseases: from pathogenesis to novel therapeutic strategies. *Cell Mol Immunol* (2016) **13**:316–27. doi:10.1038/cmi.2015.104

37. Butt Y, Kurdowska A, Allen TC. Acute lung injury: a clinical and molecular review. *Arch Pathol & Lab Med* (2016) **140**:345–50. doi:10.5858/arpa.2015-0519-ra

38. Mokrá D. Acute lung injury - from pathophysiology to treatment. *Physiol Res* (2020) **69**:S353–S366. doi:10.33549/physiolres.934602

39. Zhang H-Y. Intestinal endotoxemia plays a central role in development of hepatopulmonary syndrome in a cirrhotic rat model induced by multiple pathogenic factors. *World J Gastroenterol* (2007) **13**:6385. doi:10.3748/wjg.v13.i47.6385

40. Soulaidopoulos S, Cholongitas E, Giannakoulas G, Vlachou M, Goulis I. Review article: update on current and emergent data on hepatopulmonary syndrome. *World J Gastroenterol* (2018) **24**:1285–98. doi:10.3748/wjg.v24.i12.1285

41. Petruk G, Puthia M, Petrlova J, Samsudin F, Strömdahl AC, Cerps S, et al. SARS-CoV-2 spike protein binds to bacterial lipopolysaccharide and boosts proinflammatory activity. *J Mol Cell Biol* (2020) **12**:916–32. doi:10.1093/jmcb/mjaa067

42. Chen H, Bai C, Wang X. The value of the lipopolysaccharide-induced acute lung injury model in respiratory medicine. *Expert Rev Respir Med* (2010) **4**:773–83. doi:10.1586/ers.10.71

43. Peng D, Chen Y, Sun Y, Zhang Z, Cui N, Zhang W, et al. Saikosaponin A and its epimers alleviate LPS-induced acute lung injury in mice. *Molecules* (2023) **28**:967. doi:10.3390/molecules28030967

44. Ye R, Liu Z. ACE2 exhibits protective effects against LPS-induced acute lung injury in mice by inhibiting the LPS-TLR4 pathway. *Exp Mol Pathol* (2020) **113**:104350. doi:10.1016/j.yexmp.2019.104350

45. Chen M, Liu J, Yang W, Ling W. Lipopolysaccharide mediates hepatic stellate cell activation by regulating autophagy and retinoic acid signaling. *Autophagy* (2017) **13**:1813–27. doi:10.1080/15548627.2017.1356550

46. Wang L-T, Liu K-J, Sytwu H-K, Yen M-L, Yen BL. Advances in mesenchymal stem cell therapy for immune and inflammatory diseases: use of cell-free products and human pluripotent stem cell-derived mesenchymal stem cells. *Stem Cells Translational Med* (2021) **10**:1288–303. doi:10.1002/sctm.21-0021

47. Yuan Y-G, Wang J-L, Zhang Y-X, Li L, Reza AMMT, Gurunathan S. Biogenesis, composition and potential therapeutic applications of mesenchymal stem cells derived exosomes in various diseases. *Int J Nanomedicine* (2023) **18**:3177–210. doi:10.2147/ijn.s407029

48. Massa M, Croce S, Campanelli R, Abbà C, Lenta E, Valsecchi C, et al. Clinical applications of mesenchymal stem/stromal cell derived extracellular vesicles: therapeutic potential of an acellular product. *Diagnostics (Basel)* (2020) **10**:999. doi:10.3390/diagnostics10120999

49. Jayaramayya K, Mahalaxmi I, Subramaniam MD, Raj N, Dayem AA, Lim KM, et al. Immunomodulatory effect of mesenchymal stem cells and mesenchymal stem-cell-derived exosomes for COVID-19 treatment. *BMB Rep* (2020) **53**:400–12. doi:10.5483/bmbrep.2020.53.8.121

50. Carvalho SN, Lira DC, Oliveira GP, Thole AA, Stumbo AC, Caetano CE, et al. Decreased collagen types I and IV, laminin, CK-19 and α-SMA expression after bone marrow cell transplantation in rats with liver fibrosis. *Histochem Cell Biol* (2010) **134**:493–502. doi:10.1007/s00418-010-0746-2

51. Behnke J, Kremer S, Shahzad T, Chao C-M, Böttcher-Friebertshäuser E, Morty RE, et al. MSC based therapies—new perspectives for the injured lung. *J Clin Med* (2020) **9**:682. doi:10.3390/jcm9030682

52. Xu Y, Zhu J, Feng B, Lin F, Zhou J, Liu J, et al. Immunosuppressive effect of mesenchymal stem cells on lung and gut $CD8^+$ T cells in lipopolysaccharide-induced acute lung injury in mice. *Cell Prolif* (2021) **54**:e13028. doi:10.1111/cpr.13028

53. Liu A, Zhang X, He H, Zhou L, Naito Y, Sugita S, et al. Therapeutic potential of mesenchymal stem/stromal cell-derived secretome and vesicles for lung injury and disease. *Expert Opin Biol Ther* (2020) **20**:125–40. doi:10.1080/14712598.2020.1689954

54. Lopes-Pacheco M, Robba C, Rocco PRM, Pelosi P. Current understanding of the therapeutic benefits of mesenchymal stem cells in acute respiratory distress syndrome. *Cell Biol Toxicol* (2020) **36**:83–102. doi:10.1007/s10565-019-09493-5

55. Zhuang X, Jiang Y, Yang X, Fu L, Luo L, Dong Z, et al. Advances of mesenchymal stem cells and their derived extracellular vesicles as a promising therapy for acute respiratory distress syndrome: from bench to clinic. *Front Immunol* (2023) **14**:1244930. doi:10.3389/fimmu.2023.1244930

56. Kwak M-S, Kim E, Jang EJ, Lee C-H. The association of non-alcoholic fatty liver disease with lung function: a survey design analysis using propensity score. *Respirology* (2018) **23**:82–8. doi:10.1111/resp.13127

57. Goldberg DS, Fallon MB. The art and science of diagnosing and treating lung and heart disease secondary to liver disease. *Clin Gastroenterol Hepatol* (2015) **13**:2118–27. doi:10.1016/j.cgh.2015.04.024

58. Raevens S, Boret M, De Pauw M, Fallon MB, Van Vlierberghe H. Pulmonary abnormalities in liver disease: relevance to transplantation and outcome. *Hepatology* (2021) **74**:1674–86. doi:10.1002/hep.31770

59. Shikata F, Sakaue T, Nakashiro K, Okazaki M, Kurata M, Okamura T, et al. Pathophysiology of lung injury induced by common bile duct ligation in mice. *PLoS One* (2014) **9**:e94550. doi:10.1371/journal.pone.0094550

60. Nassef NA-A, Abd-El Hamid MS, Abusikkien SA, Ahmed AI. Quercetin ameliorates acute lung injury in a rat model of hepatopulmonary syndrome. *BMC Complement Med Ther* (2022) **22**:320. doi:10.1186/s12906-022-03785-w

61. Han H, Ma Q, Li C, Liu R, Zhao L, Wang W, et al. Profiling serum cytokines in COVID-19 patients reveals IL-6 and IL-10 are disease severity predictors. *Emerging Microbes & Infections* (2020) **9**:1123–30. doi:10.1080/22221751.2020.1770129

62. Zhang Y, Su J. Interleukin-2 family cytokines: an overview of genes, expression, signaling and functional roles in teleost. *Developmental & Comp Immunol* (2023) **141**:104645. doi:10.1016/j.dci.2023.104645

63. Tayal V, Kalra BS. Cytokines and anti-cytokines as therapeutics--an update. *Eur J Pharmacol* (2008) **579**:1–12. doi:10.1016/j.ejphar.2007.10.049

64. Wei H, Li B, Sun A, Guo F. Interleukin-10 family cytokines immunobiology and structure. *Adv Exp Med Biol* (2019) **1172**:79–96. doi:10.1007/978-981-13-9367-9_4

65. Rahman T, Das A, Abir MH, Nafiz IH, Mahmud AR, Sarker MR, et al. Cytokines and their role as immunotherapeutics and vaccine adjuvants: the emerging concepts. *Cytokine* (2023) **169**:156268. doi:10.1016/j.cyto.2023.156268

66. Sharma A, Chakraborty A, Jaganathan BG. Review of the potential of mesenchymal stem cells for the treatment of infectious diseases. *World J Stem Cells* (2021) **13**:568–93. doi:10.4252/wjsc.v13.i6.568

67. Wu G, Meininger CJ, McNeal CJ, Bazer FW, Rhoads JM. *Role of L-Arginine in nitric oxide synthesis and health in humans* (2021). p. 167–87.

68. Atzler D, Gore MO, Ayers CR, Choe C, Böger RH, de Lemos JA, et al. Homoarginine and cardiovascular outcome in the population-based Dallas heart study. *Arteriosclerosis, Thromb Vasc Biol* (2014) **34**:2501–7. doi:10.1161/atvbaha.114.304398

69. Vizoso F, Eiro N, Cid S, Schneider J, Perez-Fernandez R. Mesenchymal stem cell secretome: toward cell-free therapeutic strategies in regenerative medicine. *Int J Mol Sci* (2017) **18**:1852. doi:10.3390/ijms18091852

70. Rani S, Ritter T. The exosome - A naturally secreted nanoparticle and its application to wound healing. *Adv Mater* (2016) **28**:5542–52. doi:10.1002/adma.201504009

EBM Experimental Biology and Medicine

EBM is the official journal of the Society for Experimental Biology and Medicine

Experimental Biology and Medicine (EBM) is a global, peer-reviewed journal dedicated to the publication of multidisciplinary and interdisciplinary research in the biomedical sciences.

Discover more of our Special Issues

See more →

Contact

development@ebm-journal.org

See more

ebm-journal.org

publishingpartnerships.frontiersin.org/our-partners